Top Quark Spin and QCD Corrections in Event Generation

Lisa Hartgring

Top Quark Spin and QCD Corrections in Event Generation

Lisa Hartgring

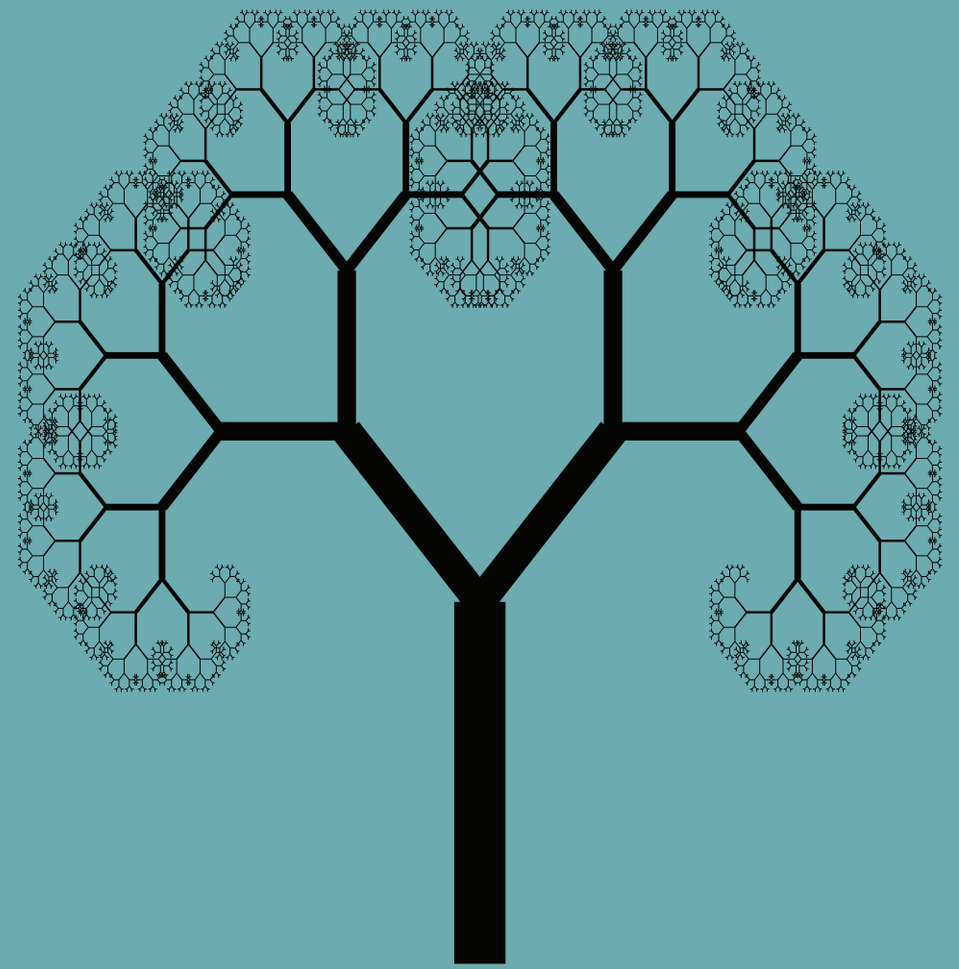

Lisa Hartgring

Top Quark Spin and QCD Corrections in Event Generation

Lisa Hartgring

Cover design: Gabriel Ybeles Smit.
Printed by: Proefschriftmaken.nl || Uitgeverij BOXPress.
Published by: Uitgeverij BOXPress, 's-Hertogenbosch.

This work is part of the research programme of the Foundation for Fundamental Research on Matter (FOM), which is part of the Netherlands Organisation for Scientific Research (NWO), programme 104 "Theoretical Particle Physics in the Era of the LHC".

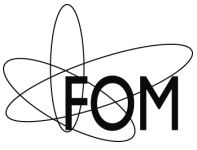

Top Quark Spin and QCD Corrections in Event Generation

ACADEMISCH PROEFSCHRIFT

ter verkrijging van de graad van doctor
aan de Universiteit van Amsterdam
op gezag van de Rector Magnificus
prof. dr. D.C. van den Boom
ten overstaan van een door het college voor promoties
ingestelde commissie,
in het openbaar te verdedigen in de Agnietenkapel
op vrijdag 5 juli, te 14:00 uur

door

Lisa Christina Hartgring

geboren te Eindhoven

Promotor:	prof. dr. E.L.M.P. Laenen
Overige leden:	prof. dr. S.C.M. Bentvelsen
	prof. dr. R.M. Godbole
	prof. dr. J. de Boer
	dr. W.J.P. Beenakker
	dr. P.Z. Skands
	dr. M. Vreeswijk

Faculteit der Natuurwetenschappen, Wiskunde en Informatica

Contents

The material presented in this thesis is based on the following publications.

Publications

L. Hartgring, E. Laenen and P. Skands, *Antenna Showers with One-Loop Matrix Elements*, *submitted to JHEP*.

G. Belanger, R. Godbole, L. Hartgring and I. Niessen, *Top Polarization in Stop Production at the LHC*, *accepted by JHEP*.

R.M. Godbole, L. Hartgring, I. Niessen and C.D. White, *Top polarisation studies in H^-t and Wt production*, *JHEP* **1201** (2012) 011.

Conference Proceedings

R.M. Godbole, L. Hartgring, I. Niessen and C.D. White, *Polarisation Studies in H^-t Production*, *Prospects for Charged Higgs Discovery at Colliders*.

R.M. Godbole, L. Hartgring, I. Niessen and C.D. White, *Top Polarisation in H^-t and Wt Production*, *Les Houches 2011: Physics at TeV Colliders New Physics Working Group Report*

Chapter 1

Introduction

The start of the Large Hadron Collider (LHC) in 2009 located at CERN, Geneva, has opened a new window for the search of elementary particles and will provide stringent tests for proposed theoretical frameworks of these particles and their forces. Our current understanding is described by the Standard Model (SM). This theory describes the interaction of six quarks and six leptons by the strong, weak and electromagnetical force, mediated by bosons. The model is completed with the Higgs mechanism that provides mass to the particles, and is largely confirmed by the recent discovery of the what seems to be SM Higgs boson. The model has been tested to impressive accuracy. Successful though it is, it fails to provide an explanation for astronomical observations as dark matter and energy. Moreover, the model only takes three fundamental forces into account, neglecting the force of gravity. One therefore often views the SM as an effective theory of a larger model.

Usage of the SM as an effective theory is sufficient to describe previous experiments. These unanswered questions however, have motivated proposals of more encompassing theories such as supersymmetry, strong dynamics models, etc.. While we expect the validity of the SM to be limited, it is a central question of modern particle physics where and how such new physics will show itself. The collision energy of the LHC is up to seven times larger than its predecessor the Tevatron at Fermi National Accelerator Laboratory, USA, and will allow for the testing of such new physics. The question posed translates to where and how to look for the deviations of the SM as predicted by these new theories, and this demands an increasingly higher accuracy of SM predictions. Standard Model predictions for collider observables are made using perturbative expansions in the coupling of the theory. The calculations can be depicted by Feynman diagrams, named after their inventor, representing a graphical interface for complicated mathematical expressions. The most interesting part of the collision takes place in the heart of the beam pipe at the primary interaction point, creating both stable and short-lived particles detected through their decay products. The prediction of a scattering process therefore takes all possible particles into account that may have propagated the intermediate state, given a certain initial and final state. The leading order (LO) contribution is defined by the sim-

plest diagrams, corresponding to those with the fewest vertices, possible in accordance with the required external particles. The next-to-leading-order (NLO) correction is given by diagrams that are two orders higher in the coupling. In most cases only the Quantum Chromodynamics (QCD) corrections, that dominate quark and gluon interactions, need to be taken into account. An example is given in fig. 1.1. The figure on the left depicts the leading order contribution to the scattering of a quark-antiquark pair, and the two rightmost figures examples of next-to-leading-order corrections. Being a quantum theory the predictions require the absolute value squared of the sum of diagrams, which explains that two orders higher in the coupling yields a diagram with a loop which gets contracted with a LO diagram, or diagrams with an additional final state particle contracted with itself.

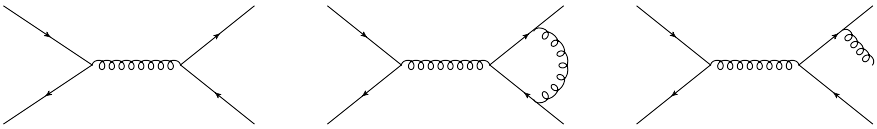

Figure 1.1: Examples of Feynman diagrams for the scattering of a quark and antiquark pair producing an intermediate gluon. The figure on the left denotes a LO diagram, and the two rightmost figures NLO diagrams.

For a proton-proton collider as the LHC the description is complicated by the initial state. Perturbative QCD cannot describe the strong binding effects that cause bound states as in the case of a proton. This makes it impossible to describe proton-proton collisions exactly. The factorization theorem allows one to separate the calculation in two parts, a hard interaction accounting for the small distance scattering of two partons (quarks or gluons), and the prediction of finding a certain parton in the proton [1, 2]. The parton model presents a basic picture of why we are allowed to view partons as individual non-interacting proton constituents. The relativistic proton is Lorentz contracted, while the interaction time between partons within the proton is time dilated, and therefore the proton can essentially be regarded as individual partons with a momentum fraction x while crossing the colliding proton. It is possible to prove [3] that such a picture holds under the influence of QCD corrections, with the derivation leading to the factorization theorem. Parton Distribution Functions (PDF) are fitted to sets of well calibrated data such as from Deep Inelastic Scattering (DIS). The cross-section σ for a scattering $pp \to jl$ can now be written as

$$\sigma_{pp\to jl} = \sum_{ik} \int \mathrm{d}x_1 \mathrm{d}x_2 f_{i/p}(x_1, \mu_F^2) f_{k/p}(x_2, \mu_F^2) \sigma_{ik\to jl}(Q^2, \mu_F^2), \qquad (1.1)$$

with x_1 and x_2 the energy fractions of the partons i and k, the PDFs are indicated with the function f, Q^2 indicates the scale of the hard interaction and μ^2 the factorization scale at which the hard scattering is separated from long distance interactions.

The hard scattering process, the perturbatively calculated piece, will yield an expression dependent on the momenta of the external particles, and needs to be integrated over unobserved phase space in order to obtain the total cross-section. Generally these expressions get increasingly more complicated as more massive particles and/or more than two final state particles are involved. This drives one to the use of numerical methods in order to solve the integrations. A naive approach uses an estimate of the average value to calculate the integrand I over its whole domain. For a one-dimensional function $g(x)$, with $x \in [a, b]$ this corresponds to

$$I = \int_a^b g(x)\mathrm{d}x \simeq \frac{(b-a)}{N} \sum_{i=1}^{N} g(x_i) + \mathcal{O}\left(\frac{1}{\sqrt{N}}\right), \tag{1.2}$$

with i denoting random points chosen from a uniform distribution between a and b. The central limit theorem states that the error to this estimate of the integrand may be approximated by $1/\sqrt{N}$ for large values of N. An obvious improvement of the approach is to focus on regions that yield the largest contribution to the integral. An interesting by-product of the calculation is the generation of an 'event', associating Feynman diagrams with explicit values for the momentum vectors of the particles. The complete cross-section is approximated by

$$\sigma = \int \frac{\mathrm{d}\sigma(x_1, \ldots, x_n)}{\mathrm{d}x_1 \ldots \mathrm{d}x_n}\, \mathrm{d}x_1 \ldots \mathrm{d}x_n. \tag{1.3}$$

The phase space of a cross-section containing N outgoing particles requires integration over $3N-4$ variables, accounted for by the variables x_i. We may naively interpret eq.(1.3) as the generation of an event with a weight $\mathrm{d}\sigma/\mathrm{d}x_1 \ldots \mathrm{d}x_n$. The weight indicates the importance of that phase-space point to the integrand. Therefore these distributions need to be unweighted in order for event generators to create events with the same weight. Such a procedure can be implemented with a 'hit-and-miss' approach. The algorithm requires the sacrifice of some events, to allow for the remainder to share equal weights. This approach consists of the following steps

- Select an event
- Generate a random number between zero and the maximum weight present.
- If the random number is smaller or equal to the weight accept the event, and reject otherwise.

We have assumed all weights to be positive definite. An intuitive way of understanding this, is by comparing the weights of two events, w_1 and w_2. Assuming $w_2 > w_1$, the probability for accepting w_2 is w_2/w_1 times larger than the probability of accepting w_1. As the random numbers are generated uniformly, we expect that when considering enough events, there will eventually be w_2/w_1 times more events accepted that started with a weight w_2 than events that started with a weight w_1. Because it can be time consuming to sacrifice events, the choice is often made to use all events with the allocated weights.

The previous procedure automatically generates distributions in x_i. The accuracy can, in principle, be made as high as desired given sufficiently large N.

With this description of events it is possible to simulate signals and background, and thereby explore the influence of new physics in collider events. One approach that is gaining much interest is to focus on the spin of the particle. The spin of a particle influences the angular orientation of its decay products. While, for instance, a top quark always carries spin-$\frac{1}{2}$, the preference for spin up or spin down (polarization) can be different depending on the model. Event simulation is used to investigate if spin information present in the hard scattering can be measured at the detector level. The top quark decays before the strong force causes it to hadronize, and thereby retains possibly interesting spin information in the top decay products. We start with exploring the spin dynamics in top production in chapter 2 together with the definition of various laboratory frame observables allowing for a connection between a theory's parameters and its decay products through the use of polarization. In chapter 3 the effect of NLO corrections to the observables is examined for the SM in comparison to Two Higgs Doublet Models. The focus on top polarization is completed with a survey of its sensitivity to the supersymmetric parameter space in the context of the MSSM.

For now, we have been generating events based on the Feynman diagrammatic approach. This treated the hard-scattering as a whole, creating intertwined products of momenta. An alternative way of building up a scattering event is by treating the particle radiations and interactions iteratively. Instead of requiring a certain initial and final state, the approach is to start with a specific LO process and radiate particles iteratively off the remainders of the LO process, a procedure commonly referred to as a parton shower. One can employ monopole radiation (radiation off one parent particle) or dipole radiation (radiation of a third particle between two parent particles). This transforms the LO process to a final state with additional partons. An interesting question that has to be addressed is how to incorporate the knowledge of NLO precision in such an approach. In chapter 5 a review of the VINCIA antenna shower is discussed for a Z boson decaying to two partons, together with a demonstration of the trivial matching to NLO while chapter 6 focusses on the generalization of consecutive NLO matching for an additional final state particle. The final chapter contains our conclusions.

Chapter 2

The Polarized Top Quark

Although the top quark had to settle for second place in particle popularity in the year 2012, its existence is closely related to the #1 particle: the discovered boson, be it the SM Higgs or an alternative. This relation is manifested by its heavy mass and associated large Yukawa coupling. It is also the top quark that poses an aesthetic threat to the SM. The top causes the largest, quadratically divergent, contribution to the SM Higgs one-loop mass correction thereby creating space for possible new physics to compensate this and have a natural Higgs mass value. Another important characteristic of the top quark is its large width, causing the top to decay before hadronizing, thereby retaining possibly interesting spin information. In this section we concentrate on the latter property and construct observables that reveal spin information in the top quark decay products. As we will see in chapter 3 and 4, this spin information is sensitive to new physics, which motivates the construction of observables that take advantage of this sensitivity.

2.1 The Polarized Top Cross-Section

Processes that produce a top quark, possibly in association with other particles, allow for the use of top polarization as an indicator for new physics. Polarization is a term quantifying the extent to which a particle with spin favors one spin direction over the other. Ideally the new physics will only affect the top production process, leaving the decay of the top, in essence, insensitive to it. To see that this can indeed be the case [4], we will start with investigating top production and decay, employing the Narrow Width Approximation (NWA) for the top quark. This allows us to split the spin-averaged matrix element squared $\overline{|\mathcal{M}|^2}$ into a part $\rho(\lambda, \lambda')$ that corresponds to the production of an on-shell top quark, and a part $\Gamma(\lambda, \lambda')$ that corresponds to on-shell decay of this quark

$$\overline{|\mathcal{M}|^2} = \frac{4\pi\delta(p_t^2 - m_t^2)}{\Gamma_t m_t} \sum_{\lambda,\lambda'} \rho(\lambda, \lambda')\Gamma(\lambda, \lambda') \,. \tag{2.1}$$

To obtain the averaged matrix element squared $\overline{|\mathcal{M}|^2}$, we have to sum over the top quark helicities λ and λ'. Here p_t^μ, m_t and Γ_t are the top quark momentum, mass and total decay width respectively, while $\rho(\lambda,\lambda')$ and $\Gamma(\lambda,\lambda')$ are matrices given by

$$\rho(\lambda,\lambda') = \mathcal{M}_\rho(\lambda)\mathcal{M}_\rho^*(\lambda') \quad \text{and} \quad \Gamma(\lambda,\lambda') = \mathcal{M}_\Gamma(\lambda)\mathcal{M}_\Gamma^*(\lambda')\,,$$

with $\mathcal{M}_\rho(\lambda)$ the matrix element of the production of a top quark with helicity λ and $\mathcal{M}_\Gamma(\lambda)$ the corresponding decay amplitude. Instead of summing, we can also project on these helicities to obtain the polarized cross section. To this end, we define top polarization vectors $S^{a,\mu}$ that form, together with the top momentum, an orthogonal set and are normalized to $S^a \cdot S^b = -\delta^{ab}$. We can then perform the helicity projection using the identities [5, 6]:

$$u(p_t,\lambda')\bar{u}(p_t,\lambda) = \frac{1}{2}\big(\delta_{\lambda\lambda'} + \gamma_5 \not{S}^a \tau^a_{\lambda\lambda'}\big)(\not{p}_t + m_t)\,, \tag{2.2}$$

$$v(p_t,\lambda')\bar{v}(p_t,\lambda) = \frac{1}{2}\big(\delta_{\lambda\lambda'} + \gamma_5 \not{S}^a \tau^a_{\lambda\lambda'}\big)(\not{p}_t - m_t)\,, \tag{2.3}$$

with τ^a the Pauli matrices. Since the transverse polarization is generally small, we will only consider the longitudinal polarization vector S^3 and set S^1 and S^2 to zero. The spatial part of S^3 is parallel to the top three-momentum, leading to

$$S^3 = \frac{1}{m_t}\big(|\vec{p}_t|, E_t\hat{\vec{p}}_t\big)\,. \tag{2.4}$$

Note that S^3 is not a Lorentz vector, reflecting the fact that the top quark helicity is not a Lorentz-invariant quantity. After phase space integration of $\rho(\lambda,\lambda')$ we obtain the polarization density matrix $\sigma(\lambda,\lambda')$. The top longitudinal polarization, defined along the axis S^3, is then equal to

$$P_t = \frac{\sigma(+,+) - \sigma(-,-)}{\sigma(+,+) + \sigma(-,-)}\,, \tag{2.5}$$

where $\sigma(+,+)$ ($\sigma(-,-)$) is the cross section for a positive (negative) helicity top quark. A negative (positive) polarization therefore corresponds to a left-handed (right-handed) top quark. Since the transverse polarization vectors are set to zero, the off diagonal elements $\sigma(\pm,\mp)$ yield no contribution.

2.2 Angular Distribution of Top Decay Products

The top quark decay always produces a b jet and a short-lived W boson which decays to leptons or quarks.

$$t \to W^+ b \to l^+ \nu_l\, b \tag{2.6}$$

$$\to \bar{d} u b\,. \tag{2.7}$$

The effect that the polarization of the top quark ensemble has on its decay products is most easily studied in the top quark rest frame, where the angular distribution of the decay product f is given by:

$$\frac{1}{\Gamma_f}\frac{\mathrm{d}\Gamma_f}{\mathrm{d}\cos\theta_{f,\mathrm{rest}}} = \frac{1}{2}\left(1 + \kappa_f P_t \cos\theta_{f,\mathrm{rest}}\right). \tag{2.8}$$

Here Γ is the partial decay width of the top quark, P_t is the degree of polarization in the top quark ensemble eq. 2.5 and the polar angle $\theta_{f,\mathrm{rest}}$ is the angle between the momentum of the decay product f and the top spin vector. κ_f is the analysing power of the decay product f, it is 100% for a positive lepton, and a $\bar{d}$ quark. For the u quark and ν_l its value is -31% and for the b and W the values are -39% and 39% respectively [7]. Thus we see that a positively charged lepton is the most efficient polarization analyser since one cannot easily distinguish the u and $\bar{d}$ jet in the hadronic decay. Corrections to these values of κ can originate from any nonstandard tbW couplings and/or from higher order QCD and QED corrections. The next-to-leading order QCD corrections to κ_b, κ_d, κ_u and κ_l are a few percent, decreasing its magnitude very slightly [8]. As shown explicitly in [9] the value of κ_f does not receive any corrections from an anomalous tbW coupling at leading order for l^+ and $\bar{d}$. Thus the angular distribution of the decay charged lepton in the rest frame reflects the polarization of the decaying quark faithfully even in the presence of such corrections, and hence is a good measure of polarization effects in the top production process.

We will focus on the semileptonic decay of the top quark where the top produces a charged lepton l^+, which we take to be an electron or a muon. Here and in what follows we ignore, for simplicity, off-diagonal elements in the CKM matrix. Also we only consider top quarks, since anti-tops can be distinguished using the charge of the lepton.

2.3 Polarization-Dependent Observables

Instead of using the rest frame, we wish to use polarization-dependent observables in the laboratory frame. Reconstructing the rest frame of the top at LHC is not always easy, and introduces additional uncertainties as the neutrino is only traced through missing energy and missing transverse momentum. The correlations between the polarization of the decaying top and the kinematic variables of the decay product in the lab frame are then obtained by using eq. (2.8) and appropriate Lorentz transformations. A series of earlier investigations [4, 9, 10] indicate that analogously to the situation in the top rest frame, the energy-integrated decay-lepton angular distributions in the lab frame are unaltered by any anomalous tbW coupling, to linear order in the deviation. Thus the correlation between the top polarization and angular (polar and azimuthal) distributions of the decay lepton is unchanged to the same order and not distorted by new physics influencing the decay process. It is important to note that the decay-lepton distributions in the lab frame are influenced by, besides the top quark polarization, the boost from the top quark rest frame to the laboratory frame.

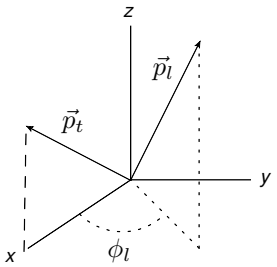

Figure 2.1: An illustration of the definition of the azimuthal angle of the lepton. The beam axis is taken in the z-direction and together with the top momentum defines the $x - z$ plane, where we take the top to be moving in the positive x-direction. The y-axis is constructed corresponding to a right-handed frame.

In order to discuss the azimuthal distribution of the decay lepton we must define a reference frame. We chose the z axis as the beam axis. Together with the top quark direction this defines the top quark production plane, containing the z and x axes, the x-axis chosen such that the top quark momentum has a positive x component. We then construct a right-handed coordinate system and define the azimuthal angle ϕ_l as the angle of the decay lepton in the (x,y) plane depicted in fig. 2.1. In the rest frame the azimuthal distribution does not depend on the longitudinal polarization, but in the lab frame it picks up a dependence on $\theta_{l,\mathrm{rest}}$ through the top boost. Consequently it can be used as a probe for the top quark polarization.

An example shape of the ϕ_l distribution for $pp \to Z' \to t\bar{b}$ may be seen in fig. 2.2. For positively polarized tops it is peaked at $\phi_l = 0$ and $\phi_l = 2\pi$, with a minimum at $\phi_l = \pi$. It should be noted that nonzero transverse momentum p_t^T also causes the ϕ_l distributions to peak near $\phi_l = 0$ and $\phi_l = 2\pi$, *independent* of the polarization state of the t quark. In other words, the peaking at $\phi_l = 0$ and 2π is caused by kinematic effects, which is expressed most clearly for an unpolarized top. It is enhanced even further for a positively polarized top. For a completely negatively polarized top, the pure polarization dependent effects can sometimes even overcome the peaking caused by kinematical effects. As can be seen in the figure, the peaks of the distribution then shift a little away from $\phi = 0$ and 2π. More importantly, they lie below those expected for the positively polarized and unpolarized top. The relative number of leptons near $\phi = 0$ and 2π is thus reduced progressively as we go from a positively polarized to unpolarized to a negatively polarized top. For normalised distributions the ordering is exactly the opposite at $\phi = \pi$ where the relative number of leptons increases as we go from a positively polarized top to a negatively polarized top. This shape motivates the following definition of the asymmetry parameter [9] which takes maximal advantage of these shape differences:

$$A_\phi = \frac{\sigma(\cos\phi_l > 0) - \sigma(\cos\phi_l < 0)}{\sigma(\cos\phi_l > 0) + \sigma(\cos\phi_l < 0)}, \tag{2.9}$$

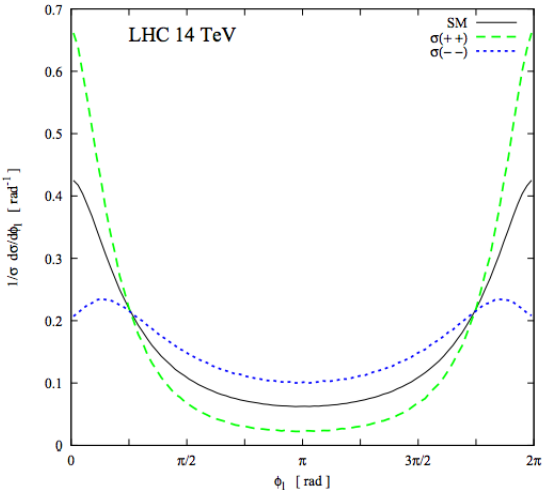

Figure 2.2: The normalized ϕ_l distribution of the positively charged decay lepton of a top quark produced via $pp \to Z' \to t\bar{t}$: the SM contribution is shown in black/solid line, the positive helicity contribution from $\sigma(+,+)$ is shown in green/big-dashed line and the negative helicity contribution from $\sigma(-,-)$ is shown in blue/small-dashed line. The figure corresponds to fig. (4) of [9].

where σ is the fully integrated cross-section. A higher top quark polarization or a stronger top boost will result in a more sharply peaked ϕ_l distribution and thus yield a higher value of A_ϕ.

Besides the azimuthal angle, we can also study the distribution of the lab frame polar angle θ_l of the lepton with respect to the top quark direction. The linear distribution in $\cos\theta_{l,\mathrm{rest}}$ in the rest frame, eq. (2.8), will be distorted by the boost. The latter will make the polar angle in the lab frame, θ_l smaller than its counterpart in the rest frame $\theta_{l,\mathrm{rest}}$. Thus, the distribution of θ_l in the lab frame is more strongly peaked towards $\theta_l = 0$ for a stronger top boost as well as for a more positively polarized top quark.

And lastly we can also use energy information of the top decay products. Although energy observables are not independent of the top quark decay [4, 11], they can provide additional information about the production process. This is especially the case when the top quarks are highly boosted, since the resulting collinearity of its decay products ruins the angular sensitivity. To select highly boosted tops we introduce the boost parameter B based on the total momentum of the top $|\vec{p}_{\mathrm{top}}|$ and the top energy E_t

$$B = \frac{|\vec{p}_{\mathrm{top}}|}{E_t}. \tag{2.10}$$

It was shown in [12] that distributions in the following ratios are sensitive to the polariza-

tion state of the top quark in a heavily boosted region:

$$z = \frac{E_b}{E_t}, \quad u = \frac{E_l}{E_l + E_b}, \tag{2.11}$$

where E_t, E_b and E_l are respectively the (lab frame) energies of the top quark, and the b quark and lepton produced by its decay. The analysis in [12] was at the LO parton level, but in practical applications one may also consider E_b to be the energy of e.g. a b jet. Note that the ranges of z and u are given by

$$0 \leq z, u \leq 1, \tag{2.12}$$

although the extremes are kinematically unavailable at high and low values due to the finite b quark and W boson masses. One may define these observables for any value of a cut on the top quark boost parameter B, but at low values of B, both z and u distributions are increasingly contaminated by contributions that are insensitive to the top quark polarization, thus reducing their effectiveness as discriminators of new physics parameters.

2.4 Wt Production

Polarization of a top quark is most easily studied for the case of Wt production in the SM. The interaction between the two particles is chiral and influences the spin behavior of the produced top quark. The coupling of the top quark to the W-field with all momenta defined incoming is of the form

$$G_{W^+\bar{t}q} = \frac{ig_2}{2\sqrt{2}} V_{tq}^* \gamma_\mu \left(1 - \gamma_5\right) \tag{2.13}$$

where V_{tq} is the element of the CKM matrix describing the mixing between the top quark and a down-type quark, and g_2 the SU(2) gauge coupling. The Vector-Axial coupling ensures that the top quark is always completely polarized at the moment of production. The leading order contributions for producing a single top quark with an associated W-

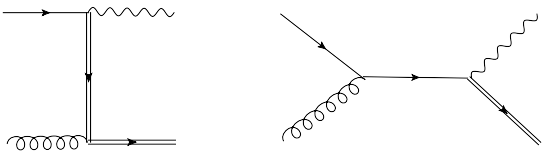

Figure 2.3: Leading order diagrams for single top production with associated W boson in the SM. The contributing processes are a t-channel (left figure) and a s-channel (right figure) diagram. The top quark is denoted by the double line.

boson are shown in fig. 2.3. Even though the top quark is completely polarized at the moment of production the mixing of left- and righthanded modes still occurs through

the presence of a massive top quark propagator in the t-channel diagram. Especially at LHC energies, the mass contribution is notable. Distributions of Wt provide the basis of comparison against which polarization effects induced by Beyond the Standard Model (BSM) physics must be measured. Let us briefly review the SM prediction, for which we employ MadGraph 5 [13, 14] to generate the LO process

$$pp \to gb \to tW^- \tag{2.14}$$

using LHAPDF [15], setting $\mu_R = m_t$ and decaying the top quark as described by eq. (2.6) for an LHC centre of mass energy of 14 TeV. Fig. 2.4a shows the azimuthal distribution of the decay lepton of the top quark. We notice that the distribution is similar to fig. 2.2, symmetric around $\phi_l = \pi$ and peaking at $\phi_l = 0$ and 2π. Complementary spin

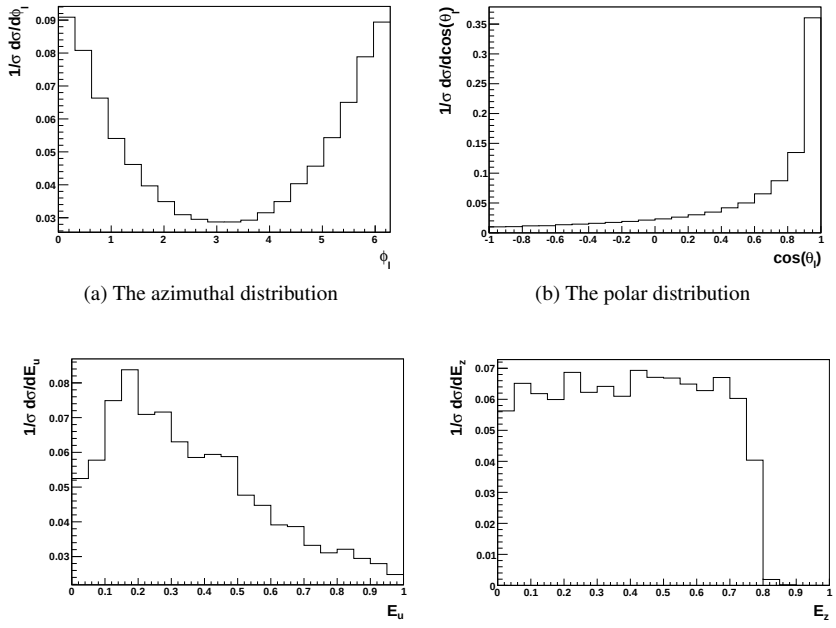

(a) The azimuthal distribution

(b) The polar distribution

(c) The u distribution

(d) The z distribution

Figure 2.4: Angular and energy distributions for the decay charged lepton of the top quark produced via Wt for LHC14. A boost cut of $B > 0.99$ has been applied to the u and z distribution to allow for a comparison with literature.

information can be found in the polar distribution fig. 2.4b. The polarization of this process was extracted from the same simulation by limiting the sum over helicity amplitudes and calculating the polarization manually. We found $P_t = -0.26$ for the production of Wt without decay. Therefore, in the rest frame, leptons are mostly emitted in the backwards region with respect to the top quark boost direction (as the spin axes are chosen

parallel to the top momentum). Fig. 2.4b shows the distribution in the lab frame where most leptons are found at $\theta_l = 0$. The shift of the peak position from $\theta = \pi$ to $\theta = 0$ is caused by the boost, and exposes the influence of the kinematics of the production process. Fig. 2.4d demonstrates the ratio of b-quark energy to top quark energy. The distribution is in accordance with a rough estimate of what one would expect for a mildly negative polarization in [12]. In [12] the (unknown) boost from the top rest frame to the lab frame is parameterized by β which is taken to unity, while we have taken $B > 0.99$. The ratio of lepton energy to lepton plus b-quark energy is largely linear fig. 2.4c, with a small positive inclination (opposite to the polarization). This result is also in accordance with the results of [12]. The plots in fig. 2.4 set the LO benchmark for a single top quark produced in the SM. The following two chapters will examine if these observables are a useful probe for BSM physics. We shall especially focus on their robustness when including higher order QCD corrections and a parton shower.

Chapter 3

Top Polarization in Ht and Wt Production

The polarization-dependent observables discussed in section 2.3 were so far studied at leading order (LO) accuracy. For a given polarization-dependent observable, such a calculation represents a best case scenario in which polarization effects in the production of the top quark are least diluted by kinematic effects. Beyond this order in QCD perturbation theory, additional radiation may carry away energy and/or angular momentum. In this section we extend the study to next-to-leading order (NLO) accuracy, including also the effects of a parton shower. Studying the observables at NLO + shower level and comparing them to the LO result provides a handle on their robustness. We start by introducing a rather generic physics scenario.

3.1 Two Higgs Doublet Model

When a top quark is produced together with a W boson in the Standard Model, the $V-A$ nature of the weak interaction eq. (2.13) implies that the top quark is always left-handed at the moment of production. If the production however is followed by a massive top propagator mixing terms arise. However, top quarks produced by BSM processes can have a different polarization than is predicted in the SM. Hence, the polarization of the produced top can help distinguish between BSM and the SM.

An example is charged Higgs plus top production, a process analogous to Wt production in the SM. The leading order contributions to this process are similar to fig. 2.3 with the W replaced by a charged Higgs boson. In contrast to the SM, this theory consists of two Higgs doublets ϕ_1, ϕ_2, predicting therefore not one, but five Higgs bosons. Motivations for introducing another doublet can for instance be found in the extension of the SM with supersymmetry. We will elaborate further on the impact of supersymmetry in the next chapter, but for now it is sufficient to know that supersymmetry postulates a symmetry between all known SM particles and their supersymmetric partners that differ

by spin-$\frac{1}{2}$. A second Higgs doublet is required in this model to preserve the cancellation of gauge anomalies, see for instance [16]. The Higgs potential is constructed from hermitian combinations of these two doublets subject to the conditions of renormalizability and gauge invariance. Focussing on the terms quadratic in the doublet fields we find

$$\begin{aligned} V(\phi_1, \phi_2) =& \lambda_1 \left(\phi_1^\dagger \phi_1 - v_1^2\right)^2 + \lambda_2 \left(\phi_2^\dagger \phi_2 - v_2^2\right)^2 \\ &+ \lambda_3 \left[\left(\phi_1^\dagger \phi_1 - v_1^2\right) + \left(\phi_2^\dagger \phi_2 - v_2^2\right)\right]^2 + \dots \end{aligned} \tag{3.1}$$

The occurrence of $v_i = \langle \phi_i \rangle$ with $i = 1, 2$ denotes that we are now dealing with two vacuum expectation values. These parameters are commonly varied together according to their ratio $\tan(\beta) = v_2/v_1$. Observing the production of a charged Higgs particle would provide very valuable information on the structure of the Higgs sector. Studies have shown [17, 18] that top polarization can be used to extract information on the model parameters of a Two Higgs Doublet Model (2HDM). However, these analyses were carried out only at LO in perturbation theory. While the higher order corrections coming from the chirality and parity conserving QCD interactions will not affect the top polarisation, they can change the kinematics of the produced top quark and hence it is important to verify that the conclusions of the LO analysis are robust against NLO corrections.

In our investigation of the effects of NLO corrections we will assume that the charged Higgs boson has a larger mass than the top quark, so that the top quark cannot decay to it. A general form for a charged Higgs-top quark interaction is

$$G_{H^- tb} = iV_{tb}(a - b\gamma_5).$$

This reduces to its SM equivalent of Wt production by setting $a = b = \frac{1}{2\sqrt{2}} g$, with g the $SU(2)$ gauge coupling. For later event simulation we must make explicit choices for these parameters. We have followed the approach of [19], that derives a specific form of a and b based on the counterterms resulting from the charged Higgs Yukawa couplings. We will consider a type II two Higgs doublet model, where the up type quarks couple to one of the Higgs doublets and down type quarks couple to the other Higgs doublet. The coupling of the charged Higgs to the top and bottom quarks is given by

$$G_{H^- t\bar{b}} = -\frac{i}{v\sqrt{2}} V_{tb} \Big[m_b \tan\beta (1 - \gamma_5) + m_t \cot\beta (1 + \gamma_5) \Big]. \tag{3.2}$$

Here the vacuum expectation values of the two Higgs doublets are $v \cos\beta = v_1$ and $v \sin\beta = v_2$, with $v^2 = v_1^2 + v_2^2$. Now that we have established the fundamental interactions for a BSM single top production mode let us discuss the effects of NLO corrections to the polarization.

3.2 Effects of NLO Corrections to Polarization Dependent Observables

The NLO correction to the Ht production includes QCD interactions, which conserve parity and chirality. Kinematic effects on the other hand do change when going to NLO + shower accuracy. In particular, as will be shown explicitly in fig. 3.1, the boost of the top quark, as measured by the B parameter of eq. (2.10), increases a few percent in the highest bin with respect to the LO boost due to the higher order corrections.

For the LO computation of the $H^- t$ production process, we use MadGraph 5 [13, 14], where we extended the Standard Model to include the charged Higgs coupling. Contributing diagrams at LO are comparable to those in fig. 2.3 where the W-boson must be exchanged with a charged Higgs boson. The NLO calculation matched to a parton shower was performed using the MC@NLO software package described in [19–24], with spin correlations between the partons in the hard scattering and the Higgs and/or top decay products, implemented according to the algorithm of [25][1].

The Wt production process poses a conceptual problem at NLO, due to the fact that some of the real emission diagrams beyond LO involve an intermediate top quark pair. The contribution from such diagrams is large when the $\bar{t}$ becomes resonant, reflecting an interference between the Wt and top-pair production processes. How to most accurately model the sum of Wt and top-pair production then becomes a topic of debate, and there are two main points of view. The first is that all singly and doubly resonant diagrams must be combined, thus including all interference (and off-shell) effects (see, for example, [31, 32]). A major deficiency of such calculations, however, is that they typically do not include NLO corrections, which for top pair production are known to be large. NLO corrections for the $WWb\bar{b}$ final state have been presented [33], also including decay of the W bosons [34], in the so-called four flavour scheme in which all initial state b quarks are explicitly generated via gluon splitting, although these results have yet to be interfaced with a parton shower.

The second point of view is that singly and doubly resonant contributions may be safely regarded as separate production processes, which may be meaningfully combined subject to suitable analysis cuts, an approach followed by e.g. [20, 29, 35, 36]. This amounts to defining a subtraction term, which removes doubly resonant contributions from the Wt cross-section. A potential deficiency of such an approach is that gauge invariance is violated by terms $\sim \mathcal{O}(\Gamma_t/m_t)$, where Γ_t is the top quark width, although it is usually (convincingly) argued that this is more a problem of principle than one of practice. Another way to think about this procedure is that the subtraction term avoids the double counting that would result upon naïvely adding the Wt and top pair cross-sections at NLO. Such on-shell subtraction schemes are in fact a common feature in many NLO calculations involving extensions to the Standard Model, in which intermediate heavy particles abound (see e.g. [37–40]). Indeed, in this context, the interference problem is usually referred to in terms of being a double counting issue.

[1] Alternative methods for matching NLO computations with a parton shower have been presented in [26, 27] and chapter 5 and 6. See also [28–30] for implementations of the processes discussed in this chapter.

It is not our intention to revisit the issue on the validity of on-shell subtraction schemes. But, in order to discuss Wt production at all, we must necessarily take the view that it makes sense to separate singly and doubly resonant production modes. For a detailed recent discussion of this viewpoint, see [41]. In that paper, it was argued that Wt is unambiguous for suitable analysis cuts, and we will assume the validity of this approach in what follows.

The MC@NLO code for Wt production includes two definitions of Wt production, labelled Diagram Removal (DR) and Diagram Subtraction (DS), where the difference between these is intended to represent the systematic uncertainty due to interference with top pair production. Roughly speaking, DS subtracts doubly resonant (i.e. top pair) contributions at the cross-section level (thus is gauge invariant up to terms $\sim \mathcal{O}(\Gamma_t/m_t)$), and DR subtracts such contributions at the amplitude level. The difference between these then mostly measures the interference between Wt and $t\bar{t}$ production, up to ambiguities in the subtraction term. However, one only trusts each calculation if the DR and DS results agree closely, which relies upon the imposition of suitable analysis cuts for reducing the interference. We will not implement such cuts in the calculation of the observables for H^-t production as this study aims to present a first investigation of the effect of NLO corrections + parton shower without the complication of a full experimental analysis. Despite this, we will show the results obtained from both the DR and DS calculations.

3.3 Results for H^-t Production

In the previous chapter, we reviewed the observables which are designed to be sensitive to the polarization state of produced top quarks. In this section, we study these observables for single top production in association with a charged Higgs boson. The latter does not occur in the Standard Model of particle physics, but exhibits a somewhat generic presence in possible extensions, including supersymmetry.

The top quark polarization in the H^-t production process does not follow directly from eq. (3.2). As explained in detail in Ref. [17], the polarization vanishes if $m_H = 6m_t$ and if $\tan\beta = \sqrt{m_t/m_b}$. The latter point in parameter space cancels the axial contribution in eq. (3.2). In addition, it was shown in figure 4 of that paper that the $\tan\beta$ dependence of the polarization is different for different Higgs masses. For Higgs masses below $6m_t$ it is negative if $\tan\beta < \sqrt{m_t/m_b}$ and positive for higher values of $\tan\beta$. The polarization for higher Higgs masses has the opposite behaviour. In the rest of this section, we will often show distributions for $m_H = 200$ GeV and $m_H = 1500$ GeV as representative examples. For a given value of $\tan\beta$, the former is more strongly polarized than the latter.

One may study how the observables of section 2.3 vary throughout the two dimensional parameter space $(m_H, \tan\beta)$. In what follows, we will do this at LO and NLO, as specified in section 3.2. Note that the aim of this section is not to undertake a fully comprehensive phenomenological analysis, including all relevant backgrounds together with realistic experimental cuts. Rather, we wish to study the efficiency of the different observables that reflect the polarization of the parent top, and in particular their robustness

when one includes higher order effects.

In order to present results, we consider the LHC with a centre of mass energy of 14 TeV, and define parameters as follows: the top mass and width are $m_t = 172.5$ GeV and $\Gamma_t = 1.4$ GeV respectively. The W mass and width are respectively $m_W = 80.42$ GeV and $\Gamma_W = 2.124$ GeV. Factorization and renormalization scales are set to $\mu_r = \mu_f = m_t$. We calculate LO and MC@NLO results using MSTW 2008 LO and NLO parton sets [42–44]. Note that the b mass entering the Yukawa coupling is run as in [45], from a pole mass of $m_b = 4.95$ GeV [2].

As explained in section 2.3, the polarization-dependent observables are affected considerably by the kinematics of the top. Therefore we first briefly discuss the boost parameter B and the top transverse momentum p_t^T. On the left-hand side of fig. 3.1, the distribution of the boost parameter is shown for two different values of the charged Higgs mass. On the right-hand side, the LO and NLO + parton shower distributions are compared. The distribution is much more strongly peaked for the high Higgs mass, as expected from the fact that the top quark must recoil against the heavy particle. In addition we see that the NLO+parton shower effects increase the boost parameter slightly. This can be traced back to the definition of eq. (2.10), coupled with the fact that the energy of the top quark softens more on average than its momentum when higher order effects are included.

3.3.1 Azimuthal Angle ϕ_l

Fig. 3.2 shows the ϕ_l distribution defined in section (2.9) for two different values of $\tan\beta$, and two different charged Higgs masses at NLO + parton shower. For $\tan\beta = 5$, there is a pronounced difference between the two ϕ_l distributions at different mass values, with the higher mass value showing more asymmetry. At high $\tan\beta$, there is very little difference between the two Higgs mass values. The reason for this behaviour can be traced back to the polarization of the top. At low $\tan\beta$ a light Higgs yields a negatively polarized top, so in the rest frame the lepton tends to be emitted in the backward direction (cf. eq. (2.8)). For a heavy Higgs the top is positively polarized for low values of $\tan\beta$, so the lepton is emitted in the forward direction. Since the top is boosted more for higher Higgs masses, the kinematics enhance this polarization effect. For large $\tan\beta$, the top polarization has the opposite sign, so in that case the kinematics cancel the effect of the polarization.
In fig. 3.3 the ϕ_l distribution is shown at LO and MC@NLO level for $\tan(\beta) = 5$ and two different charged Higgs masses. The results can be compared to figure 6 of [17], and indeed the qualititative trend of the curves is the same as in [17]. In the case of a high Higgs mass the distribution becomes slightly flatter due to the NLO corrections and parton shower. This is caused by competing kinematic effects. As shown in fig. 3.1, the top boost increases slightly due to the higher order corrections, but the p_t^T distribution is typically softer compared to LO, and progressively more so for higher Higgs masses as the top then showers more on average. The higher top boost leads to a sharper ϕ_l

[2] Strictly speaking, one should run the b mass at one-loop order for the LO results, and two-loop order for the NLO results. To facilitate a more direct comparison between the LO and MC@NLO results we adopt the LO prediction, given that the relative proportion of right- and left-handed $H^- t$ couplings is governed by the value of $m_b(\mu_r)/m_t(\mu_r)$. We have checked that the difference in running is a small effect.

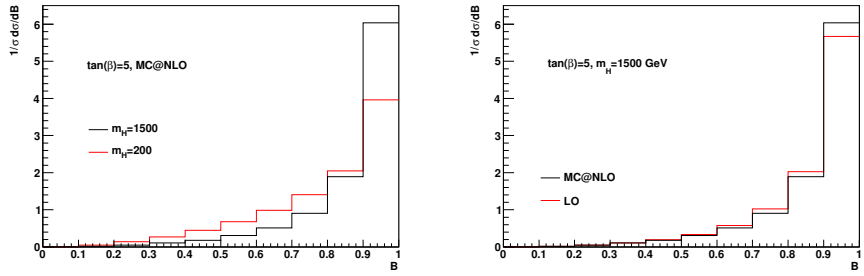

Figure 3.1: The distribution of the boost parameter of in $H^- t$ production for $\tan\beta = 5$ and two different Higgs masses is shown on the left-hand side. On the right-hand side the boost parameter is shown at LO and NLO plus parton shower level.

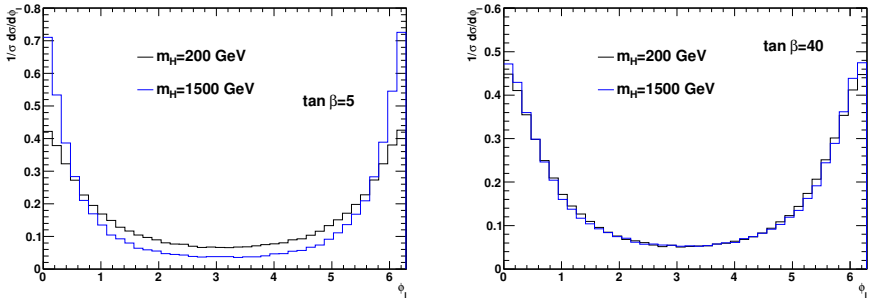

Figure 3.2: Azimuthal angle (ϕ_l) of the decay lepton from the top quark, as defined in the text, at NLO plus parton shower level.

distribution, but for high Higgs masses the effect of the softer p_t^T distribution is stronger, resulting in a flatter distribution in the end. We can quantify this further by calculating the asymmetry parameter of eq. (2.9). We show this in fig. 3.4, for the two Higgs mass values used above and a range of $\tan\beta$ values. Both LO and MC@NLO results are shown for comparison, where for the MC@NLO results we include an error band stemming from statistical uncertainty. The shape of fig. 3.4 is very similar to the results of [17]: for the large charged Higgs mass value, a high asymmetry is observed for low $\tan\beta$, which decreases at large $\tan\beta$. For the low charged Higgs mass value, the opposite trend is seen.

The MC@NLO results show less of a difference between the two Higgs mass values than the LO results. This is caused by the competing kinematic effects we already saw in fig. 3.3. The higher top boost leads to a larger value of the asymmetry A_ϕ, but for high Higgs masses the effect of the softer p_t^T distribution is stronger, yielding a net reduction

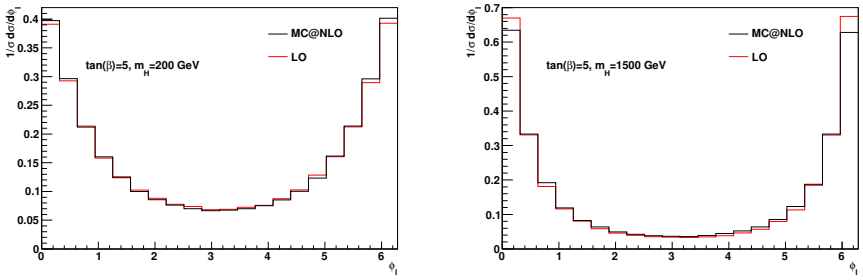

Figure 3.3: Azimuthal angle (ϕ_l) of the decay lepton from the top quark, as defined in the text, comparing LO and NLO + parton shower.

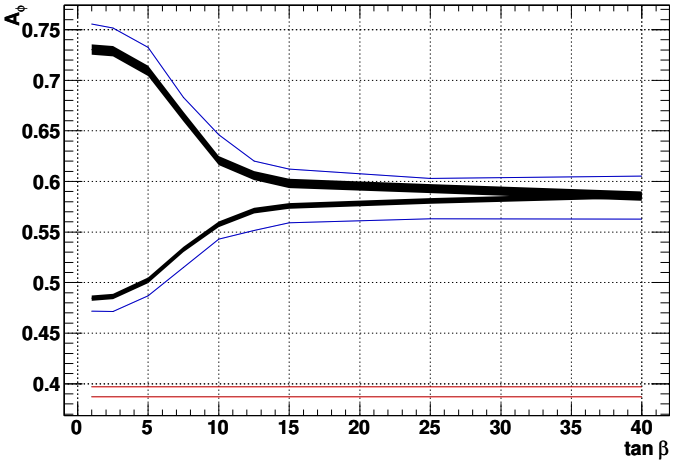

Figure 3.4: Azimuthal asymmetry parameter for $H^- t$ production, as defined in eq. (2.9). LO (MC@NLO) results are shown in blue (black), for $m_H = 200$ GeV (lower curves) and $m_H = 1500$ GeV (upper curves). The error band is statistical. Results for Wt production, using both the DR and DS approaches in [20], are shown in red.

of A_ϕ. At NLO, the difference between the two Higgs mass values is smaller than at LO, even at low $\tan\beta$. However, a pronounced asymmetry is still visible, with a strong dependence on the charged Higgs parameters, so the azimuthal asymmetry appears to be quite robust with respect to higher order corrections.

We see that the difference between the DR and DS results is much less than the difference between Wt and $H^- t$ production, which gives us confidence that the interference

issue does not get in the way of getting an estimate of the asymmetry parameter for Wt. Thus, the fact that Wt and H^-t production lead to rather different A_ϕ values (for essentially any choice of m_H or $\tan\beta$), as has already been observed at LO [17], remains true at NLO and after a parton shower has been applied.

3.3.2 Polar Angle θ_l

One may also consider the polar angle between the decay lepton and the top quark direction. Fig. 3.5 shows the NLO+parton shower results for the same extremal values of $\tan\beta$ and m_H as in fig. 3.2. We see that the distribution is more sensitive to the Higgs mass at small $\tan\beta$ than at large $\tan\beta$, which is again due to the enhancement (cancellation) of the polarization effects by the kinematics at low (high) $\tan\beta$.

The distribution of θ_l at LO and MC@NLO level is shown in fig. 3.6. As with the ϕ_l distribution, the NLO distribution strongly resembles the LO results. The NLO distribution is peaked towards $\theta_l = 0$ somewhat more due to the slight increase in the top boost parameter.

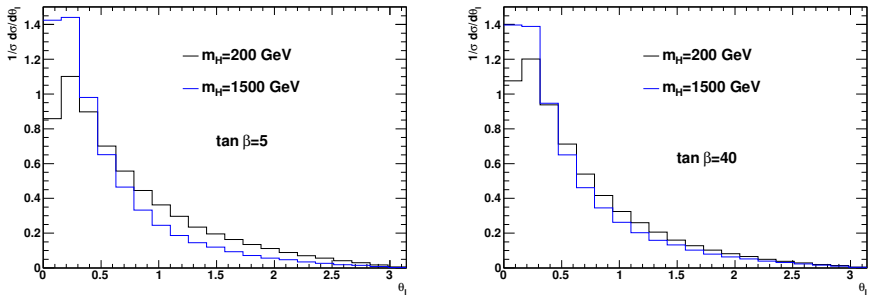

Figure 3.5: Polar angle (θ_l) of the decay lepton from the top quark, measured with respect to the top quark direction, at NLO plus parton shower level.

In all cases, the distribution shows a strong peak at low values of θ_l, with a fall-off at higher values. For normalized distributions it follows that a distribution which has a slower fall-off must correspondingly have a lesser peak, and vice versa. This motivates the definition of the following asymmetry parameter:

$$A_\theta = \frac{\sigma(\theta_l < \pi/4) - \sigma(\theta_l > \pi/4)}{\sigma(\theta_l > \pi/4) + \sigma(\theta_l < \pi/4)}. \tag{3.3}$$

We have here used $\pi/4$ as representative of the point at which distributions corresponding to different points in parameter space cross each other. However, we have found no obvious analytic justification for this result, so this number can in principle be varied in order to enhance the asymmetry.

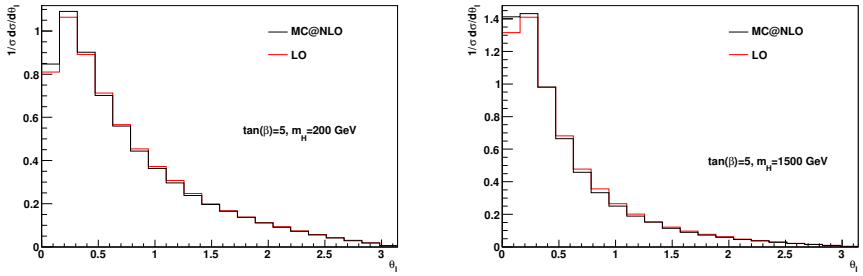

Figure 3.6: Polar angle (θ_l) of the decay lepton from the top quark, measured with respect to the top quark direction, at LO and NLO plus parton shower level.

Results for the polar asymmetry parameter are shown in fig. 3.7. Again we show both LO and MC@NLO results, where a statistical uncertainty band is included for the latter. One sees that the MC@NLO values of A_θ are higher than the LO results, as expected from

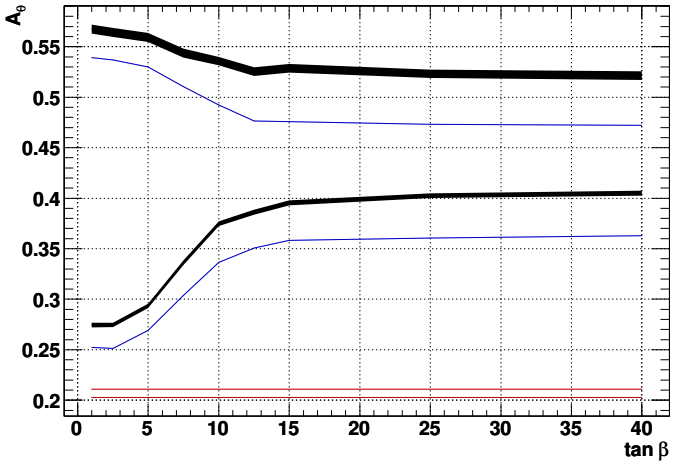

Figure 3.7: Polar asymmetry parameter for $H^- t$ production, as defined in eq. (3.3). LO (MC@NLO) results are shown in blue (black), for $m_H = 200$ GeV (lower curves) and $m_H = 1500$ GeV (upper curves). The error band is statistical. Results for Wt production, using both the DR and DS approaches in [20], are shown in red.

the higher value of the top boost at MC@NLO level compared to LO. In contrast to the azimuthal asymmetry, there is a significant difference between the extremal charged Higgs mass values at large $\tan\beta$. This makes the polar angle very useful as a complementary

observable to the azimuthal angle, as the latter is relatively insensitive to the charged Higgs mass at large $\tan\beta$.

Similarly to the azimuthal case, one sees from fig. 3.7 that typical values for the polar asymmetry are markedly different to the result obtained for Wt production, as estimated by the DR and DS results. Again this is presumably a reliable conclusion, given that the difference between the two Wt results is much less than the difference between the $H^- t$ and Wt results. This information is a potentially valuable tool in being able to distinguish charged Higgs boson production from the Wt background.

3.3.3 Energy Ratio Observables

In the previous sections, we presented results for angular distributions of the decay lepton in $H^- t$ and Wt production, finding these to be robust discriminators of the charged Higgs parameter space, as well as of use in distinguishing a charged Higgs signal from the Standard Model background. In this section, we consider the energy ratios z and u of eq. (2.11), which were first defined in [12].

Note that both the z and u observables depend on the energy of the b quark emanating from the top quark decay. In a leading order calculation, this can be straightforwardly identified. In an experimental environment, one must use event selection cuts which require the presence of a tagged b jet, and use the energy of this jet in constructing eq. (2.11). A full phenomenological analysis is beyond the scope of this chapter: we here wish to present a first analysis of the z and u parameters in the context of $H^- t$ production, unshrouded by the full complications of an experimental analysis. There is then a choice to be made regarding which energy to use in presenting results from MC@NLO. One option is to use the energy of the b-flavoured hadron that contains the b quark from the top decay, requiring this to be stable. However, to facilitate a more direct comparison with the LO results, we instead define E_b via the energy conservation relation

$$E_b = E_t - E_l - E_\nu, \tag{3.4}$$

where E_t, E_l and E_ν are the energies of the top quark, decay lepton and decay neutrino respectively. The latter is, of course, unmeasurable in a real experiment but can be identified in a Monte Carlo event generator. Our definition of E_b then means that our comparisons between LO and MC@NLO results measure the collective effect of a single hard additional emission (from the NLO matrix element), together with the parton shower, but with no non-perturbative contributions from e.g. hadronization or the underlying event. We deem such an approach to be valid in assessing the robustness of energy ratio observables against perturbative higher order corrections, which is our present aim. For a realistic situation an alternative definition implementing analysis cuts in terms of jets would allow for E_b to be the energy of the b-jet which enters the cuts.

The energy ratios of eq. (2.11) are more sensitive to the top quark polarization in the kinematic region in which the decaying top quark is highly boosted. It is important to check which values of a cut on the boost parameter are sufficient in order to isolate the desired sensitivity to the top quark polarization.

The energy ratios of eq. (2.11) can provide additional information when the top is boosted and the resolution of the top decay products is insufficient. First we will investigate the dependence of the influence of a boost cut on the energy ratios z and u of eq. (2.11) for different values of this cut in fig. 3.8. One sees that the results with a cut

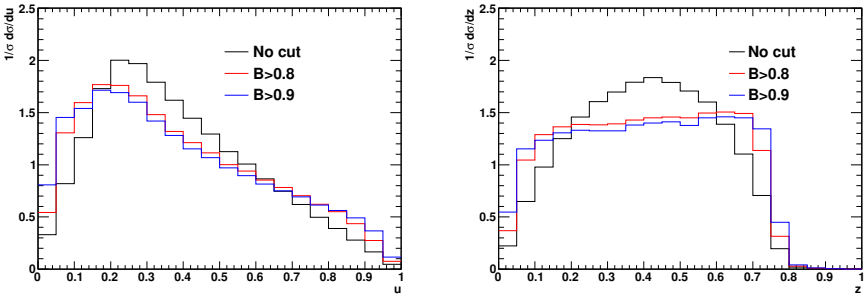

Figure 3.8: Distribution of u (left-hand plot) and z (right-hand plot) for $\tan\beta = 1$ and $m_H = 200$ GeV, at NLO plus parton shower level. Results are shown for different cut values on the boost parameter B of eq. (2.10).

are markedly different from those with no cut (as expected). However, the difference between results with $B > 0.9$ and $B > 0.8$ is much less, suggesting that a cut of $B > 0.8$ is sufficient.

The distribution of u at MC@NLO level after the cut $B > 0.8$ is applied is shown in fig. 3.9 for two values of m_H.

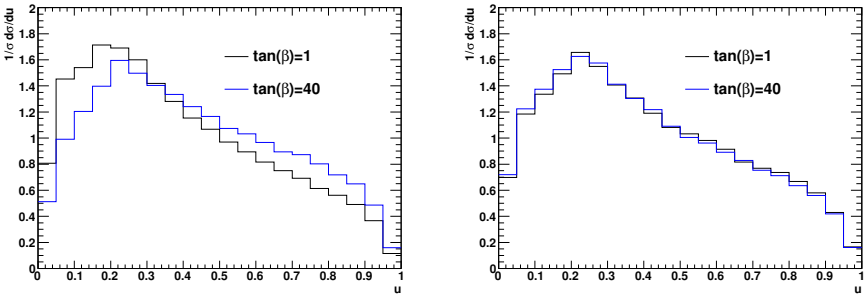

Figure 3.9: Distribution of u, as defined in eq. (2.11), where a cut on the boost parameter $B > 0.8$ has been applied, at NLO plus parton shower level. Results are shown for $m_H = 200$ GeV (left-hand plot) and $m_H = 1500$ GeV (right-hand plot).

The shape of the plots can be compared to the corresponding figures in [12], which are presented for the ideal case in which the top quark is completely polarized and infinitely

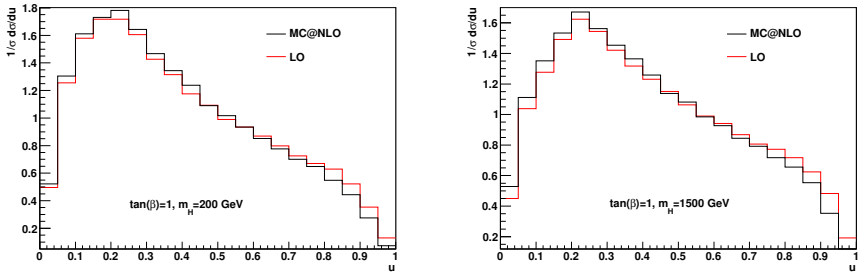

Figure 3.10: Distribution of u with a cut on the boost parameter $B > 0.8$.

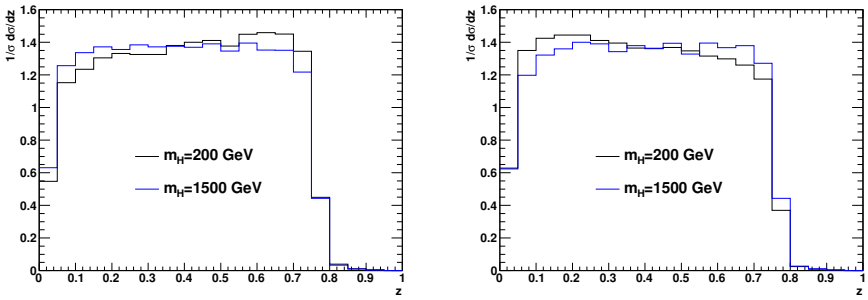

Figure 3.11: Distribution of z, as defined in eq. (2.11), where a cut on the boost parameter $B > 0.8$ has been applied, at NLO plus parton shower level. Results are shown for $\tan\beta = 1$ (left-hand plot) and $\tan\beta = 40$ (right-hand plot).

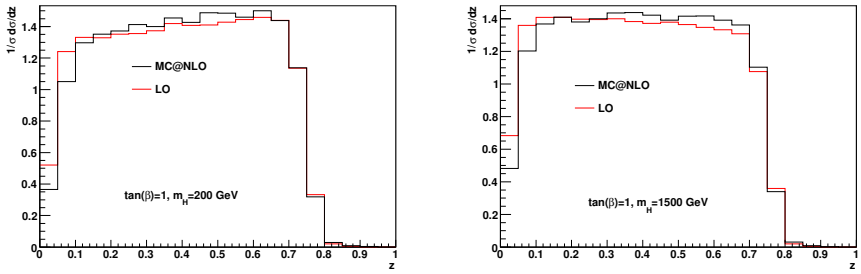

Figure 3.12: Distribution of z at LO and MC@NLO level, with a boostcut of $B > 0.8$.

boosted, i.e. $P_t = \pm 1$ and $B \to 1$. The latter seem to show a much more pronounced difference between the curves for positive and negative helicity top quarks. This is mostly due to the fact that in our case the top quarks are not completely polarized. The high Higgs mass in particular does not yield a strong top quark polarization. For the lower Higgs mass, the shapes are broadly consistent with the results of [12]: for the negatively polarized top quarks ($\tan\beta = 1$), the distribution falls off more sharply for higher values of u. Also, the curvature of the distributions is different for lower values of u for the two different $\tan\beta$ values.

The u variable at LO and MC@NLO level with a boostcut of $B > 0.8$ is shown in fig. 3.10. We see that the general shape does not change when including NLO+parton shower corrections.

We may also consider the z distribution, which is shown for our two extremal $\tan\beta$ values in fig. 3.11. The plots have three distinct regimes. Firstly, there is a sharp fall-off as $z \to 0$, due to the finite mass of the b quark. Then, there is an intermediate regime $0.1 \lesssim z \lesssim 0.7$, over which the z distribution is approximately linear, with the sign of the slope correlated with the polarization of the top quark (i.e. positive and negative for negatively and positively polarized top quarks respectively). Finally, there is another fall-off as $z \to 1$, due to the finite W boson mass. Again one sees very little correlation for the charged Higgs mass of 1500 GeV due to the small value of the polarization.

In fig. 3.12 we see that this is not due to the NLO and parton shower effects. The distribution is changed by these effects, but the correlation with the charged Higgs mass is not very strong even at LO. For the lower Higgs mass we also see that the NLO+parton shower corrections change the distribution more than for the angular distributions.

For the angular observables of the previous section, we used asymmetry parameters which efficiently distill the difference between different regions of the charged Higgs parameter space into single numbers. It is perhaps useful to also adopt this strategy for the energy ratios u and z. Regarding the former, one may first note that the normalisation of the distribution means that a slower fall-off above the peak region entails less events below the peak region. One may exacerbate this effect by defining the corresponding asymmetry parameter

$$A_u = \frac{\sigma(u > 0.215) - \sigma(u < 0.215)}{\sigma(u > 0.215) + \sigma(u < 0.215)}. \tag{3.5}$$

Here $u \simeq 0.215$ is chosen as the approximate position of the peak, motivated by the analysis of [12]. As in the case of the polar angle asymmetry of eq. (3.3), however, this choice can in principle be varied in order to enhance the result.

The behaviour of A_u is shown in fig. 3.13, for a cut on the boost parameter of $B > 0.8$. For comparison purposes, we also show the result one would obtain with no cut on the boost parameter, where the u observable suffers significant contamination from contributions which are insensitive to the top quark polarization. As expected, the A_u variable has more discriminating power for the lower Higgs mass, since the top is more strongly polarized in that case. In addition one sees that the cut on the boost parameter has a larger effect for the lower Higgs mass than for the higher one, although this effect is somewhat weaker at MC@NLO level, where the top is more boosted on average. Generally, there is

more of a pronounced difference between the LO and MC@NLO values than in the case of the angular asymmetries considered in the previous section. Furthermore, decorrelation with LO is more pronounced for heavier Higgs masses, due presumably to the fact that the top quark showers more on average.

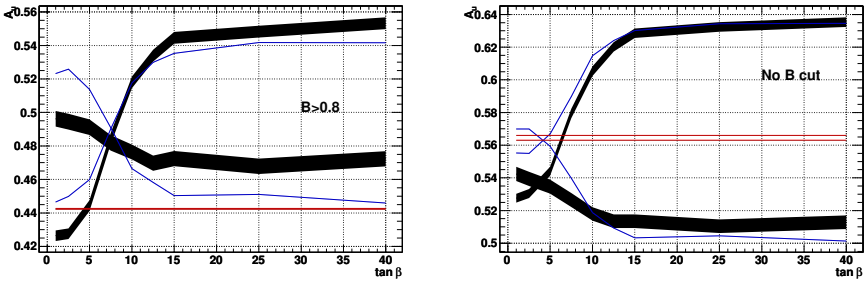

Figure 3.13: The asymmetry parameter A_u for H^-t production, as defined in eq. (3.5). LO (MC@NLO) results are shown in blue (black), for $m_H = 200$ GeV (upper curves at large $\tan\beta$) and $m_H = 1500$ GeV (lower curves at large $\tan\beta$). The error band is statistical. Results for Wt production, using both the DR and DS approaches in [20], are shown in red (in the left-hand plot the DS and DR results are on top of each other).

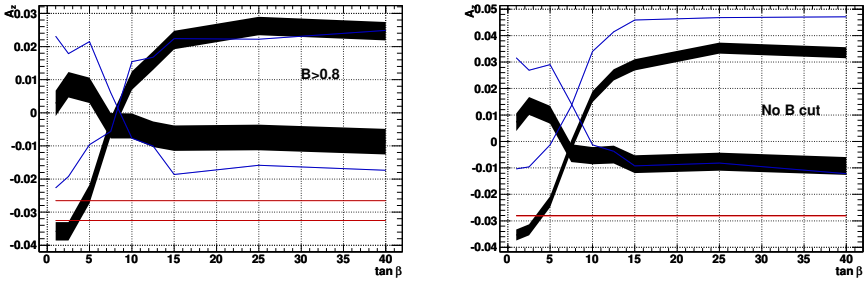

Figure 3.14: The asymmetry parameter A_z for H^-t production, as defined in eq. (3.5). LO (MC@NLO) results are shown in blue (black), for $m_H = 200$ GeV (upper curves at large $\tan\beta$) and $m_H = 1500$ GeV (lower curves at large $\tan\beta$). The error band is statistical. Results for Wt production, using both the DR and DS approaches in [20], are shown in red (in the right-hand plot the DR and DS results are on top of each other).

As for the angular asymmetry, we also show results for Wt production in fig. 3.13. Before a cut on the boost parameter is applied, the Wt result sits more or less in the middle of the H^-t results over most of the range in $\tan\beta$. This is not the case once a cut is applied, and indeed a significant difference is observed between the Wt and H^-t

results. Admittedly, this difference appears larger (and thus more useful) for smaller charged Higgs masses, and is only 3% or so for the largest Higgs mass we consider.

We may also define an asymmetry parameter for the energy ratio z of eq. (2.11). This is perhaps most conveniently done by considering only the linear regime in fig. 3.11, occuring at intermediate values of z, as it is the sign of the slope in this kinematic region that distinguishes the cases of positive and negatively polarized tops. We therefore define

$$A_z = \frac{\sigma(0.1 \leq z \leq 0.4) - \sigma(0.4 < z \leq 0.7)}{\sigma(0.1 \leq z \leq 0.4) + \sigma(0.4 < z \leq 0.7)}. \tag{3.6}$$

We have chosen the values at which to define the intermediate region by eye from fig. 3.11. Again, these could be varied in order to maximise the resulting asymmetry.

The behaviour of A_z is shown in fig. 3.14. A first notable feature is the lack of smoothness, even in the LO results. This is due to the fact that the boundaries of the intermediate regime will themselves depend on the value of $\tan\beta$, leading to fluctuations such as those observed in the figure. It may be that such fluctuations can be ameliorated by tuning of these boundaries, with a corresponding trade-off in the size of the asymmetry observed. The sign of the asymmetry flips for each charged Higgs mass as the full range in $\tan\beta$ is scanned, which is expected since the sign of the polarization changes. Note that there is again a marked difference between the LO and NLO results, particularly for the higher Higgs mass, and that the boost cut has a larger effect for the lower Higgs mass.

As before, one may compare the H^-t and Wt results. Here, though, a note of caution is necessary, because the difference between the DR and DS results for Wt appears more pronounced for this parameter. In particular, it varies considerably before and after the boost cut is applied. This greater variation is perhaps exacerbated by the smallness of the asymmetry (which is at best only a few percent), but also suggests that interference with top pair production may be an issue in interpreting the Wt results. It is nevertheless the case that the difference with Wt is most pronounced at either low Higgs mass and high $\tan\beta$, or high Higgs mass and low $\tan\beta$. In both these cases, the sign of the top polarization in H^-t production is opposite to the one in Wt production. This results in a small asymmetry of opposite sign to the Wt case, but roughly comparable in size.

To summarise, we have here presented results for a number of angular and energy-related distributions and, building upon the analysis of [9, 17], defined a corresponding asymmetry parameter for each that efficiently encodes the difference in these distributions for different regions in the charged Higgs parameter space, as well as the differences between Wt and H^-t production. All of these asymmetries seem to be fairly robust against NLO and parton shower corrections. In addition, they complement each other, since different observables are sensitive to different parts of the parameter space. This suggests that they may indeed be very useful in isolating a charged Higgs boson, with subsequent identification of its properties. In the following section, we consider a second context in which such observables may be useful, namely that of isolating Wt production itself as a signal.

3.4 Results for Wt Production

In the previous section, we examined the angular and energy distributions introduced in section 2.3 in H^-t production, and defined asymmetry parameters which are potentially highly useful in elucidating the properties of a charged Higgs boson. In this section, we investigate whether these same observables have anything useful to say about Standard Model Wt production.

There are three production modes for a single top quark in the Standard Model. Two of these, the so-called $s-$ and $t-$ channel modes, have been observed in combination at both the Tevatron [46–49] and LHC [50–52]. The theoretical state of the art is also highly advanced, and includes fixed order computations [53–57], NLO plus parton shower implementations [58, 59], resummed results [60], and finite top width corrections [61, 62]. For related phenomenological studies, see [63–66]. As already stated in the introduction, Wt production offers a complementary window through which to look at top quark interactions, being sensitive to corrections to the Wtb vertex, but not to four fermion operators which may affect the $s-$ and $t-$ channel modes. The investigation of Wt production as a signal in its own right was first explored in [67]. Since then, computations have been carried out at NLO [35, 36], and also matched to a parton shower at this accuracy [20, 29].

The aim of this section is to examine angular observables and energy ratios for both Wt and top pair production, for semi-realistic analysis cuts, and to reflect upon whether these results may be useful in enhancing the signal to background ratio of the former process. To this end, we adopt the following Wt signal cuts, similar to those used in [41]:

Wt signal cuts

1. The presence of exactly 1 b jet with $p_T > 50$ GeV and $|\eta| < 2.5$. No other b jets with $p_T > 25$ GeV and $|\eta| < 2.5$.

2. The presence of exactly 2 light flavour jets with $p_T > 25$ GeV and $|\eta| < 2.5$. In addition, their invariant mass should satisfy 55 GeV$< m_{j_1 j_2} <$ 85 GeV.

3. Events are vetoed if the invariant mass of the b jet and light jet pair satisfies

$$150 \quad \text{GeV} \quad < \sqrt{(p_{j_1} + p_{j_2} + p_b)^2} \quad < \quad 190 \quad \text{GeV}.$$

4. The presence of exactly 1 isolated lepton with $p_T > 25$ GeV and $|\eta| < 2.5$. The lepton should satisfy $\Delta R > 0.4$ with respect to the two light jets and the b jet, where R is the distance in the (η, ϕ) plane.

5. The missing transverse energy should satisfy E_T^{miss} >25 GeV.

Here the first cut is the most useful one in getting rid of top pair production, as one expects two b jets on average in $t\bar{t}$ production, but only one b jet in Wt. The other cuts pick out semi-leptonic decays[3]. That is, one W boson decays to leptons (we would want

[3]Note that to increase the statistics in our analysis, we will explicitly generate semi-leptonic decays using MC@NLO. The above analysis cuts, however, will still affect the shapes of distributions.

this to be the W boson from the top quark decay), and the other decays to quarks. We thus expect two light jets whose invariant mass reconstructs the W mass, as well as a lepton and missing energy from the neutrino. The only difference with respect to the cuts used in [41] is the presence of an additional cut involving the invariant mass of the b jet and light jet pair, restricting this to be different than the top mass. This ensures that the selected semi-leptonic events are such that the top quark in Wt decays leptonically, and the W hadronically, as is required in order to use the decay lepton as a marker of top quark polarization effects.

It was shown in [41] that, for these signal cuts (minus the invariant mass requirement for the three jets, which was unnecessary in that analysis), Wt is a well-defined scattering process in that interference with pair production can be neglected. This was found by comparing the DR and DS results from MC@NLO. The results in this section were obtained using the DR subtraction method. Furthermore, the Wt cross-section was found to be larger than the scale-variation uncertainty associated with the top pair cross-section. If this had not been true, then Wt production would be swallowed up in the uncertainty of the top pair prediction, and much more care would be needed in order to be able to claim that it can be observed independently. We thus use the above cuts as an example of a fairly minimal analysis which guarantees that Wt is a well-defined signal. We will see that even for this analysis, the angular and energy-related observables defined in section 2.3 display pronounced differences between Wt and top pair production.

Note that in this section, in order to be more realistic, we consider distributions constructed from the isolated lepton entering the cuts. This is not guaranteed to be the decay lepton from the top quark, although the likelihood of this is increased by the event selection cuts. Also, we assume that the top quark direction is reconstructed with perfect resolution. In practice this would be done by considering the four-momenta of the b jet and isolated lepton passing the cuts, together with missing energy. A full determination of the uncertainty induced in the reconstruction of the top quark (also including detector effects) is beyond the scope of the present study. Note that in Wt and $W\bar{t}$ production, we assume that the top and antitop quark is reconstructed respectively. In top pair production, one constructs either the top or antitop quark which decays to give the isolated lepton passing the selection cuts. In contrast to the H^-t results of the previous section, we present results for a centre of mass energy of 7 TeV. Jets are clustered using the k_T algorithm [68] with D=0.7.

We first consider the azimuthal angle ϕ_l, whose distribution is shown in fig. 3.15 for both Wt and top pair production.

The first thing to notice is that there is a distinct shape difference between the Wt and top pair curves. The Wt results include a slight peak structure at $\theta = \pi$, due to the contribution from events in which the W boson decays leptonically, rather than the top quark. This structure is missing in the case of top pair production, due to the symmetrical nature of the final state. For the choice of analysis cuts given above, one may evaluate the asymmetry parameter A_ϕ, which is shown in tab. 3.1. The values for Wt and top pair production are significantly different. This is potentially a useful distinguishing feature between the two production processes.

Next, we consider the polar angle θ_l, again defined in terms of the isolated lepton

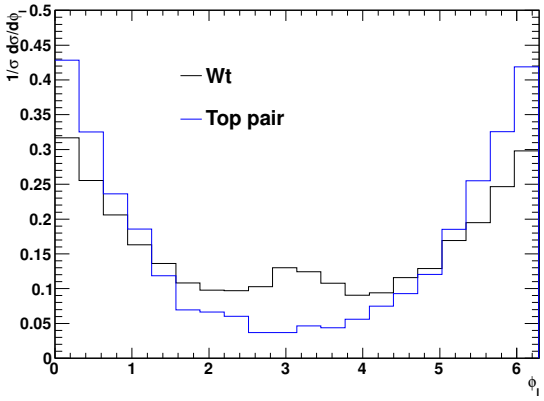

Figure 3.15: Azimuthal angle distribution of the isolated lepton which enters the Wt signal cuts, for both Wt and top pair production, at NLO plus parton shower level.

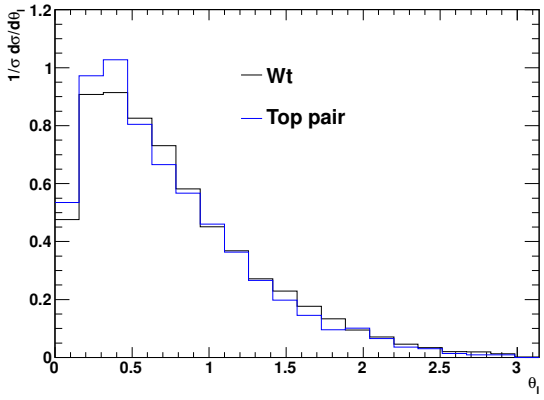

Figure 3.16: Polar angle distribution of the isolated lepton which enters the Wt signal cuts, for both Wt and top pair production, at NLO plus parton shower level.

B_{cut}	Wt	Top pair
0	0.33 ± 0.01	0.63 ± 0.02
0.8	0.41 ± 0.02	0.70 ± 0.05
0.9	0.42 ± 0.03	0.70 ± 0.07
0.95	0.44 ± 0.04	0.68 ± 0.08

Table 3.1: Results for the azimuthal asymmetry parameter A_ϕ of eq. (2.9), evaluated using the isolated lepton entering the Wt selection cuts, and for different values of a cut $B > B_{cut}$ on the boost parameter of the top quark.

B_{cut}	Wt	Top pair
0	0.02 ± 0.01	0.26 ± 0.02
0.8	0.18 ± 0.02	0.38 ± 0.04
0.9	0.49 ± 0.03	0.75 ± 0.07
0.95	0.70 ± 0.05	0.97 ± 0.10

Table 3.2: Results for the polar asymmetry parameter A_θ of eq. (3.3), evaluated using the isolated lepton entering the Wt selection cuts, and for different values of a cut $B > B_{cut}$ on the boost parameter of the top quark.

entering the Wt signal cuts. The distribution of this angle is shown in fig. 3.16. There is a notable difference between the Wt and top pair production, due to the negative polarization of the top in the former case. The corresponding asymmetry parameters A_θ are shown in tab. 3.2. Again the results are different between the two production processes which, as in the azimuthal case, is a potentially useful discriminator between the two processes.

In the case of H^-t production considered in section 3.3, we also considered various observables which depended upon the boost of the top quark. This is clearly of practical importance for heavy charged Higgs masses, which do indeed lead to heavily boosted top quarks in a sizeable fraction of events, as is clear from fig. 3.1. One expects boosted top observables to be less useful in Wt production, due to the fact that the W boson is much lighter. Nevertheless, it is perhaps worth examining the dependence of various observables on the boost parameter of the top quark. If sizeable differences between Wt and top pair production were to be observed, the impact on the signal to background ratio would then outweigh the loss in signal cross-section.

The distribution of the boost parameter B of eq. (2.10) is shown for both Wt and top pair production in fig. 3.17, and one sees that there is a reasonable fraction of events in both cases which have $B > 0.8$, albeit not as large a fraction as in the H^-t case of the previous section. This is not surprising, given that charged Higgs masses of at least 200 GeV were considered there, so that the top recoiled against a much more massive particle than a W boson. Here we also have a lower centre of mass energy. The ϕ_l distributions for the two processes are shown in fig. 3.18 for different values of a cut $B > B_{cut}$. One

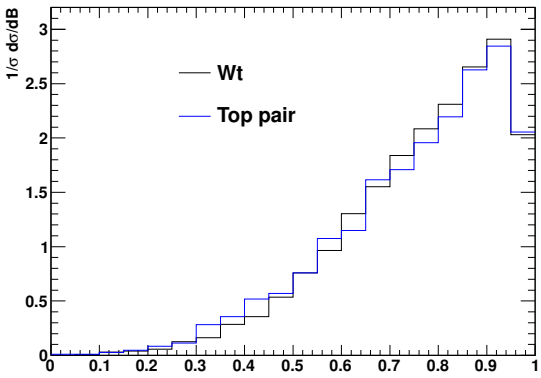

Figure 3.17: Distribution of the boost parameter B of eq. (2.10), at NLO plus parton shower level.

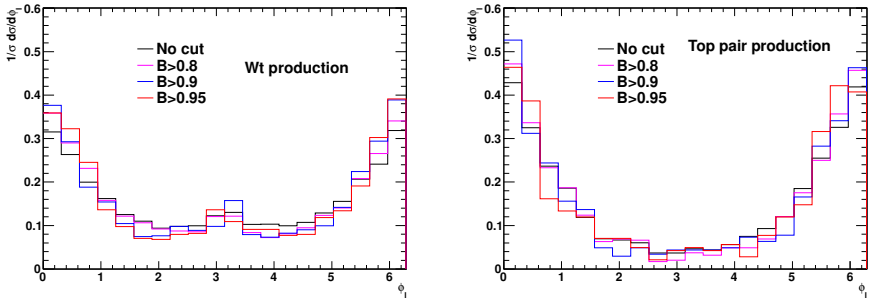

Figure 3.18: Azimuthal angle distribution of the isolated lepton which enters the Wt signal cuts, for Wt and top pair production, for different values of a cut $B > B_{cut}$ on the boost parameter of eq. (2.10), at NLO plus parton shower level.

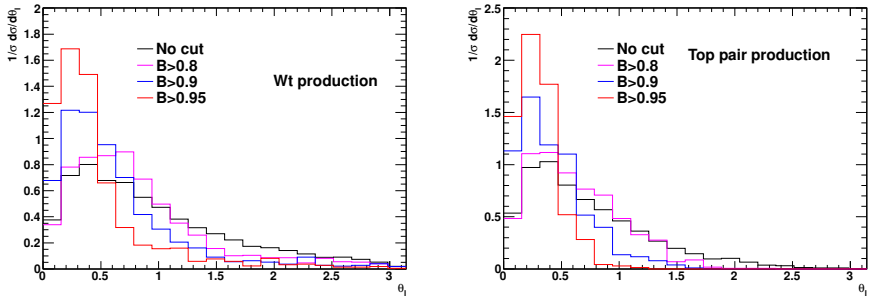

Figure 3.19: Polar angle distribution of the isolated lepton which enters the Wt signal cuts, for Wt and top pair production, for different values of a cut $B > B_{cut}$ on the boost parameter of eq. (2.10), at NLO plus parton shower level.

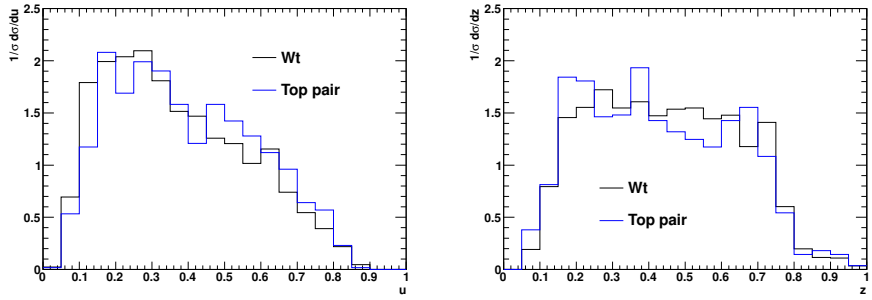

Figure 3.20: Distributions of u and z, as defined in eq. (2.11), where a cut on the boost parameter $B > 0.8$ has been applied, at NLO plus parton shower level.

sees that, whilst there is some dependency on the boost parameter, the qualitative features remain identical. The corresponding asymmetries A_ϕ are given in tab. 3.1. One sees that the absolute value of the difference between the asymmetries for the two processes is roughly independent of the boost cut. However, the relative difference decreases.

One expects a much greater effect from the boost on the polar angle distribution, as the requirement of a boosted top will concentrate the decay products in polar angle. The θ_l distributions as a function of B_{cut} are shown in fig. 3.19.

The effect of the higher boost cut is to increase the peak region of the distribution at the expense of the tail, as expected. The corresponding A_θ values are collected in tab. 3.2. Unsurprisingly, both sets of results display an increase in A_θ as the boost cut is increased. This implies that a boost cut is actually detrimental in this case, as the relative difference between the asymmetry parameters in the two processes decreases.

Finally, we present results for the energy ratios of eqs. (2.11), which were shown to

be useful for $H^- t$ production in section 3.3. In that case, we defined the energy of the b quark via eq. (3.4), which is possible in a Monte Carlo study but not in a real experiment. Here, given that we have explicitly implemented analysis cuts in terms of jets, we define E_b to be the energy of the b jet which enters the cuts. Then the distributions of z and u, with a cut on the boost parameter of $B > 0.8$, are shown in fig. 3.20. The first thing to note is that the results for the u distribution do not show a significant difference between Wt and top pair production. This is perhaps not so surprising given that we have already seen in section 3.3 that oppositely polarized top quarks tend to exhibit smaller differences in energy-related distributions than in angular distributions. Here we are essentially probing the difference between a polarized top quark and one which is unpolarized on average, and thus one expects an even smaller difference in behaviour.

The z distribution in fig. 3.20 shows some difference between the Wt and top pair distributions. However, the top pair result does not closely resemble the flat profile one would expect for unpolarized top quarks, due presumably to that fact that the shape has been sculpted somewhat by the event selection cuts, in particular those which implement restrictions on jet invariant masses.

Given the above results, it does not seem particularly useful to examine the asymmetry parameters of eqs. (3.5, 3.6) in the present context. Nevertheless, the fact that a shape difference persists in the z distribution between Wt and top pair production still makes this a potentially useful observable in discriminating the two processes, perhaps as an ingredient in a neural net analysis. One must also bear in mind the result for the polar asymmetry from above, namely that a boost cut will decrease the relative difference between the angular asymmetries in Wt and top pair production. Thus, and perhaps unsurprisingly, the utility of boost cuts in Wt production is somewhat limited.

3.5 Conclusion

In this chapter, we have examined the role that observables that are sensitive to top quark polarization can play in exploring the parameter space of charged Higgs models, and also in distinguishing $H^- t$ production from (Standard Model) Wt production. In particular, we examined the azimuthal and polar angles ϕ_l and θ_l of [9, 17], and the energy ratios z and u of [12], defining corresponding asymmetry parameters analogous to that already defined for the azimuthal angle in [17]. Importantly, we found that polarization effects are robust up to NLO and including parton shower corrections[4]. At this level, each of the asymmetry parameters showed significant difference between different regions in the charged Higgs parameter space $(m_H, \tan\beta)$, and also between $H^- t$ and Wt production. The full set of asymmetries taken together thus provides a potentially highly useful probe of charged Higgs properties. Angular observables are sensitive only to corrections to the production of a top quark, and the polar angle is able to discriminate between charged Higgs masses at high $\tan\beta$ values, where the azimuthal angle cannot. Energy observables are sensitive to corrections to both the production and decay of top quarks. Although more

[4] A similar robustness has already been observed in (Standard Model) $s-$ and $t-$ channel single top production [66].

difficult to construct (owing to the need for a cut on the boost parameter of the top quark), they give useful complementary information, particularly on the value of the charged Higgs mass at intermediate and high $\tan\beta$ values.

As a second application of these observables, we considered the problem of distinguishing Standard Model Wt production from top pair production, which is a significant background. Under the assumption that it is meaningful to separate Wt and top pair production, we observed significant differences, for semi-realistic Wt analysis cuts, between angular distributions relating to the isolated lepton entering the cuts. It is worth pointing out that the cuts we used are fairly minimal in terms of signal to background ratio [41]. Nevertheless, large differences are obtained between the two production processes, which suggests that our findings would persist in a more realistic study, including detector effects etc.

One may also consider boosted top quark observables in Standard Model Wt production, and we gave a couple of examples in section 3.4. These seem less useful than in H^-t production, however. In the angular observables, a cut on the boost parameter does not increase the absolute difference between the asymmetry parameters for Wt and top pair production, and decreases the relative difference. For energy observables, one sees only a small difference between the u distributions even when a boost cut is applied. This is due mainly to the fact that one is comparing a polarized top quark in Wt with an (on average) unpolarized top quark in top pair production, rather than an oppositely polarized top quark. A larger difference is observed in the z distribution, which may yet be a useful observable in distinguishing Wt and top pair production.

To summarise, the observables studied in this paper are useful probes of both H^-t and Wt production, and seem to be robust against higher order perturbative corrections. They therefore deserve further investigation.

Chapter 4

Top Polarization in Stop Production

In the previous chapter we have explored the robustness of top quark polarization under the influence of NLO corrections. These corrections were studied for the production of a top quark with associated charged Higgs boson for a 2HDM. The influence of polarization measured in the angular distributions of the top quark decay product was compared to the mass of the Higgs boson and found to be an interesting probe. In this chapter we will explore a more stringent model that naturally requires the existence of such an additional Higgs doublet. We will investigate a significant top quark production mode, and examine whether polarization can be used as a probe for such a model's parameters.

4.1 Supersymmetry

As explained in the introduction, the SM leaves a few questions unanswered, for instance it failed to include gravity. At LHC energies one is still able to ignore this fundamental force but gravity inevitably becomes more important as we approach the Planck scale. Other weaknesses of the SM include its inadequacy to provide a dark matter candidate. These shortcomings create space for new models, based on somewhat more exotic assumptions, to provide a more accurate description. One of these is supersymmetry.

The mass of the Higgs boson in the SM is extraordinarily sensitive to loop corrections of the fermions as it is not protected by any symmetry in the way chiral symmetry protects fermion masses. If the SM is regarded as an effective theory, the corrections to the Higgs mass depend quadratically on the energy scale Λ, where new physics sets in. Therefore a large amount of fine-tuning is required between the bare mass and the loop corrections to remain with a Higgs mass of 125 GeV as Λ will be at least a few orders higher. This artifact of the SM is commonly referred to as the Hierarchy Problem, as it is related to the hierarchy of energy scales. Supersymmetry (SUSY) postulates the existence of a symmetry between fermions and bosons that allows for a natural cancellation of these

quadratic divergences, leaving more benign logarithmic divergences. It also implies the existence of supersymmetric partners to all known SM particles, with the same mass and electric charge, but differing by spin-$\frac{1}{2}$. Regarding nomenclature, fermionic partners receive +s(calar) in front of their name while the names of the supersymmetric partners of the bosons are appended with +ino in the rear. For a detailed review of supersymmetry we refer the reader to [16, 69].

Searches for light-flavoured squarks and gluinos at the Large Hadron Collider (LHC) have so far come up empty [70–73]. Theoretical pointers for the expected mass scales for SUSY breaking, accounting for SUSY particles to be massive, come from naturalness arguments [74–76]. In SUSY, the low mass of the observed Higgs boson, is naturally stable under large radiative corrections, provided the supersymmetry breaking scale is not too large. In particular, the gluinos and most squarks can be quite heavy, as long as the top squark, or stop, is relatively light so that SUSY has a solution to offer to the hierarchy problem as suggested originally [77, 78]. The upper limit on the allowed stop masses for a given Higgs mass depends on the amount of fine tuning that is tolerated [79–81].

The recent Higgs results [82, 83] suggest, in the context of SUSY, a Higgs boson mass quite close to the upper bound on the mass of the lightest Higgs state. This points towards at least one relatively heavy stop [84, 85], which naturally leads us to consider models with one light stop and at least one light neutralino. The lightest neutralino is a mixed state of the superpartner of the $U(1)$ hypercharge, the superpartner of the W boson and the neutral higgsinos. This is the minimal 'light' SUSY particle content that one needs in order to account for the observational hints of BSM physics such as Dark Matter (DM) and Baryon Asymmetry in the Universe (BAU). It is therefore interesting to investigate possibilities of such a light stop search at the LHC. Current constraints on the gluino mass increase the interest for a direct stop pair search, even though the cross section is much smaller than the total squark-gluino cross-section. For example at $\sqrt{s} = 8$ TeV the direct stop cross section at NLL level is ~ 85 fb for $m_{\tilde{t}} = 500$ GeV, [86–89] a value for the stop mass that is currently allowed by the data. Results on stop searches in direct stop pair production have been presented both by the ATLAS [90–93], and the CMS [94–97] collaborations. However, the interpretation of these searches has some model-dependence and usually limits are quoted in simplified models. In any case, present data allows for top squarks well below the TeV scale.

One new aspect of the stop search phenomenology is the possible presence of a top quark, a stop decay product, with possibly non-zero polarization. Since the top quark decays before it hadronizes, the polarization can have implications for the kinematic distributions of the decay products of the stop and hence on the search strategies. If a stop is discovered, the top polarization can play a role in determining the properties of the stop and light neutralino.

4.2 Top Polarization from Stop Decay

In [98] it was shown that for a top quark originating from stop $\tilde{t}$ decay

$$\tilde{t}_1 \to t\,\tilde{\chi}_i^0, \tag{4.1}$$

where $\tilde{\chi}_i^0$, $i = 1, 4$ accounts for the four neutralinos, the following expression for the polarization holds

$$P_t(\tilde{t}_1 \to t\,\tilde{\chi}_i^0) = \frac{\big((G_i^R)^2 - (G_i^L)^2\big) f_1}{(G_i^R)^2 + (G_i^L)^2 - 2G_i^R G_i^L f_2}\,, \tag{4.2}$$

where f_1 and f_2 are kinematical factors which in the stop rest frame reduce to

$$f_1 = \frac{\lambda^{\frac{1}{2}}(m_{\tilde{t}}^2, m_t^2, m_{\tilde{\chi}}^2)}{m_{\tilde{t}}^2 - m_t^2 - m_{\tilde{\chi}}^2}\,, \qquad\qquad f_2 = \frac{2m_t m_{\tilde{\chi}}}{m_{\tilde{t}}^2 - m_t^2 - m_{\tilde{\chi}}^2}\,, \tag{4.3}$$

with $\lambda(x, y, z) = x^2 + y^2 + z^2 - 2xy - 2xz - 2yz$ the Källén function. The quantities G_i^L and G_i^R are the stop couplings to the neutralino $\tilde{\chi}_i^0$ and a left- or right-handed top respectively. If we ignore mixing in the flavour sector and choose the mixing matrices to be real, they are given by [99]

$$\begin{aligned} G_i^L &= -\sqrt{2} g_2 \left(\frac{1}{2} Z_{i2} + \frac{1}{6}\tan\theta_W Z_{i1}\right)\cos\theta_{\tilde{t}} - \frac{g_2 m_t}{\sqrt{2} M_W \sin\beta} Z_{i4}\sin\theta_{\tilde{t}}\,, \\ G_i^R &= \frac{2\sqrt{2}}{3} g_2 \tan\theta_W Z_{i1}\sin\theta_{\tilde{t}} - \frac{g_2 m_t}{\sqrt{2} M_W \sin\beta} Z_{i4}\cos\theta_{\tilde{t}}\,, \end{aligned} \tag{4.4}$$

where g_2 is defined in section. 2.4, θ_W is the weak mixing angle and M_W is the W mass. The polarization then depends on the SUSY parameters through the neutralino mixing matrix Z, the stop mixing angle $\theta_{\tilde{t}}$ and the ratio of the two Higgs vacuum expectation values, $\tan\beta$. Moreover it is clear from eq. (4.2) that the top polarization is affected by the masses involved and, perhaps less obviously, by the stop boost. Let us now discuss these effects in turn.

4.2.1 Stop and Neutralino Mixing

The top polarization eq. (2.5) depends on the couplings $G_i^{L,R}$, eq. (4.4), which contain the stop mixing $\theta_{\tilde{t}}$ and neutralino mixing. The neutralino mixing matrix is constructed from the neutral section of the SUSY Lagrangian [100],

$$\begin{aligned} \mathcal{L}^n = &-\frac{g_2}{2}\lambda_3(v_1\tilde{h}_0^1 - v_2\tilde{h}_0^2) + \frac{g_Y}{2}\lambda_0(v_1\tilde{h}_1^0 - v_2\tilde{h}_2^0) + \mu\tilde{h}_1^0\tilde{h}_2^0 \\ &- \frac{1}{2}M_2\lambda_3\lambda_3 - \frac{1}{2}M_1\lambda_0\lambda_0 + h.c. \end{aligned} \tag{4.5}$$

The first and second term arise from mixing terms of the electroweak sector, the third term comes from the Higgs superfield in the superpotential and the last two terms are soft

breaking gaugino mass terms contracting using the fully antisymmetric tensor. The Higgs scalars have taken their vacuum expectation values v_1 and v_2, λ_0, λ_3 denote two gaugino fields and $\tilde{h}_1^0, \tilde{h}_2^0$ two higgsino field components. g_1 is the $U(1)_Y$ hyper charge coupling and g_2 as defined in the previous section. Eq. (4.5) can be rewritten as

$$\mathcal{L}^n = -\frac{1}{2}(\psi^0)^T \mathcal{M}_n \psi^0 + h.c. \tag{4.6}$$

with $(\psi^0)^T = (\lambda_0, \lambda_3, \tilde{h}_1^0, \tilde{h}_2^0)$. The neutralino mixing matrix, Z is determined by the diagonalization of the neutralino mass matrix M_n

$$M_n = \begin{pmatrix} M_1 & 0 & -M_Z c_\beta s_W & M_Z s_\beta s_W \\ 0 & M_2 & M_Z c_\beta s_W & -M_Z s_\beta c_W \\ -M_Z c_\beta s_W & M_Z c_\beta c_W & 0 & -\mu \\ M_Z s_\beta s_W & -M_Z s_\beta c_W & -\mu & 0 \end{pmatrix} \tag{4.7}$$

$$\begin{pmatrix} \tilde{\chi}_1^0 \\ \tilde{\chi}_2^0 \\ \tilde{\chi}_3^0 \\ \tilde{\chi}_4^0 \end{pmatrix} = Z \begin{pmatrix} \lambda_0 = \tilde{B}^0 \\ \lambda_3 = \tilde{W}^0 \\ \tilde{h}_1^0 \\ \tilde{h}_2^0 \end{pmatrix}, \tag{4.8}$$

with M_1 and M_2 the bino and Wino gaugino masses and M_Z the Z^0 mass, $s_W = \sin\theta_W$, $c_W = \cos\theta_W$, $s_\beta = \sin\beta$ and $c_\beta = \cos\beta$.

The stop mixing angle $\theta_{\tilde{t}}$ is derived in a similar way by diagonalization of the stop mass matrix in the $L - R$ basis, leading to the mass eigenstates $\tilde{t}_1$ and $\tilde{t}_2$

$$M_{\tilde{t}}^2 = \begin{pmatrix} m_{\tilde{t}_L}^2 + \Delta_L + m_t^2 & -m_t(A_t + \mu\cot\beta) \\ -m_t(A_t + \mu\cot\beta) & m_{\tilde{t}_R}^2 + \Delta_R + m_t^2 \end{pmatrix}, \tag{4.9}$$

$$\begin{pmatrix} \tilde{t}_1 \\ \tilde{t}_2 \end{pmatrix} = \begin{pmatrix} \cos\theta_{\tilde{t}} & \sin\theta_{\tilde{t}} \\ -\sin\theta_{\tilde{t}} & \cos\theta_{\tilde{t}} \end{pmatrix} \begin{pmatrix} \tilde{t}_L \\ \tilde{t}_R \end{pmatrix}, \tag{4.10}$$

with $m_{\tilde{t}_{L,R}}$ the soft masses of the left- and right-handed stop, A_t the top trilinear coupling, μ the Higgs mass parameter, and $\Delta_L = (\frac{1}{2} - \frac{2}{3}\sin\theta_W^2) M_Z^2 \cos 2\beta$,
$\Delta_R = (\frac{2}{3}\sin\theta_W^2) M_Z^2 \cos 2\beta$.

Our subsequent investigations of the top polarization will be guided by a few salient aspects in this mixing, which we now discuss.

Firstly, one notes that the strength of the bino ($\tilde{B}$) coupling to stop-top is proportional to the top hypercharge. As a result, a bino-like neutralino couples more strongly to the right-handed (RH) components than to the left-handed (LH) ones, yielding a more positive top polarization than one might naively expect from a given stop mixing.

Secondly, recall that the Wino $\tilde{W}$ only couples to the left-handed stop components, producing left-handed top quarks only. According to eq. (4.2), a pure Wino thus always leads to $P_t = -f_1$ in the stop rest frame. As a result, polarization cannot be used to distinguish between different stop mixing for Wino-type neutralinos. In the rest of the paper we will thus limit ourselves to neutralinos with a small Wino component.

Thirdly, for the intermediate to large values of $\tan\beta$ that are allowed for the Higgs mass constraint, $\sin\beta \approx 1$, therefore the couplings in eq. (4.4) and hence the top polarization only mildly depend on $\tan\beta$.

Finally, the stop-top-neutralino coupling does not involve the first higgsino component $\tilde{h}_1^0$. Ignoring the Wino component, the key variables in the neutralino mixing matrix are thus the bino component Z_{i1} and the second higgsino component Z_{i4}. The relative sign between the bino and the higgsino components can impact the polarization because of the term proportional to $G_i^R G_i^L$ in eq. (4.2). This can be seen in fig. 4.1, where the top polarization in the stop rest frame is plotted as a function of the bino content for both left- and right-handed stops. The righthand pane in fig. 4.1 zooms into the region with high bino-content. The results are shown for both relative signs of Z_{i1} and Z_{i4} and also for stops that are not entirely left- or right-handed.

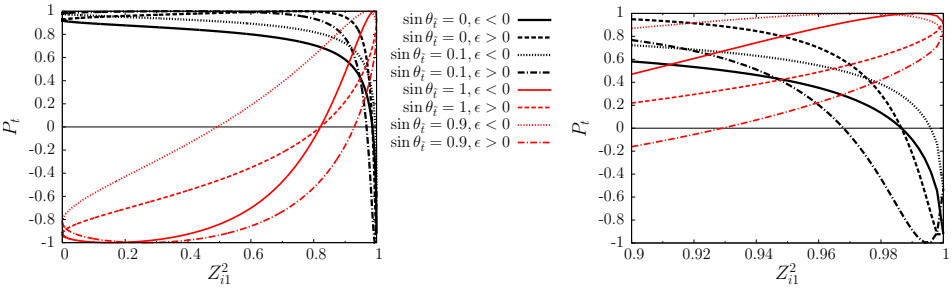

Figure 4.1: Dependence of the top polarization on the neutralino content in the stop rest frame. The red thin lines correspond to right-handed stops, while the black thick lines correspond to left-handed stops. Results are shown for pure as well as slightly mixed stops, and for different relative signs of Z_{i1} and Z_{i4}. We have taken $Z_{i4} = \epsilon\sqrt{(1 - Z_{i1}^2)}$, $\epsilon = \pm 1$ to approximate the higgsino-content for a given bino-content and have taken $m_t = 173.1$ GeV, $m_{\tilde{t}} = 500$ GeV, $m_{\tilde{\chi}} = 200$ GeV and $\tan\beta = 10$. The plot on the right shows the behaviour for high bino-content.

The figure shows that in general the polarization behavior is as expected: dominantly right-handed stops produce a negative top polarization when they decay to a higgsino, and a positive polarization when they decay to a bino. Left-handed stops have the opposite behaviour. Notice that in correspondence to the first aspect mentioned above, for right-handed stops in particular, even a slight change in the stop mixing angle has a large effect on the polarization. We observe that the polarization for left-handed stops is not very sensitive to the exact neutralino content when it is higgsino-like and that the polarization varies very rapidly from 1 to -1 for an almost pure bino. Moreover, the maximum polarization $P_t = \pm 1$ cannot occur for a decay into a pure bino or higgsino due to the mass effects in eq. (4.2). This effect becomes more pronounced for smaller stop-neutralino mass differences.

For a complementary perspective we show in fig. 4.2 the dependence of the top polarization on the stop mixing for a top quark that originates from a stop that is at rest. For both the pure bino state and the dominantly higgsino state, the polarization indeed behaves as one would expect from eq. (4.2). As in fig. 4.1, we see that the polarization

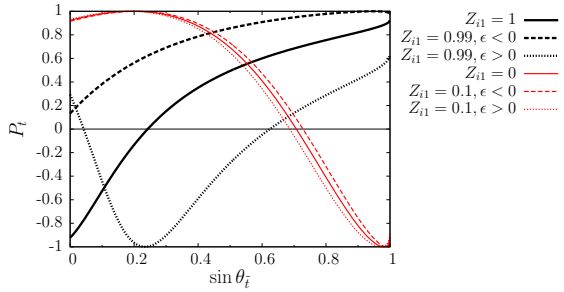

Figure 4.2: Dependence of the top polarization on the stop mixing in the stop rest frame. The red thin lines correspond to higgsino-like neutralinos, while the black thick lines correspond to bino-like neutralinos. Results are shown for pure as well as slightly mixed neutralinos, and for different signs of μ. We fix the parameters as in fig. 4.1

is very sensitive to small fluctuations in the bino component for $Z_{i1} \approx 1$. In this case, both terms in the G_i^R coupling in eq. (4.4) become relevant, the first is suppressed by the stop mixing and the second by the higgsino mixing, hence the large fluctuation in the polarization for small values of $\sin\theta_{\tilde{t}}$.

4.2.2 Masses

We have already seen that the stop and neutralino masses influence the polarization. This effect is shown in fig. 4.3.

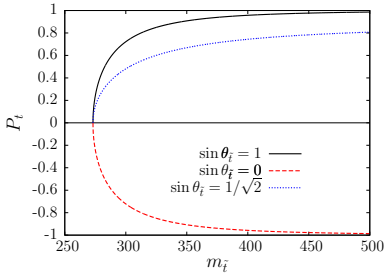

Figure 4.3: Dependence of the top polarization in the stop rest frame on the stop-neutralino mass difference for a neutralino that is purely bino and different stop mixing. We have taken $m_t = 173.1$ GeV, $m_{\tilde{\chi}} = 100$ GeV and $\tan\beta = 10$.

We see that a small mass difference between the stop and the neutralino leads to a smaller polarization due to the f_1 and f_2 functions in eq. (4.3). For mass differences of 200-300 GeV, this dependence is negligible as the polarization tends to ± 1 as is seen in the figure. Note that the top originating from a completely mixed stop resembles a right-handed stop because of the effect of the hypercharge mentioned in the previous section.

We have seen in figs. 4.1 and 4.2 that masses can have more intricate effects for mixed states due to the contribution of the f_2 function.

4.2.3 Stop Boost

So far we have studied the top polarization in the stop rest frame. However, as we can see from eq. (2.4), the polarization vector S^3 is not a Lorentz vector. Thus the polarization is frame-dependent. We can quantify this effect using the stop boost parameter

$$B_{\tilde{t}} = \frac{|\vec{p}_{\tilde{t}}|}{E_{\tilde{t}}} \,. \tag{4.11}$$

The dependence of the polarization is plotted in fig. 4.4, showing that the polarization is reduced with increasing stop boost.

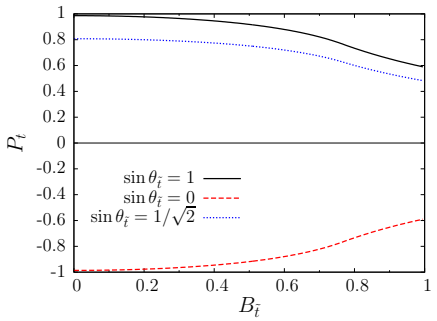

Figure 4.4: The dependence of the top polarization on the stop boost for a neutralino that is purely bino ($Z_{11} = 1$) and different stop mixing is shown. We have taken $m_t = 173.1$ GeV, $m_{\tilde{t}} = 500$ GeV, $m_{\tilde{\chi}} = 100$ GeV and $\tan\beta = 10$.

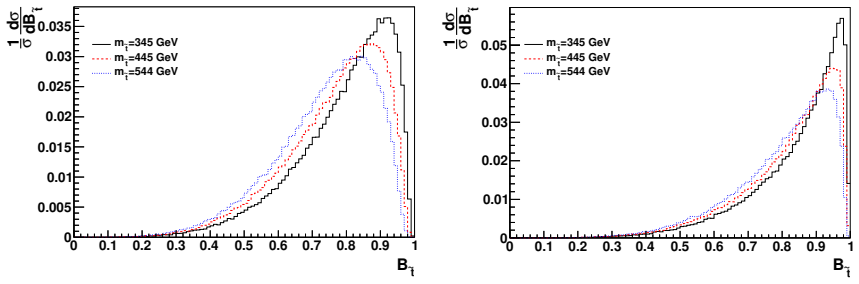

Figure 4.5: The distribution of the stop boost at the LHC with an 8 TeV CM energy for different stop masses is shown on the left-hand side and 14 TeV CM energy on the right-hand side. Both distributions have been generated with Madgraph [13, 14].

Note that the polarization is obtained after integration over the top direction, and hence depends only on the boost. The precise magnitude of the effect depends on the masses

involved, since the boost-dependence of the result originates from the large mass of the top quark, more precisely from the fact that the produced top quark is non-relativistic. For relevant stop and neutralino masses, the boost that the top obtains from the stop decay has the same order of magnitude as the stop boost. Although this sounds like a serious complication for studying the polarization at the LHC, the situation is in fact not that bad. The plots of fig. 4.5 show the distribution of the stop boost at the LHC with a CM energy of 8 and 14 TeV. We see that within the relevant range of stop masses, the boost distribution is fairly constant. Thus, the effect of the boost will reduce the polarization for all stop masses, but the explicit mass dependence due to the boost is small.

4.3 Sensitivity to SUSY Parameters

The top polarization in the stop rest frame is thus mostly sensitive to the stop and neutralino masses and mixing. In the previous section, we have varied one of the relevant parameters at a time. In this section, we examine the dependence of the polarization on the MSSM parameters. We choose parameters such that the value of the light stop mass is around 500 GeV. This mass leads to a large production cross section and has sufficient phase space for the stop to decay in a top and a neutralino for a wide range of values for the neutralino mass. Furthermore, this mass satisfies the limits from direct stop production at the 7 TeV LHC. The ATLAS Collaboration has excluded a stop up to nearly 500 GeV when the neutralino is massless, but they provide no limit if the LSP is heavier than 150 GeV [91].

First we choose fixed values for the soft parameters in the stop sector, and then vary M_1 and μ, given in eq. (4.5), which show the dependence on the neutralino composition. The four sets of soft parameters are given in tab. 4.1. We set $M_2 = 4M_1$ to decouple the wino-state by making the wino mass inaccessible and we fix $M_3 = 1.5$ TeV, $M_A = 1$ TeV. For the soft parameters in the sfermion sector, we choose a common mass for all sleptons, $M_{\tilde{l}} = 800$ GeV, and for the first and second generation of squarks, $M_{\tilde{q}_i} = 2$ TeV. All trilinear couplings except A_t are set to zero. The supersymmetric spectrum and the Higgs masses are computed with the program SuSPect [101], which includes radiative corrections to the masses.

We do not impose any constraints on the model at this point. However, the parameters of the stop sector are chosen such that the Higgs mass is within the measured range ($m_H = 125.7 \pm 0.4$ GeV, the average of CMS and ATLAS results [82, 83]) for a large fraction of the explored parameter space while allowing for an additional 2-3 GeV theoretical uncertainty. Expectations for different observables from the flavour or dark matter sector are not taken into account at this point. They will be briefly discussed at the end of this section.

The dependence of the top polarization and stop branching ratio $BR(\tilde{t}_1 \to t\tilde{\chi}_1^0)$ on the Higgs mass parameter μ and gaugino mass M_1 is displayed in fig. 4.6 - 4.9 for the four different choices of stop parameters presented in tab. 4.1. We only consider the region where the decay $\tilde{t}_1 \to t\tilde{\chi}_1^0$ is kinematically accessible. Note that the maximal variation of the Higgs mass in the $|\mu| < 1$ TeV, $M_1 < 750$ GeV plane is about 3 GeV, within the

	$M_{\tilde{Q}_3}$ (TeV)	$M_{\tilde{u}_3}$ (TeV)	A_t (TeV)	$\tan\beta$
LH	0.49	2.00	3.00	10
XLH	0.55	1.40	2.40	20
XRH	1.05	0.60	1.88	20
RH	2.00	0.45	2.40	10
	$M_{\tilde{t}_1}$ (GeV)	$\sin\theta_{\tilde{t}}$	$\cos\theta_{\tilde{t}}$	M_h(GeV)
LH	521.	-0.126	0.992	126.4
XLH	510.	-0.223	0.975	124.8
XRH	498.	0.946	-0.323	124.0
RH	508.	0.996	-0.095	125.5

Table 4.1: Choices of parameters in the stop sector for two mostly LH and two mostly RH stops. In each case we also consider a partly mixed light stop (XLH and XRH). The bottom rows specify the light stop mass, the stop mixing and the Higgs mass for $|\mu| = 300$ GeV, $M_1 = 250$ GeV.

theoretical uncertainties, while corrections to $m_{\tilde{t}_1}$ of the order of 30 GeV can be found for large values of M_2 due to the quark/gaugino loop correction.

The dominantly left-handed stop

As we have discussed in the previous section, the case of a left-handed stop implies $P_t \approx -1$ when the LSP is bino-like ($|\mu| \gg M_1$) and $P_t \approx 1$ when the LSP is higgsino-like ($|\mu| \ll M_1$). This behavior is illustrated on the left-hand side of fig. 4.6 for $\mu < 0$. Note the rapid transition between $P_t = 1 \to -1$ in the region where one goes from a bino to a higgsino LSP ($M_1 \approx \mu$). When the LSP almost becomes pure bino, the top polarization starts to deviate from -1. For instance at the point $M_1 = 100$ GeV, $\mu = -600$ GeV the top polarization is only $P_t \approx -0.73$. This is caused by the stop becoming mixed instead of purely LH, with $\sin\theta_{\tilde{t}} = -0.127$. Finally, the kinematic effects which induce $P_t \to 0$ arise at the boundary of the white region.

In order to exploit the top polarization as an observable, the branching ratio for $\tilde{t}_1 \to t\tilde{\chi}_1^0$ must be large enough. The contours of the stop to LSP branching ratio are displayed in the right panel of fig. 4.6. Large branching ratios are found over most of the parameter space, with two exceptions. The first occurs near the kinematic limit where the three-body decay $\tilde{t}_1 \to bW\tilde{\chi}_1^0$ dominates and the second occurs for low values of M_1. The latter behaviour is a peculiarity due to the fact that we have set $M_2 = 4M_1$. Thus for low values of M_1 and of M_2 the lightest chargino, which is dominantly wino, drops below the mass of the stop and the decay $\tilde{t}_1 \to b\tilde{\chi}_1^+$ becomes dominant. If in addition μ is small, the decay into the second chargino becomes possible as well.

In the region where the LSP is mostly higgsino $|\mu| < M_1$, the mass of the two lightest neutralinos and of the lightest chargino are of the same order. Thus the stop can decay into $t\tilde{\chi}_1^0, t\tilde{\chi}_2^0$ as well as into $b\tilde{\chi}_1^+$. The chargino channel is only at the few percent level while the decay into the LSP increases with the higgsino component, reaching a maximum of 70%. An important fact to keep in mind is that the two lightest neutralinos will have

higgsino-components of similar magnitude. Thus the polarization of the top in the two processes $\tilde{t}_1 \to t\tilde{\chi}^0_{1,2}$ is similar for the higgsino LSP. Therefore both decay modes can be exploited to measure the top polarization, as will be demonstrated below. In the region where the LSP is a bino, $M_1 < |\mu|$, the branching ratio into the LSP is nearly 100%, except for low values of μ, where the channels $b\tilde{\chi}^+_1$ (for $|\mu| < 500$ GeV) and $t\tilde{\chi}^0_2$ (for $|\mu| < 380$ GeV) also become accessible.

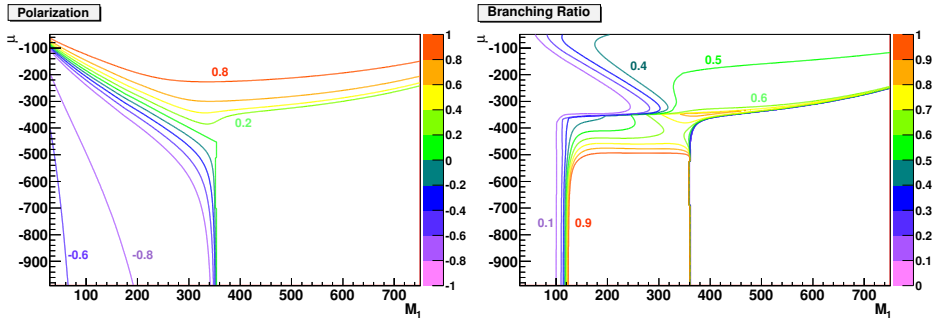

Figure 4.6: Contours of the top polarization in the top rest frame for $\mu < 0$ and a dominantly LH stop (left panel) with the LH parameters in tab. 4.1. Branching ratios for $\tilde{t}_1 \to t\tilde{\chi}^0_1$ (right panel). In the bottom right corner, the decay is not kinematically accessible.

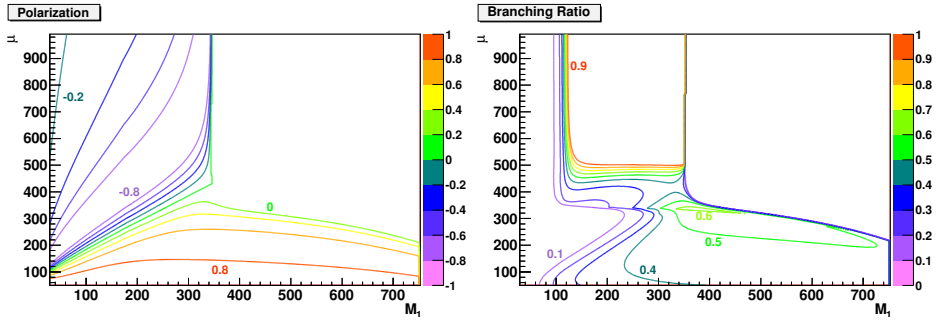

Figure 4.7: Same as fig. 4.6 for $\mu > 0$ and a mixed but dominantly LH stop corresponding to the XLH parameters in tab. 4.1. In the upper right corner the decay is not kinematically accessible.

For $\mu > 0$, the polarization and the branching ratio contours have roughly the same behaviour, so we do not illustrate this case. Rather, we consider a case where the light stop is still dominantly left-handed but where the mixing angle is larger, $\sin\theta_{\tilde{t}} = -0.223$, see the XLH parameters in tab. 4.1. Fig. 4.7 shows that for the mixed case the polarization and branching ratio contours are rather similar to the previously discussed LH case. The main difference lies in the bino region at large μ and small M_1, where the polarization is generally not maximal. As we have explained above, the mixing implies that the main contribution to the G_i^R coupling comes from the first term in eq. (4.4), causing $|P_t| < 1$.

We therefore conclude that in the bino case, the top polarization is quite sensitive to the mixing in the stop sector.

The dominantly right-handed stop

Next we consider the case of a dominantly right-handed stop. The polarization contours for $\mu < 0$ are shown in fig. 4.8 for a mixed RH stop and fig. 4.9 for a pure RH stop. We notice the expected behaviour of $P_t \approx 1$ when the LSP is bino-like ($|\mu| \gg M_1$) and $P_t \approx -1$ when the LSP is higgsino-like ($|\mu| \ll M_1$). As before, the kinematic effects (at the boundary of the white region) bring $P_t \to 0$. Note the rapid sign flip in the polarization as one goes from the bino/higgsino region. The only impact of larger stop mixing, as illustrated in fig. 4.8, lies in the higgsino region ($\mu < M_1$): when the mixing in the stop sector is larger, the top polarization is not maximal. This is due to the second term in eq. (4.4) dominating the G_i^R coupling, thus leading to a larger value for G_i^R and $|P_t| < 1$.

In both the pure and mixed RH stop cases, the behaviour of the branching ratio contours are rather similar. The branching ratio $\tilde{t}_1 \to t\tilde{\chi}_1^0$ is above 90% in the bino region, except near the kinematic limit where the stop decays only into 3-body, and at low values of M_1 for the mixed RH stop. As mentioned above, this is caused by the channel $\tilde{t}_1 \to b\tilde{\chi}_1^+$ becoming kinematically accessible, which is only possible through the LH component of the light stop. In the higgsino LSP region, the BR never becomes very large (up to roughly 25% for $t\tilde{\chi}_1$ and to 20% for $\tilde{\chi}_2, \tilde{\chi}_3$). Here the main decay channel is into $b\tilde{\chi}_1^+$ which has a partial width that is proportional to the top Yukawa coupling for a RH stop and is therefore much larger than in the case of a LH stop where the width is determined by the bottom Yukawa coupling. Thus for a RH stop and a higgsino LSP, it will be more difficult to measure the top polarization due to the suppressed rate.

Decays into heavier neutralinos

For a higgsino LSP, the branching ratio of the stop into the lightest neutralino can be rather small. However, in this case the top polarization is almost the same when one considers the decay $\tilde{t}_1 \to t\tilde{\chi}_1^0$ or $t\tilde{\chi}_2^0$ as illustrated in fig. 4.10. For the dominantly LH stop (left panel), the difference between the polarizations in the two channels never exceeds 10% when $M_1 > \mu$ which marks the onset of the higgsino LSP region. For the RH stop (right panel) the difference between the polarizations can reach 30% when $M_1 \approx \mu = 280\text{GeV}$ although both polarizations quickly become almost equal as M_1 is increased and thus the higgsino fraction of the neutralinos. The difference between the top polarization in the two higgsino channels is purely a kinematic effect due to the smaller mass splitting between the stop and the second neutralino. This effect is more pronounced for the RH stop case simply because the mass of $\tilde{t}_1$ is lower. Note that since the two lightest neutralinos are almost degenerate, the decay of the second neutralino into the LSP is accompanied by soft leptons and basically has the same missing E_T signature as the LSP. Therefore both decay channels can be used to determine the top polarization.

In the above, we have considered the behaviour of the top polarization without worrying about other constraints on the model. We will now briefly comment on the impact

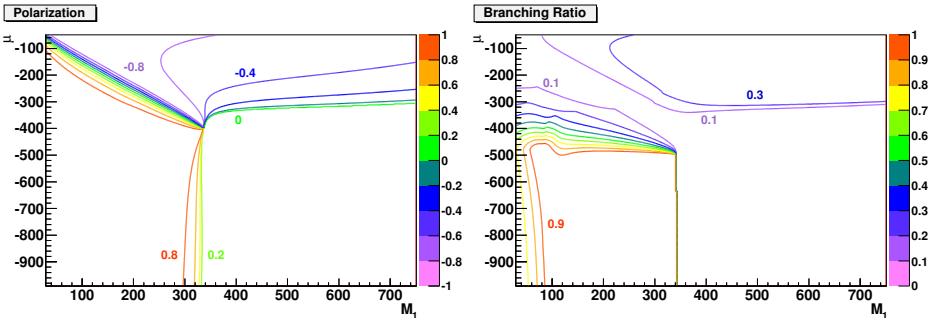

Figure 4.8: Contours of the top polarization in the top rest frame for $\mu < 0$ and a mixed dominantly RH stop (left). Branching ratios for $\tilde{t}_1 \to t\tilde{\chi}_1^0$ (right)

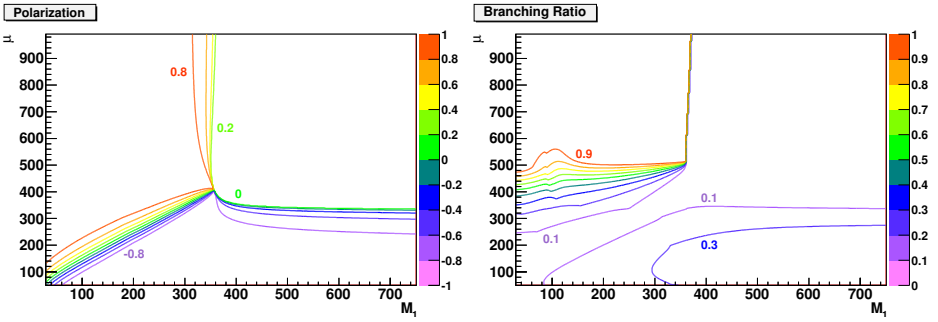

Figure 4.9: Same as fig. 4.8 for $\mu > 0$ and dominantly RH stop.

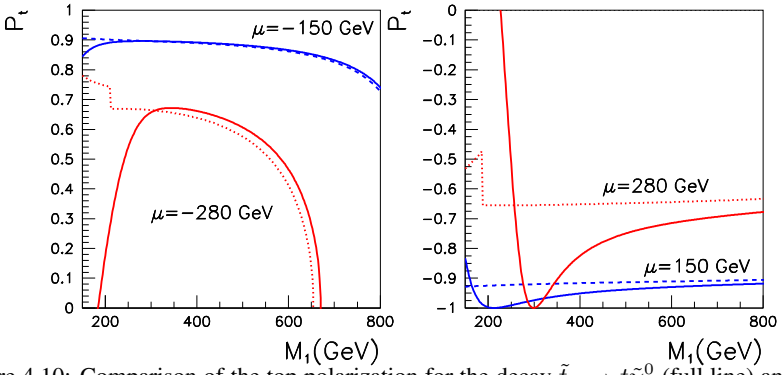

Figure 4.10: Comparison of the top polarization for the decay $\tilde{t}_1 \to t\tilde{\chi}_1^0$ (full line) and $\tilde{t}_1 \to t\tilde{\chi}_2^0$ (dashed line) as a function of the gaugino mass M_1 for $|\mu| = 150$ GeV (blue) and $|\mu| = 300$ GeV (red). SUSY parameters are fixed as in tab. 4.1 for a dominantly LH stop (left panel) and a dominantly RH stop (right panel).

of these constraints. The dark matter relic density for the bino case is typically much too large. It is however possible to bring it to a reasonable value. Decreasing the mass of the sleptons to just above the LSP mass adds an important contribution from coannihilation processes. This would have no impact on the polarization observables discussed here. By contrast the relic density is typically too small in the higgsino region. This only means that the neutralino cannot form all of the dark matter. Moreover constraints on observables from the flavour sector can easily be satisfied. The branching ratio for $B_s \to \mu^+\mu^-$, for instance, remains near the SM value since we are considering only moderate values of $\tan\beta$ and a heavy pseudoscalar.

4.4 Top Polarization: Effect on Decay Kinematics and Observables

We first study the effect of the polarization of the decaying top on the kinematics of the lepton produced in its semi-leptonic decay in this section, eq. (2.8), and assess the possible effects top polarization can have for the search strategies for the stop. Further we study qualitatively if top polarization at the LHC, measured via this semi-leptonic decay can be a useful probe for the neutralino and stop mixing parameters when there is prior knowledge on SUSY masses.

To examine the effect of the top polarization on the kinematic distributions of the semi-leptonic top quark decay product we have generated sets of events with Madgraph [13, 14]. This set of benchmarks has been selected based on the degree of top polarization in the stop rest frame as well as a roughly constant mass difference between stop and neutralino. The physical parameters corresponding to these benchmarks are listed in tab. 4.2. We have generated the process

$$p\,p \to \tilde{t}\,\bar{\tilde{t}} \to t\,\tilde{\chi}_1^0\,\bar{\tilde{t}} \to l^+\,\nu_l\,b\,\tilde{\chi}_1^0\,\bar{\tilde{t}} \tag{4.12}$$

We took 8 TeV as LHC centre of mass energy and use the following parameter values: the top mass and width are $m_t = 173.1$ GeV and $\Gamma_t = 1.50$ GeV, and the W mass and width are $m_W = 79.82$ GeV and $\Gamma_W = 2.0$ GeV. The factorization and renormalization scales were set to $\mu_R = \mu_F = m_{\tilde{t}}$. It was shown in the previous chapter that NLO corrections do not change the qualitative features of the lab-frame observables constructed out of the angular variables, so we show leading-order (LO) results, which were calculated using the CTEQ6L1 [102] pdf set. Here we implicitly assume that the anti-stop decays hadronically and have generated events where only the stop has decayed. Note however that the antitop could easily be distinguished from the top using the sign of the lepton. Hence, exploiting the information from events where the stop decays hadronically and the anti-stop leads to a final state with an (anti)lepton would provide increased sensitivity.

4.4.1 Effect of Top Polarization on E_l and p_T^l

In this subsection we show the effect of the top polarization on the energy E_l and the transverse momentum p_T^l of the lepton produced in the decay of the top in the laboratory

P_t	$m_{\tilde{t}}$ (GeV)	$m_{\tilde{\chi}_1^0}$ (GeV)	$\sin(\theta_{\tilde{t}})$	Z_{i1}	Z_{i4}	$\tan(\beta)$
1	500.0	318.6	0.998	0.958	-0.176	7.8
0.5	500.0	321.1	0.998	0.988	-0.0866	7.8
0	500.0	320.5	-0.124	0.975	-0.128	10.0
-0.5	501.1	319.2	0.995	0.440	-0.618	20.0
-0.8	502.0	319.3	-0.0988	0.0232	-0.190	35.0
1	500.7	130.2	0.9928	0.9976	-0.0188	10.
0.5	499.6	129.7	0.9987	0.9164	-0.2112	29.6
0	500.1	129.3	-0.05954	0.9729	-0.1017	35.0
-0.5	500.1	130.3	-0.05948	0.9865	-0.06113	35.0
-1	499.4	130.0	-0.05911	0.9990	-0.007184	35.0

Table 4.2: Set of benchmarks sorted by polarization. The upper five correspond to small mass differences and the lower five to large mass differences. The mass of the second neutralino is shown for the cases where its branching is non-zero.

frame for our benchmark points. These two distributions in the laboratory depend on the angular distribution of the lepton given in eq. (2.8) in the top rest frame, as well as the energy and the p_T of the decaying top which decides the direction and the magnitude of the boost to the laboratory frame. Since the angular distribution of eq. (2.8) depends on the polarization of the decaying top, the E_l and p_T^l distributions have a dependence on the top polarization. Most of the decay leptons in the rest frame come in the forward direction for a positively polarized t quark , i.e. the direction of the would-be momentum of the t quark in the laboratory. Thus after a boost from the rest frame to the lab frame the energies of these leptons are increased. Similarly, for negative polarized t quarks most of the decay leptons come out in the backward direction w.r.t. the lab momentum of the t quark. This results in an opposite boost direction and hence a decrease in the energy of the leptons. The effect on the p_T distribution of the lepton in the laboratory is further also affected by the p_T of the t quark as well.

Fig. 4.11 shows the E_l distribution in the laboratory for three different polarizations of the parent top quark: 1, 0 and -1, being depicted in blue, red and black respectively. Since, for the three cases in each figure, the mass difference between the stop and the top is nearly the same, the entire difference in the distributions can only be due to polarization of the decay top. Consistent with the qualitative argument given above, the peak of the E_l distribution shifts to lower energies for the left polarized top with respect to an unpolarized top and to higher energies for the right polarized one. The shift is higher for the case of large mass differences (with peaks occurring at respectively 26, 42 and 66 GeV) compared to the small mass difference (with peaks occuring at 34.5, 37.5 and 40.5 GeV). Since one puts cuts on the lepton kinematic variables to reduce the background from the SM tops (which would have polarization zero) one sees that such cuts will be less effective for a left polarized top and it will be even more so for the case of large mass differences. The distributions for the transverse momentum of the lepton, shown in fig. 4.12 shows similar features. For small mass differences the transverse momentum distribution of a

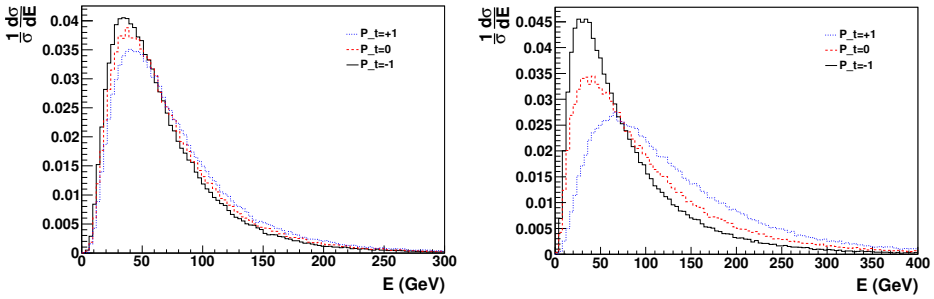

Figure 4.11: The distribution in the energy of the lepton coming from the decay of the top quark, for three different polarizations of the decaying t quark: 1,0 and -1 being given by the blue, red and the black lines respectively. The left graph represents benchmarks with a small mass difference and the right graph benchmarks with a large mass difference between stop and neutralino.

polarization of -1, 0 and $+1$ respectively peaks at 24, 26 and 31 GeV. For large mass differences the distribution of a polarization of -1, 0 and $+1$ respectively peaks at 23, 23 and 40 GeV. In fact we also notice that the shifts in the p_T^l distributions are substantial compared to the possible effects which would come from changes in the $p_T^{\bar{t}}$ distribution coming from NLO effects [87, 103, 104]. So, this effect needs to be taken into account even in an analysis that neglects the NLO effects on the stop production.

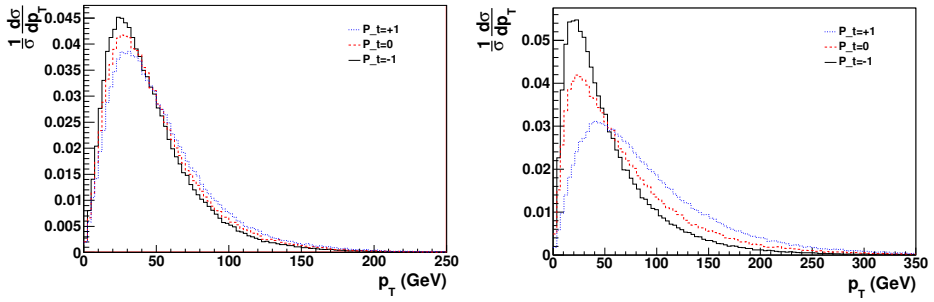

Figure 4.12: The distribution in P_T of the lepton coming from the decay of the top quark. The left graph represents benchmarks with a small mass difference and the right graph benchmarks with a large mass differences between stop and neutralino.

Thus we clearly see that the current limits quoted on the stop quark mass from direct production, using the $t\tilde{\chi}_1^0$ channel, will depend on the amount of top polarization and in addition the effect of the mass difference $m_t - m_{\tilde{\chi}_1^0}$. This needs to be kept in mind while assessing the limits being quoted currently. The observation above also means that the searches for the stop with SUSY parameters, that give rise to negatively polarized tops are in fact doubly challenged as the single top background will also produce top quarks

that are negatively polarized. Whereas for the case of positively polarized top quarks being produced by SUSY, one can use the above distribution to discriminate effectively against the background coming from single top quark production.

This also means that, in principle, information on the energy of the lepton may be used as a 'measure' of the parent top polarization. In fact, for heavily boosted top quarks, studying distributions in fractional energy of the decay lepton and b quark has been shown to carry information about the top polarization [12]. In fact a recent study demonstrates their use for the case of hadronically decaying tops, at the 14 TeV LHC [105]. It should be noted, however, as mentioned earlier, that the energy distributions of the decay products can be affected by the anomalous tbW coupling and hence are less robust a measure of the top polarization of the parent top quark, than the angular observables as discussed in the previous chapter and [4]. We discuss these in the next subsection.

4.4.2 Observables

In this subsection we focus on the observables that will give us a measure of the polarization of the top quark, using angular observables of the decay lepton. The leptonic decay has the highest analyzing power and is furthermore unaffected by an anomalous tbW coupling to leading order as explained in chapter 2. We explore utility of various asymmetries constructed out of the ϕ_l and θ_l distributions, as in [17, 106, 107] and chapter 3.

Azimuthal asymmetries

The azimuthal distributions of the charged lepton from top decay for selected benchmarks are plotted in fig. 4.13. The left plot contains the benchmarks with a small mass difference between stop and neutralino, and the right plot those with a large mass difference. The distributions, in general, follow the behavior as described in section 2.3.

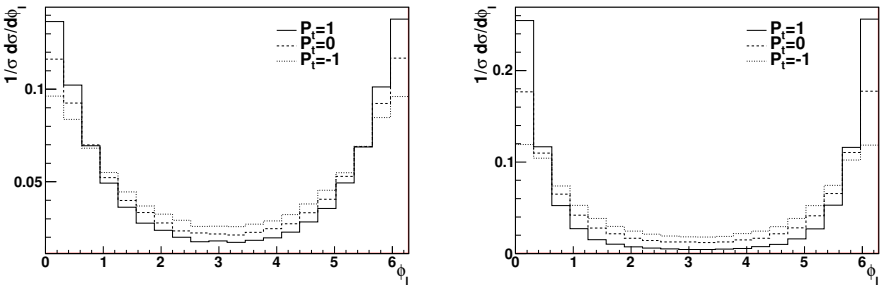

Figure 4.13: The azimuthal ϕ_l distribution of the decay lepton of the top quark. The left graph represents benchmarks with a small mass difference and the right graph benchmarks with a large mass difference between stop and neutralino.

The distributions in fig. 4.13 seem to be well separated by their polarization value. Therefore we quantify this with the asymmetry parameter A_ϕ eq. 2.9.

The polarization is influenced by the boost to the stop labframe (section 4.2.3). We will treat the transverse momentum (p_T) of the top as a crude qualifier of this boost and apply a cut on p_T [9]. Thereby attempting to reduce the polluting effect of the kinematics on the angular distribution. We have defined an adaptive cut as

$$\frac{p_T^{max}}{x} < p_T < x\, p_T^{max} \,. \tag{4.13}$$

We define both a strict ($x = 1.5$) and loose ($x = 2$) cut. The results for these choices are given in tab. 4.3.

P_t (cut)	A_ϕ (nc)	A_ϕ (lc)	A_ϕ (sc)	A_ϕ (nc)	A_ϕ (lc)	A_ϕ (sc)
+1	0.57	0.51	0.48	0.87	0.90	0.90
+0.5	0.53	0.45	0.41	0.81	0.84	0.84
0	0.48	0.42	0.39	0.69	0.67	0.64
-0.5	0.44	0.37	0.34	0.61	0.60	0.58
-1.0	0.39	0.33	0.29	0.55	0.50	0.46

Table 4.3: Relative azimuthal asymmetry parameter for the process as defined in eq. (4.12). The left side of the table denotes small mass differences and the right side large mass differences between stop and neutralino. An adaptive cut is applied on the transverse momentum as defined in eq. (4.13). The abbreviations following the asymmetry variable, denoted between brackets: nc, lc and sc respectively indicate no cut, a loose cut and a strict cut.

From tab. 4.3 we notice that the asymmetry parameter A_ϕ is large for positive polarizations, decreases for lower polarizations and reaches its lowest value at a negative polarization. As expected, the p_T cut improves the asymmetry parameter. In the case of a small mass difference, the effect is small. For large mass differences however, the two p_T cuts in eq. (4.13) enhance the separation of different polarizations. This is natural, as a large stop-neutralino mass difference endows the top with more kinetic energy.

Polar asymmetries

We can apply a similar analysis to the distribution in the polar angle, defined as the angle between top direction and decay lepton in the lab frame. The distributions are shown in fig. 4.14. We notice a peaking in the direction of the top boost which is again strongest for a positive polarization and weakest for a negative polarization. Again the large mass difference cases show a stronger correlation with the polarization P_t than the small mass difference cases. Because the distribution of θ_l is non-symmetric we have more choice for an asymmetry parameter definition that quantifies the shape differences and have chosen the definition of eq. (3.3).

This definition allows for a negative A_θ. It is of course possible to define the asymmetry parameter such that all values are positive. However, in an experimental analysis, the definition of A_θ will be tuned to enhance the effects of polarization. As the outcome of this procedure will depend on the masses of the sparticles, we will use the definition given in eq. (3.3) to show the qualitative effect. The value of A_θ, shown in tab. 4.4, is lowest for

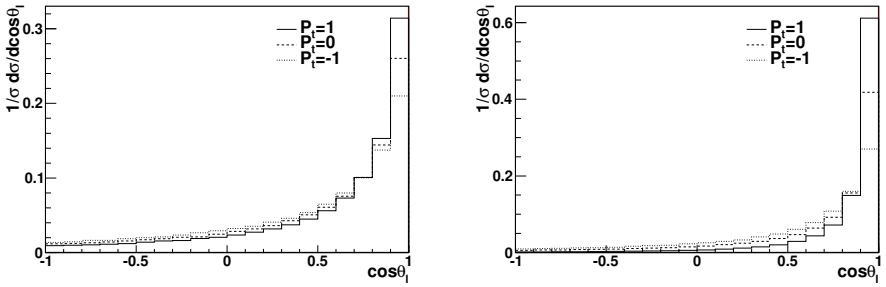

Figure 4.14: The polar distribution θ_l of the decay lepton of the top quark. Polarizations in the left figure are chosen such that there is a small mass difference between stop and neutralino. In the right figure the mass difference is large.

P_t (cut)	A_θ (nc)	A_θ (lc)	A_θ (sc)	A_θ (nc)	A_θ (lc)	A_θ (sc)
+1	0.12	0.02	-0.02	0.66	0.66	0.64
+0.5	0.06	-0.05	-0.08	0.55	0.55	0.52
0	-0.001	-0.10	-0.13	0.32	0.25	0.20
-0.5	-0.06	-0.14	-0.17	0.18	0.12	0.07
-1.0	-0.12	-0.20	-0.22	0.06	-0.03	-0.10

Table 4.4: Relative polar asymmetry parameter for the process as defined in eq. (4.12). The left side denotes benchmarks with a small mass difference and the right side large mass differences between stop and neutralino. An adaptive cut is applied on the transverse momentum as defined in eq. (4.13). The abbreviations following the asymmetry variable, denoted between brackets: nc, lc and sc respectively indicate no cut, a loose cut and a strict cut.

negative polarization, increases as the polarization increases and reaches its highest value at a polarization of $P_t = +1$. The adaptive cut again has little effect for the small mass differences but enhances mildly the separation of A_θ for large mass differences and can therefore be a useful probe for polarization.

Impact of the stop neutralino mass difference

We have seen in section 4.2.2 that the polarization depends on the mass difference between the stop and the neutralino, more precisely on $\Delta m = m_{\tilde{t}_1} - m_{\tilde{\chi}_1^0} - m_t$, and that the asymmetry parameter A_ϕ is highest for a high polarization for both mass differences. So far we have been studying the effects of polarization whilst keeping this difference constant. However, when we vary Δm, the asymmetry values corresponding to different polarizations are not well separated anymore. For example, we consider a new benchmark with a mass difference that falls in between the two cases in tab. 4.2. For this point $P_t = 0$, $m_{\tilde{t}} = 508.9$ GeV, $m_{\tilde{\chi}_1^0} = 292.4$ GeV, $\sin\theta_{\tilde{t}} = 0.1234$, and yet the asymmetry $A_\phi = 0.56$ is quite similar to the value for the benchmark $P_t = 0.5$ in tab. 4.3 which has $A_\phi = 0.53$.

The mass difference for these points varies from $\Delta m = 43$ GeV for the former and $\Delta m = 6$ GeV for the latter. Imposing the adaptive cut on the p_T of the top enhances the differences between the two benchmarks, but neither cuts are able to isolate the purely polarization induced behavior. For the $P_t = 0$ benchmark we get $A_\phi = 0.55(0.53)$ for the loose (strict) cut to be compared with $A_\phi = 0.45(0.41)$ for the $P_t = 0.5$ benchmark. We conclude that varying the mass difference slightly has a large effect on the angular distributions and therefore pollutes the information about polarization present in these angular distributions. Thus, detailed mass measurements will be needed in addition to the polarization-dependent observables, to extract information about the top polarization from these.

Decays to $\tilde{\chi}_2^0, \tilde{\chi}_3^0$

Thus far we have studied the case where the stop decays to one, generic neutralino type. We next examine the case where we allow for a decay to multiple neutralino types. Two large mass difference benchmarks of tab. 4.2 have stop branching ratios to several neutralino types, those with A) $P_t = 0.5$ and B) $P_t = 0$. In case A the heavier neutralino masses are $m_{\tilde{\chi}_2^0} = 207$ GeV, $m_{\tilde{\chi}_3^0} = 213$ GeV while in case B, $m_{\tilde{\chi}_2^0} = 276$ GeV, $m_{\tilde{\chi}_3^0} = 282$ GeV. The heavier neutralinos are higgsino-like so that the polarization is close to $P_t = -1$ in case A which has a RH stop and to $P_t = 1$ in case B with a LH stop. We have listed the separate contributions to P_t and the asymmetries A_ϕ and A_θ in tab. 4.5. The difference in the asymmetries between various neutralino channels is somewhat less than naively expected. This is because the mass difference Δm is smaller for heavier neutralinos, thus reducing the difference in the asymmetries as discussed above. This effect is particularly noticeable for the second case where despite the fact that $P_t = 0(1)$ for the light (heavier) neutralinos, all three neutralinos give rise to almost the same asymmetries.

	Case A				Case B			
decay to	A_ϕ	A_θ	P_t	BR	A_ϕ	A_θ	P_t	BR
χ_1^0	0.81	0.55	0.5	6.5%	0.69	0.32	0.0	2.7%
χ_2^0	0.53	0.04	-1.0	20%	0.71	0.34	0.99	29.3%
χ_3^0	0.53	0.05	-0.88	18%	0.69	0.31	0.96	29.8%

Table 4.5: Azimuthal and polar asymmetry parameter for the process as defined in eq. (4.12) allowing for decays of the stop to a certain neutralino type. The polarization and branching fraction for the decay into each neutralino channel is also specified. Case A and Case B correspond respectively to the second and third rows of the large mass difference benchmarks in tab. 4.2 .

With the theoretical prediction on the rest frame polarization per decay mode on the basis of eqs. (4.3) and (4.4), the lab frame distributions can then be predicted after combination with the appropriate Lorentz transformations. The asymmetry parameter for all decays is a sum of the individual values weighted by branching ratios. The extent to which A_ϕ depends on the angular distribution of a certain decay mode therefore depends strongly on the branching fractions. The results including adaptive cuts for the two benchmarks of tab. 4.5 are shown in tab. 4.6. Clearly the asymmetries are dominated by

the heavier neutralino decay channels for case A while they receive similar contributions from all three neutralino channels for case B.

	$P_t(t\tilde{\chi}_1^0)$	A_ϕ (nc)	A_ϕ (lc)	A_ϕ (sc)	A_θ (nc)	A_θ (lc)	A_θ (sc)
A	+0.5	0.58	0.53	0.50	0.13	0.03	-0.02
B	0	0.70	0.69	0.68	0.32	0.26	0.22

Table 4.6: Azimuthal and polar asymmetry parameter for the process as defined in eq. (4.12 (allowing for decays of the stop to all neutralino types. An adaptive cut is applied on the transverse momentum as defined in eq. (4.13). The abbreviations following the asymmetry variable, denoted between brackets: nc, lc and sc respectively indicate no cut, a loose cut and a strict cut.

4.5 Conclusion

The phenomenology of the third generation sfermions has always been an interesting subject to explore as this can yield non-trivial information about SUSY parameters. In view of the ever increasing upper limits on the masses of the strongly interacting sparticles that are being extracted from LHC data and the observation of a light, single Higgs-like particle, naturalness considerations within the MSSM leads to the possibility of third generation sfermions that are much lighter than the first two generations. Thus direct pair production cross-sections of both stops and sbottoms can be large enough to be probed within the 8 TeV run of the LHC. The top quarks produced in these decays are generally polarized and this polarization holds information about mixing in the squark sector, mixing in the chargino/neutralino sectors as well as on the top velocity, hence on the mass difference between the squark and the neutralino/chargino. The parameters that affect the top polarization will influence the effectiveness of the searches for stops. Thus, the limits extracted will not only depend on the stop and neutralino mass but also on the assumed polarization. Indeed, the polarization can affect the energies of decay leptons and hence the optimization of cuts to reduce the background from the QCD produced unpolarized top. Since the top polarization goes to zero in the limit of a small stop-neutralino mass difference, the polarization-induced kinematic effects will be particularly important for models where this mass difference is large. This is an important factor to keep in mind in analyses using simplified models with large mass differences. To obtain a conservative limit, one should use a model which produces a completely negatively polarized top quark.

Let us briefly summarize our findings. We have explored the possible values of the top polarization in the decay of the lightest stop into a top and a neutralino and we have scanned the parameter space which is consistent with a 125.7 GeV Higgs. We find that the bino content of the neutralino is a critical parameter and that due to the largeness of the hypercharge for the right-handed top which drives the bino-stop-top coupling, a mixed stop often behaves like a RH stop. A dominantly RH stop produces a negative top polarization when it decays into a higgsino and a positive polarization when the decay is into a bino, and vice-versa for a LH stop. This implies that these events can be separated more

easily from the top pair background, as a positive top polarization leads to more energetic leptons. The LH stop with a higgsino LSP and the RH stop with a bino LSP could be more tightly constrained at the LHC than the other two combinations. We have also shown that although small branching ratios into the lightest neutralino can occur especially for the decay into a higgsino, similar polarizations for the decay into the two higgsino states imply that we can exploit both decay modes to measure the top polarization. Finally, a small mass difference between the stop and the neutralino leads to a very small polarization.

We then analyzed the kinematics of the decay products of the top arising from stop decay into a top and a neutralino in the laboratory frame. Since the majority of the top quarks in the SM background are unpolarized the stop search is particularly challenged in the $t\tilde{\chi}_1^0$ mode for points in the parameter space which give rise to tops with negative polarization. The spectrum of the electron energy as well as transverse momentum of the lepton, softens (hardens) for negatively (positively) polarized top quarks respectively, compared to an unpolarized top quark. This modification of the position of the peak increases with increasing value of $m_{\tilde{t}} - m_{\tilde{\chi}_1^0}$. For the electron energy spectrum the shift is -30 GeV for $m_{\tilde{t}} - m_{\tilde{\chi}_1^0} \sim 320$ GeV and -16 GeV for $m_{\tilde{t}} - m_{\tilde{\chi}_1^0} \sim 130$ GeV. Thus we see that even with the same kinematics, the reach of a particular search using the lepton is less efficient for negatively polarized tops. This effect is more pronounced for large mass differences between the stop and the neutralino.

Finally, as in chapter 3, we have studied lab-frame observables and defined asymmetries in the polar and azimuthal angle. These asymmetries have both a polarization-dependent and independent part and provide a useful probe for top polarization provided the masses of the particles involved are known, since the polarization is very sensitive to mass differences. In conclusion, study of the top polarization can provide useful information on supersymmetric parameters at the LHC when the supersymmetric partner of the top is discovered.

Chapter 5

Antenna Showers

Many predictions for differential cross-sections at colliders are based on a fixed order description where matrix elements are computed for all allowed initial states with a given final state, F, plus a limited number of additional partons. The LO description has the minimal number (often zero) of additional partons. For improved accuracy, one includes matrix elements with one extra parton beyond leading order and one loop correction (NLO) and so forth. Parton showers offer an alternative approach, by iteratively constructing the particle scattering. One also starts from matrix elements for the desired hard process, F, but additional radiation is now generated stochastically via a shower algorithm, which is essentially Markovian. This is a unitary process, with probability one, and therefore does not change the probability of the underlying hard process to occur. The number of final state partons is now not predetermined, and can take an infinity of different values. The two approaches have complementary strengths and weaknesses and current focus lies on uniting the two prescriptions. Matching procedures have been developed for MC@NLO, used in chapter 3, and POWHEG [26,108,109]. This chapter will focus on a prescription for matching the VINCIA antenna shower [27, 110] to NLO accuracy for $e^+e^- \to 2$ jets. The two parton final state allows for an educational demonstration of the matching procedure as the NLO correction takes a concise form. The leptonic initial state allows for a cleaner environment for the development of a matching procedure, which will be formalized for hadronic initial states in a later stage.

5.1 The VINCIA antenna shower

We will start with a discussion of the basic principle of an antenna shower which will also serve as an introduction to the basic notation and conventions that will be used in later sections and the next chapter.

5.1.1 The Formal Basis of Antenna Showers

Antenna showers are based on the factorization of (squared) colour-ordered QCD amplitudes in soft and collinear limits, which can be expressed as follows

$$|M(\ldots,p_i,p_j,\ldots)|^2 \overset{i||j}{\to} g_s^2\,\mathcal{C}\,\frac{P(z)}{s_{ij}}\,|M(\ldots,p_i+p_j,\ldots)|^2 \tag{5.1}$$

$$|M(\ldots,p_i,p_j,p_k,\ldots)|^2 \overset{j_g \text{ soft}}{\to} g_s^2\,\mathcal{C}\,A_g(s_{ij},s_{jk},s_{ijk})\,|M(\ldots,p_i,p_k,\ldots)|^2 \tag{5.2}$$

with $g_s^2 = 4\pi\alpha_s$ the strong coupling and the subscript g in the second line emphasizing that the soft limit is only relevant for gluons. In the collinear limit (first line), $P(z)$ are the Altarelli-Parisi splitting kernels [111], z is the energy fraction taken by parton i (with a fraction $(1-z)$ going to parton j), and $\mathcal{C}$ is a colour factor, which we discuss below. This limit forms the basis for traditional parton showers, such as those in the PYTHIA generator [112].

In the soft-gluon limit (second line), the function A has dimension GeV^{-2}, and is called an antenna function, with the parent particles labelled with i and j and the additional radiation taking on an index k as illustrated in fig. 5.1 for a quark antiquark antenna. For unpolarized massless partons[1], its leading term is the so-called eikonal or dipole factor,

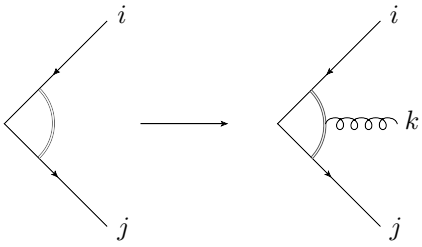

Figure 5.1: Illustration of our labeling convention for a quark antiquark antenna. The parent partons are labelled with index i and j and the radiated gluon receives index k.

$$A_{\mathrm{Eik}}(s_{ij},s_{jk},s_{ijk}) = \frac{2s_{ik}}{s_{ij}s_{jk}}\,, \tag{5.3}$$

where $s_{ik} = s_{ijk} - s_{ij} - s_{jk}$ for massless partons. It was found early on that this factor can be reproduced by a traditional parton shower by imposing the requirement of angular ordering of subsequent emissions [114]. This gave rise to the angular-ordered showers [115, 116] in the HERWIG and HERWIG++ generators [117, 118] as well as the imposition of an angular-ordering constraint [112, 119] in the JETSET and PYTHIA generators [120, 121].

In fixed-order calculations, dipole [122] and antenna [123–125] functions are frequently used to define subtraction terms. These functions include additional subleading

[1] In the context of massive particles, replace s_{ab} by $2p_a\cdot p_b$ in all expressions. For a more complete treatment, see [113].

terms, beyond the eikonal one, which are necessary to correctly describe both soft and collinear limits in all regions of phase space. In the parametrization we shall use, their most general forms, for the branching process $IK \to ijk$, are

$$A_{\text{Emit}}(s_{ij}, s_{jk}, m^2_{IK}) = \frac{1}{m^2_{IK}} \left(\frac{2y_{ik}}{y_{ij}y_{jk}} + \frac{y_{jk}(1-y_{jk})^{\delta_{ig}}}{y_{ij}} + \frac{y_{ij}(1-y_{ij})^{\delta_{kg}}}{y_{jk}} + F_{\text{Emit}} \right) \tag{5.4}$$

$$A_{\text{Split}}(s_{ij}, s_{jk}, m^2_{IK}) = \frac{1}{m^2_{IK}} \left(\frac{y^2_{jk} + y^2_{ik}}{2y_{ij}} + F_{\text{Split}} \right) , \tag{5.5}$$

for gluon-emission and gluon-splitting processes, respectively, with the parent antenna invariant mass, $m^2_{IK} = (p_I + p_K)^2 = (p_i + p_j + p_k)^2$ and the scaled invariants,

$$y_{ij} = \frac{s_{ij}}{m^2_{IK}} \quad ; \quad y_{jk} = \frac{s_{jk}}{m^2_{IK}} , \tag{5.6}$$

and we use the notation $\delta_{ig} = 1$ if parton i is a gluon and zero otherwise. The functions F_{Emit} and F_{Split} allow for the presence of non-singular terms, which are in principle arbitrary. A logical choice would be $F = 0$, but this would not be invariant under reparametrizations of the antenna functions across the gluon-collinear singular limits [110]. Since the F functions can anyway be made useful in the context of uncertainty estimates [27, 110], we therefore leave them as functions whose forms we are free to choose.

In the soft-gluon limit, the eikonal factor is reproduced by the first term in eq. (5.4). In the collinear $q \to qg$ limit, the AP splitting kernel also is reproduced. For collinear $g \to gg$ and $g \to q\bar{q}$ branchings, one must sum over the contributions from two neigbouring antennae, which together reproduce the AP splitting kernel. Limits that are both soft and collinear are also correctly reproduced [125].

In the antenna context, the colour factors are $2C_F$ for $q\bar{q} \to qg\bar{q}$, C_A for $gg \to ggg$[2], and $2T_R$ for gluon splitting to $q\bar{q}$, again using the normalization convention adopted in [110]. However, for $qg \to qgg$ there is a genuine subleading ambiguity whether to prefer, say, $2C_F$, C_A, or something interpolating between them [126]. At fixed order, the question of subleading colour can in fact be dealt with quite elegantly, by using C_A for all antennae and then including an additional $q\bar{q}$ antenna with a negative colour factor, $-C_A/N_C^2$, spanned between the two endpoint quarks, for each $qg \ldots \bar{q}$ chain [127]. In the context of an antenna-based shower, however, it is desirable to use only positive-definite antenna functions, and a prescription for absorbing the negative one into the positive ones was given in [110]. In the context of this work, however, we shall largely ignore subleading-colour aspects and, unless explicitly stated otherwise, assign a colour factor

[2]Note that in a process like $H^0 \to gg$, there are two gg antennae at the Born level, and hence the antenna approximation to $H^0 \to ggg$ is twice as large as the single $gg \to ggg$ antenna. Likewise, the collinear limit of a gluon is obtained by summing over the contributions from both of the dipoles/antennae it is connected to. One must also include a sum over permutations of the final-state gluons, if comparing to a summed matrix-element expression.

C_A to the $qg \to qgg$ antenna function, thereby overcounting the collinear limit in the quark direction by a factor $C_A/(2C_F) \simeq 1 + 1/N_C^2$.

The renormalization scale used to evaluate the strong coupling in the antenna function, $g_s^2 = 4\pi\alpha_s(\mu_{\rm PS})$, is typically chosen proportional to $p_\perp$ (following [128]). As alternatives, we shall also consider $\mu_{\rm PS}^2 \propto m_D^2 = 2\min(s_{ij}, s_{jk})$, and, as an extreme case which connects with fixed-order calculations, the invariant mass of the antenna, $\mu_{\rm PS}^2 \propto m_{IK}^2$.

A final aspect concerns the phase-space factorization away from the collinear limit. Within the framework of collinear factorization (and hence, in traditional parton showers), the momentum fraction, z, is only uniquely defined in the exactly collinear limit; outside that limit, the choice of z is not unique. In addition, a prescription must be adopted for ensuring overall momentum conservation, leading to the well-known ambiguities concerning recoil strategies (see e.g. [129]). In antenna showers, on the other hand, the antenna function is defined in terms of the unique branching invariants, s_{ij} and s_{jk}, over all of phase space, and the phase space itself has an exact Lorentz-invariant and momentum-conserving factorization,

$$\mathrm{d}\Phi_n = \mathrm{d}\Phi_{n-1} \times \mathrm{d}\Phi_{\rm Ant} \,, \tag{5.7}$$

with

$$\mathrm{d}\Phi_{\rm Ant} = \frac{1}{16\pi^2 m_{IK}^2} \mathrm{d}s_{ij}\mathrm{d}s_{jk}\frac{\mathrm{d}\phi}{2\pi} \tag{5.8}$$

for massless partons (for massive ones, see [113]), with the ϕ angle parametrizing rotations around the antenna axis, in the CM of the antenna. Note the equality signs; no approximation is involved in this step. The only remaining phase-space ambiguity, outside the singular limits, is present when specifying how the post-branching momenta are related to the pre-branching ones. This is defined by a kinematics map, the antenna equivalent of a recoil strategy, which we here take to be of the class defined by [27, 123].

5.1.2 Constructing a Shower Algorithm

In a shower context, the amplitude and phase-space factorizations above imply that we can interpret the radiation functions (AP splitting kernels or dipole/antenna functions) as the probability for a radiator (parton or dipole/antenna) to undergo a branching, per unit phase-space volume,

$$\frac{\mathrm{d}P(\Phi)}{\mathrm{d}\Phi} = g_s^2 \, \mathcal{C} \, A(\Phi) \,, \tag{5.9}$$

where we use Φ as shorthand to denote a phase-space point. (If there are several partons/dipoles/antennae, the total probability for branching of the event as a whole is obtained as a sum of such terms.)

An equally fundamental object in both analytical resummations and in parton showers is the Sudakov form factor, which defines the probability for a radiator *not* to emit anything, as a function of the shower evolution parameter, Q (i.e., similarly to a jet veto, with Q playing the role of the jet clustering scale; we return to the choice of functional form for the shower evolution scale in section 5.1.3). In the all-orders shower construction,

these factors generate the sum over virtual amplitudes plus unresolved real radiation, and hence their first-order expansions play a crucial role in matching to next-to-leading order matrix elements. We here recap some basic properties. The Sudakov factor, giving the no-emission probability between two values of the shower evolution parameter, Q_1 and Q_2 (with $Q_1 > Q_2$), is defined by

$$\Delta(Q_1^2, Q_2^2) \;=\; \exp\left(-\int_{Q_2^2}^{Q_1^2} \frac{\mathrm{d}P(\Phi)}{\mathrm{d}\Phi}\,\mathrm{d}\Phi\right) \;=\; \exp\left(-\int_{Q_2^2}^{Q_1^2} g_s^2\,\mathcal{C}\,A(\Phi)\,\mathrm{d}\Phi\right)\,, \tag{5.10}$$

where it is understood that the integral boundaries must be imposed either as step functions on the integrand or by a suitable transformation of integration variables, accompanied by Jacobian factors.

This description has a very close analogue in the simple process of nuclear decay, in which the probability for a nucleus to undergo a decay, per unit time, is given by the nuclear decay constant,

$$\frac{\mathrm{d}P(t)}{\mathrm{d}t} \;=\; c_N\,. \tag{5.11}$$

The probability for a nucleus existing at time t_1 to remain undecayed before time t_2, is

$$\Delta(t_2, t_1) = \exp\left(-\int_{t_1}^{t_2} c_N\,\mathrm{d}t\right) \;=\; \exp\left(-c_N\,\Delta t\right)\,. \tag{5.12}$$

This case is especially simple, since the decay probability per unit time, c_N, is constant. By conservation of the total number of nuclei (unitarity), the activity per nucleon at time t, equivalent to the "resummed" decay probability per unit time, is minus the derivative of Δ,

$$\frac{\mathrm{d}P_{\mathrm{res}}(t)}{\mathrm{d}t} \;=\; -\frac{\mathrm{d}\Delta}{\mathrm{d}t} \;=\; c_N\,\Delta(t, t_1)\,. \tag{5.13}$$

In QCD, the emission probability varies over phase space, hence the probability for an antenna not to emit has the more elaborate integral form of eq. (5.10). By unitarity, the resummed branching probability is again minus the derivative of the Sudakov factor,

$$\frac{\mathrm{d}P_{\mathrm{res}}(\Phi)}{\mathrm{d}\Phi} \;=\; g_s^2\,\mathcal{C}\,A(\Phi)\,\Delta(Q_1^2, Q^2(\Phi))\,, \tag{5.14}$$

with $Q^2(\Phi)$ the shower evolution scale (typically chosen as a measure of invariant mass or transverse momentum, see section 5.1.3), evaluated at the phase-space point Φ.

In shower algorithms, branchings are generated with this distribution, starting from a uniformly distributed random number $\mathcal{R} \in [0, 1]$, by solving the equation,

$$\mathcal{R} = \Delta(Q_1^2, Q^2) \tag{5.15}$$

for Q^2. For an initial distribution of "trial" branching scales, we do not use the full antenna function, eq. (5.4), as the evolution kernel, but only its leading singularity,

$$A_T \;=\; \frac{2m_{IK}^2}{s_{ij}s_{jk}} \;=\; \frac{2}{p_{\perp A}^2}\,, \tag{5.16}$$

where $p_{\perp A}$ is the ARIADNE definition of transverse momentum [130], which is also the one used in VINCIA. This reflects the universal $1/p_\perp^2$ behaviour of soft-gluon emissions. In addition to the trial scale, Q, two complementary phase-space variables are also generated (which we usually label ζ and ϕ [110]), according to the shape of A_T over a phase-space contour of constant Q. From these, the model-independent set of trial phase-space variables (s_{ij}, s_{jk}, ϕ) are determined by inversion of the defining relations $Q(s_{ij}, s_{jk})$ and $\zeta(s_{ij}, s_{jk})$, and the full kinematics (i.e., four-momenta) of the trial branching can then be constructed [27].

To decide whether to accept the trial or not, we note that the function A_T differs from the eikonal in eq. (5.3) by the replacement of s_{ik} in the numerator by m_{IK}^2. By accepting the trial scales generated by A_T with the probability

$$P_{\rm eik} \;=\; \frac{A_{\rm eik}}{A_T} \;=\; \frac{s_{ik}}{m_{IK}^2} \;\leq\; 1\,, \tag{5.17}$$

the eikonal approximation can be recovered, by virtue of the veto algorithm [129, 131, 132]. Crucially, any other function that has the eikonal as its soft-collinear limit could equally well be imprinted on the trial distribution by a similar veto. Two particularly relevant choices are the full physical antenna function, eq. (5.4) (which includes additional collinear-singular terms in addition to the eikonal) and the GKS-corrected antenna function (which also incorporates a multiplicative factor that represents tree-level matching in VINCIA),

$$P^{\rm LL}_{\rm accept} \;=\; \frac{A_{\rm Emit}}{A_T}\,, \tag{5.18}$$

$$P^{\rm LO}_{\rm accept} \;=\; P^{\rm LL}_{\rm accept}\, R_n\,, \tag{5.19}$$

with $A_{\rm Emit}$ given in eq. (5.4) and R_n the n-parton tree-level GKS matching factor [110], to which we return in section 5.2.1.

Note that, for gluon-splitting antenna functions ($Xg \to Xq\bar{q}$), we use $Q = m_{q\bar{q}}$, with a trial function $\propto 1/m_{q\bar{q}}^2$, and again implement the physical antenna function, eq. (5.5), and LO matching corrections by vetos. We also include the so-called ARIADNE factor, $P_{\rm Ari}$, defined by

$$A_{\rm Split} \;\to\; P_{\rm Ari}\, A_{\rm Split} \;=\; \frac{2s_N}{s_P + s_N}\, A_{\rm Split}\,, \tag{5.20}$$

with s_N the invariant mass squared of the colour neighbour on the other side of the splitting gluon and $s_P = m_{IK}^2$ the invariant mass squared of the parent (splitting) antenna. This does not modify the singular behavior (as will be elaborated upon below), and was shown to give significantly better agreement with the $Z \to qq\bar{q}\bar{q}$ matrix element in [133].

Explicit solutions to eq. (5.15) using the trial function defined by eq. (5.16) were presented in [110], for fixed and first-order running couplings. In the context of the present work, two-loop running has been implemented using a simple numerical trick, as follows: given a value of $\alpha_s(M_Z)$, we determine the corresponding two-loop value of $\Lambda_{\rm QCD}^{\rm 2-loop}$. We then use that Λ value in the one-loop solutions in [110], and correct the resulting

distribution by inserting an additional trial accept veto:

$$P^{2-\mathrm{loop}}_{\mathrm{accept}} \;=\; \frac{\alpha_s^{2-\mathrm{loop}}(Q,\Lambda^{2-\mathrm{loop}}_{\mathrm{QCD}})}{\alpha_s^{1-\mathrm{loop}}(Q,\Lambda^{2-\mathrm{loop}}_{\mathrm{QCD}})}\,. \tag{5.21}$$

Due to the faster pace of 2-loop running, $\alpha_s^{2-\mathrm{loop}}(Q,\Lambda) < \alpha_s^{1-\mathrm{loop}}(Q,\Lambda)$, hence this accept probability is guaranteed to be smaller than or equal to unity.

A final point concerns if there are several "competing" radiators (equivalent to several competing nuclei, and/or several competing available decay channels for each nucleus). In this case, the trial with the highest value of Q is selected (corresponding to the one happening at the earliest time, t), and consideration of any other branchings (decays) are postponed temporarily. After a branching, any partons involved in that branching are replaced by the post-branching ones, and any postponed trial branchings involving those partons are deleted. The evolution is then restarted, from the scale Q of the new configuration, until there are no radiators left with trial branching scales larger than a fixed, lower, cutoff, normally identified with the hadronization scale, $Q_{\mathrm{had}} \sim 1\,\mathrm{GeV}$.

5.1.3 Evolution and Ordering

In order to solve eq. (5.15) we need to specify the form of eq. (5.10), which takes us from one scale Q_1^2 to a lower scale Q_2^2. We change variables to parametrize the integral by the ordering variable, Q, and another, complementary (but otherwise arbitrary), phase-space variable which we denote by ζ. The generic evolution integral now reads

$$\mathcal{A}\left(Q_1^2,Q_2^2\right) = \int_{Q_2^2}^{Q_1^2} g_s^2\,\mathcal{C}\,\mathrm{d}Q^2\mathrm{d}\zeta\,|J|\,A(Q^2,\zeta) \tag{5.22}$$

with $|J|$ denoting the Jacobian of this transformation. For branchings involving gluon emission, we consider three possible choices for the ordering variable: dipole virtuality m_D, transverse momentum, and the energy of the emitted parton, E_j^* (in the CM of the parent antenna), with the following definitions,

$$Q^2_{E1} \;= m^2_D \;= 2m^2_{IK}\min(y_{ij},y_{jk})\,, \tag{5.23}$$

$$Q^2_{E2} \;= 4p^2_\perp \;= 4m^2_{IK}\,y_{ij}y_{jk}\,, \tag{5.24}$$

$$Q^2_{E3} \;= 4E^{*2}_j \;= m^2_{IK}\,(y_{ij}+y_{jk})^2 \;=\; x_j^2\,m^2_{IK}\,, \tag{5.25}$$

with the energy fraction $x_j = 2E_j^*/m_{IK}$.

All three options are available as ordering variables in the VINCIA shower Monte Carlo. They are illustrated in fig. 5.2, where contours of constant value of $y_E = Q^2_E/m^2_{IK}$ are shown for each variable, as a function of y_{ij} and y_{jk}. For completeness, we show both the case of a linear (top row) and quadratic (bottom row) dependence on the branching invariants, for each variable. Since the ordering variable raised to any positive power will result in the same relative ordering of emissions within a given antenna, the distinction

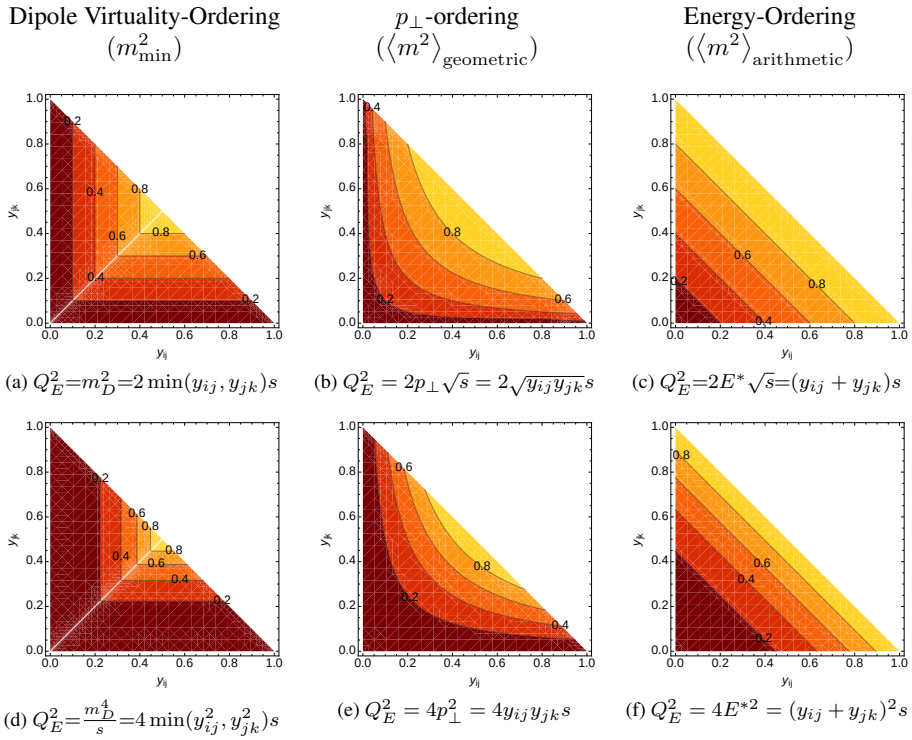

(a) $Q^2_E{=}m^2_D{=}2\min(y_{ij},y_{jk})s$ (b) $Q^2_E = 2p_\perp\sqrt{s} = 2\sqrt{y_{ij}y_{jk}}s$ (c) $Q^2_E{=}2E^*\sqrt{s}{=}(y_{ij}+y_{jk})s$

(d) $Q^2_E{=}\frac{m^4_D}{s}{=}4\min(y^2_{ij},y^2_{jk})s$ (e) $Q^2_E = 4p^2_\perp = 4y_{ij}y_{jk}s$ (f) $Q^2_E = 4E^{*2} = (y_{ij}+y_{jk})^2 s$

Figure 5.2: Contours of constant value of $y_E = Q^2_E/m^2_{IK}$ for evolution variables linear (*top*) and quadratic (*bottom*) in the branching invariants, for virtuality-ordering (*left*), $p_\perp$-ordering (*middle*), and energy-ordering (*right*). Note that the energy-ordering variables intersect the phase-space boundaries, where the antenna functions are singular, for finite values of the evolution variable. They can therefore only be used as evolution variables together with a separate infrared regulator, such as a cut in invariant mass, not shown here.

between linear and quadratic forms does not affect individual antenna Sudakov factors. It does, however, affect the "competition" between different antennae, and the choice of restart scale for subsequent evolution after a branching has taken place, as will be discussed further below.

In labeling the columns in fig. 5.2, we have also emphasized that mass-ordering, as defined here, corresponds to choosing the smallest of the daughter antenna masses as the "resolution scale" of the branching, whereas $p_\perp$ and energy correspond to using the geometric and arithmetic means of the daughter invariants, respectively. Naively, each of these could be taken as a plausible measure of the resolution scale of a given phase-space point. We shall see below which ones lead to better agreement with the one-loop matrix elements.

$y_E = \frac{Q^2}{s_{ijk}}$	$\frac{m_{jk}^2}{s}$	$\frac{m_D^2}{s}$	$\frac{m_D^4}{s^2}$	$\frac{2p_\perp}{\sqrt{s}}$	$\frac{4p_\perp^2}{s}$	$\frac{2E^*}{\sqrt{s}}$	$\frac{4E^{*2}}{s}$
$\lvert J(y_E,\zeta_1)\rvert$	$\frac{y_E}{(1-\zeta_1)^2}$	$\frac{y_E}{4(1-\zeta_1)^2}$	$\frac{1}{8(1-\zeta_1)^2}$	$\frac{y_E}{4\zeta_1(1-\zeta_1)}$	$\frac{1}{8\zeta_1(1-\zeta_1)}$	y_E	$\frac{1}{2}$
$\lvert J(y_E,\zeta_2)\rvert$	1	$\frac{1}{2}$	$\frac{1}{4\sqrt{y_E}}$	$\frac{y_E}{2\zeta_2}$	$\frac{1}{4\zeta_2}$	1	$\frac{1}{2\sqrt{y_E}}$

Note : $|J(Q^2,\zeta)| = s_{ijk}|J(y_E,\zeta)|$

Table 5.1: Jacobian factors for all combinations of evolution variables and ζ choices.

We consider two possible definitions for the complementary phase-space variable ζ,

$$\zeta_1 \;=\; \frac{y_{ij}}{y_{ij}+y_{jk}} \tag{5.26}$$

$$\zeta_2 \;=\; y_{ij}\;. \tag{5.27}$$

We emphasize that the choice of ζ has no physical consequences, it merely serves to reparametrize the Lorentz-invariant phase space. We may therefore let the choice be governed purely by convenience, and, for each antenna integral, select whichever of the above definitions give the simplest final expressions. The corresponding Jacobian factors, for each of the evolution-variable choices we shall consider, are listed in tab. 5.1.

Note that, for the special case of the m_D^2 and m_D^4 variables, which contain the non-analytic function $\min(y_{ij}, y_{jk})$, the ζ definitions in eqs. (5.26) and (5.27) apply to the branch with $y_{ij} > y_{jk}$. For the other branch, y_{ij} and y_{jk} should be interchanged. With this substitution, the Jacobians listed in tab. 5.1 apply to both branches[3].

For branchings involving gluon splitting, $g \to q\bar{q}$, we restrict our attention to two possibilities, ordering in $p_\perp$, defined as above, and ordering in gluon virtuality, defined as

$$Q_{E4}^2 \;=\; m_{g^*}^2 \;=\; m_{q\bar{q}}^2 \quad \text{(for gluon splitting)}\;. \tag{5.28}$$

Note that the normalization factors for the ordering variables have in all cases been chosen such that the maximum value of the ordering variable is m_{IK}^2.

Since the phase space for subsequent branchings is limited both by the scale Q_E of the previous branching (according to strong ordering) and by the invariant mass of the antenna m_j, the effective "restart scale", after a branching in a strongly ordered shower, is given by

$$Q_{Rj}^2 = \min(Q^2, m_j^2)\;, \tag{5.29}$$

for each antenna j.

Depending on the choice and value of Q, one or both daughter antennae after a splitting may have a non-trivial restriction on the phase space available for subsequent branching. Conversely, if $Q > m_j$, there is no such restriction. Physically, we distinguish between the case in which the strong-ordering condition implies a non-trivial constraint on the evolution of the produced antennae, eating into the phase-space that would otherwise be accessible, and the case in which the strong-ordering condition does not imply such a constraint.

[3]This corresponds to replacing y_{ij} by $\max(y_{ij}, y_{jk})$ in the numerator of eq. (5.26) and in eq. (5.27).

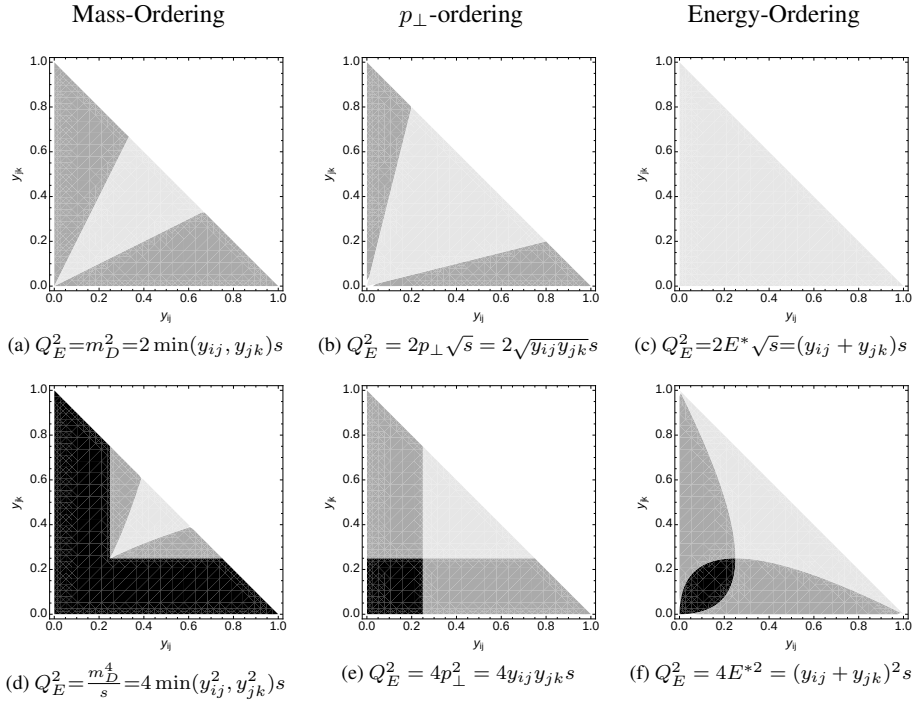

Figure 5.3: Illustration of the regions of 3-parton phase space in which the subsequent evolution of the qg and $g\bar{q}$ antennae is restricted (from above) by the strong-ordering condition. See the text for further clarification of this plot. *Black:* both antennae restricted. *Dark Gray:* one antenna restricted, the other unrestricted. *Light Gray:* both antennae unrestricted. *Top/Bottom:* Q^2 linear/quadratic in the branching invariants, for mass-ordering (*left*), $p_\perp$-ordering (*middle*), and energy-ordering (*right*).

The regions of $q\bar{q} \to qg\bar{q}$ phase space in which either zero, one, or both of the daughter antennae (qg and $g\bar{q}$ respectively) are constrained by the ordering condition are illustrated in fig. 5.3, for each of the choices of evolution variable under consideration. The black shaded areas correspond to regions in which both the qg and $g\bar{q}$ antennae are restricted, by having $Q < m_j$. The darker gray shaded areas show regions in which only one of the antennae is restricted, while the other will still be allowed to evolve over its full phase space. In the light-gray shaded areas, both of the antennae are allowed to evolve over all of their available phase spaces, equivalent to the ordering condition imposing no constraint on the subsequent evolution. We recall that we are here discussing the *upper* boundary on the subsequent evolution, hence the infrared[4] (IR) poles are not affected.

To further clarify the meaning of the plots in fig. 5.3, let us discuss panel (e) as an example. The coordinates, (y_{ij}, y_{jk}), represent the 3-parton state before it evolves to a

[4]Note: we use the word infrared to refer collectively to soft and/or collinear regions of phase space.

4-parton state, and each point corresponds to a specific value of the evolution variable at hand, cf. fig. 5.2. Assuming ordering in $p_\perp$ and using subscript (3) for quantities evaluated in the 3-parton state, the value of the evolution variable for a specific (y_{ij}, y_{jk}) point is $Q^2_{E(3)} = 4p^2_{\perp(3)} = 4y_{ij}y_{jk}s$, with $s = m_Z^2$ at the Z pole. The further evolution of the shower, from a 3- to a 4-parton state, involves a sum over all possible branchings of the qg and $g\bar{q}$ antennae. Consider the qg one. Its branchings can again be characterized by two invariants (s_1, s_2), both of which will be smaller than m^2_{qg}. However, depending on the value of m^2_{qg} (or, equivalently, y_{ij}) the $p_\perp$ of the new configuration, $4p^2_{\perp(4)} = 4s_1s_2/m^2_{qg}$ may actually be *larger* than $4p^2_{\perp(3)}$. In a strongly ordered shower, such configurations are not allowed, and would be discarded. Whether this situation can occur or not, for one or both of the qg and $g\bar{q}$ antennae, as a function of (y_{ij}, y_{jk}), is what fig. 5.3 reveals, for each type of ordering variable.

The mathematical consequence is that, in the dark- and black-shaded regions, respectively, the upper boundary of one or both of the qg and $g\bar{q}$ antenna integrals is set by the evolution variable, rather than by phase space. This creates an important difference between the integrals generated by a shower algorithm and those used for IR subtractions in traditional fixed-order applications (for which the integrals always run over all of phase space). In particular, we see that the strong-ordering condition will generate additional logarithms involving $s_{ij}/Q^2_{E(3)}$ as argument. For a "good" choice of evolution variable, these logarithms should explicitly cancel against ones present in the one-loop matrix elements, a question we shall return to in detail in section 6.2.

Several interesting structures can be seen in fig. 5.3. Firstly, the linearized variables imply less severe constraints on the subsequent evolution than the quadratic ones. This is easy to understand given that the linearized variables, $Q_{\rm lin}$, are related to the quadratic ones, $Q_{\rm qdr}$, by

$$Q^2_{\rm lin} = Q_{\rm qdr}\, m_{IK} \ , \tag{5.30}$$

and hence $Q_{\rm lin} > Q_{\rm qdr}$, implying a higher absolute restart scale for the linearized ordering variables.

It is also apparent that, for a given choice of linearity, mass-ordering reduces the phase-space for further evolution more than $p_\perp$-ordering does, which in turn is more constraining than energy-ordering. In this comparison, however, it becomes important to recall that the traditional ordering variables used, e.g., in VINCIA, are the *linearized* mass-ordering and the *quadratic* $p_\perp$ and energy-ordering variables[5]. Within that group, $p_\perp$-ordering appears to be the most restrictive, followed by energy-ordering, with (traditional, linearized) mass-ordering leading to the most open phase space for the subsequent evolution.

We are now able to fully specify the boundaries of the evolution integrals in eq. (5.22). For each Q_E contour (see fig. 5.2), the integration limits in ζ are listed in tab. 5.2. Combined with a Q_E interval and an antenna function, these boundaries account for the integrated tree-level splitting probability when going from one scale Q_1^2 to another Q_2^2, as

[5]This distinction comes about from using quantities that are similar to a squared mass, squared transverse momentum, and squared energy, respectively.

Ordering		Q_E^2	$\zeta_{\min}(Q_E^2)$ $\quad$ $\zeta_{\max}(Q_E^2)$	$3 \to 4$ restriction
$p_\perp$	l	$2m_{IK}^2\sqrt{y_{ij}y_{jk}}$	$\frac{1\mp\sqrt{1-Q_E^4/m_{IK}^4}}{2}$	$\theta\left(m_{\text{ant}}^2 - 2\sqrt{s_{ij}s_{jk}}\right)$
	s	$4m_{IK}^2\, y_{ij}y_{jk}$	$\frac{1\mp\sqrt{1-Q_E^2/m_{IK}^2}}{2}$	$\theta\left(m_{\text{ant}}^2 - 4\frac{s_{ij}s_{jk}}{s}\right)$
m_D	l	$2m_{IK}^2\min(y_{ij}, y_{jk})$	$\frac{Q_E^2}{2m_{IK}^2}$ $\quad$ $1-\frac{Q_E^2}{2m_{IK}^2}$	$\theta\left(m_{\text{ant}}^2 - 2\min(s_{ij}, s_{jk})\right)$
	s	$4m_{IK}^2\min(y_{ij}^2, y_{jk}^2)$	$\sqrt{\frac{Q_E^2}{4m_{IK}^2}}$ $\quad$ $1-\sqrt{\frac{Q_E^2}{4m_{IK}^2}}$	$\theta\left(m_{\text{ant}}^2 - 4\frac{\min(s_{ij}^2, s_{jk}^2)}{s}\right)$
E^*	l	$m_{IK}^2\,(y_{ij}+y_{jk})$	0 $\quad$ 1	1
	s	$m_{IK}^2\,(y_{ij}+y_{jk})^2$	0 $\quad$ 1	$\theta\left(m_{\text{ant}}^2 - \frac{(s_{ij}+s_{jk})^2}{s}\right)$

Table 5.2: Boundaries corresponding to the ordering variables portrayed in fig. 5.2, with m_{ant}^2 corresponding to the active $3 \to 4$ dipole s_{qg} or $s_{g\bar{q}}$, and $s = m_Z^2$ at the Z pole. The labelling l and s in the ordering column indicate the choice of linear and squared for the ordering variables. We have chosen ζ_2 as the energy sharing variable for m_D and $p_\perp$ ordering and ζ_1 for E^* ordering, with ζ defined as in eq. (5.26) and eq. (5.27). The energy variable will lead to infinities if the hadronization scale is not imposed as a cut-off.

expressed by eq. (5.22). The last column in tab. 5.2 tells when the $3 \to 4$ ordering condition is active. In fig. 5.3 this corresponds to a region darkening due to the restriction, with its shade determined by the amount of restricted dipoles.

Finally, we note that the dependence on Q in eq. (5.29) causes explicit non-Markovian behavior at the 4-parton level and beyond, since the value of Q then depends explicitly on which branching was the last to occur. A more strictly Markovian variant of this is obtained by letting the $\min()$ function act on all possible Q values (corresponding to all possible colour-connected clusterings) of the preceding topology. In that case, a single Q value can be used to characterize an entire n-parton topology, irrespective of which branching was the last to occur. Since the distinction between Markovian and non-Markovian shower restart conditions only enters starting from the $4 \to 5$ parton evolution step, it will not affect our discussion of the second-order $2 \to 3$ branching process. For completeness, we note that the strongly ordered showers in VINCIA are of the ordinary non-Markovian type, while the smoothly ordered ones are Markovian.

5.1.4 Smooth Ordering

In addition to traditional (strongly ordered) showers, we shall also consider so-called smooth ordering [110]: applying the ordering criterion as a smooth dampening factor instead of as a step function. This is not as radical as it may seem at first. Applying a jet algorithm to any set of events will in general result in some small fraction of unordered clustering sequences. This is true even if the events were generated by a strongly ordered shower algorithm, if the jet clustering measure is not strictly identical to the shower ordering variable. An example of this, for strong ordering in $p_\perp$ and in m_D, clustered with the k_T algorithm, can be found in [134].

In smooth ordering, the only quantity which must still be strictly ordered are the an-

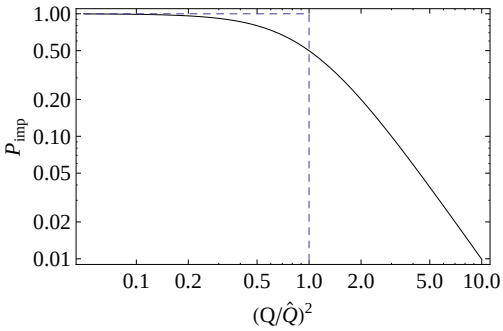

Figure 5.4: The smooth-ordering factor (*solid*) compared to a strong-ordering Θ function (*dashed*).

tenna invariant masses, a condition which follows from the nested antenna phase spaces and momentum conservation. Within each individual antenna, and between competing ones, the measure of evolution time is still provided by the ordering variable, which we therefore typically refer to as the "evolution variable" in this context (rather than the "ordering variable"), in order to prevent confusion with the strong-ordering case. The evolution variable can in principle still be chosen to be any of the possibilities given above, though we shall typically use $2p_\perp$ for gluon emission and $m_{q\bar{q}}$ for gluon splitting.

In terms of an arbitrary evolution variable, Q, the smooth-ordering factor is [134]

$$P_{\rm imp} \;=\; \frac{\hat{Q}^2}{\hat{Q}^2 + Q^2}\;, \tag{5.31}$$

where Q is the evolution scale associated with the current branching, and $\hat{Q}$ measures the scale of the parton configuration before branching. A comparison to the strong-ordering step function is given in fig. 5.4, on a log-log scale.

In the strongly-ordered region of phase-space, $Q \ll \hat{Q}$, we may rewrite the $P_{\rm imp}$ factor as

$$P_{\rm imp} \;=\; \frac{1}{1+\frac{Q^2}{\hat{Q}^2}} \;\overset{Q\ll\hat{Q}}{=}\; 1 - \frac{Q^2}{\hat{Q}^2} + \dots\;. \tag{5.32}$$

Applying this to the $2 \to 3$ antenna function whose leading singularity, eq. (5.16), is proportional to $1/Q^2$, we see that the overall correction arising from the $Q^2/\hat{Q}^2$ and higher terms is finite and of order $1/\hat{Q}^2$; a power correction. The LL singular behaviour is therefore not affected. However, at the multiple-emission level, the $1/\hat{Q}^2$ terms do modify the *subleading* logarithmic structure, starting from $\mathcal{O}(\alpha_s^2)$, as we shall return to below.

In the *unordered* region of phase-space, $Q > \hat{Q}$, we rewrite the $P_{\rm imp}$ factor as

$$P_{\rm imp} \;=\; \frac{\hat{Q}^2}{Q^2}\,\frac{1}{1+\frac{\hat{Q}^2}{Q^2}} \;\overset{Q\gg\hat{Q}}{=}\; \frac{\hat{Q}^2}{Q^2}\left(1 - \frac{\hat{Q}^2}{Q^2} + \dots\right)\;, \tag{5.33}$$

which thus effectively modifies the leading singularity of the LL $2 \to 3$ function from $1/Q^2$ to $1/Q^4$, removing it from the LL counting. The only effective terms $\propto 1/Q^2$ arise from finite terms in the radiation functions, if any such are present, multiplied by the $P_{\rm imp}$ factor. Only a matching to the full tree-level $2 \to 4$ functions would enable a precise control over these terms. Up to any given fixed order, this can effectively be achieved by matching to tree-level matrix elements, as will be discussed in section 5.2.1. Matching beyond the fixed-order level is beyond the scope of this chapter. We thus restrict ourselves to the observation that, at the LL level, smooth ordering is equivalent to strong ordering, with differences only appearing at the subleading level.

The effective $2 \to 4$ probability in the shower arises from a sum over two different $2 \to 3 \otimes 2 \to 3$ histories, each of which has the tree-level form

$$\hat{A}\, P_{\rm imp}\, A \;\propto\; \frac{1}{\hat{Q}^2}\,\frac{\hat{Q}^2}{\hat{Q}^2+Q^2}\,\frac{1}{Q^2} \;=\; \frac{1}{\hat{Q}^2+Q^2}\,\frac{1}{Q^2}\,, \tag{5.34}$$

thus we may also perceive the combined effect of the modification as the addition of a mass term in the denominator of the propagator factor of the previous splitting. In the strongly ordered region, this correction is negligible, whereas in the unordered region, there is a large suppression from the necessity of the propagator in the previous topology having to be very off-shell, which is reflected by the $P_{\rm imp}$ factor. Using the expansion for the unordered region, eq. (5.33), we also see that the effective $2 \to 4$ radiation function, obtained from iterated $2 \to 3$ splittings, is modified as follows,

$$P_{2\to4} \;\propto\; \frac{1}{\hat{Q}^2}\frac{\hat{Q}^2}{Q^2}\,\frac{1}{Q^2} \;\to\; \frac{1}{Q^4} + \mathcal{O}(...)\,, \tag{5.35}$$

in the unordered region. That is, the intermediate low scale $\hat{Q}$, is *removed* from the effective $2 \to 4$ function, by the application of the $P_{\rm imp}$ factor.

Finally, to illustrate what happens to the Sudakov factors, we illustrate the path through phase space taken by an unordered shower history in fig. 5.5. An antenna starts showering at a scale equal to its invariant mass, $\sqrt{s}$, and a first $2 \to 3$ branching occurs at the evolution scale $\hat{Q}$. This produces the overall Sudakov factor $\Delta_{2\to3}(\sqrt{s},\hat{Q})$. A daughter antenna, produced by the branching, then starts showering at a scale equal to its own invariant mass, labeled $\sqrt{s_1}$. However, for all scales larger than $\hat{Q}$, the $P_{\rm imp}$ factor suppresses the evolution in this new dipole so that no leading logs are generated. To leading approximation, the effective Sudakov factor for the combined $2 \to 4$ splitting is therefore given by

$$\Delta^{\rm eff}_{2\to4} \;\sim\; \Delta_{2\to3}(\sqrt{s},\hat{Q})\,, \tag{5.36}$$

in the unordered region. Thus, we see that a dependence on the intermediate scale $\hat{Q}$ still remains in the effective Sudakov factor generated by the smooth-ordering procedure. Since $\hat{Q} < Q$ in the unordered region, the effective Sudakov suppression of these points might be "too strong". This situation is of course better than in the strongly ordered case, in which these points are zero, but it does suggest that a correction to the Sudakov factor may be desirable, in the unordered region. A study of $Z \to 4$ jets at one loop would be required to shed further light on this question.

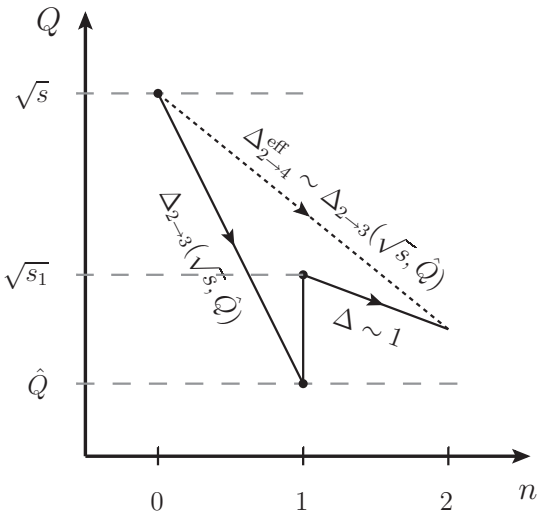

Figure 5.5: Illustration of scales and Sudakov factors involved in an unordered sequence of two $2 \to 3$ branchings, representing the smoothly ordered shower's approximation to a hard $2 \to 4$ process.

Having presented introductory aspects of (antenna) showers, we now turn to a detailed discussion of how we match them to higher fixed-order calculations.

5.2 Matched Antenna Showers

In this section we will discuss the matching of the antenna shower to fixed-order accuracy, thereby restoring knowledge concerning the finite terms.

5.2.1 Tree-Level Matching

The strategy for matching to tree-level matrix elements used in VINCIA was defined by GKS in [110] and is tightly related to the veto algorithm outlined above. The philosophy is to view the shower produced by the smoothly ordered antenna functions as generating an all-orders approximation to QCD, which can be systematically improved, order by order, by including one more factor in the accept probability, called the matrix-element correction. For a given trial branching, the full trial accept probability, up to the highest matched number of partons, is then obtained as a product of the ordinary trial-accept probability in the shower, multiplied by this extra correction factor.

Since the shower is already correct in the soft and collinear limits, the matrix-element correction factor will tend to unity in those limits, but it can deviate on either side of unity outside those limits. As long as the combined accept probability is still smaller than

unity, a probabilistic accept/reject step can still be applied, without having to worry about reweighting the events (which would be required if the total accept probability should exceed unity). It is also important to define the factor only in terms of physical cross sections (here represented by LO matrix elements), which guarantees positivity. (Again, if it were allowed to become negative, one would have to introduce negative-weight events, but this is avoided in the GKS strategy as defined in [110]).

As we have seen, the shower furnishes an all-orders approximation to QCD. The aim is, for each resolved parton/jet multiplicity, to match the answer provided by the shower to an, ideally, all-orders exact expression, by applying a multiplicative correction factor, schematically [110, 112]

$$\text{Matched} \;=\; \text{Approximate}\,\frac{\text{Exact}}{\text{Approximate}}\,. \tag{5.37}$$

At tree level, we in fact know only the first term in the expansion of the numerator, and we therefore expand the shower approximation to the same level. For n partons, assuming the approximation has already (recursively) been matched to the preceding order,

$$\text{Exact} \;\to\; |M_n|^2 \tag{5.38}$$

$$\begin{aligned}\text{Approximate} \;&\to\; \sum_j g_{Tj}^2\,\mathcal{C}_{Tj}\,A_{Tj}\,P_{\text{accept}}\,|M_{n-1_j}|^2 \\ &=\; \sum_j g_j^2\,\mathcal{C}_j\,P_{\text{imp}}\,P_{\text{Ari}}\,A_j\,|M_{n-1_j}|^2\,,\end{aligned} \tag{5.39}$$

where the subscript "T" indicates trial quantities (cf. section 5.1.2), we have suppressed the dependence on phase-space points, Φ, and the subscript j in the $(n-1)$-parton matrix element indicates the configuration obtained by performing the inverse shower step that removes parton j from the n-parton state.

The factors in eq. (5.39) are easy to calculate if a tree-level matrix-element (ME) generator is available to provide the $|M|^2$ factors. The total ME-corrected accept probability is thus simply eq. (5.19),

$$P_{\text{accept}}^{\text{LO}} \;=\; P_{\text{accept}}\,R_n \;=\; P_{\text{accept}}\,\frac{|M_n|^2}{\sum_j g_j^2\,\mathcal{C}_j\,P_{\text{imp}}\,P_{\text{Ari}}\,A_j\,|M_{n-1_j}|^2}\,. \tag{5.40}$$

As mentioned above, this factor should be positive and smaller than unity, in order to avoid having to reweight any events. In practice, we have found the trial function defined in eq. (5.16) to guarantee this for all processes we have so far considered, mainly consisting of $Z \to n$ and $H \to n$ partons. As shown in [110], it is also possible to absorb subleading-colour corrections into this matching factor in a positive-definite way, but since subleading colour goes beyond the scope of our study we do not reproduce the arguments here.

The fact that these factors change the distribution of the final set of generated events to the correct matrix-element answer can be explained by following the steps of the algorithm and summing over all possible branching histories. We start from Born-level

matrix-element events, and generate trial shower branchings, for a trial approximation to the $(B+1)$-parton matrix element of:

$$|M^{\rm Trial}_{B+1}|^2 = \sum_i g^2_{Ti}\,\mathcal{C}_{Ti}\,A_{Ti}\,|M^{\rm LO}_{B_i}|^2\,, \tag{5.41}$$

with i running over all possible single-parton clusterings that correspond to allowed shower branchings. Applying the LO accept probability, eq. (5.40), changes this to

$$\begin{aligned}
&\to \quad \sum_i g^2_{Ti}\,\mathcal{C}_{Ti}\,A_{Ti}\,P^{\rm LO}_{\rm accept}\,|M^{\rm LO}_{B_i}|^2 \\
&= \quad \sum_i g_i^2\,\mathcal{C}_i\,P_{\rm imp}\,P_{\rm Ari}\,A_i\,\frac{|M^{\rm LO}_{B+1}|^2}{\sum_j g^2_{sj}\,\mathcal{C}_j\,P_{\rm imp}\,P_{\rm Ari}\,A_j\,|M^{\rm LO}_{B_j}|^2}|M^{\rm LO}_{B_i}|^2 \\
&= \quad |M^{\rm LO}_{B+1}|^2\,.
\end{aligned} \tag{5.42}$$

That is, summed over shower histories, numerators and denominators are designed to cancel exactly, leaving only the LO matrix element for B+1 partons, as desired. Due to the full phase-space coverage and explicitly Markovian nature of the smoothly ordered shower algorithm, this procedure is straightforward to iterate for Born + 2, 3, etc partons[6].

To provide a connection with antenna subtraction, which will be useful when we extend to NLO matching below, we can rewrite the ratio in eq. (5.37) by a trivial rearrangement,

$$\text{Matched} \;=\; \text{Approximate}\left(1 + \frac{\text{Exact} - \text{Approximate}}{\text{Approximate}}\right)\,. \tag{5.43}$$

The numerator in this equation is very similar to a standard antenna-subtracted matrix element, though we emphasize that our antennae are of course modified by the presence of the $P_{\rm imp}$ and $P_{\rm Ari}$ factors.

Let us finally re-emphasize that since we apply the correction factor to the antenna functions themselves, thereby modifying the probability for a branching to occur, the probability for a branching *not* to occur is also modified. These corrections will therefore also be present in the Sudakov factors generated by the corrected shower evolution. The fact that the correction factor, R_n, is unity in all LL singular limits (since the shower functions are guaranteed to match the matrix-element singularities there) implies that the LL properties of the Sudakov factors are not affected by this modification. However, the tower of subleading logarithms *is* changed, for better or worse. While it is known that finite terms do not exponentiate our corrections here also include a more subtle aspect, namely a resummation of the subleading logarithms present in the higher-order matrix elements. At this level, however, we cannot be sure that this procedure produces the *correct* subleading logarithms of a formally higher-order resummation. Therefore, we view it at

[6]That is not the case for ordinary strongly ordered frameworks, due to the presence of dead zones in phase space and to the generally non-Markovian shower restart conditions. For such algorithms, addition of events in the dead zones [135], with CKKW-like Sudakov-factor prescriptions for multi-leg matching [136, 137], would presumably be necessary.

present merely as an interesting, and hopefully beneficial, side-effect of unitarity-based matching. The examination of formally subleading terms carried out in the next chapter is a first step towards a more rigorous study of these aspects.

5.2.2 One-Loop Matching at the Born Level

For the Born level, at NLO, the GKS matching strategy [110] reduces to the POWHEG one [26, 108, 109]. We nonetheless begin by recapitulating the steps used to derive the one-loop correction to the Born-level matrix element, in our notation to demonstrate the matching in an educational way. We then continue to higher multiplicities.

As our basis for one-loop matching we take the tree-level strategy described in section 5.2.1. Since the corrections are applied as modifications to the branching probabilities, without adding, subtracting, or reweighting events, the total inclusive rate after tree-level matching to any number of partons, is still just the leading-order, Born-level one. By the same token, after one-loop matching, at the integrated level, the total NLO correction to the inclusive rate must therefore just be the NLO "K-factor",

$$K^{\mathrm{NLO}} \;=\; \frac{\sigma^{\mathrm{NLO}}_{\mathrm{inc}}}{\sigma^{\mathrm{LO}}_{\mathrm{inc}}}\,. \tag{5.44}$$

For processes like Z decay, where the NLO correction has no dependence on the Born-level kinematics, this is trivial to implement as an overall reweighting factor on the Born-level events,

$$K^{\mathrm{NLO}}_{Z} \;=\; 1 + V_Z \;=\; 1 + \frac{\alpha_s}{\pi}\,, \tag{5.45}$$

where we have introduced the notation V for the NLO correction term, anticipating a similar notation for the multileg case below. Note that one could equally trivially normalize to NNLO or to data, as desired for the application at hand (we note though that such a normalization choice does not, by itself, ensure NNLO precision for any quantity besides the total inclusive rate).

However, for more complicated cases, where the NLO correction does depend on the Born-level kinematics, it is worth illustrating the general procedure for deriving a fully differential K-factor, that can be applied to the Born-level events, for each phase-space point. This also serves as a useful warm-up exercise for the multi-leg case below.

At NLO, we may distinguish between inclusive and exclusive rates for the first time. Either can in principle be used to derive matching equations between showers and fixed-order calculations, but the exclusive one is best suited for deriving expressions at the fully differential level. We recall that the exclusive n-jet cross section is defined as the cross section for observing n *and only* n jets, while the inclusive n-jet cross section counts the number of events with n *or more* jets. One therefore has the trivial relation

$$\sigma^{\mathrm{incl}}_{n}(Q) = \sum_{k\geq n} \sigma^{\mathrm{excl}}_{k}(Q)\,. \tag{5.46}$$

with Q the resolution scale of whatever (IR safe) algorithm is used to define the jets.

Inclusive Born

The total inclusive rate produced by the tree-level matched shower is just the Born-level matrix element,

$$\text{Approximate} \;\rightarrow\; |M_2^0|^2 \,, \tag{5.47}$$

where the subscript indicates the parton multiplicity (2 for $Z \rightarrow q\bar{q}$ decay) and the superscript indicates the loop order beyond the Born level (0 indicates the Born loop order). Because cancellation of real and virtual corrections is exact in both the unmatched shower as well as in the tree-level matching scheme described above, there are no further corrections to consider for the inclusive rate. In other words, the total integrated cross section produced by the shower is obtained merely by integrating eq. (5.47) over all of the Born-level phase space. We now seek a correction term, V_2, such that

$$\text{Matched} \;\rightarrow\; (1 + V_{2Z})\, |M_2^0|^2 \tag{5.48}$$

gives the correct inclusive NLO rate. From eq. (5.45), we know that the correction term for Z decay is

$$V_{2Z} \;=\; \frac{\alpha_s}{\pi} \,. \tag{5.49}$$

A systematic way of deriving this result, which can be applied to arbitrary processes, is provided by considering the cross section at the exclusive level.

Exclusive Born

The shower expression for the exclusive $Z \rightarrow q\bar{q}$ rate (defined at the hadronization cutoff, which is the lowest meaningful resolution scale in the perturbative shower) is

$$|M_2^0|^2\, \Delta(s, Q_{\text{had}}^2) \;=\; |M_2^0|^2 \left(1 - \int_{Q_{\text{had}}^2}^{s} \mathrm{d}\Phi_{\text{ant}}\; g_s^2\, \mathcal{C}\; A_{g/q\bar{q}} + \mathcal{O}(\alpha_s^2)\right) \,, \tag{5.50}$$

where we have expanded the Sudakov factor Δ to first order. Due to the presence of the hadronization scale, this expression is IR finite and can be defined in 4 dimensions. The colour factor for $q\bar{q} \rightarrow qg\bar{q}$ is

$$\mathcal{C}_{g/q\bar{q}} = 2C_F \,, \tag{5.51}$$

and we assume that the antenna function, A, is either the one derived from Z decay [138] or has been matched to it, using LO matching. That is,

$$g_s^2\; 2C_F\; A_{g/q\bar{q}} \;=\; \frac{|M_3^0|^2}{|M_2^0|^2} \,. \tag{5.52}$$

We first consider the limit $Q_{\text{had}} \rightarrow 0$, in which case the expression becomes

$$|M_2^0|^2\, \Delta(s, 0) \;=\; |M_2^0|^2 \left(1 - \int_{0}^{s} \mathrm{d}\Phi_{\text{ant}}\; g_s^2\; 2C_F\; A_{g/q\bar{q}} + \mathcal{O}(\alpha_s^2)\right) \,, \tag{5.53}$$

which can only be defined in the presence of an IR regularization scheme. We shall here use dimensional regularization, working in $d = 4 - 2\epsilon$ dimensions. Below, we rederive the matching equations in 4 dimensions, for $Q_{\rm had} \neq 0$, and show that the *same* final matching factors are obtained in both cases.

At NLO, the exclusive $Z \to q\bar{q}$ rate at "infinite" perturbative resolution is

$$|M_2^0|^2 \;+\; 2\,\mathrm{Re}[M_2^0 M_2^{1\,*}] \;=\; |M_2^0|^2 \left(1 + \frac{2\,\mathrm{Re}[M_2^0 M_2^{1\,*}]}{|M_2^0|^2}\right) , \tag{5.54}$$

where we have written the right-hand side in a form similar to eq. (5.53), in d dimensions. Because the resolution scale has been taken to zero, there are no unresolved 3-parton configurations to include. The virtual matrix element is

$$\frac{2\,\mathrm{Re}[M_2^0 M_2^{1\,*}]}{|M_2^0|^2} \;=\; \frac{\alpha_s}{2\pi}\, 2C_F \,\left(2I_{q\bar{q}}(\epsilon, \mu^2/s) - 4\right) , \tag{5.55}$$

with the function $I_{q\bar{q}}$ used to classify the ϵ divergences [125, 139, 140]. Note that we have modified the definition of I to make it explicitly dimensionless, see appendix A. On the shower side, the integral of the $Z \to qg\bar{q}$ antenna in eq. (5.53) is [125]

$$\int_0^s \mathrm{d}\Phi_{\rm ant}\, 2C_F\, g_s^2\, A_{g/q\bar{q}} \;=\; \frac{\alpha_s}{2\pi}\, 2C_F \,\left(-2I_{q\bar{q}}(\epsilon, \mu^2/s) + \frac{19}{4}\right) , \tag{5.56}$$

and, not surprisingly, the difference comes out to be exactly $\alpha_s/\pi \times |M_2^0|^2$. Writing this correction as a multiplicative K-factor, we obtain eq. (5.45).

As a cross-check, we now repeat the derivation in 4 dimensions, reinstating the hadronization scale. The fixed-order side is then

$$|M_2^0|^2 \left(1 + \frac{2\,\mathrm{Re}[M_2^0 M_2^{1\,*}]}{|M_2^0|^2} \;+\; \int_0^{Q_{\rm had}^2} \mathrm{d}\Phi_{\rm ant}\, g_s^2\, \mathcal{C}\, A_{g/q\bar{q}}\right) , \tag{5.57}$$

where the integral that has been added corresponds to unresolved 3-parton configurations, with A again given by eq. (5.52). Though eq. (5.50) is now defined entirely in 4 dimensions, we still need dimensional regularization to regulate the two last terms in the fixed-order expression. In principle, the integral in the last term could be carried out explicitly, but it is simpler to rewrite it as

$$\int_0^{Q_{\rm had}^2} \mathrm{d}\Phi_{\rm ant}\, g_s^2\, \mathcal{C}\, A_{g/q\bar{q}} \;=\; \int_0^{m_Z^2} \mathrm{d}\Phi_{\rm ant}\, g_s^2\, \mathcal{C}\, A_{g/q\bar{q}} - \int_{Q_{\rm had}^2}^{m_Z^2} \mathrm{d}\Phi_{\rm ant}\, g_s^2\, \mathcal{C}\, A_{g/q\bar{q}} \tag{5.58}$$

where the first term is just the full antenna integral, eq. (5.56), and the second term is identical to the one appearing in eq. (5.50), with which it cancels completely, cf. the definition of the tree-level matching, eq. (5.52). The final correction term is therefore again exactly equal to $\alpha_s/\pi \times |M_2^0|^2$.

Note that the scale and scheme dependence of the α_s/π correction is not specified since its ambiguity is formally of order α_s^2. For definiteness we take the renormalization scale for this correction to be proportional to the invariant mass of the system,

$\mu_R = k_\mu^{\rm inc}\sqrt{\hat{s}}$ (so that $\mu_R = k_\mu^{\rm inc} m_Z$ at the Z pole), with $k_\mu^{\rm inc}$ thus representing the free parameter that governs the choice of renormalization scale for the total inclusive rate for $Z \to$ hadrons. We shall consider both one-loop and two-loop running options. The value of $\alpha_s(m_Z)$ will be determined from LEP data in the next chapter.

5.3 Conclusion

This chapter started with an introduction of the VINCIA antenna shower. The shower can be evolved by three different types of ordering variables p_T, m_D and E^*. Implications of the strong ordering requirement were investigated for $e^+e^- \to 3$ partons. Moreover, a different type of ordering, allowing for a higher phase space occupation in comparison with strong ordering was introduced. The smooth ordering allows a restart scale for the shower which is slightly above the generated emission scale. It was demonstrated that the procedure of smooth ordering only affects the subleading terms generated by the shower. The VINCIA shower therefore provides an ordering prescription that lies in between a strong ordered and unordered shower, and reduces the dead zone of additional radiation. Then we proceeded to derive NLO matching terms for $e^+e^- \to 2$ jets. It was shown that such a matching may be derived for an exclusive cross-section. The case of two jets was special however, as the lack of additional radiation on the Born amplitude only allows NLO accuracy by changing the weight of the event. In the next chapter, the consecutive matching to three jets of the shower will be implemented for NLO accuracy by adapting the branching probability.

Chapter 6

One-Loop Matching for $Z \to 3$ Partons

In the previous chapter the VINCIA antenna-shower algorithm was presented followed by a first description for NLO matching for $Z \to 2$ partons. The two parton case is special for two reasons. Firstly because of the absence of renormalization terms and secondly, since the lack of additional radiation required a special treatment to match the event to NLO accuracy, by adapting the weight. Consecutive NLO matching will employ a rescaling of the accept probability to incorporate knowledge of the NLO calculation in a unitary approach. This chapter will focus on generalizing the approach for an additional parton in the final state and is therefore the key step to a fully general framework that allows for an arbitrary number of partons.

6.1 Constructing a Matching Term

The approximation to the 3-parton exclusive rate produced by a shower matched to (at least) NLO for the 2-parton inclusive rate and to LO for the 3-parton one, is

$$\text{Approximate } \to \; (1 + V_2) \, |M_3^0|^2 \, \Delta_2(m_Z^2, Q_3^2) \, \Delta_3(Q_{R3}^2, Q_{\rm had}^2) \, , \tag{6.1}$$

where M_3^0 is the tree-level $Z \to q g \bar{q}$ matrix element and Q_{R3} denotes the "restart scale". For strong ordering, Q_{R3} is equal to Q_3, while, for smooth ordering, it is given by the nested antenna phase spaces, i.e., by the successive antenna invariant masses. The subscripts on the two Sudakov factors Δ_2 and Δ_3 make it explicit that they refer to the event as a whole, see the illustration in fig. 6.1. Again, we have the choice whether we wish to work in 4 dimensions, with a non-zero hadronization scale, $Q_{\rm had}$, or in d dimensions with the hadronization scale taken to zero. We have maintained the hadronization scale in eq. (6.1), though we shall see below that the dependence on it does indeed cancel in the final result.

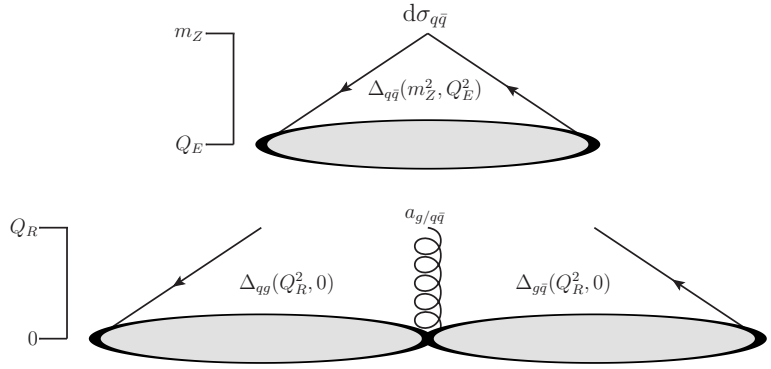

Figure 6.1: Illustration of the evolution scales and Sudakov factors appearing in the exclusive 3-jet cross section, eq. (6.1).

The 2-parton Sudakov factor, Δ_2, is generated by the (matched) evolution from 2 to 3 partons,

$$\Delta_2(m_Z^2, Q_3^2) \;=\; 1 - \int_{Q_3^2}^{m_Z^2} \mathrm{d}\Phi_{\mathrm{ant}}\; g_s^2\; 2C_F\; A_{g/q\bar{q}} + \mathcal{O}(\alpha_s^2)\,, \tag{6.2}$$

with $A_{g/q\bar{q}}$ again defined by eq. (5.52). Notice that the integral only runs from the starting scale, m_Z^2, to the 3-parton resolution scale, Q_3^2, hence this integral is IR finite, though it does contain logarithms. In the remainder of this chapter, we shall work only with the leading-colour part of the Sudakov and matrix-element expressions, hence from now on we replace $2C_F$ in the above expression by C_A,

$$\Delta_2^{\mathrm{LC}}(m_Z^2, Q_3^2) \;=\; 1 - \int_{Q_3^2}^{m_Z^2} \mathrm{d}\Phi_{\mathrm{ant}}\; g_s^2\; C_A\; A_{g/q\bar{q}} + \mathcal{O}(\alpha_s^2)\,. \tag{6.3}$$

The 3-parton Sudakov factor, Δ_3, imposes exclusivity and is given by

$$\Delta_3(Q_{R3}^2, Q_{\mathrm{had}}^2) \;=\; 1 - \sum_{j=1}^{2} \int_{Q_{\mathrm{had}}^2}^{Q_{R3}^2} \mathrm{d}\Phi_{\mathrm{ant}}\; g_s^2\; (C_A\; A_{Ej} \;+\; 2T_R\; A_{Sj}) + \mathcal{O}(\alpha_s^2)\,, \tag{6.4}$$

where the index j runs over the qg and $g\bar{q}$ antennae, and we use subscripts E and S for gluon emission and gluon splitting, respectively. We have implicitly assumed smooth ordering here, which implies that the upper boundaries on the integrals are given by the respective dipole invariant masses (squared), s_j. Note also that we must take into account all modifications that are applied to the LL antenna functions, including P_{imp}, P_{Ari}, and LO matrix-element matching factors. (We do not write out these factors here, to avoid clutter.) I.e., the antenna functions in the above expression must be the ones actually generated by the shower algorithm, including the effect of any modifications imposed by vetos.

For strong ordering, there are no $P_{\rm imp}$ factors, and the upper integral boundary is instead $\min(Q_3^2, s_j)$,

$$\Delta_3(Q_3^2, Q_{\rm had}^2) \;=\; 1 - \sum_{j=1}^{2} \int_{Q_{\rm had}^2}^{\min(Q_3^2, s_j)} \mathrm{d}\Phi_{\rm ant}\; g_s^2 \;(C_A\, A_{Ej} \;+\; 2T_R\, A_{Sj}) + \mathcal{O}(\alpha_s^2)\,. \tag{6.5}$$

However, since strong ordering is not able to fill the entire 4-parton phase space [110, 141], full NLO matching can only be obtained for the smoothly ordered variant. It is nonetheless interesting to examine both types of shower algorithms, since even in the strongly ordered case, we may compare the Sudakov logarithms arising at $\mathcal{O}(\alpha_s^2)$ to those present in the fixed-order calculation.

On the fixed-order side, the expression for the 3-parton exclusive rate is simply

$$\text{Exact} \;\to\; |M_3^0|^2 \;+\; 2\,\mathrm{Re}[M_3^0 M_3^{1*}] \;+\; \int_0^{Q_{\rm had}^2} \frac{\mathrm{d}\Phi_4}{\mathrm{d}\Phi_3} |M_4^0|^2\,, \tag{6.6}$$

where the last term represents 4-parton configurations in which a single parton is unresolved with respect to the hadronization scale. For Z decay, d-dimensional expressions for the virtual matrix element have been available since long [125, 139, 142, 143]. Details on the calculation and in particular its renormalization, are given in appendix B, in a notation convenient for our purposes.

We now seek a fully differential matching factor, $K_3 = 1 + V_3$, such that the expansion of

$$\text{Matched} \;=\; (1 + V_3)\;\text{Approximate}\,, \tag{6.7}$$

reproduces the exact expression, eq. (6.6), to one-loop order. ("Approximate" here stands for the tree-level matched shower approximation, eq. (6.1).) Trivial algebra yields

$$\begin{aligned} V_3^{\rm LC} \;=\; & \left[\frac{2\,\mathrm{Re}[M_3^0 M_3^{1*}]}{|M_3^0|^2}\right]^{\rm LC} \;-\; V_2 \\ & + \int_{Q_3^2}^{m_Z^2} \mathrm{d}\Phi_{\rm ant}\; g_s^2\; 2C_A\, A_{g/q\bar{q}} \;+\; \sum_{j=1}^{2} \int_0^{s_j} \mathrm{d}\Phi_{\rm ant}\; g_s^2\; (C_A\, A_{Ej} \;+\; 2T_R\, A_{Sj}) \\ & + \int_0^{Q_{\rm had}^2} \frac{\mathrm{d}\Phi_4}{\mathrm{d}\Phi_3} \frac{|M_4^0|^2}{|M_3^0|^2} \;-\; \sum_{j=1}^{2} \int_0^{Q_{\rm had}^2} \mathrm{d}\Phi_{\rm ant}\; g_s^2\; (C_A\, A_{Ej} \;+\; 2T_R\, A_{Sj})\,, \end{aligned} \tag{6.8}$$

where we have reinstated d-dimensional forms of the one-loop matrix element and of the divergent $3 \to 4$ terms. For a shower matched to $|M_4^0|^2$ at leading order, the last two terms will cancel, by definition of the matched antenna functions (even for an unmatched shower, the difference could at most be a finite power correction in the hadronization scale, since the matrix element and the shower antenna functions have the same singular-

ities), yielding:

$$V_{3Z}^{\mathrm{LC}} = \left[\frac{2\,\mathrm{Re}[M_3^0 M_3^{1*}]}{|M_3^0|^2}\right]^{\mathrm{LC}} - V_{2Z} + \int_{Q_3^2}^{m_Z^2} \mathrm{d}\Phi_{\mathrm{ant}}\, g_s^2\, 2C_A\, A_{g/q\bar{q}} + \sum_{j=1}^{2} \int_0^{s_j} \mathrm{d}\Phi_{\mathrm{ant}}\, g_s^2\, \left(C_A\, A_{Ej} + 2T_R\, A_{Sj}\right). \tag{6.9}$$

Rewriting the remaining integrals in terms of a set of standardized antenna subtraction terms, writing out the ordering functions for gluon emission and gluon splitting, O_E and O_S, explicitly, and denoting the ARIADNE factor for gluon splitting by P_A, we arrive at the following master equation for the second-order correction to the 3-jet rate:

$$\begin{aligned} V_{3Z}^{\mathrm{LC}} &= \left[\frac{2\,\mathrm{Re}[M_3^0 M_3^{1*}]}{|M_3^0|^2}\right]^{\mathrm{LC}} - V_{2Z} + \sum_{j=1}^{2} \int_0^{s_j} \mathrm{d}\Phi_{\mathrm{ant}} g_s^2 \left(C_A A_{Ej}^{\mathrm{std}} + n_F A_{Sj}^{\mathrm{std}}\right) \\ &+ \int_{Q_3^2}^{m_Z^2} \mathrm{d}\Phi_{\mathrm{ant}}\, g_s^2\, C_A\, A_{g/q\bar{q}}^{\mathrm{std}} + \int_{Q_3^2}^{m_Z^2} \mathrm{d}\Phi_{\mathrm{ant}}\, g_s^2\, C_A\, \delta A_{g/q\bar{q}} \\ &- \sum_{j=1}^{2} \int_0^{s_j} \mathrm{d}\Phi_{\mathrm{ant}}\, g_s^2 \left(C_A\,(1-O_{Ej})\, A_{Ej}^{\mathrm{std}} + n_F\,(1-O_{Sj})\, P_{A_j}\, A_{Sj}^{\mathrm{std}}\right) \\ &+ \sum_{j=1}^{2} \int_0^{s_j} \mathrm{d}\Phi_{\mathrm{ant}} g_s^2 \left(C_A\, \delta A_{Ej} + n_F\, \delta A_{Sj}\right) - \sum_{j=1}^{2} \int_0^{s_j} \mathrm{d}\Phi_{\mathrm{ant}} g_s^2 n_F \left(1 - P_{A_j}\right) A_{Sj}^{\mathrm{std}}, \end{aligned} \tag{6.10}$$

with the standardized Gehrmann-Gehrmann-de Ridder-Glover (GGG) subtraction terms defined by [125]:

$$\begin{aligned} A_{g/q\bar{q}}^{\mathrm{std}} &= a_3^0\ (= A_3^0) \quad , \quad \int_0^s \mathrm{d}\Phi_{\mathrm{ant}}\, g_s^2\, A_{g/q\bar{q}}^{\mathrm{std}} = \frac{\alpha_s}{2\pi}\left(-2I_{q\bar{q}}^{(1)}(\epsilon,\mu^2/s) + \frac{19}{4}\right) \\ A_{g/qg}^{\mathrm{std}} &= d_3^0 \quad , \quad \int_0^s \mathrm{d}\Phi_{\mathrm{ant}}\, g_s^2\, A_{g/qg}^{\mathrm{std}} = \frac{\alpha_s}{2\pi}\left(-2I_{qg}^{(1)}(\epsilon,\mu^2/s) + \frac{17}{3}\right) \\ A_{\bar{q}/qg}^{\mathrm{std}} &= e_3^0\ (= \tfrac{1}{2}E_3^0) \quad , \quad \int_0^s \mathrm{d}\Phi_{\mathrm{ant}}\, g_s^2\, A_{\bar{q}/qg}^{\mathrm{std}} = \frac{\alpha_s}{2\pi}\left(-2I_{qg,F}^{(1)}(\epsilon,\mu^2/s) - \frac{1}{2}\right) \end{aligned} \tag{6.11}$$

whose IR limits and integrated pole structures were examined thoroughly in [125, 139, 140], though we have here rewritten the IR singularity operators $I^{(1)}$ in explicitly dimensionless forms, see appendix A. (The alphabetical labeling in eqs. (6.11) corresponds to the notation used in [125].)

The first line and first term on the second line in eq. (6.10) represent a standard antenna-subtracted one-loop matrix element, normalized to the Born level, with the standardized subtraction terms tabulated in eq. (6.11), and the additional finite term V_{2Z} originating from the NLO matching at the preceding order; see section 5.2.2, eq. (5.49).

The subsequent terms express the difference between the simple fixed-order subtraction carried out in the first line and the actual terms that are generated by a matched Markovian antenna shower. Physically, these terms represent the difference between the evolution of a single dipole (the original $q\bar{q}$ system) and evolution of two dipoles (the post-branching $qg\bar{q}$ system), with a transition occuring at the branching scale Q_3. As mentioned above, the O_{Ej} and O_{Sj} factors in the third line represent the ordering criterion imposed in the evolution, either strong or smooth. For smooth ordering, they are

$$1 - O_{Ej} = 1 - \frac{Q_3^2}{Q_{Ej}^2 + Q_3^2} , \tag{6.12}$$

$$1 - O_{Sj} = 1 - \frac{Q_3^2}{m_{q\bar{q}}^2 + Q_3^2} , \tag{6.13}$$

with Q_{Ej} the evolution variable used for gluon emissions, while for strong ordering, the factor $(1 - O_j)$ can be removed if the integral boundaries are replaced by $[Q_3^2, s_j]$ (note: this replacement should only be done in the third line).

The last term in eq. (6.10) is an artifact of the ARIADNE factor, P_{Ari}, which was introduced in section 5.1.2 and is applied to gluon-splitting antennae in VINCIA. Summed over the two "sides" of the splitting gluon, this produces the same collinear singularities as the standard gluon-splitting antenna, but in highly asymmetric configurations in which the splitting gluon is near-collinear to a neighbouring colour line, the ARIADNE factor produces a strong suppression, which improves the agreement with the tree-level 4-parton matrix element [133], and which then generates an additional logarithm.

Notice that all but the δA terms are defined in terms of standarized antenna functions, and the corresponding integrals can be carried out analytically, once and for all. We give explicit forms for each of these terms, for each choice of evolution variable, in the following section.

The only terms of eq. (6.10) that need to be integrated numerically are thus the δA terms, which express the difference between the standardized antenna functions and those generated by the actual (matched) shower evolution, which may have different finite terms and/or be matched to the LO 4-parton matrix element. Nonetheless, since the previous lines already contain most of the structure, we expect these functions to be relatively well-behaved and numerically sub-leading. Specifically, the δA terms for gluon emission and gluon splitting, respectively, are defined by

$$\delta A_{Ej}^{\mathrm{LC}} = O_{Ej} \left(R_{4E}^{\mathrm{LC}} A_{Ej}^{\mathrm{LL}} - A_{Ej}^{\mathrm{std}} \right) , \tag{6.14}$$

$$\delta A_{Sj}^{\mathrm{LC}} = O_{Sj} \, P_{Aj} \left(R_{4S} A_{Sj}^{\mathrm{LL}} - A_{Sj}^{\mathrm{std}} \right) , \tag{6.15}$$

with A^{LL} the unmatched shower antenna function (as defined in [113, 133]) and the second-order LO matching factors, R_{4E} and R_{4S} (for $Z \to qgg\bar{q}$ and $Z \to q\bar{q}'q'\bar{q}$, respectively), defined as in eq. (5.40), but including only the leading-colour terms in R_{4E}^{LC}. For strong ordering, similarly to above, the O_j factors can be removed by changing the integration boundaries of the δA terms to $[0, Q_3^2]$.

Finally, we note that one could in principle equally well have defined eq. (6.10) without the terms on the third line. The δA terms in eqs. (6.14) and (6.15) would then likewise have to be defined without $P_{\rm imp}$ and $P_{\rm Ari}$ factors. However, while this would give a seemingly cleaner relation with standard fixed-order subtraction, the behaviour of the (numerical) integrals over the δA terms would be more difficult, due to over-subtraction in the unordered regions. (Showers without either a strong-ordering condition or a smooth-ordering suppression greatly overestimate the real-radiation matrix elements in the unordered region [110, 133, 144].) Numerically, it is therefore more convenient to integrate the contributions represented by the third line in eq. (6.10) analytically, leaving only the suppressed terms in eq. (6.15) to be integrated over numerically.

To be specific, the numerical integration over the δA terms is performed by rewriting the δA integrals in dimensionless MC form, as:

$$\frac{\alpha_s}{2\pi} C_A \sum_{j=1}^{2} \frac{1}{4} \frac{1}{N} \sum_{i=1}^{N} \left(\, s_j \, \delta A_j(\Phi_i) \, \right) \, , \tag{6.16}$$

and similarly for the gluon-splitting terms, with Φ_i a number of random (uniformly distributed) antenna phase-space points. The common factor 1/4 arises from combining the prefactor $8\pi^2$ above with the area of the phase-space triangle, $1/2$, and the factor $1/(16\pi^2)$ from the phase-space factorization, $\mathrm{d}\Phi_{\rm ant}$. For smooth $p_\perp$-ordering with an arbitrary normalization factor $N_\perp$ (so $Q_E^2 = N_\perp p_\perp^2$), the ordering factors, O_j, reduce to:

$$O_E(q_i g_j, \bar{q}_k \to q_a g_b g_c, \bar{q}_k) \;=\; \frac{y_{jk}}{y_{jk} + x_{ab} x_{bc}} \, , \tag{6.17}$$

$$O_E(q_i, g_j \bar{q}_k \to q_i, g_a g_b \bar{q}_c) \;=\; \text{same with } i \leftrightarrow k \, , \tag{6.18}$$

$$O_S(q_i g_j, \bar{q}_k \to q_a \bar{q}'_b q'_c, \bar{q}) \;=\; \frac{N_\perp y_{jk}}{N_\perp y_{jk} + x_{bc}} \, , \tag{6.19}$$

$$O_S(q_i, g_j \bar{q}_k \to q_i, \bar{q}'_c q'_b \bar{q}_a) \;=\; \text{same with } i \leftrightarrow k \, , \tag{6.20}$$

where we have used y with ijk indices for the scaled invariants in the original $qg\bar{q}$ topology and x with abc indices for the integration variables in the antenna phase space. Note also that the y values are normalized to the full 3-parton CM energy (squared), while the x values are normalized to their respective dipole CM energies (squared).

6.1.1 The Renormalization Term

A further ingredient to be discussed is the choice of renormalization scale on both the fixed order and parton shower sides of the calculation, as these scales are in general chosen differently in both sides. Hence a translation term arises at second order, which must account for this difference, keeping in mind that, as the scale evolves from one to the other, flavour thresholds are passed. Our aim is to have the flexibility to use fixed order matrix elements renormalized according to their usual scheme, while maintaining the freedom to make a different choice on the shower side.

The fixed order calculations for Z-decay to jets to which we match are customarily renormalized in a version of the $\overline{\rm MS}$ scheme called the Zero-Mass Variable Flavour Number Scheme (ZM-VFNS). In this scheme the bare QCD coupling is renormalized as

$$g_b = \mu^\epsilon g(\mu_R^2)\left[1 + \frac{\alpha_s(\mu_R^2)}{8\pi}\left\{\left(-\frac{1}{\epsilon} + \gamma_E - \ln 4\pi + \ln\frac{\mu_R^2}{\mu^2}\right)\beta_0\right\}\right] \tag{6.21}$$

with $\beta_0 = (11C_A - 2n_F)/3 \equiv \beta_0^F$ and n_F is the number of light flavours. One thus ignores flavours that are heavier than the scale of the calculation, both in the virtual and in the real calculations. Once all the UV poles are cancelled, one has a running coupling that depends on the number of light flavours for the scale μ_R at hand. One then changes the flavour number when a threshold is crossed. For our present case of Z boson decay to jets we take $n_F = 5$ for μ_R not too different from the Z-boson mass.

Let us be more specific about the matching of α_s across flavour thresholds. At one loop,

$$\alpha_s^{(n_F)}(\mu_R) = \frac{4\pi/\beta_0^F}{\ln(\mu_R^2/\Lambda_F^2)}\,. \tag{6.22}$$

The value of Λ_F depends on the number of active flavours, as follows. When passing flavour thresholds the following one-loop matching conditions are imposed

$$\alpha_s^{(5)}(m_b) = \alpha_s^{(4)}(m_b), \qquad \alpha_s^{(4)}(m_c) = \alpha_s^{(3)}(m_c)\,. \tag{6.23}$$

These conditions can be satisfied if Λ_F obeys the matching conditions

$$\ln\frac{\Lambda_F^2}{\Lambda_{F+1}^2} = \frac{2}{3\beta_0^F}\ln\frac{m_{F+1}^2}{\Lambda_{F+1}^2}\,. \tag{6.24}$$

With these conditions one can also express α_s values for different flavour numbers into eachother. E.g. if $m_c < \mu_R < m_b$, one can express $\alpha_s^{(4)}(\mu_R)$ in terms of $\alpha_s^{(5)}(\mu_R)$ by the relation

$$\alpha_s^{(4)}(\mu_R) = \alpha_s^{(5)}(\mu_R)\frac{1}{\frac{\beta_0^4}{\beta_0^5} + \left(1 - \frac{\beta_0^4}{\beta_0^5}\right)\frac{\alpha_s^{(5)}(\mu_R)}{\alpha_s^{(5)}(m_b)}}\,. \tag{6.25}$$

For completeness we briefly review how this n_F-dependent UV singularity occurs in the context of the (inclusive) 3-jet rate, in the case where we only consider massless quarks [142,143]. In the virtual contribution, the only one-loop diagram for $Z \to q\bar{q}g$ that is sensitive to the number of flavours is the quark self-energy correction on the external gluon. The self-energy diagram itself, being scaleless, is zero in dimensional regularization. However, renormalization of the coupling amounts to adding a n_F counterterm on the exteral gluon line proportional to

$$n_F\frac{2}{3\epsilon}\left(\frac{\mu^2}{\mu_R^2}\right)^\epsilon\,. \tag{6.26}$$

The real contribution contributes a n_F dependent (collinear) $1/\epsilon$ pole as well, from gluon-splitting

$$- n_F \frac{2}{3\epsilon} \left(\frac{\mu^2}{s} \right)^{\epsilon} . \tag{6.27}$$

In the sum over real and virtual contributions the poles cancel, as guaranteed by the KLN theorem, leaving a logarithm of the form

$$n_F \frac{2}{3} \ln \left(\frac{s}{\mu_R^2} \right) . \tag{6.28}$$

On the shower side a related prescription is used, in which the running coupling is evaluated at a shower scale $\mu_{\rm PS}$, such that the scale again depends on the number of flavours. Depending on the value of $\mu_{\rm PS}$, a corresponding value of n_F is chosen, as well as of the QCD scale Λ_F. This is often different from that for a fixed order calculation. To give a specific example, matrix elements will typically be renormalized at a scale characteristic of the total CM energy, i.e., $\mu^2_{\rm ME} = s$ an event-independent value, while resummation arguments imply one best chooses a running scale, such as $\mu_{\rm PS} = p_\perp$, for shower applications [128, 145], which can differ per event.

Shifting to a different scale for α_s of a given flavour number is quite straightforward. Translating from a shower scale $\mu_{\rm PS}$ to a matrix-element scale $\mu_{\rm ME}$ amounts to replacing, for an antenna function

$$a_{g/q\bar{q}}\big|_{\mu_R=\mu_{\rm PS}} \to \left(1 + \alpha_s \frac{11N_C - 2n_F}{12\pi} \ln \left(\frac{\mu^2_{\rm ME}}{\mu^2_{\rm PS}} \right) + \mathcal{O}(\alpha_s^2) \right) \, a_{g/q\bar{q}}\big|_{\mu_R=\mu_{\rm ME}} . \tag{6.29}$$

For coherent parton-shower models, the arguments presented in [145] also motivate a change to a "Monte Carlo" scheme for α_s, in which $\Lambda_{\rm QCD}$ is rescaled, for each n_F, by the so-called CMW factor ~ 1.5 (with some mild flavour dependence), relative to its $\overline{\rm MS}$ value. If the shower model being matched employs this scheme, then a further rescaling of the renormalization-scale argument, $\mu_{\rm PS} \to \mu_{\rm PS}/k_{\rm CMW}$, should be used in eq. (6.29), with

$$k_{\rm CMW} \;=\; \exp\left(\frac{67 - 3\pi^2 - 10n_F/3}{2(33 - 2n_F)} \right) \;=\; \begin{cases} 1.513 & n_F = 6 \\ 1.569 & n_F = 5 \\ 1.618 & n_F = 4 \\ 1.661 & n_F = 3 \end{cases} \tag{6.30}$$

for $N_c = 3$. The translation of renormalization scale (and scheme) yields then an additional term to be added to the definition of V_3 in eq. (6.10),

$$V_{3\mu} \;=\; -\frac{\alpha_s}{2\pi} \frac{11N_C - 2n_F}{6} \ln \left(\frac{\mu^2_{\rm ME}}{\mu^2_{\rm PS}} \right) \;=\; -\frac{\alpha_s}{2\pi} \frac{\beta_0}{2} \ln \left(\frac{\mu^2_{\rm ME}}{\mu^2_{\rm PS}} \right) . \tag{6.31}$$

By inserting the above term, which enters at overall order $\alpha_s^2 \ln(\mu^2_{\rm ME}/\mu^2_{\rm PS})$, the two calculations can be compared consistently at one-loop accuracy.

Note that if several different shower paths populate the same fixed-order phase-space point, then each path will in general be associated with a distinct $\mu_{\rm PS}$ value. Thus, one $V_{3\mu}$ term arises for each shower path, weighted by the relative contribution of each path to the total. Since for our case there is only one antenna contributing to $Z \to qg\bar{q}$, this particular complication does not arise here.

We finally alert the reader regarding the use of different flavour number α_s's in the master equation (6.10). In that equation cancellation of $1/\epsilon$ divergences take place, already in the first line of the right hand side. For this cancellation it is important that the subtraction terms, originating from the shower expansion and listed in eq. (6.11), use $\alpha_s^{(5)}$ renormalized as in the fixed order calculation. All subsequent terms in the master equation are finite, and constitute differences of unordered and strongly ordered shower based terms, which are also finite, and beyond NLO.

6.1.2 Leading-Colour One-Loop Correction for Z → 3 Jets

Combining the results above, in particular eqs. (6.10), (6.11), and (6.31), we obtain the complete expression for the leading-colour[1] one-loop correction for Z → 3 Jets,

$$
\begin{aligned}
V_{3Z}(q,g,\bar{q}) \;=\; & \left[\frac{2\,\mathrm{Re}[M_3^0 M_3^{1*}]}{|M_3^0|^2}\right]^{\rm LC} \;-\; \frac{\alpha_s}{\pi} \;-\; \frac{\alpha_s}{2\pi}\left(\frac{11N_C-2n_F}{6}\right)\ln\left(\frac{\mu^2_{\rm ME}}{\mu^2_{\rm PS}}\right) \\
& + \frac{\alpha_s C_A}{2\pi}\left[-2I^{(1)}_{qg}(\epsilon,\mu^2/s_{qg}) - 2I^{(1)}_{qg}(\epsilon,\mu^2/s_{g\bar{q}}) + \frac{34}{3}\right] \\
& + \frac{\alpha_s n_F}{2\pi}\left[-2I^{(1)}_{qg,F}(\epsilon,\mu^2/s_{qg}) - 2I^{(1)}_{g\bar{q},F}(\epsilon,\mu^2/s_{g\bar{q}}) - 1\right] \\
& + \frac{\alpha_s C_A}{2\pi}\left[8\pi^2\int_{Q_3^2}^{m_Z^2} \mathrm{d}\Phi_{\rm ant}\, A^{\rm std}_{g/q\bar{q}} \;+\; 8\pi^2\int_{Q_3^2}^{m_Z^2}\mathrm{d}\Phi_{\rm ant}\,\delta A_{g/q\bar{q}}\right. \\
& \left. - \sum_{j=1}^{2} 8\pi^2\int_0^{s_j}\mathrm{d}\Phi_{\rm ant}\,(1-O_{Ej})\,A^{\rm std}_{g/qg} \;+\; \sum_{j=1}^{2} 8\pi^2\int_0^{s_j}\mathrm{d}\Phi_{\rm ant}\,\delta A_{g/qg}\right] \\
& + \frac{\alpha_s n_F}{2\pi}\left[-\sum_{j=1}^{2} 8\pi^2\,P_{Aj}\int_0^{s_j}\mathrm{d}\Phi_{\rm ant}(1-O_{Sj})\,A^{\rm std}_{\bar{q}/qg}\right. \\
& \left. + \sum_{j=1}^{2} 8\pi^2\int_0^{s_j}\mathrm{d}\Phi_{\rm ant}\,\delta A_{\bar{q}/qg} - \frac{1}{6}\,\frac{s_{qg}-s_{g\bar{q}}}{s_{qg}+s_{g\bar{q}}}\ln\left(\frac{s_{qg}}{s_{g\bar{q}}}\right)\right],
\end{aligned}
\tag{6.32}
$$

where:

[1] We use the usual MC definition of leading colour and include terms $\propto C_A$ and $\propto n_F$ but neglect ones $\propto 1/C_A$.

- the first line contains the full (leading-colour) one-loop matrix element, the V_{2Z} correction from one-loop matching at the preceding order, and the $V_{3\mu}$ term from the choice of shower renormalization scale;
- the second line contains the standardized subtraction term arising from the $qg \to qgg$ and $g\bar{q} \to gg\bar{q}$ antennae;
- the third line contains the standardized subtraction term arising from the $qg \to q\bar{q}'q'$ and $g\bar{q} \to \bar{q}'q'\bar{q}$ antennae;
- the fourth to last lines contain the terms arising from the difference between the (matched) shower evolution and the standardized subtraction terms, including the consequences of ordering choices and modification factors such as those arising from the Ariadne factor and from matching to the LO matrix elements.

We denote the singular subtracted 1-loop matrix element by SVirtual

$$\begin{aligned}\text{SVirtual} \;=& \left[\frac{2\,\mathrm{Re}[M_3^0 M_3^{1*}]}{|M_3^0|^2}\right]^{\mathrm{LC}} + \frac{\alpha_s C_A}{2\pi}\left[-2I_{qg}^{(1)}(\epsilon,\mu^2/s_{qg}) - 2I_{qg}^{(1)}(\epsilon,\mu^2/s_{g\bar{q}}) + \frac{34}{3}\right] \\ &+ \frac{\alpha_s n_F}{2\pi}\left[-2I_{qg,F}^{(1)}(\epsilon,\mu^2/s_{qg}) - 2I_{g\bar{q},F}^{(1)}(\epsilon,\mu^2/s_{g\bar{q}}) - 1\right] \end{aligned} \tag{6.33}$$

In section 6.2, we compute the analytical integrals corresponding to each of the shower-generated terms, for different choices of evolution variable, ordering criterion, and antenna functions.

With the one-loop matrix element expressed as in appendix B.2, it is easy to see that the infrared singularity operators in eq. (6.33) cancel, leaving only explicitly finite remainders (which may still contain logarithms of resolved scales). This then constitutes the description of the one-loop matching for $Z \to 3$ jets, having already discussed the case for two jets. In the context of eq. (5.46) we have now corrected the first two terms on the rhs to NLO accuracy.

6.1.3 One-Loop Correction for Born + 2 Partons

To illustrate how the formalism presented here generalizes to higher multiplicities, we take the case of the NLO correction to $Z \to 4$ partons. For simplicity, however, we continue to restrict our analysis of the correction factor to the leading-colour level. At NLO, the exclusive $Z \to 4$ partons rate at "infinite" perturbative resolution (similarly to above) is

$$\text{Exact} \;\to\; |M_4^0|^2 + 2\mathrm{Re}[M_4^0 M_4^{1*}]\,. \tag{6.34}$$

Labeling the 4 partons by $Z \to i,j,k,\ell$, there are two possible antenna-shower histories leading to each 4-parton configuration, with j and k the last emitted parton, respectively. Those two contributions both enter in the definition of the tree-level 4-parton

matching factor,

$$R_4 = \frac{|M_4^0(i,j,k,\ell)|^2}{A_{j/IK}|M_3^0(I,K,\ell)|^2 + A_{k/JL}|M_3^0(i,J,L)|^2} \,, \tag{6.35}$$

such that their sum reproduces the full 4-parton matrix element. Note that a separate such factor is applied to $Z \to qgg\bar{q}$ and $Z \to q\bar{q}'q'\bar{q}$, and that we have suppressed colour and coupling factors here, for compactness (we ignore the small, non-singular extra interference terms for the special case where all four quarks have the same flavour). The antenna functions, A, are understood to include all such factors, as well as any $P_{\rm imp}$ and $P_{\rm ari}$ factors appropriate to the branchings at hand. For a general n-parton matrix element, the denominator contains one term for each possible clustering.

Labeling the $IK \to ijk$ history by A and the $JL \to jk\ell$ one by B, the sum over the two histories yields

$$R_4 \Delta_4(Q_4,0) \sum_{\alpha\in A,B} A^\alpha_{3\to4}|M_3^\alpha|^2 \Delta_2(m_Z^2, Q_3^\alpha)\Delta_3(Q_3^\alpha, Q_4^\alpha) \prod_{m=2}^{3}(1+V_m^\alpha) \,, \tag{6.36}$$

where it is understood that α is an index, not a power, and the last product factor takes into account the NLO matching at the preceding multiplicities. Expanding the Sudakov factors to first order and using the definition of the NLO correction factor at the preceding multiplicity, eq. (6.9), this becomes

$$\begin{aligned} R_4 \left(1 - \sum_k \int_0^{s_k} \mathrm{d}\Phi_{\rm ant} R_5\, A_{4\to5}\right) \sum_{\alpha\in A,B} A^\alpha_{3\to4}|M_3^\alpha|^2 \times \\ \left[1 + \frac{2\mathrm{Re}[M_3^0 M_3^{1*}]^\alpha}{|M_3^\alpha|^2} + \sum_j \int_0^{Q_4^\alpha} \mathrm{d}\Phi_{\rm ant} A^\alpha_{3\to4}\right] \,, \end{aligned} \tag{6.37}$$

which we can rewrite as

$$\begin{aligned} &|M_4|^2 \left(1 - \sum_k \int_0^{s_k} \mathrm{d}\Phi_{\rm ant} R_5\, A_{4\to5}\right) \\ &+ R_4 \sum_{\alpha\in A,B} A^\alpha_{3\to4}|M_3^\alpha|^2 \left(\frac{2\mathrm{Re}[M_3^0 M_3^{1*}]^\alpha}{|M_3^\alpha|^2} + \sum_j \int_0^{Q_4^\alpha} \mathrm{d}\Phi_{\rm ant} A^\alpha_{3\to4}\right) \,, \end{aligned} \tag{6.38}$$

where we again emphasize that the antenna functions are understood to include all relevant coupling, $P_{\rm imp}$, and $P_{\rm ari}$ factors. The first term represents the new subtraction that the shower generates at 4 partons, while the second represents part of the NLO correction to the preceding multiplicity. For one of the histories (the one followed by the "current" event), this correction has already been evaluated and can be reused. The contribution from the other history will have to be recomputed, however. In general, there will be one subtraction to perform at the n-parton level, and there will be $m \sim n - n_{\rm Born} - 1$ new

subtractions that have to be done at the $(n-1)$-parton level, in addition to the one that was already done during the evolution of the current event.

Clearly, there is an undesirable scaling behavior built into this, which will make NLO matching at many partons quite computing intensive. An alternative, which eliminates the sum over histories, is that of sector showers, see e.g., [133, 146].

6.2 Sudakov Integrals

In this section, we work out the standardized Sudakov integrals appearing in the second and third line of eq. (6.10), for each choice of evolution variable. We also study the soft and collinear limits of the Sudakov integrals and compare them to those of the one-loop matrix element. This provides an explicit check of whether the first-order expansion of the Sudakov factors generates the correct logarithms present in the fixed-order calculation.

Given our choice of the GGG antenna functions as our standard ones, the relevant terms are

$$g_s^2 \left[C_A \int_{Q_3^2}^{s} a_3^0 \, \mathrm{d}\Phi_{\mathrm{ant}} - \sum_{j=1}^{2} C_A \int_0^{s_j} (1 - O_{E_j}) \, d_3^0 \, \mathrm{d}\Phi_{\mathrm{ant}} \right. \\ \left. - \sum_{j=1}^{2} 2\, T_R \, n_F P_{A_j} \int_0^{s_j} (1 - O_{S_j}) \, e_3^0 \, \mathrm{d}\Phi_{\mathrm{ant}} \right] \tag{6.39}$$

The general form of the first term, which originates from the $2 \to 3$ branching step, is

$$g_s^2 C_A \int_{Q_3^2}^{s} a_3^0 \, \mathrm{d}\Phi_{\mathrm{ant}} = \frac{\alpha_s C_A}{2\pi} \left(\sum_{i=1}^{5} K_i I_i(s, Q_3^2) \right) \tag{6.40}$$

where the definitions for the K_i and the I_i functions are given in appendix C, for each type of antenna function and ordering variable. Their derivation and soft/collinear structure will be discussed more closely below, for each choice of ordering and evolution variable. The form of the $3 \to 4$ integrals depends on whether we work in the context of strong or smooth ordering. We shall now consider each of those cases in turn, beginning with strong ordering.

6.2.1 Strong Ordering

For strong ordering, the inverted ordering conditions in eq. (6.10), $(1 - O_{E_j/S_j})$, reduce to step functions expressing integration over the unordered region. The integration surface is thus limited from below by the phase-space contour defined by the evolution scale of the first branching, Q^2, and from above by the edge defined by the invariant mass of the antenna.

The expression generated by the $3 \to 4$ splitting case for gluon emission is

$$
\begin{aligned}
&- g_s^2 \sum_{j=1}^{2} C_A \int_0^{s_j} (1 - O_{E_j})\, d_3^0 \,\mathrm{d}\Phi_{\mathrm{ant}} \\
&= -\frac{\alpha_s C_A}{2\pi} \left(\sum_{i=1}^{5} K_i I_i(s_{qg}, Q_3^2) \right) - \frac{\alpha_s C_A}{2\pi} \left(\sum_{i=1}^{5} K_i I_i(s_{g\bar{q}}, Q_3^2) \right). \qquad (6.41)
\end{aligned}
$$

where K_i and I_i are the same as those for the $2 \to 3$ term above, though they here appear with different arguments. The remaining case is the $3 \to 4$ gluon splitting defined by

$$
\begin{aligned}
&- g_s^2 \sum_{j=1}^{2} n_F P_{A_j} \int_0^{s_j} (1 - O_{S_j})\, e_3^0 \,\mathrm{d}\Phi_{\mathrm{ant}} \\
&= -\frac{\alpha_s n_F}{2\pi} P_{A_{q\bar{q}}} H(s_{qg}, Q_3^2) - \frac{\alpha_s n_F}{2\pi} P_{A_{g\bar{q}}} H(s_{g\bar{q}}, Q_3^2). \qquad (6.42)
\end{aligned}
$$

with H defined in appendix C and P_{A_j} as defined in eq. (5.20). We will discuss the derivation of these terms in more detail in the following three sections, for strong m_D-, $p_\perp$, and energy-ordering, respectively.

Dipole Virtuality

We begin with dipole virtuality as evolution variable, which is perhaps the simplest case. We start by repeating the integrals of eq. (6.10) with the one-particle phase space defined as in eq. (5.8). In the case of dipole virtuality the contours are triangular (fig. 5.2a). We recall that, for the $g \to q\bar{q}$ terms, it is the $q\bar{q}$ invariant mass that is used as evolution variable, regardless of what choice is made for gluon emissions. The m_D scale of the previous emission still enters, however, since that defines the ordering scale applied to both emissions and splittings. The explicit forms of the terms in eq. (6.39) are:

$$
\begin{aligned}
&= \frac{\alpha_s}{4\pi} \Bigg[\frac{C_A}{s} \int_{\min(s_{qg}, s_{g\bar{q}})}^{s - \min(s_{qg}, s_{g\bar{q}})} \mathrm{d}s_1 \int_{\min(s_{qg}, s_{g\bar{q}})}^{s - s_1} \mathrm{d}s_2 \; a_3^0(s_1, s_2) \\
&- \left\{ \frac{C_A}{s_{g\bar{q}}} \Theta\left(s_{g\bar{q}} - 2s_{qg}\right) \int_{s_{qg}}^{s_{g\bar{q}} - s_{qg}} \mathrm{d}s_1 \int_{s_{qg}}^{s_{g\bar{q}} - s_1} \mathrm{d}s_2 + \frac{C_A}{s_{qg}} \Theta\left(s_{qg} - 2s_{g\bar{q}}\right) \int_{s_{g\bar{q}}}^{s_{qg} - s_{g\bar{q}}} \mathrm{d}s_1 \int_{s_{g\bar{q}}}^{s_{qg} - s_1} \mathrm{d}s_2 \right\} \\
&\quad \times d_3^0(s_1, s_2) \\
&- \left\{ \frac{n_F}{s_{qg}} \Theta\left(s_{qg} - s_{g\bar{q}}\right) P_{A_1} \int_{s_{qg}}^{s_{qg}} \mathrm{d}s_1 \int_0^{s_{qg} - s_1} \mathrm{d}s_2 + \frac{n_F}{s_{g\bar{q}}} \Theta\left(s_{g\bar{q}} - s_{qg}\right) P_{A_2} \int_{s_{g\bar{q}}}^{s_{g\bar{q}}} \mathrm{d}s_1 \int_0^{s_{g\bar{q}} - s_1} \mathrm{d}s_2 \right\} \\
&\quad \times e_3^0(s_1, s_2) \Bigg], \qquad (6.43)
\end{aligned}
$$

with $P_{A_1} = \frac{2s_{qg}}{s_{qg}+s_{g\bar{q}}}$ and $P_{A_2} = \frac{2s_{g\bar{q}}}{s_{qg}+s_{g\bar{q}}}$ as defined in eq. (5.20) and the gluon-splitting antenna e_3^0 has its singularities in s_1.

For compactness, we only show the integration for the double-pole (soft-collinear eikonal) terms present in both a_3^0 and d_3^0 here, which are the only sources of transcendentality-2 terms. The full antenna integrals, including also the lower-transcendentality terms originating from single poles and finite terms, are given in appendix C. The $T = 2$ part of the a_3^0 integral is

$$\frac{\alpha_s C_A}{4\pi}\left[\int_{\min(s_{qg},s_{g\bar{q}})}^{s-\min(s_{qg},s_{g\bar{q}})} \mathrm{d}s_1 \int_{\min(s_{qg},s_{g\bar{q}})}^{s-s_1} \mathrm{d}s_2 \, \frac{2}{s_1 s_2}\right] . \tag{6.44}$$

To evaluate this expression, we first rewrite it in a dimensionless form in terms of the rescaled integration variables $y_i = s_i/(s - \frac{1}{2}Q_3^2)$, with upper boundary 1 and lower boundary

$$\xi_{\min} = \frac{\min(s_{qg}, s_{g\bar{q}})}{s - \min(s_{qg}, s_{g\bar{q}})} . \tag{6.45}$$

The integration is over a triangular surface. The lower integration boundary cuts off the evolution variable at the value of the 3-parton evolution scale. The other boundary is determined by the total energy of the dipole before branching which here is $\sqrt{s}$. We use the integral

$$\int_x^1 \frac{\mathrm{d}y}{y} \ln\left(\frac{1-y+x}{x}\right) = \ln^2(x) - \ln(x)\ln(1+x) - \mathrm{Li}_2\left(\frac{1}{1+x}\right) + \mathrm{Li}_2\left(\frac{x}{1+x}\right) . \tag{6.46}$$

to obtain

$$\frac{\alpha_s C_A}{2\pi}\left[\ln\left(\frac{s}{\min(s_{qg}, s_{g\bar{q}})}\right)\ln\left(\frac{s-\min(s_{qg}, s_{g\bar{q}})}{\min(s_{qg}, s_{g\bar{q}})}\right) - \mathrm{Li}_2\left(\frac{s-\min(s_{qg}, s_{g\bar{q}})}{s}\right) + \mathrm{Li}_2\left(\frac{\min(s_{qg}, s_{g\bar{q}})}{s}\right)\right] . \tag{6.47}$$

To discuss the $3 \to 4$ Sudakov terms, let us for definiteness assume that we are in a 3-parton phase-space point with $s_{qg} > s_{g\bar{q}}$. The opposite case is symmetric. Again we only include the $T = 2$ terms explicitly here, with the details of the full antenna integrals relegated to appendix C.

$$\frac{\alpha_s C_A}{4\pi}\left[\int_{s_{g\bar{q}}}^{s_{qg}-s_{g\bar{q}}} \mathrm{d}s_1 \int_{s_{g\bar{q}}}^{s_{qg}-s_1} \mathrm{d}s_2 \, \frac{2}{s_1 s_2}\right] . \tag{6.48}$$

The integration is again over a triangular surface. The total energy of the dipole before branching is now $\sqrt{s_{qg}}$. The integral in eq. (6.48) corresponding to the sum over antenna integrals only contains one d_3^0 integral because the other has equal upper and lower integration boundaries. Note that this integral actually vanishes for $s_{qg} \leq Q_3^2$, which amounts to the dipole-virtuality ordering allowing the $3 \to 4$ branchings to populate their full respective phase spaces (i.e. no correction term is necessary).

Focusing on the case $s_{qg} > 2s_{g\bar{q}}$ for which the second integral is nonvanishing (which now amounts to the ordering condition imposing a nontrivial restriction on the $3 \to 4$ phase space, see fig. 5.3a), we obtain, including the $2 \to 3$ term

$$\frac{\alpha_s C_A}{4\pi}\left[\int_{\xi_{\min}}^{1} \mathrm{d}y_1 \int_{\xi_{\min}}^{1-y_1+\xi_{\min}} \mathrm{d}y_2 \, \frac{2}{y_1 y_2} \;-\; \int_{\xi'_{\min}}^{1} \mathrm{d}y'_1 \int_{\xi'_{\min}}^{1-y'_1+\xi'_{\min}} \mathrm{d}y'_2 \, \frac{2}{y'_1 y'_2}\right] \tag{6.49}$$

$y'_i = s_i/(s_{qg} - s_{g\bar{q}})$ and boundaries

$$\xi'_{\min} \;=\; \frac{s_{g\bar{q}}}{s_{qg} - s_{g\bar{q}}}\,. \tag{6.50}$$

with lower-transcendentality terms again available in appendix C. For the mirror case $s_{g\bar{q}} > 2s_{qg}$ essentially symmetric expressions are obtained, while for the intermediate cases in which the two invariants are within a factor 2 of each other, the second integral in eq. (6.49) simply vanishes.

The full double-logarithmic term from the expanded Sudakov terms in eq. (6.43), for strong ordering in dipole virtuality, is then

$$\begin{aligned}
&\frac{\alpha_s C_A}{2\pi}\left[\ln\left(\frac{s}{\frac{1}{2}Q_3^2}\right)\ln\left(\frac{s-\frac{1}{2}Q_3^2}{\frac{1}{2}Q_3^2}\right) - \mathrm{Li}_2\left(\frac{s-\frac{1}{2}Q_3^2}{s}\right) + \mathrm{Li}_2\left(\frac{\frac{1}{2}Q_3^2}{s}\right)\right.\\
&\quad +\Theta\left(s_{\max} - Q_3^2\right)\left(-\ln\left(\frac{s_{\max}}{\frac{1}{2}Q_3^2}\right)\ln\left(\frac{s_{\max}-\frac{1}{2}Q_3^2}{\frac{1}{2}Q_3^2}\right)\right.\\
&\quad\left.\left. +\mathrm{Li}_2\left(\frac{s_{\max}-\frac{1}{2}Q_3^2}{s_{\max}}\right) - \mathrm{Li}_2\left(\frac{\frac{1}{2}Q_3^2}{s_{\max}}\right)\right)\right],
\end{aligned} \tag{6.51}$$

where the Θ function ensures that the second term is only active if

$$s_{\max} = \max(s_{qg}, s_{g\bar{q}}) > 2\min(s_{qg}, s_{g\bar{q}}) = Q_3^2\,, \tag{6.52}$$

so that the expression applies over all of phase space.

We shall now consider the infrared limits of this result, and compare them to those of the one-loop matrix element. For this comparison we keep only terms that involve logarithms of the invariants. The soft limit corresponds to vanishing Q_3^2 ($\xi_{\min} \to 0$). The first line of eq. (6.51) represents the contribution of the $2 \to 3$ expanded Sudakov. To find the contribution in the soft limit, we choose to approach the limit along the diagonal of the phase space triangle. Parametrizing this by $s_{qg}/s = s_{g\bar{q}}/s \to y$ we find for this term

$$\ln^2(y) - \frac{\pi^2}{6}\,.$$

The contributions of the $3 \to 4$ Sudakovs in the soft limit are examined in two separate cases corresponding to the two regions in fig. 5.3a. In the first case given by $s_{\max} < 2s_{\min}$, corresponding to the light grey area in the figure, the step function in eq. (6.51)

yields zero. In the second case given by $s_{\max} > 2s_{\min}$, corresponding to the dark grey area in the figure, the step function is equal to one. The double logs and dilogarithms now yield a finite contribution that does not diverge in the soft limit. We can understand this by parametrizing the soft limit by λ

$$s_{qg} = \lambda s \qquad s_{g\bar{q}} = p\lambda s \qquad s_1' = \lambda\kappa s \qquad s_2' = \lambda\mu s \qquad p > 2\,, \tag{6.53}$$

so that the integral becomes

$$\int_{s_{\min}}^{s_{\max}-s_{\min}} \mathrm{d}s_1 \int_{s_{\min}}^{s_{\max}-s_1} \mathrm{d}s_2 \frac{1}{s_1 s_2} \to \int_1^{p-1} \mathrm{d}\kappa \int_1^{p-\kappa} \mathrm{d}\mu \frac{1}{\kappa\mu}\,. \tag{6.54}$$

This implies that the integration variable scales with the integration limits and is independent of the soft limit. We can also expect this behaviour from examing fig. 5.2a. The shape of the different regions does not change for different values of Q_3^2, in contrast with the case of transverse momentum, as we will see below.

After the poles cancel in eq. (6.32), the pole-subtracted version of the one-loop matrix element, SVirtual , defined in eq. (6.33), contains all the relevant terms on the matrix-element side. The transcendentality-2 terms of SVirtual are given by

$$-R(y_1, y_2) = \mathrm{Li}_2\,(y_1) + \mathrm{Li}_2\,(y_2) - \frac{\pi^2}{6} - \ln y_1 \ln y_2 + \ln y_1 \ln(1-y_1) + \ln y_2 \ln(1-y_2)\,. \tag{6.55}$$

Including the transcendentality-1 terms (see appendix B), taking the soft limit by sending $s_{qg}/s = s_{g\bar{q}}/s = y \to 0$, and keeping only logarithmic terms, the pole-subtracted matrix element (ME) reduces to

$$\text{ME:} \qquad s_{qg}/s = s_{g\bar{q}}/s = y \to 0 \qquad \frac{\alpha_s C_A}{2\pi}\left[-\ln^2(y) - \frac{10}{3}\ln(y)\right] + \frac{\alpha_s n_F}{6\pi}\ln(y), \tag{6.56}$$

The single log proportional to C_A originates from the renormalization term and the single log of the closed quark loops (proportional to n_F) arises due to the definition of the infrared singularity operator, defined in the appendix in eq. (A.3).

Taking the same limit of the Sudakov integrals for dipole virtuality eq. (6.43), but omitting for the time being the renormalization term, $V_{3\mu}$, we find for the parton shower (PS),

$$-\text{PS:} \qquad s_{qg}/s = s_{g\bar{q}}/s = y \to 0 \qquad \frac{\alpha_s C_A}{2\pi}\left[\ln^2 y + \frac{3}{2}\ln(y)\right]\,. \tag{6.57}$$

We see that the soft limit almost cancels against eq. (6.56). For an NLL-accurate shower, however, all divergent terms should match precisely, leaving at most a finite remainder in the final matching correction, eq. (6.32). In the expressions above, this holds for the $\ln^2(y)$ term but not for the single logarithms (different coefficient). Interestingly, the remainder is proportional to the QCD β function, specifically

$$\mathrm{ME} - \mathrm{PS} \;\to\; -\frac{\alpha_s}{2\pi}\frac{1}{2}\beta_0 \ln(y)\,. \tag{6.58}$$

It can therefore be absorbed in the choice of renormalization scale by solving for $\mu_{\rm PS}$ in $V_{3\mu}$, which yields:

$$\mu^2_{\rm PS} \;\propto\; y\,s\,. \tag{6.59}$$

This tells us that, in the soft limit, the specific choice of a renormalization scale that is linear in the branching invariants will absorb all logarithms up to and including $\alpha_s^2 \ln(y)$. Interestingly, this reasoning would rule out $\mu_R^2 \propto p_\perp^2$, since our $p_\perp$-definition is quadratic in the invariants, $p_\perp^2 = s_{ij}s_{jk}/s$. A better choice of renormalization scale would appear to be $\mu_R \propto m_D$, specifically

$$\mu^2_{\rm PS} \;=\; \min(s_{ij}, s_{jk}) \;=\; \frac{1}{2}m_D^2\,. \tag{6.60}$$

Taken at face value, this seems to contradict the standard literature [128] on $p_\perp$ as the optimal universal renormalization-scale choice. However, as we shall see below in fig. 6.2, there is in fact no choice of renormalization scale that absorbs *all* logarithms for this particular evolution variable; the choice $\mu_R \propto m_D$ merely manages to reabsorb the additional logarithms that are generated by the ordering condition as $y \to 0$, but leftover logs in other parts of phase space will remain uncanceled, ruining the NLL precision. In that sense, choosing $\mu_R \propto p_\perp$ would simply leave a different set of uncanceled logs, nonvanishing as $y \to 0$.

Before we show the results over all of phase space however, we first investigate a complementary interesting limit, the hard-collinear one, which is characterized by one of the invariants becoming maximal while the other vanishes. In this limit, the pole-subtracted one-loop matrix element, SVirtual , becomes

$$\text{ME:} \qquad s_{qg}/s \to 1,\; s_{g\bar{q}}/s = y \to 0 \qquad \frac{\alpha_s}{2\pi}\left[-\frac{5}{3}C_A + \frac{1}{6}n_F\right]\ln(y) \tag{6.61}$$

There are no log-squared terms in this limit, and both of the single-log terms are half as large here as they were in the soft limit.

The Sudakov integrals for m_D-ordering yield one divergent term, $-\frac{1}{6}C_A\ln(y)$, in the hard-collinear region, modulo a factor $\alpha_s/(2\pi)$. The Sudakov integral for gluon splitting in the neighbouring antenna, represented by the first term on the second-to-last line of eq. (6.32) is specified in the last line of eq. (6.43). The step function is only non-zero for the first term in the hard-collinear limit $s_{qg} \to s, s_{g\bar{q}} \to 0$ and produces a term $\frac{1}{6}P_{A_j}n_F\ln(y)$. The numerator of the corresponding Ariadne factor contains the invariant of the neighboring dipole $s_{g\bar{q}}$ which vanishes in this limit and causes the dipole splitting contribution to reduce to zero. The n_F-dependent contribution is instead shifted to the last term of eq. (6.32), which has the same limit but without the Ariadne pre-factor. The hard-collinear limit of the shower terms, including only terms involving logarithms of the invariants and not including the $V_{3\mu}$ term, is therefore

$$-\text{PS:} \qquad s_{qg}/s \to 1,\; s_{g\bar{q}}/s = y \to 0 \qquad \frac{\alpha_s}{2\pi}\left[-\frac{1}{6}C_A + \frac{1}{6}n_F\right]\ln(y)\,. \tag{6.62}$$

Again, the combination $(\mathrm{ME} - \mathrm{PS})$ relevant for computing the correction factor is proportional to the QCD β function, and in fact has exactly the same form as eq. (6.58). The conclusion is therefore that, also in this limit, all logarithms through $\alpha_s^2 \ln(y)$ can be absorbed by choosing a renormalization scale which is linear in the vanishing invariant. The particular choice which is linear in both the soft and collinear limits is $\mu_{\mathrm{PS}} \propto m_D$. To illustrate this, we show the full NLO $Z \to 3\,\mathrm{jets}$ correction factors, $(1 + V_{3Z})$, for m_D-ordering with a few different choices of renormalization scale and scheme, in fig. 6.2. Note that the axes are logarithmic, in $\ln(y_{ij}) = \ln(s_{ij}/s)$, to make the infrared limits

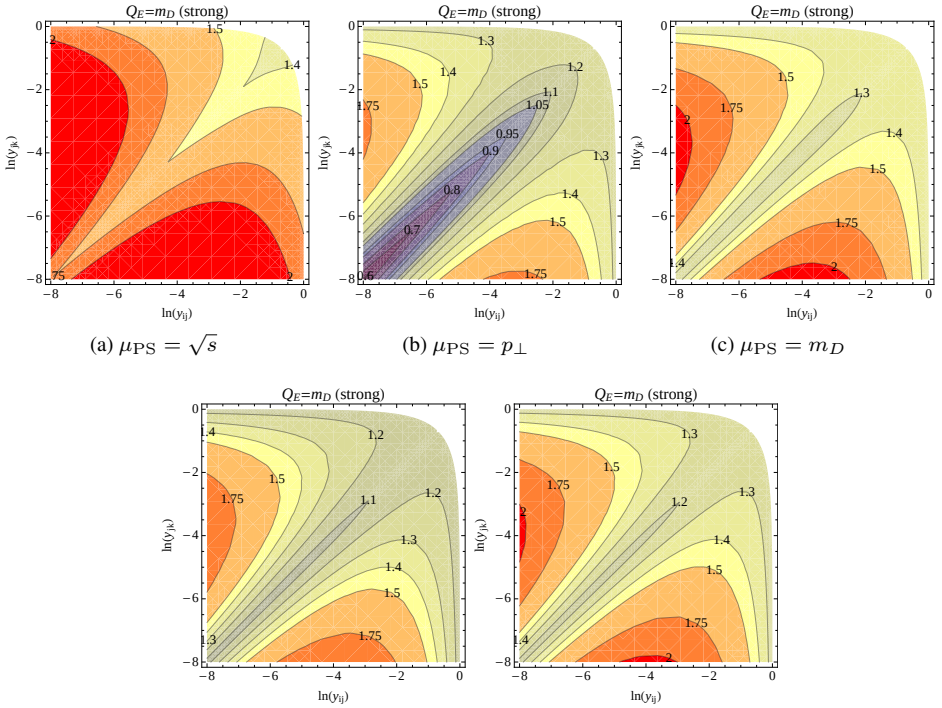

(a) $\mu_{\mathrm{PS}} = \sqrt{s}$ (b) $\mu_{\mathrm{PS}} = p_\perp$ (c) $\mu_{\mathrm{PS}} = m_D$

(d) $\mu_{\mathrm{PS}} = \frac{1}{2} m_D$, with CMW (e) $\mu_{\mathrm{PS}} = m_D$, with CMW

Figure 6.2: NLO correction factor for strong m_D-ordering, with GGG antennae. *Top row:* $\mu_R = \sqrt{s}$ (left), $\mu_R = p_\perp$ (middle), and $\mu_R = m_D$ (right). *Bottom row:* using the CMW Λ_{MC}, with $\mu_R = \frac{1}{2} m_D$ (left) and $\mu_R = m_D$ (right). For all plots, $\alpha_s = 0.12$, $n_F = 5$, and gluon splittings were evolved in m_{qq}.

clearly visible.

Without the $V_{3\mu}$ term, the correction factor looks as depicted in the top left-hand plot in fig. 6.2. The increasing contours towards the axes indicate uncanceled logarithms in the correction factor. The middle pane shows the correction factor derived for $\mu_{\mathrm{PS}} = p_\perp$. As discussed above, there is an uncanceled logarithm in the soft limit (lower left-hand corner of the plot), since $p_\perp$ is quadratic in the vanishing invariants there. However, in

the hard-collinear limits (upper left-hand and lower right-hand corners), $p_\perp$ is linear in the vanishing invariant, and hence the contours remain bounded there. In the right-hand pane, we show the choice $\mu_{\rm PS} = m_D$, which can be seen to lead to bounded correction factors (below ~ 1.3) in all three phase-space corners. Nonetheless, there is still an uncanceled divergence *between* the soft and hard collinear limits. We shall see in the section on $p_\perp$-ordering below that the cure for this is basically to choose a better evolution variable.

In the bottom row of fig. 6.2, we show a few variations on $\mu_{\rm PS} = m_D$, specifically we include the CMW rescaling of $\Lambda_{\rm QCD}$, as defined by eq. (6.30), and show how a variation of the renormalization scale by a factor of 2 affects the correction factor. In the left-hand pane, we show $\mu_{\rm PS} = \frac{1}{2}m_D$ and in the right-hand one $\mu_{\rm PS} = m_D$. Of these, the choice $\mu_{\rm PS} = \frac{1}{2}m_D$, with CMW rescaling, leads to the smallest correction factors (best LO behaviour), and this could therefore be taken as a useful default for m_D-ordering, e.g. for uncertainty estimates.

Transverse Momentum

For a shower ordered in $p_\perp$, the antenna phase-space integrals in eq. (6.10) are performed over contours such as those depicted in fig. 5.2e. The curved contours motivate a coordinate transformation from (s_1, s_2) to a basis defined as the dimensionless evolution variable $y = \frac{Q^2}{s} = \frac{4s_1s_2}{s^2}$, complemented by an energy-sharing variable, which we define as $z = \frac{s_1}{s}$. Note that the coordinate transformation depends explicitly on the total invariant mass s of the $2 \to 3$ dipole. For the $3 \to 4$ integrations, the invariant mass s is replaced by the invariant mass of the appropriate dipole (either s_{qg} or $s_{g\bar{q}}$). The integration boundaries in z are determined by the intersection of the invariant mass of the dipole with the evolution parameter Q^2. The choice of y and its integration boundaries make the effect of strong ordering especially clear since we see integration from Q^2 to the total invariant mass of the dipole (the unordered region). As before, the integration over the gluon-splitting antenna $\left(e_3^0\right)$ makes use of a different phase space integration, in $m_{q\bar{q}}$, and only uses the evolution parameter as a cut-off in the singularity of the corresponding dipole.

The contributing terms are:

$$
\begin{aligned}
g_s^2 \Bigg[& C_A \int_{Q_3^2}^{s} a_3^0 \,\mathrm{d}\Phi_{\mathrm{ant}} - \sum_{j=1}^{2} C_A \int_0^{s_j} (1 - O_{E_j})\, d_3^0 \,\mathrm{d}\Phi_{\mathrm{ant}} \\
& \qquad - \sum_{j=1}^{2} 2\, T_R\, n_F P_{A_j} \int_0^{s_j} (1 - O_{S_j})\, e_3^0 \,\mathrm{d}\Phi_{\mathrm{ant}} \Bigg] \\
= \frac{\alpha_s}{4\pi} & \left[C_A\, s\, \mathcal{A}_1 \left[\frac{Q_3^2}{s}, 1 \right] - C_A s_{qg}\, \mathcal{A}_2 \left[\frac{4 s_{g\bar{q}}}{s}, \max\left(\frac{4 s_{g\bar{q}}}{s}, 1 \right) \right] \right. \\
& \qquad \left. - s_{g\bar{q}}\, C_A\, \mathcal{A}_3 \left[\frac{4 s_{qg}}{s}, \max\left(\frac{4 s_{qg}}{s}, 1 \right) \right] \right] \\
- n_F & \left(\frac{P_{A_1}}{s_{qg}} \int_{Q_3^2}^{\max\left(Q_3^2, s_{qg}\right)} \mathrm{d}s_1 \int_0^{s_{qg} - s_1} \mathrm{d}s_2 e_3^0(s_1, s_2) \right. \\
& \qquad \left. + \frac{P_{A_2}}{s_{g\bar{q}}} \int_{Q_3^2}^{\max\left(Q_3^2, s_{g\bar{q}}\right)} \mathrm{d}s_1 \int_0^{s_{g\bar{q}} - s_1} \mathrm{d}s_2 e_3^0(s_1, s_2) \right) \Bigg]
\end{aligned}
\tag{6.63}
$$

with

$$
\mathcal{A}_n\,[a,b] = \int_a^b \mathrm{d}y_n \int_{z_{\min}^n}^{z_{\max}^n} \mathrm{d}z_n\, |\mathcal{J}_n| A_n(y_n, z_n) \qquad \text{for } n = 1, 2, 3, \tag{6.64}
$$

and

$$
y_n = 4 \frac{s_1 s_2}{m_{IK}^4},\ z_n = \frac{s_1}{m_{IK}^2},\ |\mathcal{J}_1| = \frac{m_{IK}^4}{4 z_n},\ z_{\substack{\max \\ \min}}^n = \frac{1}{2} \left(1 \pm \sqrt{1 - y_n} \right). \tag{6.65}
$$

For $n = 1$ we set $m_{IK}^2 = s$, for $n = 2$ $m_{IK}^2 = s_{qg}$ and for $n = 3$ $m_{IK}^2 = s_{g\bar{q}}$. The Ariadne factor P_{A_j} is defined in eq. (5.20). The $\max$ condition on the outer integration boundary of $\mathcal{A}_2$ and $\mathcal{A}_3$ reflect that the correction term disappears if the generated Q_3^2 is larger than the invariant mass of the dipole. As for m_D-ordering, we here work out the most divergent behavior explicitly, by focussing on the double log terms arising from the eikonal term in the antenna, and relegate the full form of the antenna integrals to appendix C. The double poles give rise to terms

$$
\frac{\alpha_s\, C_A}{2\pi} \int_{\frac{Q_3^2}{s}}^{1} \mathrm{d}y_1 \int_{z_{\min}}^{z_{\max}} \mathrm{d}z_1\, \frac{1}{y_1 z_1}\,,
$$

which lead to the following generic transcendentality-2 integrals,

$$
\begin{aligned}
\int_x^1 \frac{\mathrm{d}y_1}{y_1} \ln\left(\frac{1 + \sqrt{1 - y_1}}{1 - \sqrt{1 - y_1}} \right) \;=\; & \mathrm{Li}_2\left(\frac{1}{2} \left(1 - \sqrt{1 - x} \right) \right) - \mathrm{Li}_2\left(\frac{1}{2} \left(1 + \sqrt{1 - x} \right) \right) \\
& + \frac{1}{2} \ln\left(\frac{x}{4} \right) \ln\left[- \left(\frac{-2 + 2\sqrt{1 - x} + x}{x} \right) \right].
\end{aligned}
\tag{6.66}
$$

The double logarithm in the shower expansion is generated by a combination of the $2 \to 3$ and $3 \to 4$ Sudakov integrals, with the respective pieces adding up to

$$\frac{\alpha_s C_A}{2\pi}\left[-\frac{\pi^2}{6}+\frac{1}{2}\ln\left(\frac{s_{qg}s_{g\bar{q}}}{s^2}\right)^2+\frac{\pi^2}{3}-\frac{1}{2}\ln\left(\frac{s_{qg}}{s}\right)^2-\frac{1}{2}\ln\left(\frac{s_{g\bar{q}}}{s}\right)^2\right]. \tag{6.67}$$

We see that a partial cancellation arises between the first two terms (which come from the $2 \to 3$ Sudakov expansion) and the last three (which come from the $3 \to 4$ expansion). What remains is a log squared in both invariants $\ln(s_{qg}/s)\ln(s_{g\bar{q}}/s)$.

At the single-log level, the $3 \to 4$ terms give a numerically larger coefficient than the $2 \to 3$ ones, leading to a single log remainder. The gluon-splitting term also reduces to a single log. The overall result in the soft limit is then

$$-\text{ PS:} \qquad s_{qg} = s_{g\bar{q}} = y \to 0 \qquad \frac{\alpha_s C_A}{2\pi}\left[\ln^2(y)-\frac{1}{3}\ln(y)\right]+\frac{\alpha_s n_F}{6\pi}\ln(y) \tag{6.68}$$

Comparing with the result of the virtual correction in the soft limit, eq. (6.56), we see that the shower generates the double log terms correctly, and, similarly to the case of m_D-ordering, there is a single-log remainder which is proportional to the QCD β function. However, for $p_\perp$-ordering the constant of proportionality is 1, rather than $\frac{1}{2}$, a difference which translates to the optimal renormalization-scale choice being quadratic in the invariants in this case, rather than linear. Before commenting further on this difference, let us first consider the complementary, hard-collinear, limit.

In the hard-collinear limit, we find the same as for m_D-ordering,

$$-\text{PS:} \qquad s_{qg} = y \to 0, s_{g\bar{q}} \to s \qquad \frac{\alpha_s}{2\pi}\left[-\frac{1}{6}C_A+\frac{1}{6}n_F\right]\ln(y)\,. \tag{6.69}$$

Double logs (eikonal parts of the antenna) also appear at both the $2 \to 3$ and $3 \to 4$ levels, but cancel among each other as almost all other antenna terms do; what remains at the single-log level is the integrated difference between a quark-antiquark antenna and a quark-gluon antenna, plus the n_F-dependent 'Ariadne Log'. The only contributing Sudakov gluon splitting contribution is the second term in the last line of eq. (6.63). Integration over the $s_{g\bar{q}}$ dipole, however, is associated with an Ariadne factor carrying s_{qg} in the numerator and therefore reduces to zero. As before, we can write the remainder as half the QCD β function, which implies that a renormalization scale linear in the vanishing invariants can absorb the logarithm.

To summarize, for $p_\perp$-ordering we find that the optimal renormalization-scale choice must be quadratic in the vanishing invariants in the soft limit and linear in the hard-collinear limit. Those conditions are fulfilled by $p_\perp$ itself, thus

$$\mu^2_{\text{PS}} \propto p^2_\perp = \frac{s_{ij}s_{jk}}{s_{ijk}} \tag{6.70}$$

absorbs all logarithmic terms up to and including $\alpha_s^2\ln(y)$ in the LO couplings.

Illustrations of the full NLO correction factors, $(1+V_{3Z})$, are given in fig. 6.3. The

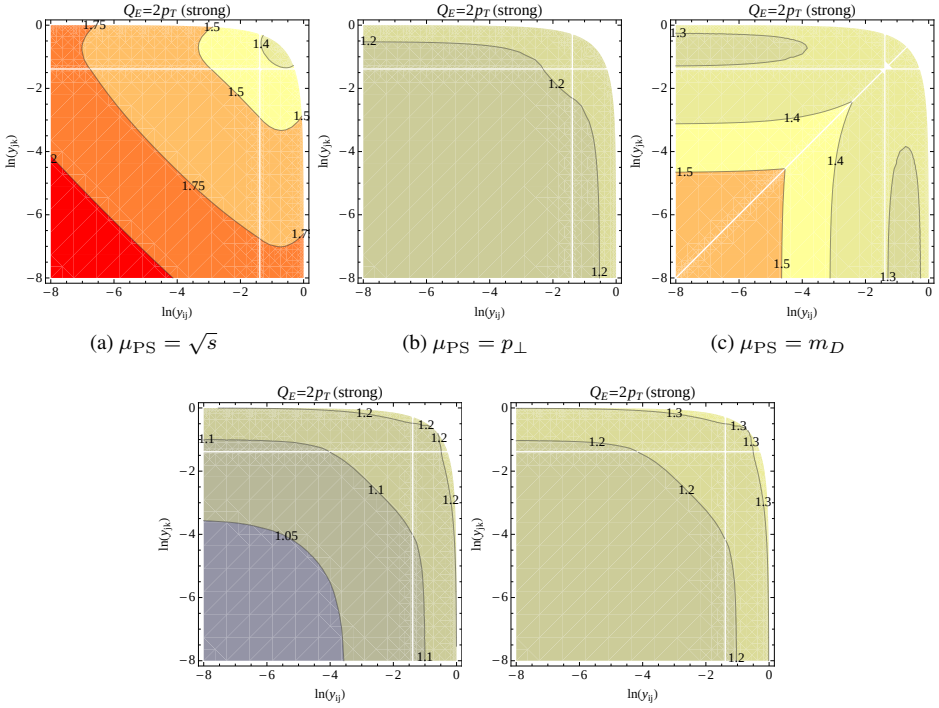

(a) $\mu_{\rm PS} = \sqrt{s}$ (b) $\mu_{\rm PS} = p_\perp$ (c) $\mu_{\rm PS} = m_D$

(d) $\mu_{\rm PS} = p_\perp$, with CMW (e) $\mu_{\rm PS} = 2p_\perp$, with CMW

Figure 6.3: NLO correction factor for strong $p_\perp$-ordering, with GGG antennae. *Top row:* $\mu_{\rm PS} = \sqrt{s}$ (left), $\mu_{\rm PS} = p_\perp$ (middle), and $\mu_{\rm PS} = m_D$ (right). *Bottom row:* using the CMW $\Lambda_{\rm MC}$, with $\mu_{\rm PS} = p_\perp$ (left) and $\mu_{\rm PS} = 2p_\perp$ (right). For all plots, $\alpha_s = 0.12$, $n_F = 5$, and gluon splittings were evolved in m_{qq}.

ordering of the plots in the top row are the same as in fig. 6.3, showing, from left to right, $\mu_{\rm PS} = \sqrt{s}$, $\mu_{\rm PS} = p_\perp$, $\mu_{\rm PS} = m_D$. Similarly to the case of strong m_D-ordering, both of the latter two choices exhibit no logarithmic divergences in the hard-collinear regions (top left and bottom right corners of the plots), but in the soft region (bottom left corner) it is here $\mu_{\rm PS} = p_\perp$ which leaves the correction factor free of logarithms. Indeed, we see that the combination of evolution and renormalization in $p_\perp$ leads to a rather flat correction factor over all of phase space, showing that this combination is indeed "better" than m_D-ordering.

In the bottom row of plots in fig. 6.3, we include the CMW factor and show the correction factors for $\mu_{\rm PS} = p_\perp$ (left) and $\mu_{\rm PS} = 2p_\perp$ (right). In particular on the left-hand pane, the NLO correction factor is essentially unity in the soft limit, while the corrections in the hard-collinear regions remain less than $\sim 20\%$. This gives some additional weight to the arguments for $p_\perp$-ordered showers with $p_\perp$ as renormalization scale being the best default choice for strongly ordered dipole-antenna showers. It also provides some ratio-

nale why one typically finds a rather large value of $\alpha_s(m_Z) \sim 0.13$ (with CMW rescaling, or $\alpha_s(m_Z) \sim 0.14$ without it) when tuning such models to LEP event shapes; there is still a genuine order 20% NLO correction in the hard resolved region (upper right-hand corner). We return to this in more detail in the context of full LO + NLO matching in section 6.3.

Energy

To put the differences between m_D and $p_\perp$ in context, we now briefly examine the case of energy ordering, which is known to produce the wrong DGLAP evolution in the collinear limit [144, 147, 148], and hence we should find larger (possibly divergent) NLO corrections.

Slicing phase space with the energy variable $Q_3^2 = s_{ijk}(y_{ij} + y_{jk})^2$, see fig. 5.2f, requires the use of an explicit infrared cut-off because the contours otherwise allow for the invariants to hit singular regions for every value of the contour. We will here use a cut-off in transverse momentum (a cut-off in dipole virtuality is also possible). The cutoff motivates us to switch to a different choice of integration variables. Therefore integration is transformed from (s_1, s_2) to the dimensionless evolution parameters $y_E^2 = \frac{Q^2}{s} = \frac{(s_1+s_2)^2}{m_{IK}^2}$ and completed with the energy sharing variable $\zeta = \frac{s_2}{m_{IK}^2}$. The interesting integrals arising from expanding the Sudakov form factor then are

$$
\begin{aligned}
& g_s^2 \left[C_A \int_{Q_3^2}^{s} a_3^0 \,\mathrm{d}\Phi_{\mathrm{ant}} - \sum_{j=1}^{2} C_A \int_0^{s_j} (1 - O_{E_j})\, d_3^0 \,\mathrm{d}\Phi_{\mathrm{ant}} \right. \\
& \left. - \sum_{j=1}^{2} 2\, T_R\, n_F P_{A_j} \int_0^{s_j} (1 - O_{S_j})\, e_3^0 \,\mathrm{d}\Phi_{\mathrm{ant}} \right] \\
& = \frac{\alpha_s}{4\pi} \left[C_A \left\{ \mathcal{AE}_1(s,1) - \mathcal{AE}_2(\min[s_{qg},1],1) - \mathcal{AE}_3(\min[s_{g\bar{q}},1],1) \right\} \right. \\
& \qquad - n_F \left(\frac{P_{A_{qg}}}{s_{qg}} \int_{Q_3^2}^{\max(Q_3^2, s_{qg})} \mathrm{d}s_1 \int_0^{s_{qg}-s_1} \mathrm{d}s_2 e_3^0(s_1, s_2) \right. \\
& \left. \left. + \frac{P_{A_{g\bar{q}}}}{s_{g\bar{q}}} \int_{Q_3^2}^{\max(Q_3^2, s_{g\bar{q}})} \mathrm{d}s_1 \int_0^{s_{g\bar{q}}-s_1} \mathrm{d}s_2 e_3^0(s_1, s_2) \right) \right]
\end{aligned}
\tag{6.71}
$$

with

$$
\mathcal{AE}_n(m_{IK}^2, 1) = \int_{\frac{Q_3^2}{m_{IK}^2}}^{1} \mathrm{d}y_E^2 \int_0^1 \mathrm{d}\zeta' \frac{1}{2} \mathcal{AE}_n^0(y_E^2, \zeta').
$$

With $\mathcal{AE}_1^0 = a_3^0$, $\mathcal{AE}_2^0 = d_3^0$ and $\mathcal{AE}_3^0 = e_3^0$. The inner integral has been rescaled to make it independent of the outer integral with $\zeta = y_E \zeta'$. To establish the cut-off, we use the relation $4\frac{s_1 s_2}{s^2} = 4p_\perp^2/s$, which we demand to be larger than the cut-off Δ. In terms of

our variables we then have the condition

$$4\zeta'(1-\zeta') > \frac{\Delta}{y_E^2}. \tag{6.72}$$

The upper and lower limits on ζ' are then

$$\zeta'_- < \zeta' < \zeta'_+, \quad \zeta'_\pm = \frac{1}{2}\left(1 \pm \sqrt{1-\frac{\Delta}{y_E^2}}\right). \tag{6.73}$$

Focussing on the eikonal integral

$$\frac{\alpha_s C_A}{4\pi}\int_{y_E^2=\frac{Q_3^2}{s}}^{1}\frac{dy_E^2}{y_E^2}\int_{\zeta'_-}^{\zeta'_+}\frac{\mathrm{d}\zeta'}{\zeta'}, \tag{6.74}$$

the result for this integral is

$$\begin{aligned}
&\frac{\alpha_s}{2\pi}\left[\mathrm{Li}_2\left(\frac{1}{2}\left(1-\sqrt{1-\Delta}\right)\right)-\mathrm{Li}_2\left(\frac{1}{2}\left(1+\sqrt{1-\Delta}\right)\right)+\frac{1}{2}\left[-2\,\mathrm{atanh}\left(\sqrt{1-\frac{\Delta}{y_E^2}}\right)\right.\right.\\
&\times\ln(4)+\mathrm{atanh}\left(\sqrt{1-\Delta}\right)\ln(16)+\ln^2\left(1-\sqrt{1-\Delta}\right)-\ln^2\left(1+\sqrt{1-\Delta}\right)\\
&-\ln^2\left(1-\sqrt{1-\frac{\Delta}{y_E^2}}\right)+\ln^2\left(1+\sqrt{1-\frac{\Delta}{y_E^2}}\right)\Bigg]-2\mathrm{Li}_2\left(\frac{1}{2}\left(1-\sqrt{1-\frac{\Delta}{y_E^2}}\right)\right)\\
&\left.+\mathrm{Li}_2\left(\frac{1}{2}\left(1+\sqrt{1-\frac{\Delta}{y_E^2}}\right)\right)\right].
\end{aligned} \tag{6.75}$$

In the soft limit $y_E^2 = 4y^2 \to 0$ this reduces to

$$-\frac{1}{2}\ln^2(\Delta)-\ln^2\left(\frac{\Delta}{4y^2}\right)-2\ln(4y^4)\ln(2)-\mathrm{Li}_2\left(\frac{\Delta}{64y^2}\right) \tag{6.76}$$

Thus we see that there are explicit non-cancelling double-logarithmic terms that involve the hadronization cutoff, Δ. Depending on the ratio between the dipole mass and the cutoff, these would lead to asymptotically divergent correction factors.

One might wonder whether using a linearized form of energy ordering would make a difference, see fig. 5.2c. Rather than go through the derivations again, we merely show the full NLO corrections in fig. 6.4, for both linear (top row) and squared (bottom row) energy ordering, for an (arbitrary) dimensionless cutoff value of $\Delta = 10^{-7}$.

From left to right in both rows, we show the three renormalization-scale choices, $\mu_{\mathrm{PS}} = p_\perp$ (left), $\mu_{\mathrm{PS}} = m_D$ (middle), and $\mu_{\mathrm{PS}} = Q_E$ (right), with the latter equal to linear energy in the top row and squared energy in the bottom one. Interestingly, the contours in the linear case are increasing towards the soft region, while they ultimately decrease in the squared case. It is clear, however, that no intelligent choice of renormalization scale

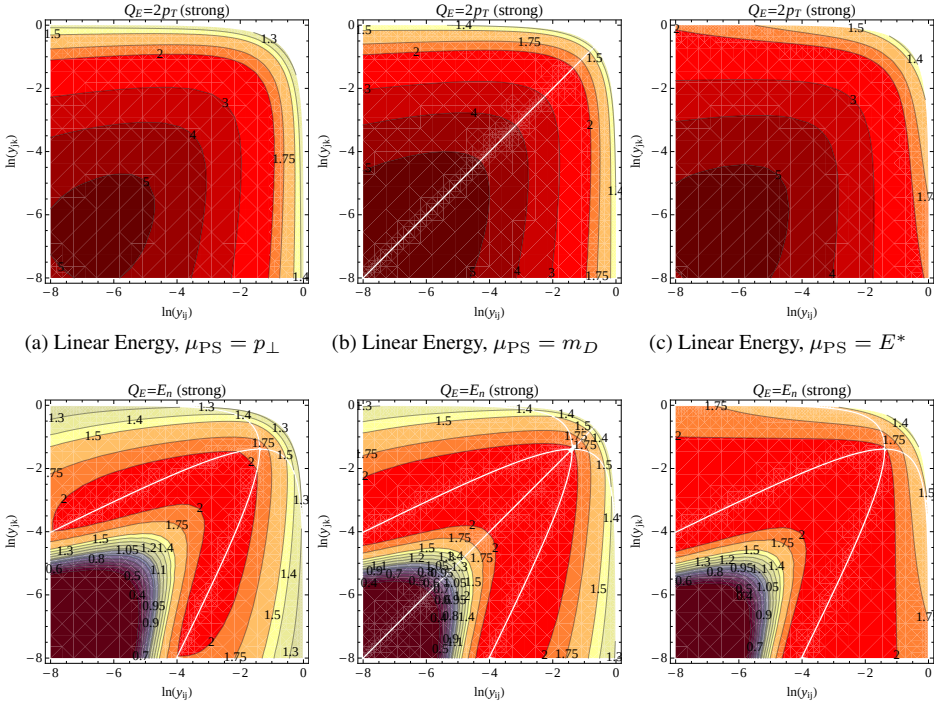

(a) Linear Energy, $\mu_{\rm PS} = p_\perp$ (b) Linear Energy, $\mu_{\rm PS} = m_D$ (c) Linear Energy, $\mu_{\rm PS} = E^*$

(d) Squared Energy, $\mu_{\rm PS} = p_\perp$ (e) Squared Energy, $\mu_{\rm PS} = m_D$ (f) Squared Energy, $\mu_{\rm PS} = E^{*2}/\sqrt{s}$

Figure 6.4: NLO correction factor for strong energy-ordering, with GGG antennae, for various renormalization-scale choices and linear (top row) and squared (bottom row) scaling of the evolution variable with gluon energy.

can absorb the infrared divergences. Moreover, any other choice of Δ would have led to different contours, due to the explicit $\ln(\Delta)$ terms, hence even if a "least bad" choice was found, it would not be universal.

As mentioned above, the main point of showing these comparisons is to place the comparison between m_D and $p_\perp$ in the previous subsections in perspective. Thus, while we saw that $p_\perp$ was generating a better-behaved correction factor than m_D, the one for m_D is still far better behaved than is the case for energy ordering. From this perspective, we still believe it could make sense, e.g., to use m_D-ordering, with the NLO correction factor included, as a conservative uncertainty variation for a central prediction based on $p_\perp$-ordering.

6.2.2 Smooth Ordering

We will now discuss the same Sudakov integrals as in the previous subsections but for the case of smooth ordering (section 5.1.4). This is especially interesting given that smooth ordering is the way VINCIA is able to fill all of phase space without significant under- or overcounting at the LO level [110]. As discussed in section 5.1.4, however, this does involve some ambiguity in what Sudakov factors are associated with the unordered points, and the NLO 3-jet correction factors should tell us explicitly whether this ambiguity generates problems at this level.

The Sudakov integrations are actually more straightforward for smooth ordering than was the case for strong ordering, since the $P_{\rm imp}$ factor regulates the integrands on the boundaries. Therefore the integrations always run over the full phase space of the system. The $2 \to 3$ splitting generates the same terms as in the strong-ordering case, eq. (6.40). Including also the $3 \to 4$ terms, the expanded Sudakov generates the following antenna integrals,

$$g_s^2 \left[C_A \int_0^s a_3^0 \, \mathrm{d}\Phi_{\rm ant} - \sum_{j=1}^{2} C_A \int_0^{s_j} \frac{Q_{E_j}^2}{Q_{E_j}^2 + Q_3^2} \, d_3^0 \, \mathrm{d}\Phi_{\rm ant} \right. \\ \left. - \sum_{j=1}^{2} 2\, T_R \, n_F P_{A_j} \int_0^{s_j} \frac{m_{q\bar{q}}^2}{m_{q\bar{q}}^2 + Q_3^2} \, e_3^0 \, \mathrm{d}\Phi_{\rm ant} \right] , \tag{6.77}$$

where Q_3 is the evolution scale evaluated on the 3-parton configuration and Q_{E_j} ($m_{q\bar{q}}$) is the scale of the $3 \to 4$ emissions (splittings) being integrated over. The full answer for the $3 \to 4$ case for gluon emission is

$$- g_s^2 \sum_{j=1}^{2} C_A \int_0^{s_j} \frac{Q_{E_j}^2}{Q_{E_j}^2 + Q_3^2} \, d_3^0 \, \mathrm{d}\Phi_{\rm ant} \\ = -\frac{\alpha_s C_A}{4\pi} \left(\sum_{i=1}^{5} K_i L_i(s_{qg}, Q_3^2) \right) - \frac{\alpha_s C_A}{4\pi} \left(\sum_{i=1}^{5} K_i L_i(s_{g\bar{q}}, Q_3^2) \right) . \tag{6.78}$$

where K_i and L_i can be found in appendix C. The full answer for the $3 \to 4$ case for gluon splitting is

$$- g_s^2 \sum_{j=1}^{2} n_F P_{A_j} \int_0^{s_j} \frac{m_{q\bar{q}}^2}{m_{q\bar{q}}^2 + Q_3^2} \, e_3^0 \, \mathrm{d}\Phi_{\rm ant} \\ = -\frac{\alpha_s n_F}{4\pi} G(s_{qg}, Q_3^2) \; - \frac{\alpha_s n_F}{4\pi} G(s_{g\bar{q}}, Q_3^2). \tag{6.79}$$

where G can be found in the appendix. We will discuss the derivation of these terms in more detail in the following two subsections, for smooth m_D- and $p_\perp$-ordering, respectively.

Dipole Virtuality

Since the $2 \to 3$ emission terms remain the same as in the case of strong m_D-ordering, we only need to rederive the $3 \to 4$ contributions to V_{3Z}, which are

$$
\begin{aligned}
&- g_s^2 \left[\sum_{j=1}^{2} C_A \int_0^{s_j} (1 - O_{Ej})\; d_3^0 \, \mathrm{d}\Phi_{\mathrm{ant}} + \sum_{j=1}^{2} 2\, T_R\, n_F P_{A_j} \int_0^{s_j} (1 - O_{Sj})\; e_3^0 \, \mathrm{d}\Phi_{\mathrm{ant}} \right] \\
&= -\frac{\alpha_s}{4\pi} \left[\frac{C_A}{s_{qg}} \left(\int_0^{\frac{1}{2}s_{qg}} \mathrm{d}s_2 \int_{s_2}^{s_{qg}-s_2} \mathrm{d}s_1\, O_{E1} + \int_0^{\frac{1}{2}s_{qg}} \mathrm{d}s_1 \int_{s_1}^{s_{qg}-s_1} \mathrm{d}s_2\, O_{E2} \right) d_3^0 \right. \\
&\qquad + \frac{C_A}{s_{g\bar{q}}} \left(\int_0^{\frac{1}{2}s_{g\bar{q}}} \mathrm{d}s_2 \int_{s_2}^{s_{g\bar{q}}-s_2} \mathrm{d}s_1\, O_{E1} + \int_0^{\frac{1}{2}s_{g\bar{q}}} \mathrm{d}s_1 \int_{s_1}^{s_{g\bar{q}}-s_1} \mathrm{d}s_2\, O_{E2} \right) d_3^0 \\
&\qquad \left. + 2n_F \left(\frac{P_{A_1}}{s_{qg}} \int_0^{s_{qg}} \mathrm{d}s_2 \int_0^{s_{qg}-s_2} \mathrm{d}s_1 + \frac{P_{A_2}}{s_{g\bar{q}}} \int_0^{s_{g\bar{q}}} \mathrm{d}s_2 \int_0^{s_{g\bar{q}}-s_2} \mathrm{d}s_1 \right) O_S\, e_3^0 \right]
\end{aligned}
\tag{6.80}
$$

with $O_{Ej} = \frac{Q_3^2}{Q_{Ej}^2+Q_3^2}$, $O_{Sj} = \frac{Q_3^2}{m_{q\bar{q}}^2+Q_3^2}$ as defined in eq. (6.12), $O_{E1} = \frac{2s_2}{Q_3^2+2s_2}$, $O_{E2} = \frac{2s_1}{Q_3^2+2s_1}$, $O_S = \frac{s_1}{s_1+Q_3^2}$ and eq. (6.13), $Q_3^2 = 2\min(s_{qg}, s_{g\bar{q}})$, and e_3^0 carrying the singularity in s_1. We will focus again on deriving the transcendality-2 terms explicitly, with the full expressions given in the appendix. We start by recalling the expression for the strongly-ordered $2 \to 3$ branching,

$$
\frac{\alpha_s C_A}{2\pi} \left[\ln\left(\frac{s}{\frac{1}{2}Q_3^2}\right) \ln\left(\frac{s-\frac{1}{2}Q_3^2}{\frac{1}{2}Q_3^2}\right) - \mathrm{Li}_2\left(\frac{s-\frac{1}{2}Q_3^2}{s}\right) + \mathrm{Li}_2\left(\frac{\frac{1}{2}Q_3^2}{s}\right) \right].
$$

To this we add the results from the eikonal term $\frac{2s_{qg}}{s_1 s_2}$ of one $3 \to 4$ gluon emission, the first line in eq. (6.80),

$$
\begin{aligned}
&- \frac{2\alpha_s C_A}{\pi} \int_0^{\frac{1}{2}} \mathrm{d}y_2 \int_{y_2}^{1-y_2} \mathrm{d}y_1 \frac{1}{y_1(y_3^2+2y_2)} \\
&= -\frac{\alpha_s C_A}{2\pi} \left[-\ln(4)\ln\left(1-\frac{1}{1+y_3^2}\right) + \ln(4)\ln\left(1+\frac{1}{1+y_3^2}\right) - 2\,\mathrm{Li}_2\left(-\frac{1}{y_3^2}\right) \right. \\
&\qquad \left. + 2\,\mathrm{Li}_2\left(\frac{1}{2+y_3^2}\right) - 2\,\mathrm{Li}_2\left(\frac{2}{2+y_3^2}\right) \right]
\end{aligned}
\tag{6.81}
$$

where we have transformed $y_i = \frac{s_i}{s_{qg}}$ for $i = 1, 2$ and $y_3^2 = \frac{Q_3^2}{s_{qg}} = 2\min(1, \frac{s_{g\bar{q}}}{s_{qg}})$. Taking the limit for the soft region $y_3^2 \to 2$ (since we take the invariants as vanishing simultaneously), we see that the remainder is just a finite term that contains no logarithms of the vanishing invariants,

$$
\frac{\alpha_s C_A}{8\pi} \left[2\ln^2(2) + \mathrm{Li}_2\left(\frac{1}{4}\right) \right]. \tag{6.82}
$$

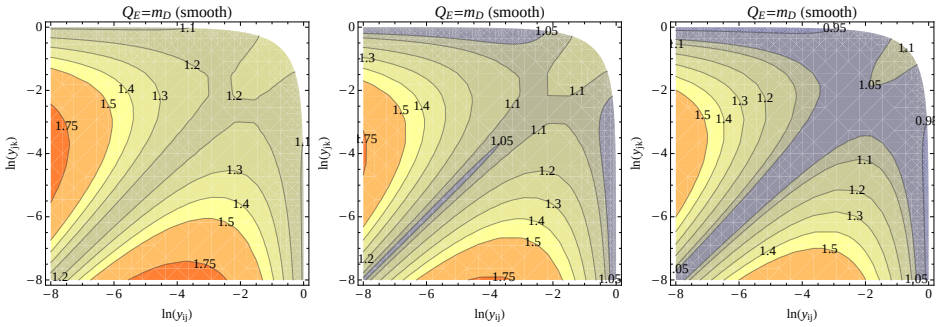

(a) $\mu_{\rm PS} = m_D$ (b) $\mu_{\rm PS} = \frac{1}{2} m_D$ (c) $\mu_{\rm PS} = \frac{1}{2} m_D$, with CMW

Figure 6.5: NLO correction factor for smooth m_D-ordering, with GGG antennae, and $\mu_{\rm PS} = m_D$ (left), $\mu_{\rm PS} = \frac{1}{2} m_D$ (middle), and $\mu_{\rm PS} = \frac{1}{2} m_D$ with CMW rescaling (right). For all plots, $\alpha_s = 0.12$, $n_F = 5$, and the evolution scale for gluon splittings was m_{qq}.

We will receive this contribution twice. Including all divergent logarithmic contributions and disregarding constant terms such as in eq. (6.82) , we find the same as in the strong-ordering case,

$$-\text{ PS:} \qquad s_{qg} = s_{g\bar{q}} = y \to 0 \qquad \frac{\alpha_s C_A}{2\pi} \left[\ln^2(y) + \frac{3}{2} \ln(y) \right] , \tag{6.83}$$

and hence the preferred choice of scale in the soft limit remains one which is linear in the vanishing invariants, such as $\mu_{\rm PS} \propto m_D$.

In the hard collinear limit the Sudakov integrals plus the 'Ariadne Log' reduce to

$$-\text{ PS:} \qquad s_{qg} = y \to 0, s_{g\bar{q}} \to s \qquad \frac{\alpha_s C_A}{2\pi} \left[-\frac{1}{6} C_A + \frac{1}{6} n_F \right] \ln(y) , \tag{6.84}$$

again the same as in the strongly ordered case, cf. eq. (6.62).

To summarize, we do not expect any qualitatively different limiting behaviour in the smoothly ordered case with respect to the strongly ordered one, though details may of course still vary. To illustrate this, we include the plots in fig. 6.5. In all cases, we use a renormalization scale $\propto m_D$, but with different prefactors, from left to right: $\mu_{\rm PS} = m_D$, $\mu_{\rm PS} = m_D/2$, and finally $\mu_{\rm PS} = m_D/2$ with CMW rescaling. In particular the latter gives correction factors very close to unity in both the soft and hard collinear limits, while we still see the leftover divergence inbetween those limits that was also present in the case of strong m_D-ordering, cf. fig. 6.2. Nonetheless, it is worth noting that for a large region of phase space, say with $m_{ij} > 0.1\, m$ (corresponding to $\ln(y_{ij}) > -4.6$), the corrections are still quite well behaved and relatively small, less than $\sim 20\%$.

Transverse Momentum

Again we only need to recompute the contributions from the $3 \to 4$ Sudakov terms, as the $2 \to 3$ ones are the same as in the strongly ordered case. The $3 \to 4$ Sudakov integrals are

$$\begin{aligned}
&- g_s^2 \left[\sum_{j=1}^{2} C_A \int_0^{s_j} (1 - O_{Ej})\; d_3^0 \, \mathrm{d}\Phi_{\mathrm{ant}} + \sum_{j=1}^{2} 2\, T_R\, n_F P_{A_j} \int_0^{s_j} (1 - O_{Sj})\; e_3^0 \, \mathrm{d}\Phi_{\mathrm{ant}} \right] \\
&= -\frac{\alpha_s}{4\pi} \left[\left(\frac{C_A}{s_{qg}} \int_0^{s_{qg}} \mathrm{d}s_2 \int_0^{s_{qg}-s_2} \mathrm{d}s_1 O_E + \frac{C_A}{s_{g\bar{q}}} \int_0^{s_{g\bar{q}}} \mathrm{d}s_2 \int_0^{s_{g\bar{q}}-s_2} \mathrm{d}s_1 O_E \right) d_3^0 \right. \\
&\qquad \left. + 2 n_F \left(\frac{P_{A_1}}{s_{qg}} \int_0^{s_{qg}} \mathrm{d}s_2 \int_0^{s_{qg}-s_2} \mathrm{d}s_1 + \frac{P_{A_2}}{s_{g\bar{q}}} \int_0^{s_{g\bar{q}}} \mathrm{d}s_2 \int_0^{s_{g\bar{q}}-s_2} \mathrm{d}s_1 \right) O_S \, e_3^0 \right]
\end{aligned} \tag{6.85}$$

with O_{Ej}, O_{Sj} as defined eq. (6.12) en eq. (6.13), specified by $O_E = \frac{4 s_1 s_2}{Q_3^2 s_{qg} + 4 s_1 s_2}$, $O_S = \frac{s_1}{s_1 + Q_3^2}$. As before we focus on explicitly calculating the transcendentality-2 contribution arising from the eikonal part of the antenna in the first term in the first line of eq. (6.85),

$$\begin{aligned}
&- \frac{\alpha_s C_A}{2\pi} \int_0^1 \mathrm{d}y_2 \int_0^{1-y_2} \mathrm{d}y_1 \frac{4 y_1 y_2}{y_3^2 + 4 y_1 y_2} \frac{1}{y_1 y_2} \\
&= -\frac{\alpha_s C_A}{2\pi} \left[-\mathrm{Li}_2 \left(-\frac{2}{-1 + \sqrt{1 + y_3^2}} \right) - \mathrm{Li}_2 \left(\frac{2}{1 + \sqrt{1 + y_3^2}} \right) \right]
\end{aligned} \tag{6.86}$$

where we have transformed $y_i = \frac{s_i}{s_{qg}}$ and $y_3^2 = \frac{Q_3^2}{s_{qg}}$. In the limit $s_{\min}/s, s_{\max}/s = y \to 0$ so that $y_3^2 \to 0$, this yields

$$\frac{\alpha_s C_A}{2\pi} \left[-\frac{1}{2} \ln^2(y) \right]. \tag{6.87}$$

Adding the contributions from the $2 \to 3$ splitting and transcendentality-1 terms, we find the following result for the soft limit

$$-\text{ PS:} \qquad s_{qg} = s_{g\bar{q}} = y \to 0 \qquad \frac{\alpha_s C_A}{2\pi} \left[\ln^2(y) - \frac{1}{3} \ln(y) \right] + \frac{\alpha_s}{6\pi} n_F \ln(y)\,, \tag{6.88}$$

as in the strongly ordered case. The double logarithm matches with SVirtual and the single logarithm can be absorbed by choosing a renormalization scale that is quadratic in the vanishing invariants, such as $\mu_{\mathrm{PS}} \propto p_\perp$.

In the hard collinear limit, the shower integrals behave as

$$-\text{PS:} \qquad s_{qg} = y \to 0, s_{g\bar{q}} \to s \qquad \frac{\alpha_s}{2\pi} \left[-\frac{1}{6} C_A + \frac{1}{6} n_F \right] \ln(y)\,, \tag{6.89}$$

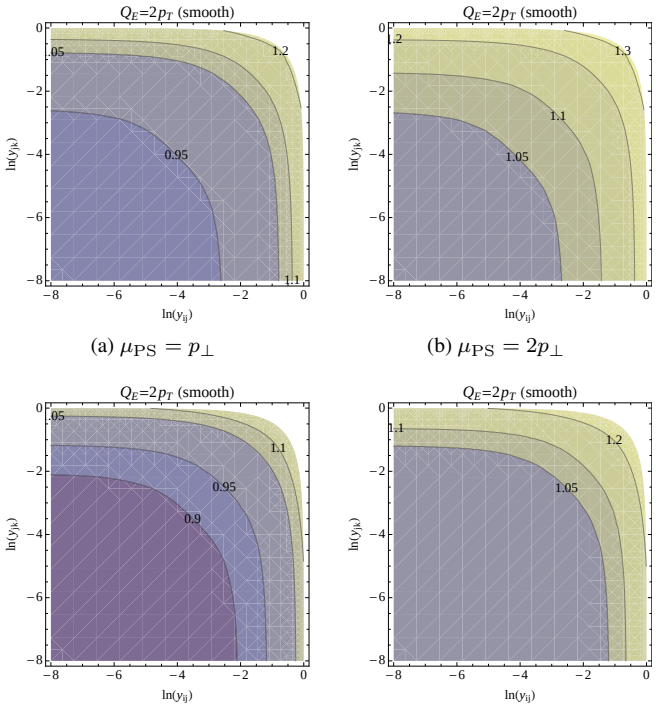

(a) $\mu_{\rm PS} = p_\perp$ (b) $\mu_{\rm PS} = 2p_\perp$

(c) $\mu_{\rm PS} = p_\perp$, with CMW (d) $\mu_{\rm PS} = 2p_\perp$, with CMW

Figure 6.6: NLO correction factor for smooth $p_\perp$-ordering, with GGG antennae, without (top row) and with (bottom row) the CMW rescaling of $\Lambda_{\rm QCD}$. The left-hand panes use $\mu_{\rm PS} = p_\perp$ and the right-hand ones $\mu_{\rm PS} = 2p_\perp$. For all plots, $\alpha_s = 0.12$, $n_F = 5$, and the evolution scale for gluon splittings was m_{qq}.

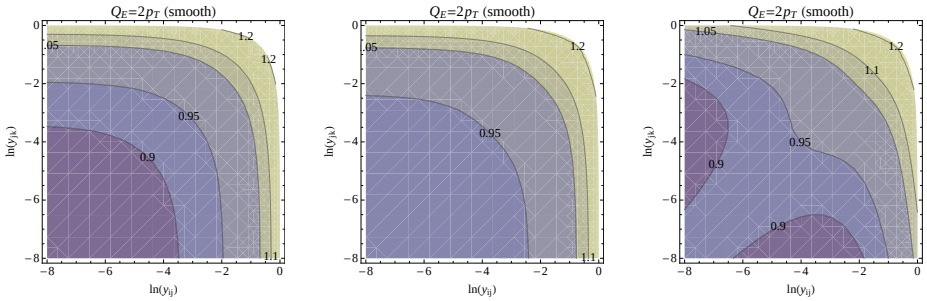

(a) $\mu_{\rm PS} = p_\perp$, $N_\perp = 1$ (b) $\mu_{\rm PS} = p_\perp$, $N_\perp = 4$, $g \to q\bar{q}$ in $p_\perp$ (c) $\mu_{\rm PS} = p_\perp$, $N_\perp = 4$, $P_{Aj} = 1$

Figure 6.7: NLO correction factor for smooth $p_\perp$-ordering, with GGG antennae: variations of how gluon splittings are interleaved with gluon emissions, see text. We used $\alpha_s = 0.12$, $n_F = 5$, and $\mu_{\rm PS} = p_\perp$.

the same as in all the other cases. This completes the argument that indeed $\mu_{\rm PS} \propto p_\perp$ is the appropriate choice also for smooth $p_\perp$-ordering.

In fig. 6.6, we show the NLO correction factors, $(1 + V_{3Z})$, for smooth $p_\perp$-ordering. The top row shows the correction factors without using the CMW rescaling of $\Lambda_{\rm QCD}$, and the plots in the bottom row include it. For the left-hand panes, we used a shower renormalization scale of $\mu_{\rm PS} = p_\perp$, and for the right-hand ones we used $\mu_{\rm PS} = 2p_\perp$.

We see that all correction factors are essentially well-behaved, with no runaway logs, similarly to the case of strong $p_\perp$-ordering. However, for the case of smooth $p_\perp$-ordering, it looks as if the CMW rescaling (bottom row) is almost doing "too much" in the soft region. Given that the CMW arguments [145] were derived explicitly by considering the subleading behaviour of strongly ordered (coherent) parton showers, we do not perceive of this as any major drawback. Instead, one should merely be aware of the slight shifts in the NLO corrections that result from applying it or not, recalling that a rescaling of Λ by the CMW factor ~ 1.5 is within the ordinary factor 2 variation of the renormalization scale that is often taken as a standard for uncertainty estimates.

The shifts caused by CMW rescaling and/or by renormalization-scale prefactors are of course fully taken into account in our implementation in the VINCIA code, and are thus reabsorbed into the one-loop matching coefficient at the matched order, stabilizing the prediction. Differences at higher orders will result from the fact that the CMW rescaling, if applied, is used for all shower branchings, while the NLO correction derived here is only applied at the $Z \to 3$ stage of the calculation.

Because smooth $p_\perp$-ordering is the default in VINCIA we wish to understand this case as best as we can, and therefore we include some further comparisons with non-default settings in fig. 6.7.

In fig. 6.7a, we modify the normalization of the evolution variable from the VINCIA default $Q_E^2 = 4p_\perp^2$ to the ARIADNE choice $Q_E^2 = p_\perp^2$. Though the normalization

factor cancels in the $P_{\rm imp}$ factor for sequential gluon emissions, it is relevant for deciding the relative ordering between gluon emissions and gluon splittings. As this plot shows, however, the modification only produces quite small differences in the NLO correction factor, and with the "wrong" sign. Thus, we retain $N_\perp = 4$ as the default in VINCIA. In fig. 6.7b, we change the evolution variable for gluon splittings to be the same as that for gluon emissions, i.e., $p_\perp$, with similar conclusions as for the previous variation. In fig. 6.7c, we switch off the Ariadne factor for gluon splittings. We notice that the NLO corrections get slightly larger. There is no change along the diagonal $y_{ij} = y_{jk}$ since the Ariadne factor is unity there, but along the edges of the plots, the NLO corrections become larger, which further motivates the choice of keeping the Ariadne factor switched on by default in VINCIA.

The overall result is that the infrared limits are generally well-behaved for $p_\perp$ evolution with $\mu_{\rm PS} \propto p_\perp$. Remaining differences amount to small finite shifts of order 10%-20% away from unity. At that level, the effective finite terms of the antenna functions also play a role, hence it is too early to draw definite conclusions just based on the plots presented here. The impact of finite terms will be studied in section 6.3 in the context of matching to the LO matrix elements for $Z \to 4$ partons, which effectively fixes the finite terms with respect to the pure-shower answers studied here.

6.2.3 Tables of Infrared Limits

The results of the preceding subsections on the infrared limits of the pole-subtracted matrix elements and of the Sudakov integrals generated by the various evolution-scale choices are collected here, in parametric form, for easy reference. The renormalization terms, $V_{3\mu}$, are not included. Tab. 6.1 expresses the limits of SVirtual , while tab. 6.2 contains the Sudakov-integral limits.

SVirtual	soft	$\left(-L^2 - \frac{10}{3}L - \frac{\pi^2}{6}\right) C_A + \frac{1}{3} n_F L$
	hard collinear	$-\frac{5}{3} L C_A + \frac{1}{6} n_F L$

Table 6.1: Limits of SVirtual , with L denoting $\ln(y)$, and $s_{qg}/s = s_{g\bar{q}}/s = y \to 0$, omitting an overall factor of $\alpha_s/2\pi$.

		strong	smooth
$p_\perp$	soft	$\left(L^2 - \frac{1}{3}L + \frac{\pi^2}{6}\right) C_A + \frac{1}{3} n_F L$	$\left(L^2 - \frac{1}{3}L - \frac{\pi^2}{6}\right) C_A + \frac{1}{3} n_F L$
	hard col.	$-\frac{1}{6} L C_A + \frac{1}{6} n_F L$	$\left(-\frac{1}{6}L - \frac{\pi^2}{6}\right) C_A + \frac{1}{6} n_F L$
m_D	soft	$\left(L^2 + \frac{3}{2}L - \frac{\pi^2}{6}\right) C_A$	$\left(L^2 + \frac{3}{2}L - \frac{\pi^2}{6}\right) C_A$
	hard col.	$-\frac{1}{6} L C_A + \frac{1}{6} n_F L$	$\left(-\frac{1}{6}L - \frac{\pi^2}{3}\right) C_A + \frac{1}{6} n_F L$

Table 6.2: Limits of strong and smooth $p_\perp$ and m_D ordering, with L denoting $\ln(y)$, with $s_{qg} = s_{g\bar{q}} = y \to 0$. Non divergent terms, such as π^2 have been omitted in the calculation of V_{3Z}, and the renormalization term in V_{3Z} is set to zero. An overall factor of $\alpha_s/2\pi$ is suppressed. Therefore p_T in the soft limit will yield a correction of $V_{3z} = -\beta_0$ while the hard collinear region of p_T and both the soft and hard collinear region of m_D add a correction of $V_{3z} = -\frac{1}{2}\beta_0$.

6.3 Results Including both LO and NLO Corrections

In the preceding section, we focussed on deriving the analytic forms of the shower integrals and comparing their infrared limits to the matrix-element expressions. It is now time to include also the finite terms arising from matching to the 4-parton tree-level matrix element, expressed by the δA terms in eq. (6.32). Our ultimate aim in this section is to include the full leading-colour one-loop corrections through second order in α_s (i.e., up to and including $Z \to 3$ partons) and combine these with the full-colour tree-level corrections through third order in α_s (i.e., up to and including $Z \to 5$ partons, the default in VINCIA). However, since we shall perform the δA integrals numerically, adding those terms to the analytic ones derived in the previous section, we first wish to examine the numerical size and precision required on the δA terms themselves.

6.3.1 Finite Antenna Terms and LO Matching Corrections

Finite-term variations of the antenna functions (and in particular fixing the finite terms via unitary LO matching corrections, such as is done in VINCIA [110]) will affect the terms generated by the $3 \to 4$ Sudakov expansions in the following way. Larger finite terms will cause an increased amount of $3 \to 4$ branchings, which in turn will *decrease* the associated Sudakov factor (in the sense of driving it closer to zero). This will feed into the NLO correction factor, which compensates and drives the final answer back towards its NLO-correct value. (Note that similar variations will not occur for the $2 \to 3$ branching step, since we treat that as fixed to the LO 3-parton matrix element throughout.) This feedback mechanism is encoded in the δA terms in eq. (6.32).

Following the reasoning above, we should expect larger antenna finite terms to *increase* the NLO correction factor (since, to stabilize the 3-parton exclusive rate, it must compensate for losing more 3-parton phase-space points to 4-parton ones), and vice versa:

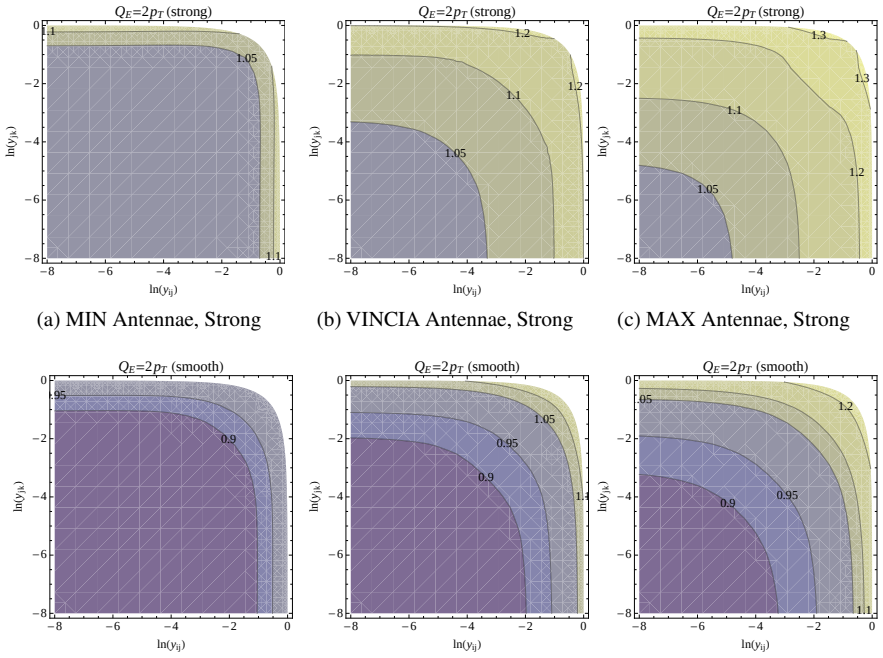

(a) MIN Antennae, Strong (b) VINCIA Antennae, Strong (c) MAX Antennae, Strong

(d) MIN Antennae, Smooth (e) VINCIA Antennae, Smooth (f) MAX Antennae, Smooth

Figure 6.8: NLO correction factor for strong (top row) and smooth (bottom row) $p_\perp$-ordering, for MIN (left), VINCIA default (middle), and MAX (right) antenna functions. We use $\mu_R = p_\perp$ combined with CMW rescaling, $\alpha_s = 0.12$, and gluon splitting in m_{qq}.

smaller finite terms should result in a *decrease* of the NLO correction. At the pure-shower level (i.e., without LO matrix-element corrections to fix the finite terms), this is illustrated by fig. 6.8.

For ease of comparison, all plots use the CMW rescaling of $\Lambda_{\rm QCD}$, $\mu_{\rm PS} = p_\perp$, $n_F = 5$, and $\alpha_s(m_Z) = 0.12$. The default antenna functions in VINCIA[2] are shown in the middle panes, for strong (top row) and smooth (bottom row) ordering, respectively. A variation with smaller finite terms for the $3 \to 4$ antenna functions is shown to the left, and one with larger finite terms on the right. As expected, the NLO correction factors react by becoming lower for smaller finite terms and higher for larger finite terms, for both strong and smooth ordering.

We emphasise that the plots in fig. 6.8 are shown purely for illustration, to give a feeling for the changes produced by finite-term variations. In the actual matched shower

[2]Note that VINCIA was recently updated with a set of helicity-dependent antenna functions [149], so the defaults shown here are not identical to the GGG ones, but are instead helicity sums/averages over the functions defined in [149].

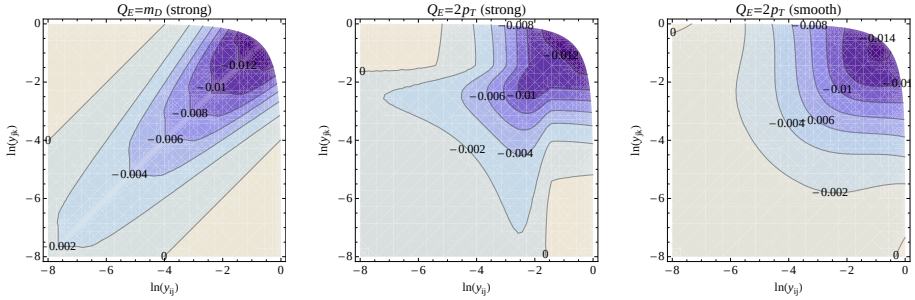

Figure 6.9: Size of δA terms differences between GGG and VINCIA default antennae.

evolution, the constraint imposed by matching to the LO 4-parton matrix elements fixes the finite terms, via the unitary procedure derived in [110], which was briefly recapped in section 5.2.1. The effective finite terms then depend on the full LO 4-parton matrix elements, and have a more complicated structure than the simple antenna functions we have so far been playing with. We shall therefore not attempt to integrate them analytically, but prefer instead to let VINCIA compute a numerical MC estimate for us.

Each point in that MC integration will involve computing at least one LO 4-parton matrix element, hence it is crucial to know how many points will be needed to obtain sufficient accuracy. Since everything else is handled analytically, this will be the deciding factor in determining the speed of the NLO-corrected algorithm. We shall perform a speed test below in section 6.3.4, but first we need to determine the accuracy we need on the δA integral.

A first analytic estimate of the size of the δA terms can be obtained by simply computing the ones produced by switching from GGG to the VINCIA default antennae (summed and averaged over helicities [149]), with the following $\mathcal{O}(1)$ finite-term differences:

$$qg \to qgg: \quad F_{\text{Emit}}^{\text{VINCIA}} - F_{\text{Emit}}^{\text{GGG}} = 1.5 - (2.5 - y_{ij} - 0.5y_{jk}) = -1 + y_{yij} + 0.5y_{jk} \,, \tag{6.90}$$

$$qg \to q\bar{q}'q': \quad F_{\text{Split}}^{\text{VINCIA}} - F_{\text{Split}}^{\text{GGG}} = 0.0 - (-0.5 + y_{ij}) \qquad = 0.5 - y_{ij} \,, \tag{6.91}$$

with F_{Emit} and F_{Split} defined in eqs. (5.4) and (5.5). The δA terms produced by these differences are plotted in fig. 6.9, for strong ordering in m_D (left) and $p_\perp$ (centre), and for smooth ordering in $p_\perp$ (right), respectively. As expected, they do come out to be numerically subleading, roughly of order $\alpha_s/(2\pi)$, relative to LO (unity), yielding corrections ranging from a few permille to about a percent of the LO result.

Finally, in fig. 6.10, we include the full LO 4-parton matrix elements and plot the distribution of numerically computed δA terms during actual VINCIA runs, for 100,000 events. The result is now represented by a one-dimensional histogram, with δA on the x-axis and relative rate on the y-axis. On the left-hand pane, the δA distribution with default settings is shown on a linear scale, while the right-hand pane shows the same result on a logarithmic scale, including variations with higher numerical accuracy.

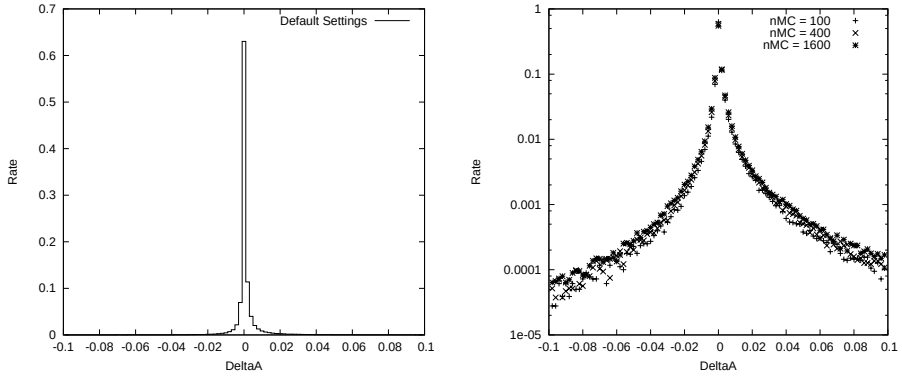

Figure 6.10: Distribution of the size of the δA terms (normalized so the LO result is unity) in actual VINCIA runs. *Left:* linear scale, default settings. *Right:* logarithmic scale, with variations on the minimum number of MC points used for the integrations (default is 100).

As mentioned above, the integration is done by a uniform Monte Carlo sampling of the δA integrands. We require a numerical precision better than 1% on the estimated size of the term (relative to LO) and, by default, always sample at least 100 MC points for each antenna integral. In the left-hand pane of fig. 6.10, we see that, even with the full 4-parton LO matrix-element corrections included, the size of the δA terms remains below one percent for the vast majority of 3-parton phase-space points.

On the logarithmic scale in the right-hand pane of fig. 6.10, however, it is evident that there is also a tail of quite rare phase-space points which are associated with larger δA corrections. Numerical investigations reveal that this tail is mainly generated by the integrals over the $g \to q\bar{q}$ terms, in particular in phase-space points in which the gluon is collinear to one of the original quarks. This agrees with our expectation that these terms are the ones to which the pure shower gives the "worst" approximation, and hence they are the ones that receive the largest matrix-element corrections. As a test of the numerical stability of the NLO corrections for these points, we increased the minimum number of MC points used for the δA integration from the default 100 (shown with "$+$" symbols) to 400 ("$\times$" symbols) and 1600 ("$*$" symbols), cutting the expected statistical MC error in half with each step, at the cost of increased event-generation time. Though we do observe a slight broadening of the distribution between the default and the higher-precision settings, the shifts should be interpreted horizontally and remain well under the required percent-level precision with respect to LO. The default settings are therefore kept at a minimum of 100 MC points, though we note that future investigations, in particular of more complicated partonic topologies, may require developing a better understanding of, and perhaps a better shower approximation to, these integrals, especially the $g \to q\bar{q}$ contribution.

For completeness, we note that the runs used to obtain these distributions were performed using the new default "Nikhef" tune of VINCIA's NLO-corrected shower, which

will be described in more detail in the following subsection. Parameters for the tune are given in appendix D.

6.3.2 LEP Results

Since we have restricted our attention to massless partons in this work, we shall mainly consider the light-flavour-tagged event-shape and fragmentation distributions produced by the L3 experiment at LEP for our validations and tuning, see [150]. We consider three possible VINCIA settings:

- New default (NLO): uses two-loop running for α_s, with CMW rescaling of $\Lambda_{\rm QCD}$. From the comparisons to event-shape variables presented in this section, we settled on a value of $\alpha_s(M_Z) = 0.122$. A few modifications to the string-fragmentation parameters were made, relative to the old default, to compensate for differences in the region close to the hadronization scale. The revised parameters are listed in appendix D, under the "Nikhef" tune.
- New default (NLO off). Identical to the previous bullet point, but with the NLO correction factor switched off.
- Old default (LO tune): uses one-loop running for α_s, without CMW rescaling of $\Lambda_{\rm QCD}$, and $\alpha_s(M_Z) = 0.139$. The string-fragmentation parameters are those of the "Jeppsson 5" tune, see appendix D.

The three main event-shape variables that were used to determine the value of $\alpha_s(M_Z)$ are shown in fig. 6.11, with upper panes showing the distributions themselves (data and MC) and lower panes showing the ratios of MC/data, with one- and two-sigma uncertainties on the data shown by darker (green) and lighter (yellow) shaded bands, respectively. The Thrust (*left*) and C-parameter (*middle*) distributions both have perturbative expansions that start at $\mathcal{O}(\alpha_s)$ and hence they are both explicitly sensitive to the corrections considered in this chapter. The expansion of the D parameter (*right*) begins at $\mathcal{O}(\alpha_s^2)$. It is sensitive to the NLO 3-jet corrections mainly via unitarity, since all 4-jet events begin their lives as 3-jet events in our framework. It also represents an important cross-check on the value extracted from the other two variables.

For a pedagogical description of the variables, see [150]. Pencil-like 2-jet configurations are to the left (near zero) for all three observables. This region is particularly sensitive to non-perturbative hadronization corrections. More spherical events, with several hard perturbative emissions, are towards the right (near 0.5 for Thrust and 1.0 for C and D). The maximal $\tau = 1 - T$ for a 3-particle configuration is $\tau = 1/3$ (corresponding to the Mercedes configuration), beyond which only 4-particle (and higher) states can contribute. This causes a noticeable change in slope in the distribution at that point, see fig. 6.11a. The same thing happens for the C parameter at $C = 3/4$, in fig. 6.11b. The D parameter is sensitive to the smallest of the eigenvalues of the sphericity tensor, and is therefore zero for any purely planar event, causing it to be sensitive only to 4- and higher-particle configurations over its entire range.

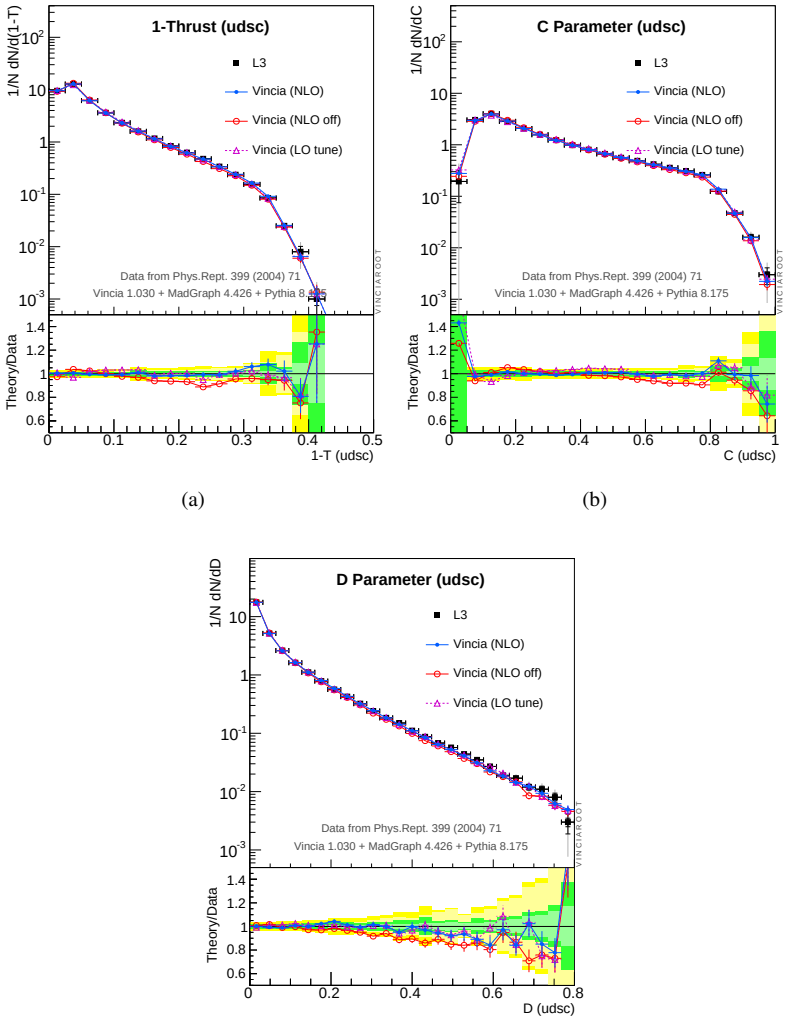

Figure 6.11: L3 light-flavour event shapes: Thrust, C, and D.

Both the new NLO tune (solid blue line with filled-dot symbols) and the old LO one (dashed magenta line with open-triangle symbols) reproduce all three event shapes very well. With the NLO corrections switched off (solid red line with open-circle symbols), the new tune produces a somewhat too soft spectrum, consistent with its low value of $\alpha_s(M_Z)$ not being able to describe the data without the benefit of the NLO 3-jet corrections.

As a further cross check, we show two further event-shape variables that were included in the L3 study in fig. 6.12: the Wide and Total Jet Broadening parameters, B_W and B_T, respectively. These have a somewhat different and complementary sensitivity to the perturbative corrections, compared to the variables above, picking out mainly the transverse component of jet structure. They are equal at $\mathcal{O}(\alpha_s)$, but B_T receives somewhat larger $\mathcal{O}(\alpha_s^2)$ corrections than B_W. Again, we see that both the old (LO) and new (NLO) defaults are able to describe the data, and that the spectrum with the new default value for $\alpha_s(M_Z)$ is too soft if the NLO corrections are switched off.

Finally, as an aid to constraining the Lund fragmentation-function parameters, the L3 study also included two infrared-sensitive observables: the charged-particle multiplicity and momentum distributions, to which we compare in fig. 6.13, with the momentum fraction defined as

$$x = \frac{2|p|}{\sqrt{s}} \,. \tag{6.92}$$

There is again no noteworthy differences between the old and new default tunes.

Having determined the value of $\alpha_s(M_Z)$ and the parameters of the non-perturbative fragmentation function, we extended the validations to include a set of jet-rate and jet-resolution measurements by the ALEPH experiment [151] (now without the benefit of light-flavour tagging), using the standard Durham k_T algorithm for e^+e^- collisions [152], as implemented in the FASTJET code [153]. We also compared to default PYTHIA 8 and, for completeness, checked that the relative production fractions of various meson and baryon species were indeed unchanged relative to the old VINCIA default.

Rather than presenting all of this information in the form of many additional plots, tab. 6.3 instead provides a condensed summary of all the validations we have carried out, via $\langle \chi^2 \rangle$ values for each of the models with respect to each of the LEP distributions, including a flat 5% "theory uncertainty" on the MC numbers. Already from this simple set of χ^2 values, it is clear that the LO models/tunes are already doing very well[3]. This agreement, however, comes at the price of using a very large ("LO") value for α_s, which is not guaranteed to be universally applicable.

The main point of the overview in tab. 6.3 is that an equally good agreement can be obtained with an $\alpha_s(m_Z)$ value that is consistent with other NLO determinations [158], specifically

$$\alpha_s(m_Z) \;=\; 0.122 \,, \tag{6.93}$$

once the NLO 3-jet corrections are included. This should carry over to other NLO-corrected processes, and hence the fragmentation parameters we have settled on should be

[3]Both VINCIA and PYTHIA are known to give quite good fits to LEP data [110, 149, 154, 155]. For comparisons including other generators and tunes, see mcplots.cern.ch.

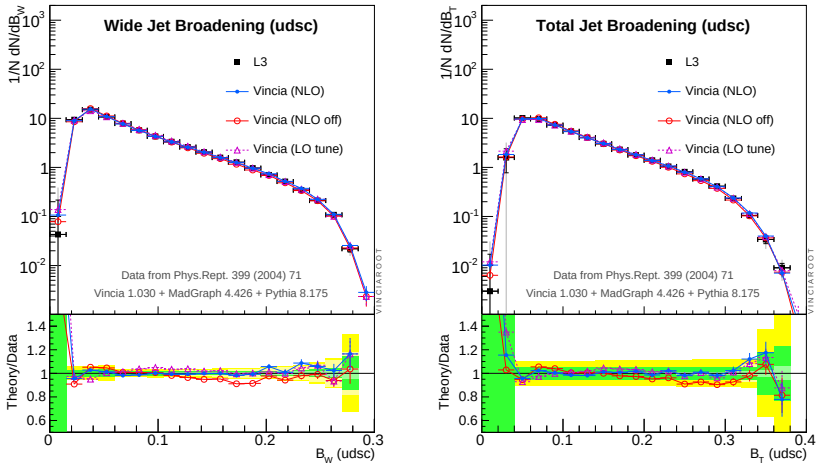

(a) (b)

Figure 6.12: L3 light-flavour event shapes: jet broadening

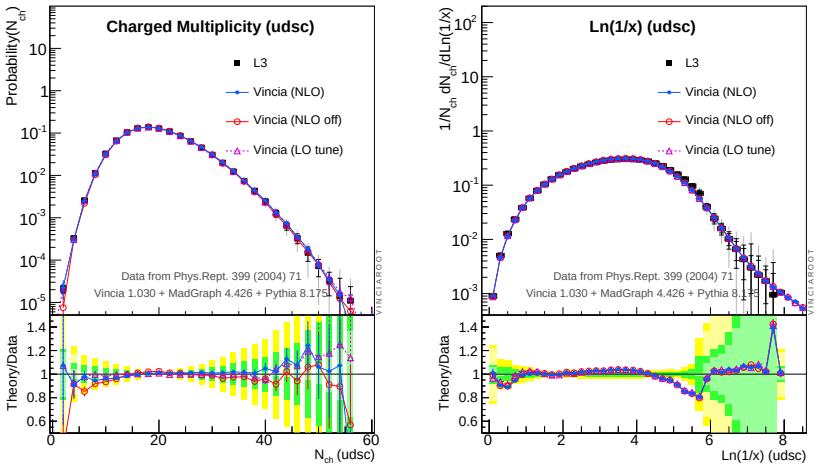

(a) (b)

Figure 6.13: L3 light-flavour fragmentation observables: charged-track multiplicity and momentum distribution.

applicable to future NLO-corrected studies with VINCIA, and can also serve as a starting point for NLO-level matching studies with PYTHIA 8. In the latter context, the 2-loop

$\langle\chi^2\rangle$ **Shapes**	T	C	D	B_W	B_T
PYTHIA 8	0.4	0.4	0.6	0.3	0.2
VINCIA (LO)	0.2	0.4	0.4	0.3	0.3
VINCIA (NLO)	0.2	0.2	0.6	0.3	0.2

$\langle\chi^2\rangle$ **Frag**	$N_{\rm ch}$	x	Mesons	Baryons
PYTHIA 8	0.8	0.4	0.9	1.2
VINCIA (LO)	0.0	0.5	0.3	0.6
VINCIA (NLO)	0.1	0.7	0.2	0.6

$\langle\chi^2\rangle$ **Jets**	$r_{1j}^{\rm exc}$	$\ln(y_{12})$	$r_{2j}^{\rm exc}$	$\ln(y_{23})$	$r_{3j}^{\rm exc}$	$\ln(y_{34})$
PYTHIA 8	0.1	0.2	0.1	0.2	0.1	0.3
VINCIA (LO)	0.1	0.2	0.1	0.2	0.0	0.2
VINCIA (NLO)	0.2	0.4	0.1	0.3	0.1	0.3

$\langle\chi^2\rangle$ **Jets**	$r_{4j}^{\rm exc}$	$\ln(y_{45})$	$r_{5j}^{\rm exc}$	$\ln(y_{56})$	$r_{6j}^{\rm inc}$
PYTHIA 8	0.2	0.3	0.2	0.4	0.3
VINCIA (LO)	0.3	0.1	0.1	0.0	0.0
VINCIA (NLO)	0.2	0.2	0.1	0.2	0.1

Table 6.3: $\langle\chi^2\rangle$ values for: *Top:* L3 light-flavour event shapes and fragmentation variables [150], and LEP average meson and baryon fractions [156, 157]. *Bottom:* Durham k_T n-jet rates, r_{nj}, and jet resolutions, y_{ij}, measured by the ALEPH experiment [151]. For the latter, the $\langle\chi^2\rangle$ calculation was restricted to the perturbative region, $\ln(y) > -8$. A flat 5% theory uncertainty was included on the MC numbers. Both default PYTHIA and the VINCIA (LO) tune use $\alpha_s(m_Z) = 0.139$ while the VINCIA (NLO) tune uses $\alpha_s(m_Z) = 0.122$.

running in particular could be retained, while the soft fragmentation parameters would presumably have to be somewhat readjusted to absorb differences between VINCIA and PYTHIA 8 near the hadronization scale[4].

6.3.3 Uncertainties

As in previous versions of VINCIA, we use the method proposed in [110] to compute a comprehensive set of uncertainty bands, which are provided in the form of a vector of alternative weights for each event. Each set is separately unitary, with average weight one[5]. The difference with respect to previous versions is that each variation now benefits

[4]The differences in soft fragmentation parameters between existing LO VINCIA and PYTHIA-8 tunes could be used as an initial guideline for such an effort, see, e.g., appendix D.

[5]VINCIA currently does not attempt to give a separate estimate of the uncertainty on the total inclusive cross section. The uncertainties it computes only pertain to shapes of distributions and the effects of cuts on the

fully from the inclusion of NLO corrections.

When setting the parameter `Vincia:uncertaintyBands = on`, the uncertainty weights are accessible through the method

```
double vincia.weight(int i=0);
```

with $i = 0$ corresponding to the ordinary event sample, normally with all weights equal to unity, and the following variations, for $i =$:

1. Default: since the user may have chosen other settings than the default, the default is included as the first variation.

2. alphaS-Hi: all renormalization scales are decreased to $\mu = \mu_{\rm def}/k_\mu$, where $\mu_{\rm def} = p_\perp$ for gluon emission and $\mu_{\rm def} = m_{q\bar{q}}$ for gluon splitting. The default value of $k_\mu = 2$ can be changed by the user. A second-order compensation for this variation is provided by the renormalization-scale sensitive term $V_{3\mu}$.

3. alphaS-Lo: $\mu = \mu_{\rm def} * k_\mu$, with similar comments as above.

4. ant-Hi: antenna functions with large finite terms (MAX [149]). This variation is already compensated for by LO matching and is not explicitly affected by the NLO corrections.

5. ant-Lo: antenna functions with small finite terms (MIN [149]), with similar comments as above.

6. NLO-Hi: branching probabilities are multiplied by a factor $(1 + \alpha_s)$ to represent unknown (but finite) NLO corrections. Is canceled by NLO matching.

7. NLO-Lo: branching probabilities are divided by a factor $(1 + \alpha_s)$. Is canceled by NLO matching.

8. Ord-pT1: $p_\perp$ ordering with alternative (user-definable) $N_\perp$ normalization factor in $Q_E^2 = N_\perp p_\perp^2$. Compensated at first order by LO matching, and at second order (Sudakov corrections) by NLO matching via ordering-sensitive terms in V_{3Z}.

9. Ord-mD: smooth m_D ordering, with similar comments as above.

10. NLC-Hi: qg emission antennae use C_A as colour factor. Compensated at first order by LO matching. Not affected by NLO matching since we only operate at leading colour.

11. NLC-Lo: qg emission antennae use $2C_F$ as colour factor, with similar comments as above.

total inclusive rate.

We emphasize that these variations are not all independent (for instance the α_s and NLO variations are highly correlated) and hence the corresponding uncertainties should not be summed in quadrature. In the VINCIAROOT plotting tool included with VINCIA, the uncertainty band is constructed by taking the max and min of the variations. See the VINCIA HTML manual for more information about the uncertainty bands and [110] for details on their algorithmic construction.

6.3.4 Speed

Although the CPU time required by matrix-element and shower/hadronization generators is still typically small in comparison to that of, say, full detector simulations, their speed and efficiency are still decisive for all generator-level studies, including tuning and validation, parameter scans, development work, phenomenology studies, comparisons to measurements corrected to the hadron level, and even studies interfaced to fast detector simulations. For this wide range of applications, the high-energy simulation itself constitutes the main part of the calculation. An important benchmark relevant to practical work is for instance whether the calculation can be performed easily on a single machine or not.

Higher matched orders are characterized by increasing complexity and decreasing unweighting efficiencies, resulting in an extremely rapid growth in CPU requirements (see e.g. [149]). At NLO, the additional issues of negative weights and/or so-called counter-events can contribute further to the demands on computing power. With this in mind, high efficiencies and fast algorithmic structures were a primary concern in the development of the formalism for leading-order matrix-element corrections in VINCIA [110, 133, 149], and this emphasis carries through to the present work. We can make the following remarks.

- The only fixed-order phase-space generator is the Born-level one. All higher-multiplicity phase-space points are generated by (trial) showers off the lower-multiplicity ones. This essentially produces a very fast importance-sampling of phase-space that automatically reproduces the dominant QCD structures.

- Likewise, the only cross-section estimate that needs to be precomputed at initialization is the total inclusive one. Thus, initialization times remain at fractions of a second regardless of the matching order.

- The matrix-element corrected algorithm works just like an ordinary parton shower, with modified (corrected) splitting kernels. In particular, all produced events have the same weights, and no additional unweighting step is required.

- Since the corrections are performed multiplicatively, in the form of $(1+\text{correction})$, with 1 being the LO answer, there are no negative-weight events and no counter-events. The only exception would be if the correction becomes larger than the LO answer, and negative. This would correspond to a point with a divergent fixed-order expansion, in which case the use of NLO corrections would be pointless anyway. Moreover, as demonstrated by the plots in the previous sections, our definitions of

	LO level $Z \to$	NLO level $Z \to$	Time / Event [milliseconds]	Speed w.r.t. PYTHIA $\frac{1}{\text{Time}}$ / PYTHIA 8
PYTHIA 8	$2, 3$	2	0.4	1
VINCIA (~~NLO~~)	$2, 3, 4, 5$	2	2.2	$\sim 1/5$
VINCIA (NLO)	$2, 3, 4, 5$	$2, 3$	3.0	$\sim 1/7$

Table 6.4: Event-generation time in VINCIA 1.0.30 compared to PYTHIA 8.176.

the corrections are analytically stable (and numerically subleading with respect to LO) over all of phase space, including the soft and collinear regions, for reasonable renormalization- and evolution-variable choices.

- The parameter variations described in section 6.3.3 can be performed together with the matching corrections to provide a set of uncertainty bands in which each variation benefits from the full corrections up to the matched orders. These are provided in the form of a vector of alternative weights for each event [110], at a cost in CPU time which is only a fraction of that of a comparable number of independent runs.

These attributes, in combination with helicity dependence in the case of the leading-order formalism [149], allow VINCIA to run comfortably on a single machine even with full-fledged matching and uncertainty variations switched on.

The inclusion of NLO corrections will necessarily slow down the calculation. The relative increase in running time relative to PYTHIA 8, is given in tab. 6.4, including the default level of tree-level matching, with and without the NLO 3-jet correction[6]. Without it (but still including the default tree-level corrections which go up to $Z \to 5$ partons), VINCIA is 5 times slower than PYTHIA. With the NLO 3-jet correction switched on, this increases only slightly, to a factor 7. For a fully showered and hadronized calculation which includes second-order virtual and third-order tree-level corrections, we consider that to still be acceptably fast. Importantly, an event-generation time of a few milliseconds per event implies that serious studies can still be performed on an ordinary laptop computer.

6.4 Outlook and Conclusions

In this work, we have investigated the expansion of a Markov-chain QCD shower algorithm to second order in the strong coupling, for $e^+e^- \to 3$ partons, and made systematic comparisons to matrix-element results obtained at the same order. Using these results, we have subjected the subleading properties of shower algorithms with different evolution/ordering variables and different renormalization-scale choices to a rigorous examination. At the analytical level, we have compared the logarithmic structures at the edge

[6]The numbers include both showering and hadronization and were obtained on a single 3.05 GHz CPU, with gcc 4.7 -O2, using default settings for PYTHIA 8 and the "Nikhef" NLO tune for VINCIA.

of phase space, and at the numerical level we have illustrated the difference between the expanded shower algorithm and the one-loop matrix element.

We find that the choice of $p_\perp$-ordering, with a renormalization scale proportional to $p_\perp$ yields the best agreement with the one-loop matrix element, over all of phase space. This elaborates on, and is consistent with, earlier findings [128, 145]. Using the antenna invariant mass, m_D, for the evolution variable still gives reasonable results in the hard regions of phase space, but leads to logarithmically divergent corrections for soft emissions, the exact form of which depends on the choice of renormalization variable. In the VINCIA code, we retain the option of using m_D mainly as a way of providing a conservative uncertainty estimate.

With the NLO 3-jet corrections included as multiplicative corrections to the shower branching probabilities, we find that we can obtain good agreement with a large set of LEP event-shape, fragmentation, and jet-rate observables with a value of the strong coupling constant of $\alpha_s(M_Z) = 0.122$. This is in strong contrast with earlier (LO) tunes of both PYTHIA and VINCIA which employed much larger values ~ 0.14 to obtain agreement with the LEP measurements.

This chapter is intended as a first step towards a systematic embedding of one-loop amplitudes within the VINCIA shower and matching formalism. To arrive at a full-fledged prescription, this will need to be extended to hadron collisions, ideally in a way that allows for convenient automation. A first step towards developing the underlying shower formalism for pp collisions was recently taken [159], and more work is in progress.

In addition, further studies should be undertaken of the impact of unordered sequences of radiation that can occur for the smooth-ordering case (it may be necessary to adopt a strategy similar to the truncated showers of the MC@NLO approach), and the mutually related issues of total normalization and how much of the (hard) corrections are exponentiated (similar to the differences between the POWHEG and MC@NLO formalisms, but here occurring at one additional order, where the relevant total normalization is the NNLO one). Finally, it would be interesting to develop an extension of this formalism that would allow second-order-corrected antenna functions to be used at every stage in the shower, thereby upgrading the precision of the all-orders resummation, a project that would involve examining the second-order corrections to branchings of qg and gg mother antennae as well.

Chapter 7

Conclusion

The large and increasing data sets from the LHC allow for a look into scenarios of possible new physics and will therefore submit the SM to additional tests of its validity. New physics should answer questions that cannot be explained by the SM. Attention therefore goes to the development of both physics observables and event generation that can assist in detecting implications of new theories.

The top quark plays a central role in this thesis as a possible window to new physics scenarios. The polarization of this heavy particle can be influenced if it is produced with or by new (unseen) particles which affects the distributions of its decay products. This is only possible because the top quark decays before it hadronizes. A second important aspect of our approach is that the top decay is insensitive to leading order to an anomalous Wtb couplings. The polarization is therefore only altered in the production process, making it a good probe for new physics. We demonstrated this in chapter 2. Moreover, we have presented a variety of laboratory frame observables there, that can be used to distinguish between different polarization types which in turn can be related to the parameters of a model.

In chapter 3 we have investigated the implications of this approach for a 2HDM, with a particular focus on the effect of NLO corrections + parton shower. We have constructed asymmetry parameters for both the polar and azimuthal angles of the decay lepton of the top quark. These observables were shown to give complementary information on the mass of a charged Higgs boson, when it is produced in association with the top quark. Moreover, the asymmetry parameters indicate a clear separation from the pure SM case. The effect of NLO corrections + shower slightly weakens the signal as was expected, but the signal remains strong enough to communicate interesting information on the model's parameters. Additionally we have also reviewed the NLO effect on energy observables for the case of a highly boosted top quark. The energy observables are affected by an anomalous Wtb coupling, and therefore are a less robust probe for polarization but still contain interesting information in the region where the angular observables lose their predictive power. The definition of a useful asymmetry parameter was found to be more challenging for these observables. The chapter was completed by employing the asymmetry param-

eter as a probe to distinguish between single top in the Wt channel and $t\bar{t}$ production, a very challenging background. We found that such asymmetries can be very helpful in this separation.

In chapter 4 we investigated the dependence of top polarization on the SUSY parameter space in the context of the MSSM. We started by investigating the effect of stop and neutralino mixing and mass effects for a stop decaying to the top quark in the stop rest frame. Additionally we investigated the influence of the stop boost to the lab frame on the top polarization. We also scanned part of the SUSY parameter space that is consistent with a 125 GeV Higgs and studied the polarization and branching ratio's dependence on the neutralino content. We find that the bino content of the neutralino is a critical parameter and that due to the large size of the hypercharge for the right-handed top, which drives the bino-stop-top coupling, a mixed stop often behaves like a RH stop. The scan also revealed that the LH stop with a higgsino LSP and the RH stop with a bino LSP could be more tightly constrained at the LHC than the same handed stop with switched LSP content. In the analysis of the decay products of the top arising from stop decay in the stop lab frame we noticed a shift in lepton energy and transverse momentum for polarized tops. The spectrum softens (hardens) for a negatively (positively) polarized top compared to an unpolarized top. Finally we studied the asymmetry parameters which are found to be an interesting probe when the masses of the particles involved are known.

Chapter 5 changed focus to event generation with an antenna based shower. A brief review of the formalism driving the VINCIA shower was presented together with the available ordering variables. We proceeded with an investigation of strong ordering implications for $e^+e^- \to 3$ parton phase space. An investigation of the matching of $e^+e^- \to 2$ partons to NLO accuracy showed that matching may be derived for an exclusive fixed-order calculation corresponding to a shower prescription that takes the hadronization scale to infinite resolution. The two-parton case however is special as the lack of additional radiation only allowed adaptation of the weight for incorporating NLO accuracy. Therefore the generalization to an additional parton was presented in chapter 6. This also required a thorough treatment of the renormalization term for the parton shower when fixing the renormalization term of the fixed order description as is generally the case. The matching term was constructed using standardized subtraction terms to allow for a generic description. We investigated the subleading properties of shower algorithms for the various ordering types and found p_T ordering, with a renormalization scale proportional to p_T yields the best agreement with the one-loop matrix element. Comparison to LEP data showed good agreement with an $\alpha_S(m_Z) = 0.122$, in comparison to LO tunes that required a higher value.

We conclude that spin information of the top quark is an interesting window for the discovery of new physics. To implement such an approach in search strategies would require extending the present study to the detector level. The first theoretical investigations however, show promising results. We also conclude that the NLO matching prescription developed for the VINCIA shower allows for consecutive matching. The unitary approach shows impressing results on speed which would enhance the current status for event simulation. Therefore it will be very interesting to extend NLO matching in VINCIA for hadronic initial states.

Appendix A

Infrared singular operators

Here we list the IR singularity operators from [125, 139, 140] as they are used in section 5.2.

$$I^{(1)}_{q\bar{q}}\left(\epsilon, \mu^2/s_{q\bar{q}}\right) = -\frac{e^{\epsilon\gamma}}{2\Gamma\left(1-\epsilon\right)}\left[\frac{1}{\epsilon^2}+\frac{3}{2\epsilon}\right]\mathrm{Re}\left(-\frac{\mu^2}{s_{q\bar{q}}}\right)^{\epsilon} \tag{A.1}$$

$$I^{(1)}_{qg}\left(\epsilon, \mu^2/s_{qg}\right) = -\frac{e^{\epsilon\gamma}}{2\Gamma\left(1-\epsilon\right)}\left[\frac{1}{\epsilon^2}+\frac{5}{3\epsilon}\right]\mathrm{Re}\left(-\frac{\mu^2}{s_{qg}}\right)^{\epsilon} \tag{A.2}$$

$$I^{(1)}_{qg,F}\left(\epsilon, \mu^2/s_{qg}\right) = \frac{e^{\epsilon\gamma}}{2\Gamma\left(1-\epsilon\right)}\frac{1}{6\epsilon}\mathrm{Re}\left(-\frac{\mu^2}{s_{qg}}\right)^{\epsilon} \tag{A.3}$$

Appendix B

One-Loop Amplitudes

B.1 Renormalization

Because a detailed derivation of the calculation of $Z \rightarrow 3$ jets can be found in [143] we restrict ourselves to listing the result in form that is convenient for our purpose. Divergences are regulated using dimensional regularization with $d = 4-2\epsilon$. Our results, before ultraviolet renormalization, are cross-checked with [143] where one must undo the renormalization in their case. In order to cancel the ultraviolet poles we need to renormalize the coupling according to (see also section 6.1.1)

$$\alpha_s^{bare} = \alpha_s(\mu_R^2)\mu^{2\epsilon}\left[1 - \frac{\beta_0}{\epsilon}S_\epsilon\left(\frac{\alpha_s(\mu_R^2)}{4\pi}\right)\left(\frac{\mu^2}{\mu_R^2}\right)^\epsilon\right] \tag{B.1}$$

where

$$\beta_0 = \frac{11N_c - 2n_F}{3} \tag{B.2}$$

and $S_\epsilon = (4\pi)^\epsilon \exp(-\epsilon\,\gamma_E)$ contains the factors characterizing the $\overline{\text{MS}}$ scheme. Due to the renormalization, the leading order calculation will generate a term quadratic in $\alpha_s(\mu_R^2)$,

$$-\frac{\alpha_s(\mu_R)^2}{4\pi}\frac{\beta_0}{\epsilon}\left[1 + \epsilon\ln\left(\frac{\mu_R^2}{\mu^2}\right)\right]\text{Born}\,, \tag{B.3}$$

which directly cancels the ultraviolet poles of the next-to-leading order calculation.

B.2 One-loop Matrix Element

The fixed-order expression relevant to matching in the VINCIA context is the one-loop matrix element normalized by the tree-level one. We decompose this into leading- and

subleading-colour pieces, as follows:

$$\frac{2\,\mathrm{Re}\left[M_3^{(1)}M_3^{0*}\right]}{|M_3^0|^2} = \frac{\alpha_s}{2\pi}(LC + QL + SL)\,, \tag{B.4}$$

with the LC piece containing the C_A part of the gluon loops, the QL one containing the quark loops, proportional to $n_F T_R$, and the SL piece containing the subleading gluon-loop corrections, proportional to $-1/N_C$. As usual in MC applications, we usually refer to "Leading Colour" as including both the N_C and T_R pieces. These are both associated with so-called planar colour flows that are simple to relate to the colour-flow representations used in Monte Carlo event generators, see e.g. [129, 160]. The subleading-colour piece is included below for completeness, but has so far been left out of the NLO matching corrections implemented in the VINCIA code.

The notation of the infrared pole structure of these terms has been written similar to the integrated antenna in [125], with the difference that we have chosen to expand the scale factor μ in the integrated antenna terms in order to obtain explicitly dimensionless logarithms.

The quark has been labelled 1, the anti-quark 2 and the gluon 3.

$$\begin{aligned}
\mathrm{LC} =& N_C \Big[\Big(2I^{(1)}_{qg}(\epsilon,\mu^2/s_{13}) + 2I^{(1)}_{qg}(\epsilon,\mu^2/s_{23}) \Big) \\
&+ \left(-R(y_{13},y_{23}) + \frac{3}{2}\ln\left(\frac{s_{123}}{\mu_R^2}\right) + \frac{5}{3}\ln\left(\frac{\mu_R^2}{s_{23}}\right) + \frac{5}{3}\ln\left(\frac{\mu_R^2}{s_{13}}\right) - 4 \right) \\
&+ \frac{1}{s_{123}\; a_3^0} \Big[2\ln(y_{13}) \left(1 + \frac{s_{13}}{s_{12}+s_{23}} - \frac{s_{23}}{s_{12}+s_{23}} - \frac{s_{23}s_{13}}{4(s_{12}+s_{23})^2} \right) \\
&+ 2\ln(y_{23}) \left(1 - \frac{s_{13}}{s_{12}+s_{13}} + \frac{s_{23}}{s_{12}+s_{13}} - \frac{s_{23}s_{13}}{4(s_{12}+s_{13})^2} \right) \\
&+ \frac{1}{2} \left(\frac{s_{13}}{s_{23}} - \frac{s_{13}}{s_{12}+s_{13}} + \frac{s_{23}}{s_{13}} - \frac{s_{23}}{s_{12}+s_{23}} + \frac{s_{12}}{s_{23}} + \frac{s_{12}}{s_{13}} + 1 \right) \Big] \Big]
\end{aligned} \tag{B.5}$$

$$\begin{aligned}
\mathrm{QL} =& 2n_F T_R \Big[\Big(2I^{(1)}_{qg,F}(\epsilon,\mu^2/s_{13}) + 2I^{(1)}_{qg,F}(\epsilon,\mu^2/s_{23}) \Big) \\
&+ \frac{1}{6} \left(\ln\left(\frac{s_{23}}{\mu_R^2}\right) + \ln\left(\frac{s_{13}}{\mu_R^2}\right) \right) \Big]
\end{aligned} \tag{B.6}$$

$$\begin{aligned}
\mathrm{SL} =& \frac{1}{N_C} \Big[\Big(2I^{(1)}_{q\bar{q}}(\epsilon,\mu^2/s_{12}) \Big) \\
&- \left(4 + \frac{3}{2}\ln(y_{12}) + R(y_{12},y_{13}) + R(y_{12},y_{23}) \right) \\
&+ \frac{1}{s_{123}\; a_3^0} \Big[R(y_{12},y_{13}) \left(\frac{s_{13}}{s_{23}} + 2\frac{s_{12}}{s_{23}} \right) + R(y_{12},y_{23}) \left(\frac{s_{23}}{s_{13}} + 2\frac{s_{12}}{s_{13}} \right) \\
&+ \ln(y_{12}) \left(\frac{4s_{12}}{s_{13}+s_{23}} + \frac{2s_{12}^2}{(s_{13}+s_{23})^2} \right) \\
&+ \frac{1}{2}\ln(y_{13}) \left(\frac{s_{13}}{s_{12}+s_{23}} + \frac{4s_{12}}{s_{12}+s_{23}} + \frac{s_{12}s_{13}}{(s_{12}+s_{23})^2} \right) \\
&+ \frac{1}{2}\ln(y_{23}) \left(\frac{s_{23}}{s_{12}+s_{13}} + \frac{4s_{12}}{s_{12}+s_{13}} + \frac{s_{12}s_{23}}{(s_{12}+s_{13})^2} \right) \\
&- \frac{1}{2} \left(\frac{s_{13}}{s_{23}} - \frac{s_{23}}{s_{13}} - \frac{s_{12}}{s_{23}} - \frac{s_{12}}{s_{13}} + \frac{s_{12}}{s_{12}+s_{13}} + \frac{s_{12}}{s_{12}+s_{23}} + \frac{4s_{12}}{s_{13}+s_{23}} \right) \Big] \Big]
\end{aligned} \tag{B.7}$$

with

$$R(y,z) = \ln(y)\ln(z) - \ln(y)\ln(1-y) - \ln(z)\ln(1-z) + \frac{\pi^2}{6} - \mathrm{Li}_2(y) - \mathrm{Li}_2(z)\,, \tag{B.8}$$

$$a_3^0 \;=\; \frac{|M_3^0|^2}{g_s^2\; C_F |M_2^0|^2} \;=\; \frac{1}{s_{123}} \left(\frac{(1-\epsilon)s_{13}}{s_{23}} + \frac{(1-\epsilon)s_{23}}{s_{13}} + 2\frac{s_{12}s_{123} - \epsilon s_{13}s_{23}}{s_{13}s_{23}} \right) (1-\epsilon)\,, \tag{B.9}$$

and the infrared singular operators, $I^{(1)}$, given in appendix A.

With the one-loop matrix element expressed in this form, cancellation of the infrared poles against the integrated antennae (see below) coming from the shower will be particularly simple and will yield an expression purely dependent on the renormalization scale, μ_R, and on the kinematic invariants s_{12}, s_{23}, and s_{12}, but not on the scale factor μ.

Appendix C

Antenna integrals

In this appendix we list the results of antenna integrals over phase space corresponding to the various evolution variables.

C.1 Strong Ordering Gluon Emission

The expressions for a gluon emitting antenna is given in eq. (5.4). With a redefinition the same antenna function reads

$$a_{g/IK}(y_1,y_2) = \frac{1}{m_{IK}^2}\left[\frac{2(1-y_1-y_2)}{y_1y_2} + \frac{y_1}{y_2} + \frac{y_2}{y_1} - \delta_{Ig}\frac{y_2^2}{y_1} - \delta Kg\frac{y_1^2}{y_2} + C_{00} + C_{10}y_1 + C_{01}y_2\right] \quad \text{(C.1)}$$

where y_1, y_2 correspond to y_{ij}, y_{jk} of eq. (5.6), respectively. Recall that the last three terms serve to give a flexible and explicit way of tracking extra non-singular terms in antennae. The phase space integral over these antenna, as determined by the evolution variable, can be written as

$$\frac{1}{16\pi^2 m_{IK}^2}\int_{Q_E^2}^{m_{IK}^2} a_{g/IK}\,|\mathcal{J}(Q^2,\zeta)|\,\mathrm{d}Q^2\,\mathrm{d}\zeta. \quad \text{(C.2)}$$

All antenna integrals in eq. (6.10) have been written in such a way that they are integrated over their whole invariant mass plus a correction term running from the evolution variable to the total invariant mass. The integrals running over the whole invariant mass contain singular regions and therefore poles while the correction terms yield finite corrections. These finite corrections are discussed per evolution variable below. We define the integrals

$$\mathcal{D}_{Q\zeta} = \frac{1}{m_{IK}^4} \int \mathrm{d}Q^2 \, \mathrm{d}\zeta \, |J| \tag{C.3}$$

$$I_1 = \mathcal{D}_{Q\zeta} \frac{1}{y_1(Q^2,\zeta) y_2(Q^2,\zeta)} \tag{C.4}$$

$$I_2 = \mathcal{D}_{Q\zeta} \frac{1}{y_2(Q^2,\zeta)} = \mathcal{D}_{Q\zeta} \frac{1}{y_1(Q^2,\zeta)} \tag{C.5}$$

$$I_3 = \mathcal{D}_{Q\zeta} \frac{y_1(Q^2,\zeta)}{2y_2(Q^2,\zeta)} = \mathcal{D}_{Q\zeta} \frac{y_2(Q^2,\zeta)}{2y_1(Q^2,\zeta)} \tag{C.6}$$

$$I_4 = \mathcal{D}_{Q\zeta} \frac{y_2^2(Q^2,\zeta)}{2y_1(Q^2,\zeta)} = \mathcal{D}_{Q\zeta} \frac{y_1^2(Q^2,\zeta)}{2y_2(Q^2,\zeta)} \tag{C.7}$$

$$I_5 = \mathcal{D}_{Q\zeta} \left[C_{00} + C_{01} y_1(Q^2,\zeta) + C_{10} y_2(Q^2,\zeta) \right]. \tag{C.8}$$

So that, in these terms, the results read

$$\frac{1}{16\pi^2 m_{IK}^2} \int_{Q_E^2}^{m_{IK}^2} \mathrm{d}Q^2 \mathrm{d}\zeta \, |J(Q^2,\zeta)| \, a_{g/IK} = \frac{1}{8\pi^2} \left(\sum_{i=1}^{5} K_i I_i \right) \tag{C.9}$$

where

$$K_1 = 1\,, \quad K_2 = -2 \quad K_3 = 2, \quad K_4 = -\delta_{Ig} - \delta_{Kg}, \quad K_5 = 1. \tag{C.10}$$

We now turn to specific cases.

C.1.1 Dipole Virtuality

The results for the individual contributing parts of the antenna function as defined in eq. (C.4) - eq. (C.8) with $\xi = \frac{\min(s_{qg}, s_{g\bar{q}})}{m_{IK}^2 - \min(s_{qg}, s_{g\bar{q}})}$ are

$$I_1 = \left[\mathrm{Li}_2\left(\frac{\xi}{1+\xi} \right) - \mathrm{Li}_2\left(\frac{1}{1+\xi} \right) + \ln(\xi) \ln\left(\frac{\xi}{1+\xi} \right) \right]$$

$$I_2 = \left[\frac{-1 + \xi - \ln(\xi)}{1+\xi} \right]$$

$$I_3 = \frac{-3 + 3\xi^2 - (2 + 4\xi)\ln(\xi)}{8\,(1+\xi^2)}$$

$$I_4 = \frac{(\xi-1)\,(11 + \xi\,(20 + 11\xi)) - 6\,(1 + 3\xi\,(1+\xi))\ln(\xi)}{36\,(1+\xi)^3}$$

$$I_5 = \frac{(-1+\xi)^2\,(C_{01} + C_{10} + 2(C_{01} + C_{10})\xi + 3C_{00}(1+\xi))}{12\,(1+\xi^3)}$$

In the case of integration over the $3 \to 4$ splittings, the definition of the integrals remains the same. Only the definition of ξ changes with

$$\xi_{3\to4} = \frac{\min(s_{qg}, s_{g\bar{q}})}{\max(s_{qg}, s_{g\bar{q}}) - \min(s_{qg}, s_{g\bar{q}})} \tag{C.11}$$

C.1.2 Transverse Momentum

The results for the individual contributing parts of the antenna function as defined in eq. (C.4) - eq. (C.8) are

$$I_1 = \left[-\mathrm{Li}_2\left(\frac{1}{2}\left(1+\sqrt{1-y_3^2}\right)\right) + \mathrm{Li}_2\left(\frac{1}{2}\left(1-\sqrt{1-y_3^2}\right)\right) - \frac{1}{2}\ln\left(\frac{4}{y_3^2}\right)\ln\left(\frac{1-\sqrt{1-y_3^2}}{1+\sqrt{1-y_3^2}}\right)\right]$$

$$I_2 = \left[-2\sqrt{1-y_3^2} + \ln\left(\frac{1+\sqrt{1-y_3^2}}{1-\sqrt{1-y_3^2}}\right)\right]$$

$$I_3 = \left[-\frac{1}{2}\sqrt{1-y_3^2} + \frac{1}{4}\ln\left(\frac{1+\sqrt{1-y_3^2}}{1-\sqrt{1-y_3^2}}\right)\right]$$

$$I_4 = \left[-\frac{13\sqrt{1-y_3^2}}{36} + \frac{1}{36}y_3^2\sqrt{1-y_3^2} + \frac{1}{3}\ln\left[1+\sqrt{1-y_3^2}\right] - \frac{\ln\left(y_3^2\right)}{6}\right]$$

$$I_5 = \frac{1}{24}\left[2\left(3C_{00} - (C_{01}+C_{10})(-1+y_3^2)\sqrt{1-y_3^2} - 3\,C_{00}\,y_3^2\ln\left(\frac{1+\sqrt{1-y_3^2}}{1-\sqrt{1-y_3^2}}\right)\right)\right].$$

With $y_3^2 = \frac{Q_3^2}{m_{IK}^2}$ and $m_{IK}^2 = s$. In the case of the $3 \to 4$ splittings the only adaptation takes place in the former definition where m_{IK}^2 is set equal to s_{qg} or $s_{g\bar{q}}$ dependent on which dipole is being integrated over.

C.1.3 Energy Ordering

The results for this evolution parameter are

$$
\begin{aligned}
I_1 = &\operatorname{Li}_2\left(\frac{1}{2}\left(1-\sqrt{1-\Delta}\right)\right) - \operatorname{Li}_2\left(\frac{1}{2}\left(1+\sqrt{1-\Delta}\right)\right) + \frac{1}{2}\left[-2\ \operatorname{atanh}\left(\sqrt{1-\frac{\Delta}{y_3}}\right)\right. \\
&\times \ln(4) + \operatorname{atanh}\left(\sqrt{1-\Delta}\right)\ln(16) + \ln^2\left(1-\sqrt{1-\Delta}\right) - \ln^2\left(1+\sqrt{1-\Delta}\right) \\
&\left. - \ln^2\left(1-\sqrt{1-\frac{\Delta}{y_3}}\right) + \ln^2\left(1+\sqrt{1-\frac{\Delta}{y_3}}\right)\right] - 2\operatorname{Li}_2\left(\frac{1}{2}\left(1-\sqrt{1-\frac{\Delta}{y_3}}\right)\right) \\
&+ \operatorname{Li}_2\left(\frac{1}{2}\left(1+\sqrt{1-\frac{\Delta}{y_3}}\right)\right)
\end{aligned}
$$

$$
I_2 = 2\left[-\sqrt{1-\Delta} + \sqrt{-\Delta+y_3} + \operatorname{atanh}\left(\sqrt{1-\Delta}\right) - \sqrt{y_3}\ \operatorname{atanh}\left(\sqrt{1-\frac{\Delta}{y_3}}\right)\right]
$$

$$
\begin{aligned}
I_3 = &\frac{1}{4}\left[-2\sqrt{1-\Delta} + 2\sqrt{y_3(-\Delta+y_3)} + \ln(2+2\sqrt{1-\Delta}-\Delta) + (-1+y_3)\ln(\Delta)\right. \\
&\left. - y_3\ln(-\Delta+2(y_3+\sqrt{y_3(-\Delta+y_3)}))\right]
\end{aligned}
$$

$$
\begin{aligned}
I_4 = &\frac{1}{36}\left(-13\sqrt{1-\Delta} + \sqrt{1-\Delta}\Delta - \Delta\sqrt{-\Delta+y_3} + 13y_3\sqrt{-\Delta+y_3}\right. \\
&\left. +12\ \operatorname{atanh}\left(\sqrt{1-\Delta}\right) - 12y_3^{\frac{3}{2}}\ \operatorname{atanh}\left(\sqrt{1-\frac{\Delta}{y_3}}\right)\right)
\end{aligned}
$$

$$
\begin{aligned}
I_5 = &\frac{1}{24}\left(2\left(-(C_{01}+C_{10})(-\sqrt{1-\Delta} + \sqrt{1-\Delta}\Delta - \Delta\sqrt{-\Delta+y_3} + y_3\sqrt{-\Delta+y_3}\right.\right. \\
&+3C_{00}(\sqrt{1-\Delta} - \sqrt{y_3(-\Delta+y_3)}) \\
&\left.\left.+3C_{00}\Delta\ln\left(\frac{\Delta - 2(y_3+\sqrt{y_3(-\Delta+y_3)})}{-2(1+\sqrt{1-\Delta})+\Delta}\right)\right)\right)
\end{aligned}
$$

with Δ used as a cut-off on $4p_\perp^2$ and $y_3 = \frac{(s_{qg}+s_{g\bar{q}})^2}{s^2}$.

C.2 Strong Ordering Gluon Splitting

The branching of a gluon splitting into a quark antiquark pair can only take place at the $3 \rightarrow 4$ level splitting. The generation of a gluon splitting takes place through an alternative form of phase space generation than the discussed m_D, $p_\perp$ and E_n variables. Instead phase space is sampled in a triangular surface comparable to m_D ordering, yet in this case using only one cutoff, the Q^2 generated at the $2 \rightarrow 3$ level, to avoid the singular region of the gluon splitting antenna. The gluon splitting antenna is given by

$$a_{\bar{q}/qg}(y_1, y_2) = \frac{1}{m_{IK}^2}\left(\frac{(1-2y_1)}{2y_2} + \frac{y_1^2}{y_2} + C_{00} + C_{01}y_1 + C_{10}y_2\right). \tag{C.12}$$

Because the integration surface is similar for all evolution types only depending on the cutoff Q^2 the integration is demonstrated for all types

$$\begin{aligned} H &= \frac{1}{2m_{IK}^2}\int_{Q_E^2}^{m_{IK}^2} \mathrm{d}s_2 \int_0^{m_{IK}^2 - s_2} \mathrm{d}s_1 a_{\bar{q}/qg}(s_1, s_2) \\ &= \frac{m_{IK}^2}{2}\int_{y_E = \frac{Q_E^2}{m_{IK}^2}}^{1} \mathrm{d}y_2 \int_0^{1-y_2} \mathrm{d}y_1 a_{\bar{q}/qg}(y_1, y_2) \\ &= \frac{1}{72}\left[-13 + 6C_{01} + 6C_{10} + 18C_{00}(-1+y_E)^2 + 18y_E + \right. \\ &\left. y_E\left(-6C_{10}(3 + (-3+y_E)y_E + y_E(-9 + 4y_E + 6C_{01}(-3+2y_E))\right) - 12\ln(y_E)\right] \end{aligned} \tag{C.13}$$

Where the factor a half has been added for the sake of consistency with respect to the treatment of gluon emission. The factor m_{IK}^2 needs to be replaced by either s_{qg} or $s_{g\bar{q}}$ dependent on which dipole is being integrated.

C.3 Smooth Ordering Gluon Emission

The phase space integral in the case of smooth ordering differs from strong ordering by allowing integration over the whole phase space region. The inclusion of a damping factor regulates the accessible region of phase space which generates a different phase space occupancy than in the case of strong ordering. A general form for smooth ordering integration of a gluon emission antenna is

$$\frac{1}{16\pi^2 m_{IK}^2}\int_0^{m_{IK}^2} \mathrm{d}s_1 \int_0^{m_{IK}^2 - s_1} \mathrm{d}s_2 \frac{Q_{E_j}^2}{Q_{E_j}^2 + Q_3^2}\, a_{g/IK}(s_1, s_2) \tag{C.14}$$

Where we use the definition of eq. (C.1) with $s_i = y_i m_{IK}^2$, Q_3^2 denotes the branching scale and Q_{E_j} indicates the evolution variable used for gluon emission. We define the following integrals

$$\mathcal{D}_s = \frac{1}{m_{IK}^4}\int_0^{m_{IK}^2} \mathrm{d}s_1 \int_0^{m_{IK}^2-s_1} \mathrm{d}s_2 \, \frac{Q_{E_j}^2}{Q_{E_j^2}^2+Q_3^2} \tag{C.15}$$

$$L_1 = \mathcal{D}_s \frac{m_{IK}^4}{s_1 s_2} \tag{C.16}$$

$$L_2 = \mathcal{D}_s \frac{m_{IK}^2}{s_1} = \mathcal{D}_s \frac{m_{IK}^2}{s_2} \tag{C.17}$$

$$L_3 = \mathcal{D}_s \frac{s_1}{2s_2} = \mathcal{D}_s \frac{s_2}{2s_1} \tag{C.18}$$

$$L_4 = \mathcal{D}_s \frac{s_1^2}{2m_{IK}^2 s_2} = \mathcal{D}_s \frac{s_2^2}{2m_{IK}^2 s_1} \tag{C.19}$$

$$L_5 = \mathcal{D}_s \left[C_{00} + C_{01}\frac{s_1}{m_{IK}^2} + C_{10}\frac{s_2}{m_{IK}^2} \right]. \tag{C.20}$$

So that, in these terms, the results read

$$\frac{1}{16\pi^2 m_{IK}^2}\int_0^{m_{IK}^2} \mathrm{d}s_1 \int_0^{m_{IK}^2-s_1} \mathrm{d}s_2 \frac{Q_{E_j}^2}{Q_{E_j^2}^2+Q_3^2}\, a_{g/IK} = \frac{1}{8\pi^2}\left(\sum_{i=1}^{5} K_i L_i\right) \tag{C.21}$$

where

$$K_1 = 1\,, \quad K_2 = -2 \quad K_3 = 2, \quad K_4 = -\delta_{Ig} - \delta_{Kg}, \quad K_5 = 1. \tag{C.22}$$

We now turn to specific cases.

C.3.1 Smooth Mass Ordering

The only term from eq. (C.14) that requires specification is the damping factor

$$\frac{Q_{E_j}^2}{Q_{E_j}^2+Q_3^2} = \frac{\min(s_1,s_2)}{\min(s_1,s_2)+\min(s_{qg},s_{g\bar{q}})}. \tag{C.23}$$

The computation of the individual antenna parts will require separating the phase space triangle in two regions ($s_1 > s_2$ and vice versa) in order to make the damping factor

definite. After summing over these two regions we obtain the following values for gluon emission contributions

$$L_1 = 2\left[\ln(2)\ln\left(1+\frac{1}{\frac{1}{2}y_3^2}\right) - \mathrm{Li}_2\left(-\frac{1}{y_3^2}\right) - \mathrm{Li}_2\left(\frac{1}{1+\frac{1}{2}y_3^2}\right) + \mathrm{Li}_2\left(\frac{1}{2+y_3^2}\right)\right]$$

$$\begin{aligned} L_2 =& -1 + 2y_3^2\,\mathrm{arccoth}(1+2y_3^2) - \frac{1}{2}y_3^2\mathrm{arccoth}(1+y_3^2)\ln(4) + \ln\left(2+\frac{1}{\frac{1}{2}y_3^2}\right) \\ &+ \frac{1}{2}y_3^2\left(\mathrm{Li}_2\left(-\frac{1}{y_3^2}\right) + \mathrm{Li}_2\left(\frac{1}{1+\frac{1}{2}y_3^2}\right) - \mathrm{Li}_2\left(\frac{1}{2+y_3^2}\right)\right) \end{aligned}$$

$$\begin{aligned} L_3 =& \frac{1}{8}\left[-3 + \ln(4) + 2\ln\left(1+\frac{1}{y_3^2}\right) + 2y_3^2\left(\frac{1}{2}y_3^2\ln(2)\ln\left(1+\frac{1}{\frac{1}{2}y_3^2}\right)\right.\right. \\ &- \ln\left(\frac{4y_3^2}{1+2y_3^2}\right) + \ln\left(1+\frac{1}{1+2y_3^2}\right)\Big) - y_3^4\left(\mathrm{Li}_2\left(-\frac{1}{y_3^2}\right)\right. \\ &\left.\left.+\mathrm{Li}_2\left(\frac{1}{1+\frac{1}{2}y_3^2}\right) - \mathrm{Li}_2\left(\frac{1}{2+y_3^2}\right)\right)\right] \end{aligned}$$

$$\begin{aligned} L_4 =& \frac{1}{36}\left(-11 - \frac{3}{2}y_3^2(1+y_3^2) - 6\ln\left(\frac{2y_3^2}{1+2y_3^2}\right) + \frac{3}{2}y_3^2\left(4\left(3+\frac{1}{2}y_3^4\right)\right.\right. \\ &\times \arccos(1+2y_3^2) - \ln(8) + 3y_3^2\left(-\frac{1}{2}y_3^2\arccos(1+y_3^2)\ln(4) - \ln(2y_3^2)\right. \\ &\left.\left.+\ln(2+4y_3^2) + \ln\left(1+\frac{1}{1+2y_3^2}\right)\right)\right) + 6\ln\left(2+\frac{2}{1+2y_3^2}\right) \\ &+\frac{18}{8}y_3^6\,\mathrm{Li}_2\left(-\frac{1}{y_3^2}\right) + \mathrm{Li}_2\left(\frac{1}{1+\frac{1}{2}y_3^2}\right) - \mathrm{Li}_2\left(\frac{1}{2+y_3^2}\right)\Big) \end{aligned}$$

$$\begin{aligned} L_5 =& \frac{1}{48}\left[4(3C_{00}+C_{01}+C_{10}) + 3(8C_{00}+C_{01}+C_{10})y_3^2 - 6(C_{01}+C_{10})y_3^4\right. \\ &\left.-12y_3^2(1+y_3^2)(4C_{00}+C_{01}+C_{10}-(C_{01}+C_{10})y_3^2)\,\mathrm{arccoth}\left(1+2y_3^2\right)\right]. \end{aligned}$$

With $y_3^2 = \frac{2\min(s_{qg},s_{g\bar{q}})}{m_{IK}^2}$.

C.3.2 Smooth Transverse Momentum Ordering

In the case of smooth ordering for transverse momentum we find the following result for the ordering requirement

$$\frac{Q_{E_j}^2}{Q_{E_j}^2+Q_3^2} = \frac{\frac{s_1 s_2}{m_{IK}^2}}{\frac{s_1 s_2}{m_{IK}^2} + \frac{s_{qg}s_{g\bar{q}}}{s}}. \tag{C.24}$$

Where m_{IK}^2 should be replaced by s_{qg} or $s_{g\bar{q}}$ dependent on the dipole of integration. In combination with eq. (C.14) we find the following results for the partial gluon emission antenna parts

$$L_1 = -\mathrm{Li}_2\left(-\frac{2}{-1+\sqrt{1+y_3^2}}\right) - \mathrm{Li}_2\left(\frac{2}{1+\sqrt{1+y_3^2}}\right)$$

$$L_2 = -2 - \sqrt{1+y_3^2}\ln\left(\frac{-1+\sqrt{1+y_3^2}}{1+\sqrt{1+y_3^2}}\right)$$

$$L_3 = -\frac{1}{2} - \frac{1}{4}\sqrt{1+y_3^2}\ln\left(\frac{-1+\sqrt{1+y_3^2}}{1+\sqrt{1+y_3^2}}\right)$$

$$\begin{aligned} L_4 =& \frac{1}{36\sqrt{1+y_3^2}}\left[-\sqrt{1+y_3^2}(13+3y_3^2) + 3(1+\frac{1}{4}y_3^2)(1+y_3^2)\right. \\ &\left.\times\left(-\ln\left(1-\frac{\sqrt{1+y_3^2}}{1+\frac{1}{2}y_3^2}\right)+\ln\left(1+\frac{\sqrt{1+y_3^2}}{1+\frac{1}{2}y_3^2}\right)\right)\right] \end{aligned}$$

$$\begin{aligned} L_5 =& \frac{1}{12}\left(3C_{00}+C_{01}+C_{10}+3(C_{01}+C_{10})y_3^2\right. \\ &-\frac{3}{2}(C_{01}+C_{10})y_3^2\sqrt{1+y_3^2}\left(-\ln\left(1-\frac{1}{\sqrt{1+y_3^2}}\right)+\ln\left(1+\frac{1}{\sqrt{1+y_3^2}}\right)\right) \\ &\left.+\frac{3}{2}C_{00}y_3^2\left(\mathrm{Li}_2\left(-\frac{2}{-1+\sqrt{1+y_3^2}}\right)+\mathrm{Li}_2\left(\frac{2}{1+\sqrt{1+y_3^2}}\right)\right)\right). \end{aligned}$$

With $y_3^2 = \frac{4 s_{qg} s_{g\bar{q}}}{s\, m_{IK}^2}$

C.4 Smooth Ordering Gluon Splitting

Additionally we also need to consider the gluon splitting antenna function for smooth ordering. Similar to the strong ordering case, the separate generation of gluon splitting variables allows for a new choice for evolution variable and thereby a different phase space surface. As in the case of gluon emission we allow for integration over the whole phase space, using the damping factor to limit the accessible area. A general notation is the following

$$G = \frac{1}{m_{IK}^2}\int_0^{m_{IK}^2} \mathrm{d}s_1 \int_0^{m_{IK}^2-s_1} \mathrm{d}s_2 \frac{Q_{E_j}^2}{Q_{E_j^2}^2+Q_3^2}\, a_{\bar{q}/qg}(s_1,s_2). \tag{C.25}$$

With the definition for the gluon splitting antenna as in eq. (C.12).

C.4.1 Dipole Mass

With the gluon splitting antenna as defined in eq. (C.12) and the phase space integral eq. (C.25) we find the following result for the dipole mass evolution type

$$\begin{aligned} G =& \frac{1}{72 s_P^3} \big(-12(s_P^3 + 3(-1 + 2C_{00} + C_{10}) y_3^2 s_P^2 + 3(-1 + 2C_{00} - 2C_{01} + 2C_{10} \\ &+ 2C_{10}) y_3^4 s_P + (-2 - 6C_{01} + 3C_{10}) y_3^6) \operatorname{arctanh}\left(\frac{s_P}{2y_3^2 + s_P}\right) \\ &+ s_P \big((-13 + 18C_{00} + 6C_{01} + 6C_{10}) s_P^2 + 3(-4 + 12C_{00} - 6C_{01} + 9C_{10}) y_3^2 s_P \\ &-6(2 + 6C_{01} - 3C_{10}) y_3^4 + 18 s_P^2 \ln\left(\frac{s_P + y_3^2}{y_3^2}\right)\big)\big) \end{aligned} \tag{C.26}$$

With $y_3 = \frac{N' \min(s_{qg}, s_{g\bar{q}})}{s}$ and $s_P = \max(s_{qg}, s_{g\bar{q}})/s$. Note that the gluon splitting antenna has been defined with the singularity in y_2 which determines the form of the damping factor.

C.4.2 Transverse Momentum

With the gluon splitting antenna defined in eq. (C.12) and the phase space integral eq. (C.25) we find the following result for the transverse momentum evolution type

$$\begin{aligned} G =& \frac{1}{72}\Big(-13 + 18C_{00} + 6C_{01} + 6C_{10} + 3(-4 + 12C_{00} - 6C_{01} + 9C_{10}) y_3^2 \\ &- 6(2 + 6C_{01} - 3C_{10}) y_3^2 + 36 y_3^2 \operatorname{acoth}(1 + 2y_3^2) - 6(-2 + y_3^2(6C_{00}(1 + y_3^2) \\ &+ 3C_{10}(1 + y_3^2)^2 - y_3^2(3 + 2y_3^2 + 6C_{01}(1 + y_3^2)))) \ln\left(1 + \frac{1}{y_3^2}\right)\Big) \end{aligned} \tag{C.27}$$

With $y_3^2 = \frac{N s_{qg} s_{g\bar{q}}}{s\, m_{IK}^2}$.

Appendix D

NLO Tune Parameters

In tab. D.1 below, we list the perturbative and non-perturbative fragmentation parameters for the Nikhef NLO tune of VINCIA. For reference, we compare them to the current (LO) default Jeppsson 5 tune, which was used for comparisons to LO VINCIA in this paper.

Parameter	NLO Tune (Nikhef)	LO Tune (Jeppsson 5)	Comment
! * alphaS			
Vincia:alphaSvalue	= 0.122	= 0.139	! alphaS(mZ) value
Vincia:alphaSkMu	= 1.0	= 1.0	! Renormalization-scale prefactor
Vincia:alphaSorder	= 2	= 1	! Running order
Vincia:alphaSmode	= 1	= 1	! muR = pT:emit and Q:split
Vincia:alphaScmw	= on	= off	! CMW rescaling of Lambda on/off
! * Shower evolution and IR cutoff			
Vincia:evolutionType	= 1	= 1	! pT-evolution
Vincia:orderingMode	= 2	= 2	! Smooth ordering
Vincia:pTnormalization	= 4.	= 4.	! QT = 2pT
Vincia:cutoffType	= 1	= 1	! Cutoff taken in pT
Vincia:cutoffScale	= 0.8	= 0.6	! Cutoff value (in GeV)
! * Longitudinal string fragmentation parameters			
StringZ:aLund	= 0.40	= 0.38	! Lund FF a (hard fragmentation supp)
StringZ:bLund	= 0.85	= 0.90	! Lund FF b (soft fragmentation supp)
StringZ:aExtraDiquark	= 1.0	= 1.0	! Extra a to suppress hard baryons
! * pT in string breakups			
StringPT:sigma	= 0.29	= 0.275	! Soft pT in string breaks (in GeV)
StringPT:enhancedFraction	= 0.01	= 0.01	! Fraction of breakups with enhanced pT
StringPT:enhancedWidth	= 2.0	= 2.0	! Enhancement factor
! * String breakup flavour parameters			
StringFlav:probStoUD	= 0.215	= 0.215	! Strangeness-to-UD ratio
StringFlav:mesonUDvector	= 0.45	= 0.45	! Light-flavour vector suppression
StringFlav:mesonSvector	= 0.65	= 0.65	! Strange vector suppression
StringFlav:mesonCvector	= 0.80	= 0.80	! Charm vector suppression
StringFlav:probQQtoQ	= 0.083	= 0.083	! Diquark rate (for baryon production)
StringFlav:probSQtoQQ	= 1.00	= 1.00	! Optional Strange diquark suppression
StringFlav:probQQ1toQQ0	= 0.031	= 0.031	! Vector diquark suppression
StringFlav:etaSup	= 0.68	= 0.68	! Eta suppression
StringFlav:etaPrimeSup	= 0.11	= 0.11	! Eta' suppression
StringFlav:decupletSup	= 1.0	= 1.0	! Optional Spin-3/2 Baryon Suppression

Table D.1: Parameters of the "Nikhef" NLO tune, compared to those of the "Jeppsson 5" LO tune.

Bibliography

[1] R. P. Feynman, *Very high-energy collisions of hadrons*, *Phys.Rev.Lett.* **23** (1969) 1415–1417.

[2] J. Bjorken and E. A. Paschos, *Inelastic Electron Proton and gamma Proton Scattering, and the Structure of the Nucleon*, *Phys.Rev.* **185** (1969) 1975–1982.

[3] J. C. Collins, D. E. Soper, and G. F. Sterman, *Factorization of Hard Processes in QCD*, *Adv.Ser.Direct.High Energy Phys.* **5** (1988) 1–91, [hep-ph/0409313].

[4] R. M. Godbole, S. D. Rindani, and R. K. Singh, *Lepton distribution as a probe of new physics in production and decay of the t quark and its polarization*, *JHEP* **12** (2006) 021, [hep-ph/0605100].

[5] C. Bouchiat and L. Michel, *Mesure de la polarisation des electrons relativistes*, *Nuclear Physics* **5** (1958) 416 – 434.

[6] L. Michel, *Covariant description of polarization*, *Il Nuovo Cimento (1955-1965)* **14** (1959) 95–104.

[7] W. Bernreuther, *Top quark physics at the LHC*, *J.Phys.G* **G35** (2008) 083001, [arXiv:0805.1333].

[8] A. Brandenburg, Z. Si, and P. Uwer, *QCD corrected spin analyzing power of jets in decays of polarized top quarks*, *Phys.Lett.* **B539** (2002) 235–241, [hep-ph/0205023].

[9] R. M. Godbole, K. Rao, S. D. Rindani, and R. K. Singh, *On measurement of top polarization as a probe of $t\bar{t}$ production mechanisms at the LHC*, *JHEP* **11** (2010) 144, [arXiv:1010.1458].

[10] R. M. Godbole, S. D. Rindani, K. Rao, and R. K. Singh, *Top polarization as a probe of new physics*, *AIP Conf.Proc.* **1200** (2010) 682–685, [arXiv:0911.3622].

[11] J. A. Aguilar-Saavedra and J. Bernabeu, *W polarisation beyond helicity fractions in top quark decays*, *Nucl. Phys.* **B840** (2010) 349–378, [arXiv:1005.5382].

[12] J. Shelton, *Polarized tops from new physics: signals and observables*, *Phys. Rev.* **D79** (2009) 014032, [arXiv:0811.0569].

[13] J. Alwall, M. Herquet, F. Maltoni, O. Mattelaer, and T. Stelzer, *MadGraph 5 : Going Beyond*, *JHEP* **1106** (2011) 128, [arXiv:1106.0522].

[14] J. Alwall, P. Demin, S. de Visscher, R. Frederix, M. Herquet, *et. al.*, *MadGraph/MadEvent v4: The New Web Generation*, *JHEP* **0709** (2007) 028, [arXiv:0706.2334].

[15] M. Whalley, D. Bourilkov, and R. Group, *The Les Houches accord PDFs (LHAPDF) and LHAGLUE*, hep-ph/0508110.

[16] S. P. Martin, *A Supersymmetry primer*, hep-ph/9709356.

[17] K. Huitu, S. Kumar Rai, K. Rao, S. D. Rindani, and P. Sharma, *Probing top charged-Higgs production using top polarization at the Large Hadron Collider*, *JHEP* **04** (2011) 026, [arXiv:1012.0527].

[18] J. Baglio, M. Beccaria, A. Djouadi, G. Macorini, E. Mirabella, *et. al.*, *The Left-Right asymmetry of top quarks in associated top-charged Higgs bosons at the LHC as a probe of the tanβ parameter*, arXiv:1109.2420.

[19] C. Weydert *et. al.*, *Charged Higgs boson production in association with a top quark in MC@NLO*, *Eur. Phys. J.* **C67** (2010) 617–636, [arXiv:0912.3430].

[20] S. Frixione, E. Laenen, P. Motylinski, B. R. Webber, and C. D. White, *Single-top hadroproduction in association with a W boson*, *JHEP* **07** (2008) 029, [arXiv:0805.3067].

[21] S. Frixione and B. R. Webber, *Matching NLO QCD computations and parton shower simulations*, *JHEP* **0206** (2002) 029, [hep-ph/0204244].

[22] S. Frixione and B. R. Webber, *The MC@NLO 3.4 Event Generator*, arXiv:0812.0770.

[23] S. Frixione, F. Stoeckli, P. Torrielli, B. R. Webber, and C. D. White, *The MC@NLO 4.0 Event Generator*, arXiv:1010.0819.

[24] S. Frixione, P. Nason, and B. R. Webber, *Matching NLO QCD and parton showers in heavy flavor production*, *JHEP* **0308** (2003) 007, [hep-ph/0305252].

[25] S. Frixione, E. Laenen, P. Motylinski, and B. R. Webber, *Angular correlations of lepton pairs from vector boson and top quark decays in Monte Carlo simulations*, *JHEP* **04** (2007) 081, [hep-ph/0702198].

[26] S. Frixione, P. Nason, and C. Oleari, *Matching NLO QCD computations with Parton Shower simulations: the POWHEG method*, *JHEP* **0711** (2007) 070, [arXiv:0709.2092].

[27] W. T. Giele, D. A. Kosower, and P. Z. Skands, *A Simple shower and matching algorithm*, *Phys.Rev.* **D78** (2008) 014026, [arXiv:0707.3652].

[28] S. Frixione, P. Nason, and G. Ridolfi, *A Positive-weight next-to-leading-order Monte Carlo for heavy flavour hadroproduction*, *JHEP* **0709** (2007) 126, [arXiv:0707.3088].

[29] E. Re, *Single-top Wt-channel production matched with parton showers using the POWHEG method*, *Eur.Phys.J.* **C71** (2011) 1547, [arXiv:1009.2450].

[30] C. Weydert, *Associated production of top quarks and charged Higgs bosons at next-to-leading order*, *IL NUOVO CIMENTO 33 C* (2010) [arXiv:1011.6249].

[31] N. Kauer and D. Zeppenfeld, *Finite width effects in top quark production at hadron colliders*, *Phys. Rev.* **D65** (2002) 014021, [hep-ph/0107181].

[32] B. P. Kersevan and I. Hinchliffe, *A consistent prescription for the production involving massive quarks in hadron collisions*, *JHEP* **09** (2006) 033, [hep-ph/0603068].

[33] A. Denner, S. Dittmaier, S. Kallweit, and S. Pozzorini, *NLO QCD corrections to WWbb production at hadron colliders*, *Phys.Rev.Lett.* **106** (2011) 052001, [arXiv:1012.3975].

[34] G. Bevilacqua, M. Czakon, A. van Hameren, C. G. Papadopoulos, and M. Worek, *Complete off-shell effects in top quark pair hadroproduction with leptonic decay at next-to-leading order*, *JHEP* **1102** (2011) 083, [arXiv:1012.4230].

[35] J. M. Campbell and F. Tramontano, *Next-to-leading order corrections to W t production and decay*, *Nucl. Phys.* **B726** (2005) 109–130, [hep-ph/0506289].

[36] S. Zhu, *Next-to-leading order QCD corrections to b g $\rightarrow$ t W- at the CERN Large Hadron Collider*, *Phys. Lett.* **B524** (2002) 283–288.

[37] W. Beenakker, R. Hopker, M. Spira, and P. Zerwas, *Squark and gluino production at hadron colliders*, *Nucl.Phys.* **B492** (1997) 51–103, [hep-ph/9610490].

[38] T. Plehn, *Production of supersymmetric particles at high-energy colliders*, hep-ph/9809319. Ph.D. Thesis.

[39] T. Plehn and C. Weydert, *Charged Higgs production with a top in MC@NLO*, in *PoS CHARGED2010*, p. 026, 2010. arXiv:1012.3761.

[40] T. Binoth, D. Goncalves-Netto, D. Lopez-Val, K. Mawatari, T. Plehn, *et. al.*, *Automized Squark-Neutralino Production to Next-to-Leading Order*, arXiv:1108.1250.

[41] C. D. White, S. Frixione, E. Laenen, and F. Maltoni, *Isolating Wt production at the LHC*, *JHEP* **11** (2009) 074, [arXiv:0908.0631].

[42] A. D. Martin, W. J. Stirling, R. S. Thorne, and G. Watt, *Parton distributions for the LHC*, *Eur. Phys. J.* **C63** (2009) 189–285, [arXiv:0901.0002].

[43] A. D. Martin, W. J. Stirling, R. S. Thorne, and G. Watt, *Uncertainties on $alpha_S$ in global PDF analyses and implications for predicted hadronic cross sections*, *Eur. Phys. J.* **C64** (2009) 653–680, [arXiv:0905.3531].

[44] A. D. Martin, W. J. Stirling, R. S. Thorne, and G. Watt, *Heavy-quark mass dependence in global PDF analyses and 3- and 4-flavour parton distributions*, *Eur. Phys. J.* **C70** (2010) 51–72, [arXiv:1007.2624].

[45] A. Djouadi, J. Kalinowski, and M. Spira, *HDECAY: A program for Higgs boson decays in the standard model and its supersymmetric extension*, *Comput. Phys. Commun.* **108** (1998) 56–74, [hep-ph/9704448].

[46] **CDF** Collaboration, T. Aaltonen *et. al.*, *First Observation of Electroweak Single Top Quark Production*, *Phys.Rev.Lett.* **103** (2009) 092002, [arXiv:0903.0885].

[47] **D0** Collaboration, V. M. Abazov *et. al.*, *Observation of Single Top-Quark Production*, *Phys. Rev. Lett.* **103** (2009) 092001, [arXiv:0903.0850].

[48] **D0** Collaboration, V. M. Abazov *et. al.*, *Model-independent measurement of t-channel single top quark production in $p\bar{p}$ collisions at $\sqrt{s} = 1.96$ TeV*, *Phys.Lett.* **B705** (2011) 313–319, [arXiv:1105.2788].

[49] **CDF Collaboration, D0 Collaboration** Collaboration, J. Joshi, *Single Top Quark Measurements at the Tevatron*, .

[50] **ATLAS Collaboration** Collaboration, *Measurement of t-Channel Single Top-Quark Production in pp Collisions at sqrt(s) = 8 TeV with the ATLAS detector*, .

[51] **CMS** Collaboration, S. Chatrchyan *et. al.*, *Measurement of the t-channel single top quark production cross section in pp collisions at sqrt(s) = 7 TeV*, *Phys. Rev. Lett.* **107** (2011) 091802, [arXiv:1106.3052].

[52] R. Schwienhorst and f. t. A. collaboration, *Single top-quark production with the ATLAS detector in pp collisions at sqrt(s)=7TeV*, arXiv:1110.2192.

[53] B. W. Harris, E. Laenen, L. Phaf, Z. Sullivan, and S. Weinzierl, *The fully differential single top quark cross section in next-to-leading order QCD*, *Phys. Rev.* **D66** (2002) 054024, [hep-ph/0207055].

[54] J. M. Campbell, R. K. Ellis, and F. Tramontano, *Single top production and decay at next-to-leading order*, *Phys. Rev.* **D70** (2004) 094012, [hep-ph/0408158].

[55] Q.-H. Cao and C. P. Yuan, *Single top quark production and decay at next-to-leading order in hadron collision*, *Phys. Rev.* **D71** (2005) 054022, [hep-ph/0408180].

[56] Q.-H. Cao, R. Schwienhorst, and C. P. Yuan, *Next-to-leading order corrections to single top quark production and decay at Tevatron. I: s-channel process*, *Phys. Rev.* **D71** (2005) 054023, [hep-ph/0409040].

[57] Q.-H. Cao, R. Schwienhorst, J. A. Benitez, R. Brock, and C. P. Yuan, *Next-to-leading order corrections to single top quark production and decay at the Tevatron. II: t-channel process*, *Phys. Rev.* **D72** (2005) 094027, [hep-ph/0504230].

[58] S. Frixione, E. Laenen, P. Motylinski, and B. R. Webber, *Single-top production in MC@NLO*, *JHEP* **03** (2006) 092, [hep-ph/0512250].

[59] S. Alioli, P. Nason, C. Oleari, and E. Re, *NLO single-top production matched with shower in POWHEG: s- and t-channel contributions*, *JHEP* **09** (2009) 111, [arXiv:0907.4076].

[60] N. Kidonakis, *Next-to-next-to-leading-order collinear and soft gluon corrections for t-channel single top quark production*, *Phys.Rev.* **D83** (2011) 091503, [arXiv:1103.2792].

[61] P. Falgari, F. Giannuzzi, P. Mellor, and A. Signer, *Off-shell effects for t-channel and s-channel single-top production at NLO in QCD*, *Phys.Rev.* **D83** (2011) 094013, [arXiv:1102.5267].

[62] P. Falgari, P. Mellor, and A. Signer, *Production-decay interferences at NLO in QCD for t-channel single-top production*, *Phys.Rev.* **D82** (2010) 054028, [arXiv:1007.0893].

[63] Q.-H. Cao, J. Wudka, and C. P. Yuan, *Search for New Physics via Single Top Production at the LHC*, *Phys. Lett.* **B658** (2007) 50–56, [arXiv:0704.2809].

[64] Z. Sullivan, *Angular correlations in single-top-quark and W j j production at next-to-leading order*, *Phys. Rev.* **D72** (2005) 094034, [hep-ph/0510224].

[65] Z. Sullivan, *Understanding single-top-quark production and jets at hadron colliders*, *Phys. Rev.* **D70** (2004) 114012, [hep-ph/0408049].

[66] P. Motylinski, *Angular correlations in t-channel single top production at the LHC*, *Phys. Rev.* **D80** (2009) 074015, [arXiv:0905.4754].

[67] T. M. P. Tait, *The tW^- mode of single top production*, *Phys. Rev.* **D61** (2000) 034001, [hep-ph/9909352].

[68] S. Catani, Y. L. Dokshitzer, M. Seymour, and B. Webber, *Longitudinally invariant K_t clustering algorithms for hadron hadron collisions*, *Nucl.Phys.* **B406** (1993) 187–224.

[69] I. J. Aitchison, *Supersymmetry and the MSSM: An Elementary introduction*, hep-ph/0505105.

[70] **ATLAS** Collaboration, G. Aad *et. al.*, *Search for Squarks and Gluinos Using Final States with Jets and Missing Transverse Momentum with the ATLAS Detector in $\sqrt{s}$ = 7 TeV Proton-Proton Collisions*, *Phys. Lett.* **B710** (2012) 67, [arXiv:1109.6572].

[71] **ATLAS** Collaboration, *Search for squarks and gluinos with the ATLAS detector using final states with jets and missing transverse momentum and $5.8fb^{-1}$ of $\sqrt{s} = 8$TeV proton-proton collision data*, 2012. ATLAS-CONF-2012-133, see http://atlas.web.cern.ch/Atlas/GROUPS/PHYSICS/CONFNOTES/.

[72] **CMS** Collaboration, S. Chatrchyan *et. al.*, *Search for Supersymmetry at the LHC in Events with Jets and Missing Transverse Energy*, *Phys. Rev. Lett.* **107** (2011) 221804, [arXiv:1109.2352].

[73] **CMS** Collaboration, S. Chatrchyan *et. al.*, *Search for supersymmetry in hadronic final states using MT2 in pp collisions at $\sqrt{s} = 7$ TeV*, *JHEP* **1210** (2012) 018, [arXiv:1207.1798].

[74] W. Fischler, H. P. Nilles, J. Polchinski, S. Raby, and L. Susskind, *Vanishing Renormalization of the D Term in Supersymmetric U(1) Theories*, *Phys.Rev.Lett.* **47** (1981) 757.

[75] R. K. Kaul and P. Majumdar, *Naturalness in a globally supersymmetric gauge theory with elementary scalar fields*, 1981. Print-81-0373 (BANGALORE).

[76] R. K. Kaul and P. Majumdar, *Cancellation of Quadratically divergent mass corrections in globally supersymmetric spontaneously broken gauge theories*, *Nucl.Phys.* **B199** (1982) 36.

[77] R. K. Kaul, *Gauge Hierarchy in a Supersymmetric Model*, *Phys.Lett.* **B109** (1982) 19.

[78] S. Dimopoulos and H. Georgi, *Softly Broken Supersymmetry and SU(5)*, *Nucl.Phys.* **B193** (1981) 150.

[79] R. Barbieri and G. Giudice, *Upper Bounds on Supersymmetric Particle Masses*, *Nucl.Phys.* **B306** (1988) 63.

[80] B. de Carlos and J. Casas, *One loop analysis of the electroweak breaking in supersymmetric models and the fine tuning problem*, *Phys.Lett.* **B309** (1993) 320–328, [hep-ph/9303291].

[81] C. Brust, A. Katz, S. Lawrence, and R. Sundrum, *SUSY, the Third Generation and the LHC*, *JHEP* **1203** (2012) 103, [arXiv:1110.6670].

[82] **ATLAS** Collaboration, G. Aad *et. al.*, *Observation of a new particle in the search for the Standard Model Higgs boson with the ATLAS detector at the LHC*, *Phys.Lett.B* (2012) [arXiv:1207.7214].

[83] **CMS** Collaboration, S. Chatrchyan *et. al.*, *Observation of a new boson at a mass of 125 GeV with the CMS experiment at the LHC*, *Phys.Lett.B* (2012) [arXiv:1207.7235].

[84] A. Arbey, M. Battaglia, A. Djouadi, and F. Mahmoudi, *The Higgs sector of the phenomenological MSSM in the light of the Higgs boson discovery*, *JHEP* **1209** (2012) 107, [arXiv:1207.1348].

[85] V. Barger, P. Huang, M. Ishida, and W.-Y. Keung, *Scalar-Top Masses from SUSY Loops with 125 GeV mh and Precise Mw*, arXiv:1206.1777.

[86] W. Beenakker, R. Hopker, and M. Spira, *PROSPINO: A Program for the production of supersymmetric particles in next-to-leading order QCD*, hep-ph/9611232.

[87] W. Beenakker, S. Brensing, M. Krämer, A. Kulesza, E. Laenen, and I. Niessen, *Supersymmetric Top and Bottom Squark Production at Hadron Colliders*, *JHEP* **8** (2010) 1, [arXiv:1006.4771].

[88] W. Beenakker, S. Brensing, M. Krämer, A. Kulesza, E. Laenen, L. Motyka, and I. Niessen, *Squark and Gluino Hadroproduction*, *Int. J. Mod. Phys.* **A26** (2011) 2637, [arXiv:1105.1110].

[89] W. Beenakker, S. Brensing, M. Krämer, A. Kulesza, E. Laenen, and I. Niessen, "NLL-fast, a computer program which computes the squark and gluino hadroproduction cross sections including NLO SUSY-QCD corrections and the resummation of soft gluon emission at NLL accuracy." See http://web.physik.rwth-aachen.de/service/wiki/bin/view/kraemer/squarksandgluinos.

[90] **ATLAS** Collaboration, G. Aad *et. al.*, *Search for a supersymmetric partner to the top quark in final states with jets and missing transverse momentum at* $\sqrt{s} = 7$ *TeV with the ATLAS detector*, arXiv:1208.1447.

[91] **ATLAS** Collaboration, G. Aad *et. al.*, *Search for direct top squark pair production in final states with one isolated lepton, jets, and missing transverse momentum in* $\sqrt{s} = 7$ *TeV pp collisions using 4.7* fb^{-1} *of ATLAS data*, arXiv:1208.2590.

[92] **ATLAS** Collaboration, G. Aad *et. al.*, *Search for a heavy top-quark partner in final states with two leptons with the ATLAS detector at the LHC*, *JHEP* **1211** (2012) 094, [arXiv:1209.4186].

[93] **ATLAS** Collaboration, G. Aad *et. al.*, *Search for light top squark pair production in final states with leptons and b^- jets with the ATLAS detector in $\sqrt{s} = 7$ TeV proton-proton collisions*, arXiv:1209.2102.

[94] **CMS** Collaboration, S. Chatrchyan *et. al.*, *Search for direct top squark pair production in events with a single isolated lepton, jets and missing transverse energy at $\sqrt{s} = 8$ tev*, 2012. CMS-PAS-SUS-12-023.

[95] **CMS** Collaboration, S. Chatrchyan *et. al.*, *Scalar top quark search with jets and missing momentum in pp collisions at $\sqrt{s} = 7$ tev*, 2012. CMS-PAS-SUS-11-030.

[96] **CMS** Collaboration, S. Chatrchyan *et. al.*, *Search for pair production of third-generation leptoquarks and top squarks in pp collisions at $\sqrt{s} = 7$ TeV*, arXiv:1210.5629.

[97] H. A. Weber, *Search for third generation squarks at the lhc (status of light stop and sbottom searches)*, Tech. Rep. CMS-CR-2012-184. CERN-CMS-CR-2012-184, CERN, Geneva, Aug, 2012.

[98] E. Boos, H. Martyn, G. A. Moortgat-Pick, M. Sachwitz, A. Sherstnev, *et. al.*, *Polarization in sfermion decays: Determining tan beta and trilinear couplings*, *Eur.Phys.J.* **C30** (2003) 395–407, [hep-ph/0303110].

[99] M. Drees, R. Godbole, and P. Roy, *Theory and Phenomenology of Sparticles*. World Scientific, 2004.

[100] M. Drees, R. Godbole, and P. Roy, *Theory and phenomenology of Sparticles: an account of four-dimensional N=1 supersymmetry in high-energy physics*. World Scientific, Singapore, 2004.

[101] A. Djouadi, J.-L. Kneur, and G. Moultaka, *SuSpect: A Fortran code for the supersymmetric and Higgs particle spectrum in the MSSM*, *Comput.Phys.Commun.* **176** (2007) 426–455, [hep-ph/0211331].

[102] J. Pumplin, D. Stump, J. Huston, H. Lai, P. M. Nadolsky, *et. al.*, *New generation of parton distributions with uncertainties from global QCD analysis*, *JHEP* **0207** (2002) 012, [hep-ph/0201195].

[103] W. Beenakker, M. Kramer, T. Plehn, and M. Spira, *SUSY particle production at the Tevatron*, hep-ph/9810290.

[104] W. Beenakker, M. Krämer, T. Plehn, M. Spira, and P. M. Zerwas, *Stop production at hadron colliders*, *Nucl. Phys.* **B515** (1998) 3–14, [hep-ph/9710451].

[105] B. Bhattacherjee, S. K. Mandal, and M. Nojiri, *Top Polarization and Stop Mixing from Boosted Jet Substructure*, arXiv:1211.7261.

[106] R. M. Godbole, S. D. Rindani, and R. K. Singh, *Study of CP property of the Higgs at a photon collider using gamma gamma → t anti-t → lX*, *Phys.Rev.* **D67** (2003) 095009, [hep-ph/0211136].

[107] S. D. Rindani and P. Sharma, *Probing anomalous tbW couplings in single-top production using top polarization at the Large Hadron Collider*, arXiv:1107.2597.

[108] P. Nason, *A New method for combining NLO QCD with shower Monte Carlo algorithms*, *JHEP* **0411** (2004) 040, [hep-ph/0409146].

[109] S. Alioli, P. Nason, C. Oleari, and E. Re, *A general framework for implementing NLO calculations in shower Monte Carlo programs: the POWHEG BOX*, *JHEP* **1006** (2010) 043, [arXiv:1002.2581].

[110] W. Giele, D. Kosower, and P. Skands, *Higher-Order Corrections to Timelike Jets*, *Phys.Rev.* **D84** (2011) 054003, [arXiv:1102.2126].

[111] G. Altarelli and G. Parisi, *Asymptotic Freedom in Parton Language*, *Nucl. Phys.* **B126** (1977) 298.

[112] M. Bengtsson and T. Sjöstrand, *Coherent Parton Showers Versus Matrix Elements: Implications of PETRA - PEP Data*, *Phys.Lett.* **B185** (1987) 435.

[113] A. Gehrmann-De Ridder, M. Ritzmann, and P. Skands, *Timelike Dipole-Antenna Showers with Massive Fermions*, *Phys.Rev.* **D85** (2012) 014013, [arXiv:1108.6172]. 50 pages.

[114] G. Marchesini and B. Webber, *Simulation of QCD Jets Including Soft Gluon Interference*, *Nucl.Phys.* **B238** (1984) 1.

[115] G. Marchesini and B. Webber, *Monte Carlo Simulation of General Hard Processes with Coherent QCD Radiation*, *Nucl.Phys.* **B310** (1988) 461.

[116] S. Gieseke, P. Stephens, and B. Webber, *New formalism for QCD parton showers*, *JHEP* **0312** (2003) 045, [hep-ph/0310083].

[117] G. Corcella, I. Knowles, G. Marchesini, S. Moretti, K. Odagiri, *et. al.*, *HERWIG 6: An Event generator for hadron emission reactions with interfering gluons (including supersymmetric processes)*, *JHEP* **0101** (2001) 010, [hep-ph/0011363].

[118] M. Bähr, S. Gieseke, M. Gigg, D. Grellscheid, K. Hamilton, *et. al.*, *Herwig++ Physics and Manual*, *Eur.Phys.J.* **C58** (2008) 639.

[119] M. Bengtsson and T. Sjöstrand, *A Comparative Study of Coherent and Noncoherent Parton Shower Evolution*, *Nucl. Phys.* **B289** (1987) 810.

[120] T. Sjöstrand, S. Mrenna, and P. Z. Skands, *PYTHIA 6.4 Physics and Manual*, *JHEP* **0605** (2006) 026, [hep-ph/0603175].

[121] T. Sjöstrand, S. Mrenna, and P. Z. Skands, *A Brief Introduction to PYTHIA 8.1*, *Comput.Phys.Commun.* **178** (2008) 852, [arXiv:0710.3820].

[122] S. Catani and M. Seymour, *A General algorithm for calculating jet cross-sections in NLO QCD*, *Nucl.Phys.* **B485** (1997) 291, [hep-ph/9605323].

[123] D. A. Kosower, *Antenna factorization of gauge-theory amplitudes*, *Phys. Rev.* **D57** (1998) 5410, [hep-ph/9710213].

[124] D. A. Kosower, *Antenna factorization in strongly-ordered limits*, *Phys. Rev.* **D71** (2005) 045016, [hep-ph/0311272].

[125] A. Gehrmann-De Ridder, T. Gehrmann, and E. W. N. Glover, *Antenna Subtraction at NNLO*, *JHEP* **09** (2005) 056, [hep-ph/0505111].

[126] G. Gustafson, *Multiplicity distributions in QCD cascades*, *Nucl.Phys.* **B392** (1993) 251.

[127] F. A. Berends and W. Giele, *Multiple Soft Gluon Radiation in Parton Processes*, *Nucl.Phys.* **B313** (1989) 595.

[128] D. Amati, A. Bassetto, M. Ciafaloni, G. Marchesini, and G. Veneziano, *A Treatment of Hard Processes Sensitive to the Infrared Structure of QCD*, *Nucl.Phys.* **B173** (1980) 429.

[129] **MCnet** Collaboration, A. Buckley, J. Butterworth, S. Gieseke, D. Grellscheid, S. Höche, *et. al.*, *General-purpose event generators for LHC physics*, *Phys.Rept.* **504** (2011) 145, [arXiv:1101.2599].

[130] L. Lönnblad, *ARIADNE version 4: A Program for simulation of QCD cascades implementing the color dipole model*, *Comput. Phys. Commun.* **71** (1992) 15.

[131] T. Sjöstrand, *A Model for Initial State Parton Showers*, *Phys.Lett.* **B157** (1985) 321.

[132] T. Sjöstrand and M. van Zijl, *A Multiple Interaction Model for the Event Structure in Hadron Collisions*, *Phys.Rev.* **D36** (1987) 2019.

[133] J. Lopez-Villarejo and P. Skands, *Efficient Matrix-Element Matching with Sector Showers*, *JHEP* **1111** (2011) 150, [arXiv:1109.3608].

[134] J. Lopez-Villarejo and P. Skands, *Strong and Smooth Ordering in Antenna Showers*, arXiv:1203.6803. In Les Houches SM and NLO Multileg and SM MC Working Groups: Summary Report.

[135] M. H. Seymour, *Matrix element corrections to parton shower algorithms*, *Comp. Phys. Commun.* **90** (1995) 95, [hep-ph/9410414].

[136] S. Catani, F. Krauss, R. Kuhn, and B. R. Webber, *QCD Matrix Elements + Parton Showers*, *JHEP* **11** (2001) 063, [hep-ph/0109231].

[137] L. Lönnblad, *Correcting the colour-dipole cascade model with fixed order matrix elements*, *JHEP* **05** (2002) 046, [hep-ph/0112284].

[138] G. Gustafson and U. Pettersson, *Dipole formulation of qcd cascades*, *Nucl. Phys.* **B306** (1988) 746.

[139] A. Gehrmann-De Ridder, T. Gehrmann, and E. Glover, *Infrared structure of e+ e- → 2 jets at NNLO*, *Nucl.Phys.* **B691** (2004) 195, [hep-ph/0403057].

[140] A. Gehrmann-De Ridder, T. Gehrmann, E. Glover, and G. Heinrich, *Infrared structure of e+ e- → 3 jets at NNLO*, *JHEP* **0711** (2007) 058, [arXiv:0710.0346].

[141] B. Andersson, G. Gustafson, and C. Sjögren, *Comparison of the dipole cascade model versus O(alpha- s**2) matrix elements and color interference in e+ e- annihilation*, *Nucl. Phys.* **B380** (1992) 391.

[142] R. K. Ellis, D. A. Ross, and A. E. Terrano, *Calculation of Event Shape Parameters in e+ e- Annihilation*, *Phys. Rev. Lett.* **45** (1980) 1226.

[143] R. K. Ellis, D. A. Ross, and A. E. Terrano, *The Perturbative Calculation of Jet Structure in e+ e- Annihilation*, *Nucl. Phys.* **B178** (1981) 421.

[144] P. Z. Skands and S. Weinzierl, *Some remarks on dipole showers and the DGLAP equation*, *Phys.Rev.* **D79** (2009) 074021, [arXiv:0903.2150].

[145] S. Catani, B. Webber, and G. Marchesini, *QCD coherent branching and semiinclusive processes at large x*, *Nucl.Phys.* **B349** (1991) 635.

[146] A. J. Larkoski and M. E. Peskin, *Spin-Dependent Antenna Splitting Functions*, *Phys. Rev.* **D81** (2010) 054010, [arXiv:0908.2450].

[147] Y. Dokshitzer and G. Marchesini, *Monte Carlo and large angle gluon radiation*, *JHEP* **0903** (2009) 117, [arXiv:0809.1749].

[148] Z. Nagy and D. E. Soper, *Final state dipole showers and the DGLAP equation*, *JHEP* **0905** (2009) 088, [arXiv:0901.3587].

[149] A. J. Larkoski, J. J. Lopez-Villarejo, and P. Skands, *Helicity-Dependent Showers and Matching with VINCIA*, arXiv:1301.0933.

[150] **L3 Collaboration** Collaboration, P. Achard *et. al.*, *Studies of hadronic event structure in e^+e^- annihilation from 30-GeV to 209-GeV with the L3 detector*, *Phys.Rept.* **399** (2004) 71, [hep-ex/0406049].

[151] **ALEPH** Collaboration, A. Heister *et. al.*, *Studies of QCD at e+ e- centre-of-mass energies between 91-GeV and 209-GeV*, *Eur. Phys. J.* **C35** (2004) 457.

[152] W. J. Stirling, *Hard QCD working group: Theory summary*, *J.Phys.* **G17** (1991) 1567–1574.

[153] M. Cacciari, G. P. Salam, and G. Soyez, *FastJet User Manual*, *Eur.Phys.J.* **C72** (2012) 1896, [arXiv:1111.6097].

[154] A. Buckley, H. Hoeth, H. Lacker, H. Schulz, and J. E. von Seggern, *Systematic event generator tuning for the LHC*, *Eur.Phys.J.* **C65** (2010) 331, [arXiv:0907.2973].

[155] J. Alcaraz Maestre *et. al.*, *The SM and NLO Multileg and SM MC Working Groups: Summary Report*, arXiv:1203.6803.

[156] A. Buckley and M. Whalley, *HepData reloaded: Reinventing the HEP data archive*, *PoS* **ACAT2010** (2010) 067, [arXiv:1006.0517].

[157] **Particle Data Group** Collaboration, J. Beringer *et. al.*, *Review of Particle Physics (RPP)*, *Phys.Rev.* **D86** (2012) 010001.

[158] A. Pich, *Review of α_s determinations*, arXiv:1303.2262.

[159] M. Ritzmann, D. Kosower, and P. Skands, *Antenna Showers with Hadronic Initial States*, *Phys.Lett.* **B718** (2013) 1345–1350, [arXiv:1210.6345].

[160] E. Boos, M. Dobbs, W. Giele, I. Hinchliffe, J. Huston, *et. al.*, *Generic user process interface for event generators*, hep-ph/0109068.

Summary

Particle physics aims to discover, understand and describe the elementary particles that are the building blocks of all matter present in the universe. Constituents of matter are most easily found by demolition, and our universe would not look the way it does if elementary particles would reveal themselves easily. This forces scientists to an aggressive approach, colliding (composite) stable particles at the highest energy available by accelerating them to nearly the speed of light. The most powerful accelerator built so far, the *Large Hadron Collider* (LHC) has become operable in 2009. The LHC is designed to collide protons at approximately 14 TeV, equivalent to the kinetic energy present in a flying mosquito. The LHC squeezes this energy into a proton, an object which is approximately 10^{14} times smaller. The energy determines the masses of the particles that are created in the collisions as can be seen in Einstein's law of $E = mc^2$.

Before the LHC became operational, its predecessors had already discovered a variety of elementary particles. These particles are grouped into families whose members behave similarly in interactions with other particles. Three main groups can be distinguished: the leptons, quarks and bosons. The existence of an omnipresent Higgs field with associated *Higgs boson*, was predicted during the construction of the *Standard Model* (SM), the theory describing all these particles and their interactions. Only by postulating the existence of a new unseen particle, were theorists able to allocate masses to observed particles in the model. The discovery of the Higgs boson in 2012 comes 48 years after its prediction in 1964, characterizing the large time scales related to the construction of big accelerator experiments.

The Standard Model has been tested to impressive accuracy which leaves little room for unknown physics at minute length scales explored so far. However, tests of the Standard Model's validity are also provided at extremely large length scales: the movement of large scale objects in the universe studied by astrophysicists. For instance, the movement of galaxies governed by gravity, implies the existence of unseen *dark matter*, as the amount of the visible matter alone cannot explain it. Dark matter must also be made of particles, however the Standard Model does not provide a candidate particle. This motivates among other reasons, the development of more theories. One such idea is *supersymmetry*, a theory that postulates the existence of superpartners to all known Standard Model particles and that does provide a dark matter candidate. The supersymmetric particles

must have masses beyond currently explored limits, otherwise they would have already been observed in accelerator experiments. The supersymmetry can therefore only exists at very high energies, allowing a lower energy scale mechanism to break the symmetry in the particle masses. Other models are also interesting, as long as they contain the Standard Model supplemented with ideas that provide answers or insights to open questions. Collectively such theories are therefore often referred to as *Beyond the Standard Model (BSM)* theories .

While the development of increasingly large accelerator experiments requires some tens of years before they collect data, theoretical work on BSM theories continues. One of the LHC's tasks will be to exclude, or confirm, as much as possible of BSM physics and simultaneously perform precision measurements that test the Standard Model's validity. The development of strategies that *distinguish between the Standard Model and BSM theories* is thus of crucial importance for the LHC. This translates to isolating parts of the BSM that deviate from SM behavior. A very interesting approach is based on a property of subatomic particles called spin.

Spin is quantum property of a particle that relates to the physical conservation law of angular momentum. This law is comparable to Einstein's $E = mc^2$, where in this case the angular momentum of a particle is transferred elsewhere when the spin is changed. Spin was discovered by two Dutch physicists Uhlenbeck and Goudsmit in Leiden in 1925. Leptons and quarks have spin $\frac{1}{2}$, commonly referred to as fermions, while bosons have spin 0 or 1. Bosons and fermions behave very differently. For instance bosons can be in the same state while fermions always need to be in different states (when they are in one place with the same velocity). Spin relates peculiarly to our general interpretation of measuring. The type of particle (boson or fermion) determines the amount of spin to be either $\frac{1}{2}$ or 1 times the unit of spin (spin 0 is a trivial measurement). It is a quantum property that the spin is always found along the measuring axis either in the *up or down* direction, even if the measurement is followed by a measurement in perpendicular direction. Spin is thus always pointing in either way of your measuring axis regardless of the direction of your measuring axis.

Both the Standard Model and BSM theories produce particles with up and down spin (along some axis), but models can differ in their preference to produce spin up or spin down type particles. This difference can be exploited to distinguish between Standard Model and BSM theories. The asymmetry in spin is measured with *polarization*, which effectively compares the amount of particles produced with up spin, to the amount of particles produced with spin down. Interestingly, this difference is most notable when spin is measured along the direction of movement (longitudinal polarization). We use the top quark to study polarization in this thesis, as this quark immediately decays into other elementary particles instead of forming a bound state as lighter quarks do. The decay allows for the tracing of spin information. The *angular distributions* of the the top quark decay products can easily be correlated with polarization in the top rest frame. This is more complicated in the laboratory frame, where the top quark is moving, which focusses

the decay products towards the top quark direction of movement. As a result the trace of polarization in the angular distributions of the top quark decay products is weakened in the laboratory frame. It is interesting to study polarization in the laboratory frame as this relates more obviously to LHC data. The main goal of chapter 3 and 4 is to investigate the sensitivity of the angular distributions of the top decay product, to the polarization of a top quark produced in the Standard Model and a BSM theory in the laboratory frame. This approach is supplemented with a study of the correlation between polarization and the energy of the top decay product for cases where it is difficult to accurately measure the emission angle of the decay particle.

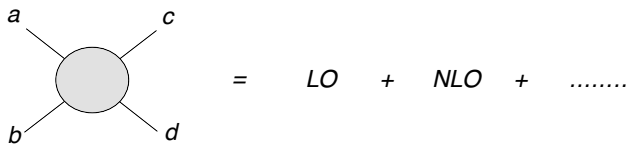

Figure D.1: Graphical representation of the prediction of a particle scattering calculated in perturbation theory.

The above approaches require accurate *theoretical predictions*, based on Standard Model and BSM theories, to test the robustness of polarization. For this we use perturbation theory, an approach that makes successively better predictions. The simplest approximation is called *Leading Order* (LO) and the first correction to it the *Next-to-Leading-Order (NLO)* term and so on. To use perturbation theory wisely requires thorough knowledge on the precision of calculations. Predictions of Standard Model observables are known to increase up to 30% when higher order corrections to the simplest approximation are taken into account. Lacking a thorough investigation of the influence of higher order terms for Standard Model observables can cause measurements to be mistaken for Standard Model deviations (and deviations are interpreted as signs for BSM). While the benefit of NLO predictions might be obvious, the calculations become increasingly complicated with each step in the perturbative series.

The idea of using polarization as a probe to distinguish between the Standard Model and BSM theories was already known. Though it had not been investigated prior to the work in this thesis, how the inclusion of NLO corrections influenced the usefulness of such approaches . Chapter 2 examined the effect of higher order corrections for producing a top quark in the Standard Model and a Two Higgs Doublet Model, a BSM with a larger Higgs sector. We found that the inclusion of *NLO weakens the signal of polarization slightly*, but that it remains sufficiently strong to distinguish between the Standard Model and BSM and provide information on the BSM parameters. A similar result was found for the energy distributions, although relating these distributions usefully to the BSM parameters was found to be more challenging and dependent on the model's parameters. This result

motivated the work in the next chapter to be carried out, at LO, where we investigated how supersymmetric parameters influence the polarization of a top quark in the context of a supersymmetic BSM. As supersymmetry has not yet been discovered, these parameters can take a wide range of values. We found that polarization can be a *useful probe for supersymmetric parameters* when the masses of sparticles are known.

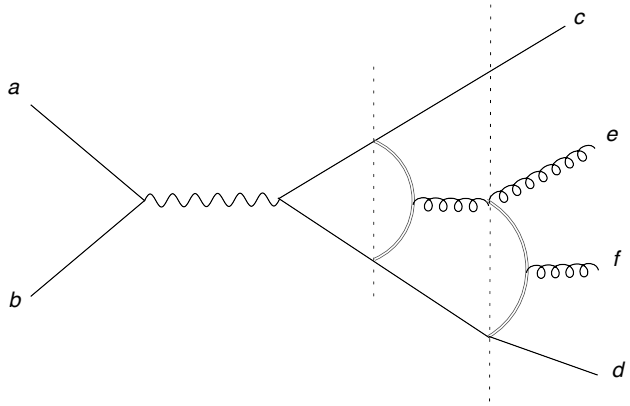

Figure D.2: Simulation of an event with an antenna shower. Initial particles a and b form a new particle that decays into particle c and d. The latter two particles then form an antenna and radiate off particle e. At the point illustrated by the second dotted line, there are two competing antennae $c-e$ and $e-d$. A computer algorithm will decide which antenna will win the competition and is allowed to radiate a particle. The line type indicates the type of particle, straight for a quark and wiggly and curly lines denote different gauge bosons.

The polarization studies have used computer simulations of particle collisions (*event simulation*). A very fast way to simulate events is by building up the collision iteratively. The starting point is a LO calculation of a particle scattering denoted in fig. D.4 by particles a and b scattering into particle c and d through a short lived particle. Additional final state particles are generated by forming an antenna between particles c and d, that together radiate a third particle e. The next evolution step has two antennae to choose from, and a computer algorithm will decide which competing antenna will win the right to radiate off another particle. The evolution is guided by a timelike parameter that terminates the shower at a preset time. In order for the generated event to behave according to what the prediction of the Standard Model or BSM theory predicts requires an additional step called matching. We have discussed the VINCIA antenna shower including its matching procedure in detail in chapter 5. The shower already contained a LO matching prescription, and the work in this thesis generalized this to a *NLO matching procedure* in chapter 6 for an electron and positron (anti-electron) decaying into three massless particles. Our approach shows impressive results on speed in comparison to existing generators.

Samenvatting

Deeltjesfysica wil de elementaire deeltjes die de bouwstenen van materie vormen ontdekken, begrijpen en beschrijven. Het slopen van materie biedt daarbij de makkelijkste kijk in de bestanddelen, en ons universum zou er niet uitzien zoals het doet, als elementaire deeltjes zichzelf makkelijk prijs zouden geven. Dit dwingt wetenschappers tot een agressieve methode, het botsen van stabiele (samengestelde) deeltjes op een zo hoog mogelijke energie door ze te versnellen tot bijna de lichtsnelheid. De meest krachtige versneller gebouwd tot nu toe, de *Large Hadron Collider* (LHC) is in 2009 in gebruik genomen. The LHC is gebouwd om protonen met ongeveer 14 TeV te laten botsen, te vergelijken met de bewegingsenergie van een vliegende mug. De LHC propt deze energie in een proton, een object dat ongeveer 10^{14} keer kleiner is. De energie bepaalt de massa's van de deeltjes die geproduceerd worden in de botsing volgens Einstein's $E = mc^2$.

Voordat de LHC operationeel werd, was al een verscheidenheid aan elementaire deeltjes ontdekt door zijn voorgangers . Deze deeltjes worden gegroepeerd in families wiens leden zich vergelijkbaar gedragen in interacties met andere deeltjes. Die deeltjes kunnen opgedeeld worden in drie basisgroepen: leptonen, quarks en bosonen. Het bestaan van een overal aanwezig Higgsveld, en het daaraan gekoppelde *Higgs boson*, werd voorspeld tijdens de ontwikkeling van het *Standaard Model* (SM), de theorie die al deze deeltjes en hun interacties beschrijft. Alleen door aan te nemen dat er nog een nieuw deeltje bestond, waren theoretici in staat om de geobserveerde deeltjes massief te maken in het model. De ontdekking van het Higgs boson in 2012 komt 48 jaar na zijn voorspelling in 1964, wat de lange tijdschaal van grote versneller experimenten kenmerkt.

Het Standaard Model is tot op indrukwekkende nauwkeurigheid getest, en dat laat weinig ruimte voor nieuwe ontdekkingen op de onderzochte lengteschalen. Proeven komen echter ook van extreem grote lengteschalen: de beweging van grote objecten in het universum bestudeerd door astrofysici. De beweging van de melkweg, gedomineerd door zwaartekracht, kan niet worden verklaard op basis van alle zichtbare materie, wat duidt op de aanwezigheid van *donkere materie*. Donkere materie moet ook opgebouwd zijn uit deeltjes, maar het Standaard Model heeft geen kandidaatdeeltje. Dit, onder andere redenen, motiveert de ontwikkeling van alternatieve modellen. Een idee heet *supersymmetrie*, een theorie die het bestaan van superpartners voorspelt van alle Standaard Modeldeeltjes en die wel een kandidaatdeeltje heeft voor donkere materie. De supersymmetrische deeltjes

moeten grotere massa's hebben dan huidig onderzochte limieten, anders waren ze al gevonden in versneller-experimenten. De supersymmetrie kan daarom alleen op hele hoge energieën bestaan, zodat een mechanisme ervoor kan zorgen dat op lagere energieën de symmetrie tussen de massa's gebroken is. Andere modellen zijn ook interessant, zolang zij het Standaard Model bevatten, aangevuld met ideeën die antwoorden of inzichten bieden aan openstaande vragen. Zulke theorieën worden vaak collectief *Boven het Standaard Model* (BSM) theorieën genoemd.

Terwijl het ontwikkelen van een nieuw versneller-experiment vaak tientallen jaren duurt voordat er botsingen plaats vinden, gaat het theoretische werk aan BSM theorieën door. Een van de taken van de LHC is om zoveel mogelijk BSM gevallen uit te sluiten, of aan te tonen, terwijl er simultaan precisiemetingen worden uitgevoerd die het Standaard Model's voorspellende kracht testen. De ontwikkeling van methodes die *onderscheid maken tussen het Standaard Model en BSM theorieën* is daarom van cruciaal belang voor de LHC. Dit betekent zoeken naar metingen waarbij een BSM iets anders voorspelt dan het Standaard Model. Een interessante strategie is gebaseerd op een eigenschap van subatomaire deeltjes genaamd spin.

Spin is een kwantumeigenschap van een deeltje die te maken heeft met de fysische behoudswet van rotatie-energie. Deze wet is vergelijkbaar met Einstein's $E = mc^2$, waarbij in dit geval de rotatie-energie ergens heen wordt overgedragen als de spin wordt veranderd. Spin is ontdekt door de twee Nederlandse natuurkundigen Uhlenbeck en Goudsmit in Leiden in 1925. Leptonen en quarks hebben spin $\frac{1}{2}$, en worden fermionen genoemd, terwijl bosonen spin 0 of 1 hebben. Bosonen en fermionen gedragen zich heel anders. Bosonen mogen bijvoorbeeld in dezelfde toestand zitten terwijl fermionen altijd in andere toestanden moeten zitten (als ze op dezelfde plek met dezelfde snelheid zijn). Verder is het maar vreemd om te interpreteren wat er met spin gemeten wordt. Het type deeltje (boson of fermion) bepaalt dat de hoeveelheid te meten spin $\frac{1}{2}$ of 1 keer de spin-eenheid is (spin 0 is een triviale meting). Het is een kwantumeigenschap dat de gehele spin altijd gevonden wordt langs de metingsas in de *omhoog of omlaag* richting, zelfs als die meting wordt gevolgd door een meting met een as loodrecht op de vorige as. Spin staat dus altijd in de richting van de as waaraan je meet, onafhankelijk van hoe de as gekozen is.

Zowel het Standaard Model als BSM theorieën produceren deeltjes met spin omhoog en omlaag (ten opzichte van een as), maar de mate waarin ze liever deeltjes met spin omhoog produceren dan spin omlaag kan wel verschillen. Dit kan gebruikt worden om onderscheid te maken tussen het Standaard Model en BSM theorieën. De asymmetrie in spinkeuze wordt gemeten met *polarisatie*, wat effectief het aantal deeltjes met spin omhoog vergelijkt met het aantal deeltjes met spin omlaag. Dit verschil is het grootst als de spin wordt gemeten langs de as van bewegen (longitudinale polarisatie). We gebruiken het top quark om polarisatie te bestuderen, omdat de top onmiddellijk vervalt in andere deeltjes in plaats van een geboden toestand te vormen zoals lichtere quarks. Het verval maakt het mogelijk om spin-informatie te traceren. De *hoekverdelingen* van de vervalsprodukten van het top quark kunnen makkelijk gecorreleerd worden met polarisatie in

het rustsysteem van de top. In het systeem waarin de top beweegt (het laboratorium systeem), is dit lastiger omdat de beweging van de top ervoor zorgt dat de vervalsprodukten sterker in de richting van beweging gefocust zijn. Als gevolg verzwakt het spoor van polarisatie in de hoekverdelingen van de top vervalsprodukten in het laboratoriumsysteem. Toch is het interessant om in het laboratoriumsysteem te werken, omdat dit makkelijk aan LHC data gerelateerd kan worden. Het doel van hoofdstuk 3 en 4 was om de gevoeligheid in de hoekverdelingen van de top vervalsprodukten te meten voor verschillen tussen het Standaard Model en een BSM theorie in het laboratorium systeem. Deze strategie is aangevuld met een studie tussen de polarisatie en de energie van het vervalsdeeltje voor situaties waar de hoek niet goed te bepalen is.

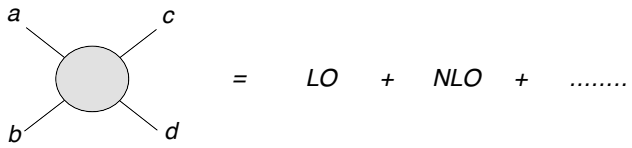

Figuur D.3: Grafische weergave van de voorspelling van een deeltjesbotsing in storingstheorie.

Bovenstaande methodes vereisen nauwkeurige *theoretische voorspellingen*, gebaseerd op Standaard Model en BSM theorieën, om de robuustheid van polarisatie te testen. We gebruiken hier storingstheorie voor, een benadering die stapsgewijs betere voorspellingen geeft. De simpelste benadering wordt *Leidende Orde* (LO) genoemd, en de eerste correctie hierop de *Na-Leidende-Order* (NLO) term en zo door. Storingstheorie kan alleen verantwoord gebruikt worden met gedegen kennis van de nauwkeurigheid van een berekening. Voorspellingen van waarneembare grootheden uit het Standaard Model kunnen wel 30 % groter worden als hogere orde correcties op de simpelste voorspelling worden toegevoegd. Wanneer de invloed van hogere orde correcties niet goed is uitgezocht, kunnen de waarneembare grootheden worden geïnterpreteerd als een afwijking van het Standaard Model (en dat wordt weer als teken voor BSM gezien). Het is duidelijk dat NLO correcties daarom van groot belang zijn, helaas worden de berekeningen steeds complexer met iedere stap in de storingsreeks.

Het principe van onderscheid maken tussen het Standaard Model en BSM theorieën op basis van polarisatie was al bekend. Maar voor het werk in dit manuscript was nog niet onderzocht hoe het meenemen van NLO correcties de kracht van het signaal zou veranderen. Hoofdstuk 2 onderzocht het effect van hogere orde correcties wanneer een top quark wordt geproduceerd in het Standaard Model en een Twee Higgs Doublet Model, een BSM met een grotere Higgs sector. We vonden dat *NLO correcties het polarisatie-signaal iets verzwakken*, maar dat het voldoende sterk blijft om onderscheid te maken tussen het Standaard Model en de BSM, en bovendien informatie geeft over BSM parameters. Eenzelfde resultaat werd gevonden voor de energiedistributies, alhoewel het moeilijker was

om deze verdelingen zinvolle voorspellingen te laten doen over de parameters van het model. Dit resultaat motiveerde om het onderzoek in het volgende hoofdstuk op LO uit te voeren, waar we onderzochten hoe supersymmetrische parameters de polarisatie van een top quark beïnvloeden in de context van een supersymmetrische BSM. Omdat supersymmetrie nog niet ontdekt is, kunnen de parameters nog veel waardes aannemen. Ons onderzoek toont aan dat polarisatie een *nuttige indicator is voor supersymmetrische parameters* mits de massa's van de supersymmetrische deeltjes bekend zijn.

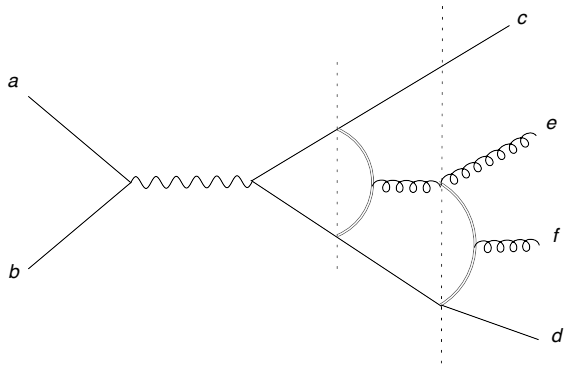

Figuur D.4: Simulatie van een botsing met een antenne-regen. Binnenkomende deeltjes a en b vormen een nieuw deeltje dat vervalt in deeltje c en d. De laatste twee deeltjes vormen samen een antenne en stralen een nieuw deeltje af. Op het punt geïllustreerd met de tweede stippellijn zijn er twee strijdende antennes $c - e$ en $e - d$. Een computer-algoritme zal beslissen welke antenne de competitie wint en een nieuw deeltje af mag stralen. Het lijntype duidt aan wat voor deeltje propageert, een rechte lijn staat voor een quark en de wiebel- en krullijn voor verschillende ijkbosonen.

De polarisatiestudies hebben gebruik gemaakt van *computersimulaties van botsingen*. Een hele snelle methode bouwt een botsing iteratief. Het startpunt is een LO berekening van een botsing, weergeven in fig. D.4 door deeltjes a en b die verstrooien naar deeltjes c en d via een onstabiel deeltje. Nieuwe deeltjes in de eindtoestand worden gegenereerd door een antenne te vormen tussen deeltjes c en d, die samen deeltje e afstralen. De volgende evolutiestap kan kiezen tussen twee antennes, en een computer-algoritme zal kiezen welke antenne het recht wint om een deeltje af te stralen. Deze evolutie wordt gefaciliteerd door een tijdachtige parameter die de evolutie op een gezette tijd stopt. Om ervoor te zorgen dat de gegenereerde botsing zich uiteindelijk gedraagt zoals het Standaard Model of de BSM voorspelt, vereist een extra stap die de koppeling naar storingstheorie maakt. We hebben in hoofdstuk 5 de VINCIA antenne-regen uitgebreid besproken inclusief gebruikte koppelingsmethode. De antenne-regen bevatte al een LO koppeling, en het werk in dit manuscript heeft dat uitgebreid naar een *NLO koppeling* in hoofdstuk 6 for een electron en positron (antielectron) die vervalt naar drie massaloze deeltjes. De methode blijkt bijzonder snel te zijn vergelijkbaar met andere methodes.

Dankwoord

Ik heb ontzettend veel geleerd gedurende mijn promotie-onderzoek, niet alleen door het werk zelf maar ook van de mensen met wie ik heb kunnen samenwerken en die mij gesteund hebben in deze periode. Graag wil ik iedereen daarvoor bedanken waarbij ik begin bij mijn promotor en begeleider Eric Laenen. Dankjewel voor de mogelijkheid om vier jaar lang onderzoek te doen bij de theoriegroep aan het Nikhef. Het uiteindelijke werk in dit manuscript heeft een heel andere wending genomen dan jij oorspronkelijk in gedachten had en ik wil je bedanken in je aanmoediging om aan andere projecten te werken. Je kennis van NLO berekeningen heeft me veel geleerd en bleek cruciaal voor andere projecten. Bovendien creëerde jij het platform waarop de top-polarisatie artikelen tot stand kwamen. Bedankt voor je onbegrensde vertrouwen in mijn vermogen om dit alles succesvol af te sluiten en je geduld om mij een kritische blik bij te brengen.

It feels like I had two additional mentors during the course of my PhD besides Eric. First I would like to thank Rohini Godbole, for sharing your knowledge of top polarization in BSM physics and especially providing excellent ideas for projects described in this thesis. Rohini, you have been a very fun and inspiring person to work with and I would like to thank you for your time and willingness to explain things. Next I would like to thank Peter Skands, unitarity matching pioneer, to give a very important project to me on a pure leap of faith. The distance between us and limited literature made this project very challenging in the start-up phase, but it had a very successful finish. Thank you also for your time, your guidance and encouragement during the course of this project. And all the fun moments we had in between or after work. I would also like to thank Stefan Prestel and Torbjörn Sjöstrand for valuable discussions on matching parton showers during my stay in Lund.

Ook zijn de bijdrages van Irene Niessen en Chris White belangrijk geweest in de totstandkoming van dit proefschrift. Chris, bedankt voor je hulp bij MC@NLO, je onvermoeibare bereidheid om vragen te beantwoorden en je fantastische gevoel voor humor. Irene wil ik bedanken voor haar kritische blik, haar persoonlijke introductie in de supersymmetrie en bovendien een vriendschap die me door de lastige momenten heen steunde. Wim Beenakker, dankjewel voor je kritische proeflezing.

I learned a lot of skills complementary to research in the PhD council. Thank you Rolf, Serena and Daniel for the hard work on the PhD student survey, I am really proud of what we achieved together and it was great to work in a team with you. As most of the research was usually done in isolation, having good office members made all the

difference for some relaxation time and I was lucky to have excellent company during the four years. Thank you Gerben, Meike, Jan, Mert, Giuseppe, Nabamita and Kalliopi. And thank you Sander Mooij, who's great jokes, and many shoulder pads supported me all the way. And Reinier who always had encouraging words. The theory department harbored quite some people of which I would like to thank a few in person. Thank you Valentin, Ivano, Thomas, Florian, Michel, Michele, Gideon, Damien, Bart, Erica, Rob, Marieke and the other members, forgive me if I have forgotten you! Jos, thank you for all your explanations of FORM and motivational speeches.

I have also met some really nice people at other Nikhef departments, thanks to Robin, Rosemarie, Hegoi, Chiara, Gossie, Dox, Marten, Mark, Daan and Roel for good breaks. And of course thanks to the homies from Nijmegen Thijs, Gijs, Yiannis, Harm, Geert-Jan en Melvin for good times when I came around Nijmegen. I'd also like to thank Jan en Jordy for spicing up the TPP meetings and Milena and Jelena for the heart to heart talks! Thanks Menelaos, Dimitrios and Milosz for excellent evenings with chilling and music.

De BKB academie was een waardevolle afwisseling van natuurkunde-onderzoek, bedankt BKB en alle leden van academie 11 voor de leuke gesprekken, interessante discussies en nieuwe skills. Bedankt aan de meiden van de Chicks Only en in het bijzonder Nienke voor alle gezellige hardloopsessies. Don's bootcamp bedankt voor alle drillsessies in het Vondel. Lucas dankjewel voor de gezelligheid in de organisatie van de Nerdnites. Carel, bedankt voor de fantastische gesprekken en feestjes, Laura W. voor gezelligheid en steun, Joost voor lekkere dineetjes, Anne voor steun en vasthoudendheid! Janna dankjewel voor een warm plekje in Nijmegen, Eva voor je goede grappen en luisterend oor en Qury bedankt voor 't luisteren en vertrouwen! Hannah, wat fijn dat jij altijd voortgang en groei zag en dat ook aan mij liet zien. Janneke en Patrick bedankt voor aanmoedigende berichten tijdens het schrijven. Thijs wat fijn dat je weer in dit land zit, jij bedankt voor je vriendschap. Tim, Esther, Maud en Jan bedankt voor de mooie feestjes. Steph bedankt voor de gezelligheid. Ed bedankt voor feestjes en heerlijke pauzes op Nikhef. Joris bedankt voor het kat-oppassen tijdens mijn CERN verblijf en je gezellige etentjes. Gabriel, bedankt voor onze mooie gesprekken en het ontwerpen van de cover. Andrea en Catherine, jullie zijn de beste buren die ik me kan wensen, bedankt voor hele fijne gesprekken, en ook kattenopvang. Daniel bedankt voor advies en gezellige hardloop- en kooksessies. Frans bedankt dat je gezellig af en toe nog mijn leven binnen komt vallen. Bas en Tanneke bedankt voor gezellige etentjes. Floris bedankt voor goede gesprekken. Huib, heel erg bedankt voor je fantastische steun! Cees dankjewel voor je aanmoediging om door te zetten. Irene K., bedankt voor het luisterend oor.

Dan wil ik nog graag mijn vriendje Johan bedanken. Bedankt voor je liefde, steun, en aanmoediging. Die laatste maanden zijn zoveel leuker geweest doordat jij er was! Als laatste de mensen die me zoveel gegeven hebben in de afgelopen vier jaar en op de moeilijkste momenten voor me klaar stonden. Hier hoort Irene N. gewoon nog een keer, thanks meid. Wilco, wat hebben we mooie feestjes gehad, maar wat heb je ook veel geluisterd en geadviseerd als ik worstelde met het onderzoek. Lucie dankjewel voor bijzonder momenten waarin we alles deelden. Laura dankjewel voor mijn plekje in Nijmegen en je toegewijde vriendschap, door dik en dun. Shanna en Hilde, ik heb van jullie allebei zoveel geleerd, jullie compassie werkte heel verzachtend en maakte alle verschil.